

Quantum Gravity and Laser Interferometry: Towards Observable Predictions

Thesis by
Yiwen Zhang

In Partial Fulfillment of the Requirements for the
degree of
Doctor of Philosophy

The logo for the California Institute of Technology (Caltech), featuring the word "Caltech" in a bold, orange, sans-serif font.

CALIFORNIA INSTITUTE OF TECHNOLOGY
Pasadena, California

2025
Defended April 3rd, 2025

© 2025

Yiwen Zhang

ORCID: 0000-0003-2355-9416

All rights reserved

ACKNOWLEDGEMENTS

I would like to express my deepest gratitude to those who have supported me throughout my PhD journey.

First, I thank my advisor, Professor Kathryn Zurek, for her supervision and financial support during parts of my PhD. Her influence played an instrumental role in helping me realize that the world beyond physics is full of wonder and possibilities, strengthening my resolve to pursue a far more rewarding and meaningful path outside academia. Furthermore, I express my deepest gratitude to my thesis committee chair, Professor Yanbei Chen, for his steadfast support, insightful guidance, and encouragement throughout the most challenging periods of my PhD. His mentorship has been crucial in both my academic progress and personal growth. I am also very grateful to my thesis committee members, Professor Clifford Cheung and Professor Lee McCuller, for their thoughtful feedback, constructive criticism, and the time they have dedicated to reviewing my work.

In addition to my thesis committee, I am deeply grateful to my postdoctoral collaborator and friend, Temple He, whose mentorship and support have been invaluable. He has guided me through research challenges with patience and encouragement, while also offering valuable life advice beyond academia. His encouragement has been instrumental in helping me navigate obstacles with resilience and optimism.

A special thanks goes out to my collaborators, whose intellectual discussions and collaborations have enriched my research experience. I am particularly thankful to Professor Cynthia Keeler, Kwinten Fransen, Allic Sivaramakrishnan, Sang-Eon Bak, Mathew Bub, Yufeng Du, and Dongjun Li for their collaboration.

I would like to thank my friends at Caltech, including Nathan Benjamin, Cyuan-Han Chang, Maria Derda, Yufeng Du, Mrunmay Jagadale, Yanky Landau, Jaeha Lee, Vincent Lee, Dongjun Li, Aike Liu, Liam O'Brien, and Yixin Xu for bringing joy and light to my PhD journey. Their laughter, support, and companionship have been a source of comfort, making the toughest moments more bearable. From after-work dinner gatherings to spontaneous adventures, their friendship has made this experience truly memorable. I am deeply grateful to Carol Silberstein for her tremendous support, from helping with day-to-day tasks to guiding me through the job search process ever since I joined the research group.

I am deeply grateful to my best friend, Christopher Yang, whose kindness and

generosity continually inspire me. When I was seriously ill with Covid, he sent me a care package filled with soup, tea, and nutritious snacks, a gesture of thoughtfulness that meant everything during that difficult time. His lifelong dedication to volunteer work has shown me the true meaning of compassion, proving that love can extend far beyond what we see. In addition, Christopher's humor has brought me endless joy, offering much-needed laughter and relief during stressful times. Our shared passion for photography and nature provided an escape and inspiration throughout my PhD journey. We embarked on countless photography trips, chasing golden-hour light, capturing wildlife, and marveling at the beauty of the natural world. Those adventures not only deepened our friendship, but also offered moments of serenity amid the demands of academic life. Christopher's companionship throughout my PhD has demonstrated that true friendships empower, uplift, and endure.

I also express my sincere gratitude to my best friend, Kevin Langhoff, whom I met at the University of Wisconsin-Madison in 2015. From the start, we built an ironclad bond. Kevin was the first to spark my passion for physics, and for nearly a decade, his support and encouragement have been unrelenting. He patiently helped me tackle challenging coursework and never stopped believing in me, even when I doubted myself. His detailed feedback — revising my personal statement five times — was instrumental in my acceptance to Caltech for my PhD. Throughout this journey, our weekly video calls and annual road trips through California's wilderness have given me motivation and a deep sense of renewal. Together, we trekked through towering redwoods, hiked along the sheer granite beside Yosemite Falls, and stood in awe under star-filled skies in Death Valley. Those journeys were more than an escape; they were a testament to the strength of our friendship, filled with conversations, laughter, and the shared wonder of discovery.

I am forever grateful to my host brother and best friend, Matthew Chimenti-Carmen, who welcomed me with open arms when I first arrived in the US in 2013. His very first words to me, "Are you a Celtics fan?", sparked a connection that would grow into a lifelong camaraderie. Although our paths diverged after high school, Matthew and his family have remained my steadfast supporters, making me feel at home even when I was far from it. For the past 12 years, they have welcomed me into their home every Christmas, offering warmth, generosity, and thoughtful gifts that reminded me that I was never alone. Matthew's friendship has supported me through life's challenges and helped me embrace a new culture with confidence. His unwavering loyalty and kindness have shaped my journey in ways that words cannot fully capture,

and I will always cherish the bond we share.

To my family, words cannot express how deeply grateful I am for their love, patience, and encouragement. Their support has been my foundation, giving me the strength to persevere through every challenge.

I especially thank my father, whose strict upbringing instilled in me the discipline to always strive for a better self. His high expectations pushed me beyond my limits, teaching me resilience, perseverance, and the value of hard work. Although his love was often expressed through tough words, it shaped me into the person I am today, always seeking growth and excellence.

My mother, on the other hand, has been my pillar of unconditional love and sacrifice. From the moment she selflessly let me go abroad to study in the US thirteen years ago, she has been my strongest supporter, always standing behind me no matter how far apart we were. She not only gave me the freedom to chase my dreams, but also accompanied me on countless adventures, from the volcanic landscapes of Hawaii to the vast wilderness of Yellowstone, from the shores of Lake Superior to the coast of San Diego. Through every mile and every minute, she has been there, reminding me that no matter where life takes me, I am never alone.

My grandmother, with great dedication, cooked almost every meal for me for nearly two decades. Her warmth and care filled my childhood with love, and her kitchen was more than a place of nourishment. It was a space where she showed her love in the most plain but profound way.

My grandfather, a man of great wisdom, played an instrumental role in shaping my early intellectual curiosity. From a young age, he tutored me in mathematics, not just teaching me numbers and equations, but cultivating in me a passion for learning and a love for discovery. His guidance sparked my intellectual journey, one that has led me to where I am today.

This material is based upon work supported by the U.S. Department of Energy, Office of Science, Office of High Energy Physics, under Award Number DE-SC0011632, and also by the Heising-Simons Foundation “Observational Signatures of Quantum Gravity” collaboration grant 2021-2817, as well as the GQuEST funding provided from the U.S. Department of Energy via FNAL: DE-AC02-07CH11359.

ABSTRACT

Understanding quantum gravity remains one of the deepest challenges in modern physics, as direct experimental access to Planck-scale effects is beyond current technological reach. However, recent theoretical advances indicate that quantum fluctuations of spacetime may produce measurable effects in precision experiments, particularly near causal horizons. This opens new avenues for testing quantum gravity phenomena through high-precision measurement techniques. This dissertation develops multiple theoretical models to characterize these effects and examines their potential observational signatures in future gravitational wave interferometers.

We begin by investigating the role of quantum fluctuations in near-horizon geometries through the lens of the AdS/CFT correspondence, which provides a powerful framework for understanding the interplay between quantum field theory and general relativity via holographic principles. By modeling stochastic energy-momentum sources in Rindler-AdS spacetime, we demonstrate that vacuum fluctuations transform the Einstein equations into a Langevin-type stochastic differential equation, leading to potentially observable fluctuations in photon traversal times. Extending this approach to Minkowski spacetime, we establish a correspondence between gravitational shockwaves and fluid dynamics, showing that near-horizon perturbations satisfy an equation analogous to that governing incompressible fluids, thereby reinforcing the membrane paradigm and hydrodynamic analogies in the context of the fluid/gravity duality. Furthermore, we construct the covariant phase space of a spherically symmetric causal diamond in Minkowski spacetime, identifying two fundamental charges that govern its evolution. These results provide a foundation for quantizing causal horizons and understanding their microscopic degrees of freedom.

Building upon these theoretical developments, we further examine a related stochastic phenomenon: the gravitational wave memory background arising from the cumulative memory steps produced by supermassive black hole mergers. After reviewing the standard stochastic gravitational wave background, gravitational memory effects, and BMS symmetries, we model the stochastic memory background using a Brownian motion framework. We show that while the cumulative memory background initially appears above the sensitivity curve of space-based interferometers like LISA, the realistic subtraction of individually resolvable merger events substantially suppresses the residual signal, making its detection more challenging. This highlights the critical importance of source subtraction when evaluating the

detectability of gravitational memory effects.

By bridging fundamental theory with experimental prospects, this dissertation contributes to the ongoing effort to uncover the quantum nature of spacetime through precision measurement techniques. Whether through detecting quantum spacetime fluctuations, gravitational memory backgrounds, or probing the symmetries of causal horizons, the pursuit of observable quantum gravity phenomena continues to expand the frontiers of both theory and experiment.

PUBLISHED CONTENT AND CONTRIBUTIONS

- [1] Sang-Eon Bak, Cynthia Keeler, Yiwen Zhang, and Kathryn M. Zurek. “Rindler fluids from gravitational shockwaves”. In: *JHEP* 05 (2024), p. 331. DOI: [10.1007/JHEP05\(2024\)331](https://doi.org/10.1007/JHEP05(2024)331). arXiv: [2403.18013](https://arxiv.org/abs/2403.18013) [hep-th].
Author contribution: YZ participated in the conception of this project, aided in the derivation of the key equations connecting gravitational shockwave geometries to their fluid duals, computed the fluctuations in photon traversal time due to quantum sources, produced all figures, and participated in the writing of the manuscript.
- [2] Mathew W. Bub, Yanbei Chen, Yufeng Du, Dongjun Li, Yiwen Zhang, and Kathryn M. Zurek. “Quantum gravity background in next-generation gravitational wave detectors”. In: *Phys. Rev. D* 108.6 (2023), p. 064038. DOI: [10.1103/PhysRevD.108.064038](https://doi.org/10.1103/PhysRevD.108.064038). arXiv: [2305.11224](https://arxiv.org/abs/2305.11224) [gr-qc].
Author contribution: YZ created the preliminary plot comparing Cosmic Explorer and Einstein Telescope strain sensitivities against the quantum gravity background predicted by the pixellon model, performed analysis on the Cardiff 3D interferometer configuration, and contributed to the writing of the manuscript.
- [3] Mathew W. Bub, Temple He, Prahar Mitra, Yiwen Zhang, and Kathryn M. Zurek. “Quantum Mechanics of a Spherically Symmetric Causal Diamond in Minkowski Spacetime”. In: *Phys. Rev. Lett.* 134.12 (2025), p. 121501. DOI: [10.1103/PhysRevLett.134.121501](https://doi.org/10.1103/PhysRevLett.134.121501). arXiv: [2408.11094](https://arxiv.org/abs/2408.11094) [hep-th].
Author contribution: YZ participated in the conception of this project, aided in the derivation of the symplectic structure and the associated Iyer-Wald charges, computed the quantum commutators of the charges, produced all figures, and contributed to the writing of the manuscript.
- [4] Yiwen Zhang and Kathryn M. Zurek. “Stochastic description of near-horizon fluctuations in Rindler-AdS”. In: *Phys. Rev. D* 108.6 (2023), p. 066002. DOI: [10.1103/PhysRevD.108.066002](https://doi.org/10.1103/PhysRevD.108.066002). arXiv: [2304.12349](https://arxiv.org/abs/2304.12349) [hep-th].
Author contribution: YZ participated in the conception of this project, derived the stochastic form of the Einstein equation near the light-sheet horizon using the ’t Hooft commutation relations, solved for the photon traversal time variance, created Figures 1–2, and contributed to the writing of the manuscript.

CONTENTS

Acknowledgements	iii
Abstract	vi
Published Content and Contributions	viii
Contents	viii
List of Figures	xi
List of Tables	xvi
Chapter I: Introduction	1
1.1 Theoretical Background	2
1.2 Laser Interferometers and Experimental Sensitivity	17
1.3 Scope and Contributions of This Dissertation	23
Chapter II: Stochastic Description of Near-Horizon Fluctuations in Rindler-AdS	29
2.1 Introduction	29
2.2 Preliminaries: Background Geometry	33
2.3 Near Horizon Metric Perturbations	35
2.4 Uncertainty in Photon Traversal Time From Near-horizon Quantum Fluctuations	41
2.5 Summary and Discussion	46
Chapter III: Rindler Fluids from Gravitational Shockwaves	47
3.1 Introduction	47
3.2 Rindler Fluids in Einstein Gravity	49
3.3 Near Horizon Fluids from Gravitational Shockwaves	54
3.4 Spacetime Fluctuations from Quantum Sources	61
3.5 Summary and Outlook	66
A1 Appendix: Derivation of the Brown-York Stress Tensor	67
Chapter IV: The Quantum Mechanics of a Spherically Symmetric Causal Diamond in Minkowski Spacetime	69
4.1 Introduction	69
4.2 Parametrization of the Causal Diamond	70
4.3 Derivation of the Symplectic Form	71
4.4 Hamiltonian Charges	74
4.5 Conclusion	78
B1 Appendix: Derivation of the Pre-symplectic Potential	79
B2 Appendix: Promotion of the Pre-symplectic Form to Symplectic Form	81
Chapter V: Quantum Gravity Background in Next-Generation Gravitational Wave Detectors	83
5.1 Introduction	83
5.2 Pixellon Model	85
5.3 High-Frequency GW Detectors	87
5.4 Extension of the Pixellon Model to Multiple Interferometers	93

5.5 Interferometer-like Experiments	99
5.6 Conclusions	112
Chapter VI: Stochastic Gravitational Wave Memory Background of Super- massive Binary Black Hole Mergers and Its Detection in LISA	113
6.1 Introduction	113
6.2 Stochastic Gravitational Wave Backgrounds: An Overview	117
6.3 Gravitational Memory and the BMS Symmetry	127
6.4 Stochastic Gravitational Wave Memory Background	135
6.5 Toward Detectability with LISA	139
6.6 Conclusion and Future Directions	151
Chapter VII: Conclusion and Outlook	153
Bibliography	155

LIST OF FIGURES

<i>Number</i>	<i>Page</i>
1.1 Pictorial depiction of the causal diamond in Rindler-AdS space anchored at the asymptotic AdS boundary. The red dashed line represents a laser trajectory traversing from the boundary to a point on the RT surface and then reflected back to the boundary [313].	11
1.2 Pictorial depiction of the quantum fluctuations modeled by gravitational shockwaves near the light-front of a causal diamond. Vacuum fluctuations T_{uu} and T_{vv} induce light cone time delay in δv and δu , respectively, on the lower and upper half of the causal diamond [312].	13
2.1 Depiction of the causal diamond in AdS space anchored at the boundary. The red solid line traces out the light signal emitted from the boundary to a point in the bulk on the Ryu-Takayanagi surface labeled by Σ_{d-2} , while the blue solid line represents the light reflected from the point in the bulk and received at the boundary. The dashed lines represents the smearing of the light-sheet horizon. The red and blue shaded region represents quantum gravity induced fluctuations of the light trajectory.	30
2.2 The causal diamond in Rindler-AdS space is foliated with a series nested causal diamonds. The separation between two adjacent diamonds is the decoherence length $\tilde{\ell}_p$. Each nested causal diamond intersects with the past (future) light front at a bifurcate horizon along the past (future) light front. The highlighted region corresponds to the near-light-sheet region of spacetime, where quantum fluctuations cause a probe photon to undergo random walk.	41

3.1	Minkowski Rindler space that represents a slice of a Minkowski diamond of size L . Blue and red dashed lines represent a series of nested causal diamonds along the past (future) light front. The shaded blue/red region is the “smearing” of the diamond due to quantum fluctuations modeled by gravitational shockwaves. This procedure is discussed in detail in Ref. [324]. In this chapter, we aim to describe the fuzzing of the light front in a Lorentz invariant manner. This leads to a hyperbolic cutoff surface (green curve), denoted as Σ_c . The proper distance between Σ_c and the bifurcate Rindler horizon is given by the relation $-uv = 4r_c/\alpha$	62
4.1	A causal diamond of radius L with null boundaries shown as solid red line. The blue dashed ellipse represents the d -dimensional bifurcation surface, while the constant u hypersurface is represented by the orange line.	72
4.2	Pictorial depiction of a series of “nested” causal diamonds. Charge H_α generates translation in null time $u \mapsto u + \lambda_\alpha$, whereas charge H_L generates shift in the size of the diamond, which corresponds to, at the bifurcate horizon \mathcal{B} , a translation in Minkowski time $\tilde{t} \mapsto \tilde{t} + \lambda_L$	79
5.1	Pixellon strain (dashed and dotted lines) overlaid with the strain sensitivities for CE [291] and ET [193] (solid lines). For CE, we have included both designs with arm lengths $L = 20$ km (orange lines) and $L = 40$ km (blue lines). The dotted lines give the pixellon strain from Eq. (5.35) computed without an IR cutoff, and the dashed lines give the same quantity including the IR cutoff from Eq. (5.28). The pixellon strain is computed with the benchmark value $\alpha = 1$	85
5.2	Plots of spherical entangling surfaces or spatial slices of the causal diamonds bounding different configurations of light beams. The shaded circles represent entangling surfaces, each of which is associated with a pixellon model. For all the figures above, we have projected the spherical entangling surface to the plane of the light beams.	94

5.3	Pixellon strain (dashed and dotted lines) overlaid with the strain sensitivities for LIGO [234] and NEMO [222] (solid lines). The LIGO data was obtained from the Livingston detector, and the NEMO data omits suspension thermal noise. The dotted lines give the pixellon strain from Eq. (5.35) computed without an IR cutoff, and the dashed lines give the same quantity including the IR cutoff from Eq. (5.28). We again compute the pixellon strain with $\alpha = 1$	100
5.4	Setup of ET. The red, blue, and purple rays correspond to the three detectors in ET, where we have only shown one of the two interferometers within each detector. We choose not to plot the mirrors at the endpoints of the light beams for simplicity.	103
5.5	The PSD $\tilde{C}_{\mathcal{T}}(\omega)$ of the cross-correlation function of two sets of interferometers within a triangular configuration like ET [Eq. (5.38), solid lines], together with the corresponding auto-correlation $\tilde{C}_{\mathcal{T}}(\omega, \theta = \frac{\pi}{3})$ of a single interferometer within this configuration [Eq. (5.31), dashed lines].	105
5.6	Schematic diagram of the optically-levitated sensor as described in Refs. [33, 21]. A dielectric sphere or microdisk is trapped in an anti-node of an optical cavity (solid orange). A second laser (dashed blue) is used to cool the sensor and read out its position. Transverse motion is cooled by additional lasers (not shown).	106
5.7	Two levitated sensors inserted into the Fabry-Pérot cavities of a Michelson interferometer, as described in Ref. [21]. The entangling surfaces corresponding to the two arms of length x_s and ℓ_m are marked by the blue and green shaded circles, respectively. Note that this diagram ignores the distances between the beam splitter and the input mirrors of the two cavities.	108
5.8	Pixellon PSD $\tilde{C}_{\mathcal{T}}^{\Delta X}(\omega, \theta)$ as it would appear in an optically-levitated sensor [Eq. (5.53), solid lines] shown alongside the PSD of an ordinary L-shaped interferometer $\tilde{C}_{\mathcal{T}}(\omega, \theta)$ [Eq. (5.31), dashed lines]. We take the length of the L-shaped interferometer to be $L = \ell_m - x_s$. All PSDs are computed without an IR cutoff.	110

5.9	The pixellon strain (dashed lines) overlaid with the predicted strain sensitivity for a stacked-disk levitated sensor (solid lines), as given by Fig. 3 of Ref. [21]. The color coding corresponds to the size ℓ_m of the levitated sensor. The pixellon strain is computed from Eq. (5.53), and we set $x_s = \ell_m/10$ throughout.	112
6.1	Expected Hellings–Downs correlation (purple dashed line) of timing residuals as a function of the angle between two pulsars, compared to recent observations (blue points with error bars) from a pulsar timing array. The green line at zero represents the no-GW hypothesis. A SGWB produces the distinctive quadrupolar correlation pattern shown by the dashed curve [247].	123
6.2	Comparison between the numerical relativity waveform h_{20} (blue curve) [242] and the step function model (red dashed line, Eq. (6.38)). Parameters: $\chi_A = \chi_B = 0, m_A = m_B, M = 60 M_\odot, r = 10$ Mpc, incl. angle = $0, \phi_{\text{ref}} = 0$	143
6.3	Mass probability density function and merger rate for SMBH population model using Eqs. (6.47) and (6.46) are shown. The shaded region denotes the $1-\sigma$ confidence interval [66].	145
6.4	Left: SGWMB energy spectrum density Ω_{mem} as a function of frequency along with its $1-\sigma$ confidence interval. Right: SGWMB characteristic strain h_c^{mem} as a function of frequency along with its $1-\sigma$ confidence interval.	146
6.5	Left: SMBH mass distribution $g_{\text{SMBH}}(M)$ computed using the mean parameter values from Table 6.1. Right: SMBH merger rate $R_{\text{SMBH}}(z)$ evaluated using the same set of mean parameters.	147
6.6	Left: SGWMB energy density spectrum (red dashed line) computed using the mean values from the SMBH population model parameters in Table 6.1, shown alongside LISA’s sensitivity curve (black solid line). Right: SGWMB characteristic strain (red dashed line) based on the same mean parameter values, plotted against LISA’s characteristic noise curve (black solid line).	147
6.7	Sky- and polarization-averaged SNR of the memory signal for equal-mass, non-spinning SMBHs as a function of the total mass M and redshift z	149

- 6.8 Left: SGWMB energy density spectrum under different SNR subtraction thresholds compared to the LISA sensitivity curve (black). The curves correspond to no subtraction (red), and SNR cuts at $\text{SNR} < 1000$ (green), $\text{SNR} < 100$ (orange), and $\text{SNR} < 10$ (magenta), respectively. Right: SGWMB characteristic strain under different SNR subtraction thresholds compared to the LISA sensitivity curve (black). The curves correspond to no subtraction (red), and SNR cuts at $\text{SNR} < 1000$ (green), $\text{SNR} < 100$ (orange), and $\text{SNR} < 10$ (magenta), respectively. 150

LIST OF TABLES

<i>Number</i>	<i>Page</i>
6.1 SMBH Model Parameters. We use $\mathcal{N}(\mu, \sigma)$ to denote normal distribution, and $\mathcal{U}_{[a,b]}$ to denote the uniform distribution [66].	144
6.2 Effective diffusion coefficient D_{eff} under different GW memory SNR thresholds.	150

Chapter 1

INTRODUCTION

Understanding quantum gravity, the unification of quantum mechanics and general relativity, remains one of the most profound open problems in theoretical physics. Although quantum field theory successfully describes the three other fundamental forces, it fails to provide an adequate framework for studying spacetime on microscopic scales, at which quantum mechanical effects become dominant. General relativity, though remarkably accurate to provide a unified description of gravity on macroscopic scales, remains a classical theory and does not incorporate the quantum fluctuations that characterize other interactions. The non-renormalizability of perturbative quantum gravity suggests that general relativity is only an effective low-energy description, requiring a more complete framework to fully capture the quantum nature of spacetime.

Apart from theoretical challenges, one of the primary obstacles in quantum gravity research is the lack of direct experimental access to Planck-scale physics, where quantum gravity effects are expected to be significant. Unlike other fundamental forces, which can be probed through high-energy particle scattering experiments, quantum gravity remains largely theoretical because of its extremely weak effects at observable scales. Traditional approaches, such as string theory [331, 46] and loop quantum gravity [77, 34, 277], provide some frameworks for quantizing gravity, but experimental validation of those theories remains elusive. In particular, a heuristic argument based on effective field theory and dimensional analysis suggests that quantum gravity fluctuations could induce length fluctuations on the order of Planck length,

$$\delta L \sim \ell_p. \tag{1.1}$$

Here δL is the length fluctuation of some experimental probe, such as an arm of a laser interferometer and ℓ_p is the Planck length, given by the expression

$$\ell_p = \sqrt{\frac{\hbar G}{c^3}} \approx 1.6 \times 10^{-35} \text{ m}. \tag{1.2}$$

No experiment is expected to reach such extreme length scales in the foreseeable future due to many technological hurdles and practical constraints. However, recent developments [314, 313, 328, 41, 329, 174, 312, 219] suggest that certain quantum

gravity effects may not be confined to the Planck scale but could leave imprints at macroscopic distances, particularly near causal horizons bounded by light-sheets.

$$\delta L \sim \sqrt{\ell_p L}, \quad (1.3)$$

where L is the length scale of the experimental probe, which ranges from several meters to several kilometers depending on specific setup. Although individually minute, these fluctuations could accumulate over macroscopic distances, potentially becoming detectable in high-precision laser interferometers. This opens the possibility of testing quantum gravity through precision measurement techniques, potentially bringing it within the reach of experiments in the near future.

This dissertation explores theoretical models that predict potentially observable quantum gravity effects, particularly in the context of laser interferometry. The first part of the dissertation focuses on developing theoretical frameworks that describe how quantum fluctuations of spacetime might influence near-horizon dynamics. The second part investigates how these fluctuations could give rise to new signals in high-precision gravitational wave detectors, raising the intriguing possibility that next-generation interferometers may offer an experimental window into quantum gravity. In addition, the second to last chapter presents a complementary classical study of stochastic gravitational wave backgrounds sourced by memory effects from supermassive binary black hole mergers, providing further context for the detection landscape relevant to space-based observatories like LISA.

Chapters 2 through 5 of this dissertation are based on the author's previously published work carried out in collaboration with others. Chapter 6 is based on the author's unpublished personal notes and presents ongoing independent work modeling a stochastic gravitational wave background sourced by memory effects from supermassive binary black hole mergers. The purpose of this introductory chapter is to provide the necessary background and context for these results. Section 1.1 reviews the theoretical landscape of quantum gravity and summarizes recent developments relevant to this dissertation. Section 1.2 discusses the state-of-the-art in gravitational wave detection technology and outlines how upcoming generations of interferometers may approach the sensitivity required to probe quantum features of spacetime.

1.1 Theoretical Background

In this section, we provide a review of the classical foundations and modern developments in quantum gravity research. We begin with an overview of Brownian

motion and the fluctuation-dissipation theorem, which serve as a fundamental model for understanding stochastic fluctuations in physical systems. We then transition to gravitational analogies by exploring the fluid/gravity correspondence, gravitational shockwaves, and their role in describing near-horizon dynamics. Finally, we discuss BMS symmetries, covariant phase space formalism, and recent advances in understanding quantum gravity fluctuations, emphasizing how these concepts contribute to our understanding of the emergent physics of vacuum fluctuations in spacetime.

Fluctuation-Dissipation and the Emergence of Stochastic Dynamics

The study of fluctuations in physical systems provides a crucial bridge between microscopic and macroscopic dynamics. Brownian motion, first described by Robert Brown and later explained by Einstein [129, 144], serves as a prototypical example of how microscopic molecular interactions manifest themselves as stochastic behavior at larger scales. The mathematics behind such stochastic dynamics is encoded in the Langevin equation [214],

$$m \frac{d\mathbf{v}}{dt} = -\lambda \mathbf{v} + \boldsymbol{\eta}(t), \quad (1.4)$$

where \mathbf{v} is the velocity of the particle undergoing Brownian motion, m is its mass, and λ is its damping coefficient. Here, $\boldsymbol{\eta}(t)$ is a noise term representing the effect of random molecular collisions experienced by the particle. The random force $\boldsymbol{\eta}(t)$ is assumed to follow a Gaussian probability distribution with correlation function

$$\langle \eta_i(t) \eta_j(t') \rangle = 2\lambda k_B T \delta_{ij} \delta(t - t'), \quad (1.5)$$

where k_B is the Boltzmann constant and T is the temperature. This equation captures the essence of Brownian motion: random thermal fluctuations drive the motion of the particle (fluctuation), while viscous damping opposes it (dissipation), ensuring that the system eventually reaches thermal equilibrium. [214, 218]. This framework has been instrumental in statistical physics, offering a template for understanding non-equilibrium dynamics in numerous contexts.

A key result in statistical mechanics that formalizes the relationship between fluctuations and dissipations is the fluctuation-dissipation theorem [76, 213]. In this theorem, the fluctuations of a system around its equilibrium are intrinsically linked to its response to external perturbations. It quantitatively relates the power spectrum of spontaneous fluctuations $S_A(\omega)$ to the imaginary part of the system's susceptibility $\chi(\omega)$ via

$$S_A(\omega) = -\frac{2k_B T}{\omega} \text{Im}[\chi(\omega)]. \quad (1.6)$$

Physically, this means that a system exhibiting large fluctuations will also have a strong dissipative response when it is driven out of equilibrium. The fluctuation-dissipation theorem underlies many fundamental results, such as the Einstein relation for Brownian motion $D = k_B T / \gamma$ and Nyquist's theorem for electrical noise $S_V(\omega) = 2k_B T R$ [61]. Its implications extend across statistical mechanics, condensed matter physics, and quantum systems, providing a deep connection between microscopic noise and macroscopic dissipation.

In the context of gravity, an intriguing question arises: can spacetime itself exhibit stochastic fluctuations analogous to Brownian motion? The search for such effects has led to the study of gravitational noise, where quantum fluctuations in spacetime may introduce fundamental stochasticity in gravitational systems [313, 314, 328, 329, 312, 219]. This idea serves as a motivation for extending fluctuation-dissipation principles to gravitational physics, particularly in the study of black hole horizons and causal diamonds.

Holographic Duality

The holographic principle suggests that a gravitational system in a given spacetime can be fully described by a lower-dimensional field theory living on its boundary. This idea was first formalized in the AdS/CFT correspondence, which proposes a precise duality between gravity in anti-de Sitter (AdS) space and conformal field theories (CFT) living on its asymptotic boundary [228]. In this framework, bulk gravitational dynamics are encoded in boundary quantum field theory observables, providing a powerful non-perturbative approach to studying strongly coupled quantum systems. The correspondence has yielded deep insights into black hole thermodynamics [172, 173, 65, 22, 278], transport properties of strongly correlated fluids [266, 266, 211, 212, 289, 51, 271, 139], and quantum information aspects of spacetime [283, 284, 285, 274, 227, 170], establishing itself as a cornerstone of modern theoretical physics.

A key insight from holography and black hole thermodynamics is the Bekenstein-Hawking entropy formula, which states that the entropy of a black hole is proportional to the area of its event horizon rather than its volume. The formula is given by

$$S_{\text{BH}} = \frac{A}{4G_N}. \quad (1.7)$$

This formula suggests that black hole entropy is holographic in nature, meaning that the fundamental degrees of freedom of the black hole are encoded on its

boundary rather than in its bulk volume [48, 179]. This observation played a pivotal role in the development of the holographic principle, which posits that the information content of a gravitational system can be encoded on a lower-dimensional surface. Furthermore, in the context of AdS/CFT, black hole entropy is related to entanglement entropy, where the entanglement between degrees of freedom across a horizon plays a crucial role in understanding the microscopic origin of gravitational entropy. The Ryu-Takayanagi formula [278, 91] extends this idea by proposing that in holographic theories, the entanglement entropy of a boundary region is given by the area of a minimal bulk surface, reinforcing the deep connection between geometry, quantum mechanics, and information theories.

Although the AdS/CFT correspondence has been extensively explored, many real-world physical systems, including our own universe, are not asymptotically AdS, but instead asymptotically flat. Extending holography to flat spacetime remains a key open problem in quantum gravity. Unlike AdS, where the negative curvature naturally provides a well-defined conformal boundary, Minkowski spacetime lacks such a structure, requiring a new approach to defining the holographic dictionary. Several proposals have emerged to address this challenge, including the Flat Space Holography program [257, 256, 295, 32, 123, 253, 255], which suggests that quantum gravity in asymptotically flat spacetime may be holographically encoded in a field theory living on null infinity ($\mathcal{I}^{+/-}$), governed by BMS symmetries [64, 279, 297, 294, 298, 188, 183, 189, 244, 35, 25].

A crucial motivation for holography in flat space comes from the study of soft theorems, gravitational memory effects, and asymptotic symmetries, which hint at an underlying holographic structure linking bulk gravitational dynamics to boundary field theories [297, 183, 298, 257]. These connections suggest that key aspects of quantum gravity in flat space, such as black hole evaporation, information retrieval, and scattering amplitudes, may be reformulated in terms of lower-dimensional, nonlocal field theories at null infinity [256, 258, 254, 260, 255]. Moreover, the recent development of Celestial Holography proposes that gravitational scattering amplitudes in four-dimensional Minkowski space can be mapped to correlation functions in a two-dimensional conformal field theory (Celestial CFT) living on the celestial sphere at null infinity [297, 257, 256, 230, 36, 249]. This perspective provides an alternative framework for understanding quantum aspects of gravity, with potential implications for black hole physics and quantum information theory.

Despite significant progress, a complete holographic formulation of quantum gravity

in flat spacetime remains an ongoing challenge. Future developments may refine our understanding of bulk reconstruction, quantum information in asymptotically flat space, and non-AdS gravitational dualities. Given its success in strongly coupled systems, the continued extension of holography beyond AdS could offer profound insights into the nature of spacetime, black holes, and the fundamental quantum structure of gravity.

Fluid/gravity Correspondence

The connection between gravity and hydrodynamics has deep historical roots, dating back to the membrane paradigm that was first developed in the late 1970s and 1980s [116, 269, 252]. This framework provided an effective description of black hole horizons as dynamical, dissipative membranes equipped with properties in hydrodynamic systems such as shear viscosity and electrical conductivity. The membrane paradigm suggests that black hole horizons behave analogously to fluid-like systems, exhibiting dissipative responses to external perturbations. This perspective, though originally formulated within classical general relativity, laid the foundation for modern developments in the fluid/gravity correspondence [132, 135, 166].

The emergence of the AdS/CFT correspondence [228] in the late 1990s provided the foundation for a more rigorous realization of the fluid/gravity correspondence. In AdS/CFT, black hole solutions to the Einstein equations in anti-de Sitter (AdS) space correspond to finite-temperature states in a strongly coupled conformal field theory (CFT) on the boundary [172, 173, 22]. Perturbations of the black hole horizon at long wavelengths and low frequency regime map directly to hydrodynamic excitations in the corresponding boundary theory, with the resulting equations reducing to the Navier-Stokes equations in the appropriate limit [266, 266, 211, 212, 289, 51, 271, 139]. This correspondence has since been extensively explored, leading to precise computations of transport coefficients such as the universal bound of the ratio of shear viscosity to entropy density, $\eta/s = 1/4\pi$, which characterizes strongly coupled fluids [266, 211, 212, 114, 57, 56, 59, 58].

The fluid/gravity correspondence has been particularly instrumental in the study of the quark-gluon plasma (QGP) produced in heavy-ion collisions. The strongly coupled nature of the QGP makes it difficult to analyze using conventional perturbative techniques, but holography provides a powerful alternative framework. In this approach, QGP is modeled as a plasma state in the $\mathcal{N} = 4$ supersymmetric Yang-Mills

(SYM) theory [265, 266, 267, 210], which shares key qualitative characteristics with QCD in the real world at high temperatures. The behavior of the QGP, including its near-perfect fluidity, can be understood through its gravitational dual: perturbations of a black hole horizon in AdS describe the collective motion of the plasma, with hydrodynamic transport properties emerging naturally from the horizon dynamics. In particular, the holographic prediction of $\eta/s = 1/4\pi$ aligns remarkably well with experimental measurements of the QGP, which exhibits extremely low viscosity close to this bound [290].

Extending this analysis beyond AdS backgrounds has remained an important area of research, particularly in asymptotically flat spacetime, where holography is less well understood. In such settings, Rindler horizons—associated with uniformly accelerating observers in Minkowski spacetime—offer a natural testbed for applying the fluid/gravity correspondence in a broader context. Recent studies [71, 70, 108, 109, 224, 264] suggest that near-horizon perturbations in Rindler spacetime obey fluid-like equations, and in appropriate limits, the dynamics of these perturbations reduce to those of an incompressible fluid, whose dynamics is governed by the Navier-Stokes equations. This realization opens the possibility that the hydrodynamic properties of horizons are not unique to AdS/CFT correspondence, but may instead be a more universal feature of gravitational systems.

By examining how fluctuations propagate near Rindler horizons, we can explore whether quantum gravity effects introduce additional dissipative behaviors, similar to those observed in strongly coupled hydrodynamic systems. Understanding these effects is crucial for extending the reach of fluid/gravity duality to more general settings and for identifying potential experimental signatures of quantum gravity fluctuations in high-precision interferometry.

Gravitational Shockwaves and Horizon Dynamics

A key feature of black hole horizons is their response to high-energy perturbations. The concept of gravitational shockwaves plays a central role in understanding how energy and information propagate across horizons. Shockwaves arise as solutions to the Einstein equations in the presence of localized high-energy matter, leading to shifts in the causal structure of spacetime [126, 1, 5, 2]. These solutions have been extensively studied in the context of AdS/CFT, where shockwave geometries provide a holographic realization of quantum scrambling and chaos [283, 285, 227, 274, 170, 23].

The Dray-'t Hooft shockwave solution [126], one of the earliest example of this phenomenon, describes how the geometry of a black hole is modified due to the passage of a high-energy particle near the horizon of a black hole. To be more specific, the shockwave solution solves the Einstein equations exactly, and the metric takes the form

$$ds^2 = -dudv + H_{uu}du^2 + \delta_{ij}dx^i dx^j, \quad (1.8)$$

where H_{uu} is given by

$$H_{uu}(u, x^i) = 8\pi G_N p_u \delta(u - u_0) f(\mathbf{x}; \mathbf{x}'), \quad (1.9)$$

where p_u is the momentum of the shock, and u_0 denotes the wavefront of the shockwave, and $f(\mathbf{x}; \mathbf{x}')$ is the Green's function of the Laplacian operator reduced from the Einstein equations. Despite its very simple appearance, the Dray-'t Hooft shockwave possesses rich dynamics and fascinating properties that are sought to link gravitational physics and quantum chaos together. Recent developments have focused on exploring the quantum nature of gravitational shockwaves, particularly in the context of quantum information theory and black hole microstructure [283, 285, 227, 274, 170]. In holographic settings, shockwaves have been linked to out-of-time-order correlators (OTOCs), providing a diagnostic for quantum chaos and information scrambling in strongly coupled field theories. Studies of shockwave amplitudes in flat space and near Rindler horizons suggest that these structures may encode subtle quantum gravity effects, including shifts in entanglement entropy and correlations across the horizon [112, 169, 312]. Additionally, recent works [312, 191, 190] have examined the role of quantum fluctuations in modifying classical shockwave solutions, leading to stochastic deviations in the shifts of photon traversal time in a causal diamond, which could serve as potential observables. These investigations provide a deeper understanding of how quantum gravity governs the response of horizons to high-energy perturbations, offering insight into the interplay between gravitational dynamics and quantum coherence. If gravitational shockwaves arising from quantum energy fluctuations lead to measurable effects, next-generation interferometers could, in principle, provide an indirect probe of such phenomena, further connecting quantum effects of the spacetime with precision gravitational wave experiments.

BMS Symmetries and Covariant Phase Space Formalism

Recent advances in theoretical physics have revealed deep connections among asymptotic symmetries, soft theorems, and celestial holography [297, 294, 298,

296, 299, 257, 256, 295]. In particular, the Bondi-Metzner-Sachs (BMS) group, which describes the asymptotic symmetries of spacetime at null infinity, has emerged as a powerful tool for understanding gravitational memory effects and soft graviton dynamics [64, 298, 259, 254, 123, 255, 253]. The realization [85, 86, 82, 84, 83, 120, 121, 80, 124, 81, 122] that black holes exhibit BMS-like symmetries at their horizons suggests that near-horizon dynamics may be governed by an extended symmetry structure, potentially constraining quantum microstates of gravity.

The role of covariant phase space formalism in general relativity has also gained attention as a method to systematically study the phase space of degrees of freedom of the horizon [201, 200, 82, 84, 244, 79, 93, 94, 95]. The symplectic structure of gravitational systems encodes fundamental information about their evolution, providing a bridge between classical and quantum descriptions. By analyzing the symplectic form of black hole and generic Killing horizons, researchers aim to uncover the fundamental quantities governing quantum gravity fluctuations [188, 183, 189, 182, 185, 186, 187, 94, 95, 147, 146, 145, 148, 152, 149, 151, 150].

One particularly exciting application of the covariant phase space formalism is the study of quantum effects in gravity, in particular for a causal diamond in Minkowski spacetime. If spacetime exhibits quantum fluctuations, these fluctuations could introduce measurable signatures in precision experiments. Recent proposals [328, 329, 219, 191, 190] suggest that gravitational wave interferometers, such as LIGO and future detectors *e.g.*, the GQuEST experiment [236, 235], could be sensitive enough to detect such quantum gravity signals. Understanding how quantum fluctuations manifest in spacetime requires a combination of techniques from statistical physics, symmetry analysis, and general relativity, all of which contribute to the ongoing search for experimental tests of quantum gravity.

The Verlinde–Zurek Effect: Quantum Fluctuations from Holographic Degrees of Freedom

The *Verlinde–Zurek (VZ) effect* refers to a recently proposed phenomenon at the intersection of quantum gravity and emergent spacetime physics. Erik Verlinde and Kathryn Zurek initiated the collaboration in 2019 to explore whether quantum gravity could produce observable fluctuations in spacetime at scales much larger than the Planck length. In their framework [313, 314], spacetime is treated holographically—meaning gravitational information is encoded on the boundary of a region (often called a causal diamond or light-sheet). They hypothesized that quantum uncer-

tainty in these holographic degrees of freedom could lead to measurable metric fluctuations, even at macroscopic scales.

Expanding on this foundation, the VZ effect posits that vacuum spacetime possesses an intrinsic jitter” or fluctuation that grows with the size of the region considered. From the perspective of the effective field theory, one might expect quantum-gravity effects to occur only at the Planck scale ($\sim 10^{-35}$ m), far too small to ever be detected. However, Verlinde and Zurek argue that if one considers a space volume bounded by a light-like surface (a causal diamond), the quantum uncertainty in the position of that boundary can accumulate like a random walk over large scales [313, 314, 41, 329, 312]. In technical terms, they suggest that the variance of length fluctuations grows linearly with the length of the path ($\langle \Delta L^2 \rangle \sim \ell_p L$, with ℓ_p the Planck length) [314, 313, 329, 174]. This scaling (often called the VZ scaling”) implies that the fluctuation of the root-mean-square in the distance is proportional to $\sqrt{\ell_p L}$. For a macroscopic length L , $\sqrt{\ell_p L}$ is still tiny, but much larger than ℓ_p alone. In other words, quantum gravity might introduce a very small but not utterly negligible uncertainty in proper distances—an effect that could, in principle, be observed with extremely sensitive instruments.

An essential feature of the VZ effect is the correlation structure of these fluctuations. Rather than being uncorrelated across space, the model features long-range, transverse correlations across the entire causal diamond [314, 312]. This ensures that the spacetime metric does not fluctuate randomly at each point, but rather undergoes coordinated distortions. Such correlated fluctuations evade constraints imposed by astrophysical observations that rule out uncorrelated Planck-scale noise. For instance, a completely uncorrelated noise model would cause blurring in distant astronomical images, which is not observed. Instead, the VZ model predicts coherent deformations that accumulate subtly over distance, consistent with observational data [217].

The origin and consistency of this area-scaling behavior are further explored in Ref. [313], where Verlinde and Zurek perform a detailed computation of the modular Hamiltonian fluctuations using the gravitational replica trick in the context of AdS/CFT correspondence. They define the modular Hamiltonian K associated with a causal diamond (see Fig.1.1) in AdS-Rindler spacetime and show that its expectation value and fluctuations obey the area law:

$$\langle K \rangle = \frac{A(\Sigma)}{4G}, \quad \langle \Delta K^2 \rangle = \frac{A(\Sigma)}{4G}, \quad (1.10)$$

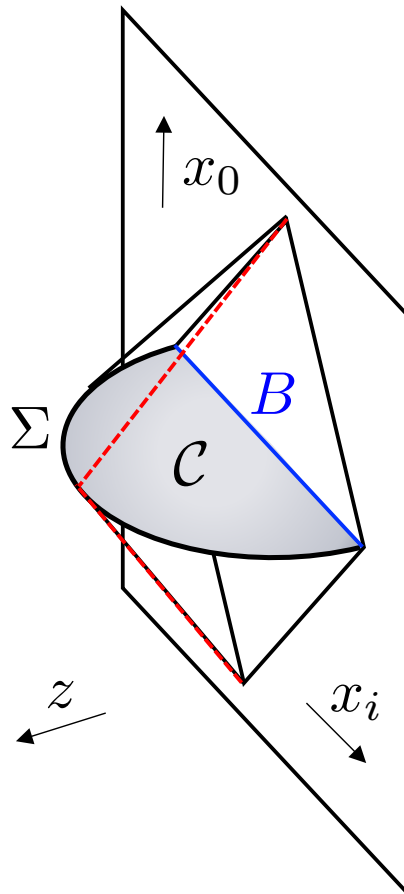


Figure 1.1: Pictorial depiction of the causal diamond in Rindler-AdS space anchored at the asymptotic AdS boundary. The red dashed line represents a laser trajectory traversing from the boundary to a point on the RT surface and then reflected back to the boundary [313].

where $A(\Sigma)$ is the area of the Ryu–Takayanagi (RT) surface anchoring the causal diamond. This result confirms that quantum fluctuations in the modular Hamiltonian—and hence the metric—scale with the area of the entangling surface. They further analyze how these fluctuations lead to observable shifts in the location of the Rindler horizon and in the traversal time of photons propagating between mirrors placed on the boundary of the causal diamond.

This bridge between quantum information-theoretic quantities and spacetime geometry highlights the novelty of their approach. By embedding modular Hamiltonians in bulk AdS geometries, they establish a precise relation between entanglement entropy, modular Hamiltonian, and back-reaction on the spacetime. This lays the groundwork for treating modular Hamiltonian fluctuations not merely as mathematical artifacts, but as physically meaningful observables that can induce geometric

distortions.

Building on this structure, Ref. [41] by Banks and Zurek proposes that near-horizon vacuum states across a wide range of geometries can be described by conformal field theories. They extend the modular fluctuation framework to flat space, de Sitter (dS), and AdS backgrounds, and find that for such causal diamonds, the fluctuations again obey an area law:

$$\langle \Delta K^2 \rangle = \langle K \rangle = \frac{A(\Sigma)}{4G_d}, \quad (1.11)$$

where G_d is the Newton constant in d spacetime dimensions. Their argument is grounded in a thermodynamic interpretation using the Cardy formula, suggesting that a 2d CFT-like behavior governs physics near generic horizons.

Furthermore, this interpretation offers a deeper symmetry-based motivation for the VZ effect. The authors explore possible connections to soft graviton theorems, the BMS symmetry group, and celestial holography, indicating that these modular fluctuations might be encoded in the infrared structure of spacetime. This suggests that VZ-type effects could be a manifestation of a more universal principle in gravitational theory.

Complementary to these approaches, Gukov, Lee, and Zurek investigate the reduction of 4D Einstein gravity to 2D Jackiw–Teitelboim (JT) gravity in Ref. [174]. This dimensional reduction simplifies the analysis of quantum fluctuations near horizons while retaining key gravitational dynamics. In particular, they model a photon traveling across a causal diamond and relate the uncertainty in its round-trip travel time to modular Hamiltonian fluctuations. Using the partition function

$$\log Z = \log \left(\int dE e^{B\sqrt{E} - \beta E} \right), \quad (1.12)$$

they derive the same fluctuation-entropy relation:

$$\langle \Delta K^2 \rangle = \langle K \rangle = S, \quad (1.13)$$

and connect it to physical observables such as photon delay times. They further show that both UV and IR scales influence the measurement uncertainty:

$$\Delta t \sim \sqrt{L\ell_p}, \quad (1.14)$$

where L is the interferometer arm length.

This mapping between Minkowski causal diamonds and $\text{AdS}_2 \times S^2$ geometries offers a powerful framework. JT gravity serves as a tractable model that retains essential

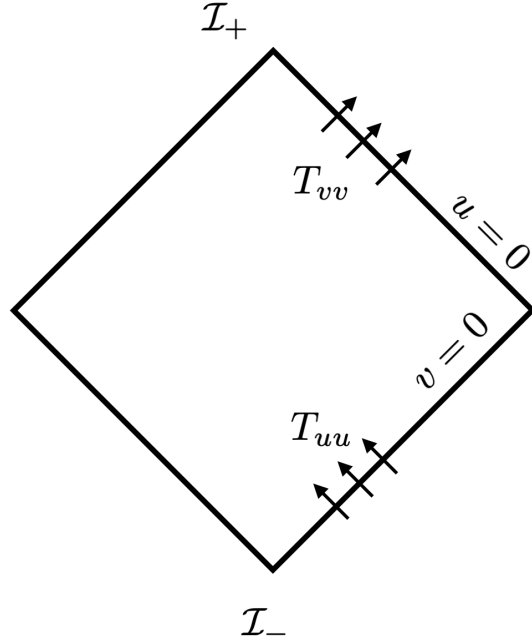


Figure 1.2: Pictorial depiction of the quantum fluctuations modeled by gravitational shockwaves near the light-front of a causal diamond. Vacuum fluctuations T_{uu} and T_{vv} induce light cone time delay in δv and δu , respectively, on the lower and upper half of the causal diamond [312].

features of near-horizon quantum dynamics, reinforcing the notion that modular Hamiltonian fluctuations have real, potentially observable consequences.

A further compelling insight comes from Ref.[312], where Verlinde and Zurek trace the origin of these fluctuations to gravitational shockwaves. They show that vacuum fluctuations in the stress-energy tensor T_{uu} and T_{vv} can induce longitudinal metric perturbations h_{uu} and h_{vv} . For a pictorial representation, see Fig.1.2. These perturbations produce coordinate shifts:

$$\delta v(u, y) = \int_{-\infty}^u du' h_{uu}(u', y), \quad \delta u(v, y) = \int_{-\infty}^v dv' h_{vv}(v', y), \quad (1.15)$$

with uncertainty relations of the form:

$$\Delta \delta u(y) \Delta \delta v(y') = \ell_p^{d-2} f(y, y'), \quad (1.16)$$

where $f(y, y')$ is the Green's function on the transverse plane. These relations resemble those proposed by 't Hooft [3, 4, 5, 2], and hint at an underlying quantum algebra on the lightfront.

To solidify this connection, they derive the effective action governing shockwave-induced fluctuations. Remarkably, this action takes the form:

$$I = \int d^{d-2}y \left[-\frac{1}{\ell_p^{d-2}} \int d\tau X^u \Delta_y \frac{dX^v}{d\tau} + \int d\tau (X^u T_{u\tau} + X^v T_{v\tau}) \right], \quad (1.17)$$

and reduces to the modular Hamiltonian on-shell. This unification of shockwave dynamics and modular fluctuation theory further strengthens the interpretation of the VZ effect as a real manifestation of quantum geometry. The authors further compute the fluctuation $\langle \Delta K^2 \rangle$ by introducing quantum commutation relations for the transverse shockwave degrees of freedom $X^u(y, \tau)$ and $X^v(y, \tau)$. These coordinates, which describe the null deformations of the causal diamond boundary, satisfy the canonical commutation relation

$$[X^u(y, \tau), X^v(y', \tau)] = i\ell_p^{d-2} f(y, y'). \quad (1.18)$$

Using this structure, they quantize the effective shockwave action and compute the variance of the modular Hamiltonian, obtaining

$$\langle \Delta K^2 \rangle = \langle K \rangle = S. \quad (1.19)$$

This result not only corroborates the area-scaling behavior derived in AdS/CFT but also demonstrates that modular fluctuations arise naturally from quantum gravitational shockwave dynamics, thereby reinforcing the interpretation of the VZ effect as a manifestation of underlying quantum geometry.

Taken together, these results demonstrate that the Verlinde–Zurek effect unites several powerful ideas in theoretical physics: holography, conformal field theory, shockwave dynamics, and experimental quantum gravity. Its area-scaling modular Hamiltonian fluctuations suggest a universal mechanism by which quantum information influences spacetime geometry. Furthermore, the close interplay between boundary observables and bulk dynamics indicates that causal diamonds serve as natural laboratories for probing quantum aspects of gravity. In particular, these insights motivate the design of interferometric setups sensitive to coherent vacuum fluctuations, and they highlight modular fluctuations as viable candidates towards observables for experimental signatures of quantum gravity.

The Pixellon Model and Quantum Fluctuations of Spacetime

The Pixellon model [328, 219] is a phenomenological framework designed to describe vacuum fluctuations in quantum gravity, particularly in relation to interferometric observables. This model arises from the desire to construct a simple yet

physically motivated description of metric fluctuations that encapsulate key insights from the AdS/CFT correspondence and holography. Notably, it captures many important features of the VZ effect, including the area-scaling of modular Hamiltonian fluctuations and long-range transverse correlations. However, while the Pixellon model reproduces several aspects of the VZ effect, their exact equivalence remains an open question.

We begin our summary with Ref. [314], which presents a concrete microscopic model based on energy fluctuations in holographic degrees of freedom. In this work, the authors argue that if Planck-scale energy fluctuations are correlated, they can accumulate in the longitudinal direction and become observable. A central result is the prediction of a variance in arm length fluctuations:

$$\left\langle \left(\frac{\Delta L}{L} \right)^2 \right\rangle \sim \frac{\ell_p}{L}, \quad (1.20)$$

which implies that the root-mean-square displacement grows as $\sqrt{L\ell_p}$. They show that if these fluctuations exhibit white-noise statistics in time but are spatially correlated across transverse directions, then the induced strain noise would evade astrophysical constraints. Importantly, the paper introduces a holographic description where the light path of a photon defines a causal diamond, and fluctuations on the bounding surface give rise to measurable effects inside the diamond.

Building upon this, Zurek introduces the Pixellon model in Ref. [328]. Motivated by AdS/CFT, where the modular Hamiltonian K obeys an area law,

$$\langle K \rangle = \langle \Delta K^2 \rangle = \frac{A(\Sigma)}{4G}, \quad (1.21)$$

Zurek proposes a thermal model for the vacuum state with a density matrix

$$\rho = \frac{e^{-\beta K}}{\text{Tr}(e^{-\beta K})}, \quad (1.22)$$

and suggests that the degrees of freedom—"pixellons"—are high-occupation bosonic excitations associated with each holographic pixel. These excitations couple gravitationally to test masses and induce position fluctuations. A key estimate of the induced gravitational potential is given by

$$2\phi = \sqrt{\frac{\alpha}{N}} = \frac{\bar{\ell}_p}{4\pi L}, \quad (1.23)$$

where $N = A/4G$ is the number of pixels and $\bar{\ell}_p$ incorporates an $O(1)$ parameter α controlling the strength of modular fluctuations. Through the Feynman-Vernon

influence functional, Zurek computes the resulting mirror displacements in an interferometer and finds that they lead to a distinct angular correlation pattern, potentially measurable in next-generation instruments.

The Snowmass 2021 white paper [329] provides a broader theoretical overview, contextualizing the Pixellon model and the VZ effect within a range of quantum gravity frameworks. Drawing on analogies to Brownian motion and the random walk model, the white paper emphasizes that UV-scale fluctuations can integrate into IR observables via cumulative processes. For instance, they show that spacetime uncertainty at a light-sheet horizon behaves as

$$\delta L^2 \sim \ell_p L, \quad (1.24)$$

a result consistent with the predictions of both the VZ and Pixellon models. Furthermore, the white paper presents a "dictionary" equating black hole entropy with modular fluctuations in causal diamonds, suggesting that the holographic structure of spacetime near horizons could be a universal feature, independent of background curvature.

Finally, the most detailed and extended treatment of the Pixellon framework appears in Ref. [219]. Here, Li, Lee, Chen, and Zurek formulate a full scalar field theory for the Pixellon, modeling it as a bosonic field ϕ with a high occupation number, coupled to the metric in a spherically symmetric configuration:

$$ds^2 = -dt^2 + (1 - \phi)(dr^2 + r^2 d\Omega^2). \quad (1.25)$$

They derive the interferometric time-delay correlation function:

$$\langle \delta T(t_1, \hat{\mathbf{n}}_1) \delta T(t_2, \hat{\mathbf{n}}_2) \rangle \propto \int d^3 p \frac{\sigma_{\text{pix}}(p)}{2\omega(p)} F(r_1, r_2, p, \Delta x), \quad (1.26)$$

where $\sigma_{\text{pix}}(p)$ is the occupation number of the Pixellon mode and F encodes the interferometer response function.

The authors model $\sigma_{\text{pix}}(p)$ as a thermal distribution:

$$\sigma_{\text{pix}}(p) = \frac{1}{\beta\omega(p)} \approx \frac{a}{\ell_p \omega(p)}, \quad (1.27)$$

where a is a dimensionless constant and $\omega(p) \sim 1/L$ sets the IR scale. Crucially, they show that this thermal distribution reproduces the area-law behavior:

$$\langle \Delta K^2 \rangle \sim \frac{A(\Sigma)}{4G}, \quad (1.28)$$

and that the resulting metric fluctuations produce angularly correlated background, a key signature of the VZ effect. In contrast to earlier works, they calculate the full power spectral density and angular response of the interferometer, including comparisons to experimental sensitivity. The Pixellon-induced background appears as a broadband signal with coherence across the transverse plane, aligning with the theoretical expectations of the VZ framework.

In summary, the Pixellon model provides a versatile, tractable tool for modeling quantum gravitational fluctuations with concrete experimental consequences. While inspired by the VZ effect and capable of reproducing many of its central features—notably the area-scaling of fluctuations and transverse coherence—the Pixellon framework is formulated independently. Whether the two are equivalent at a deeper level remains an open question. Nonetheless, their striking overlap highlights a convergence of ideas around holography, modular Hamiltonian, and interferometric observables, offering a promising direction for probing the quantum structure of spacetime.

1.2 Laser Interferometers and Experimental Sensitivity

The advent of gravitational wave interferometry has transformed our ability to probe fundamental physics. Initially designed to detect spacetime distortions caused by astrophysical events, modern interferometers have reached unprecedented sensitivity levels, raising the possibility that they could also reveal previously undetectable quantum gravity effects. The remarkable precision of these instruments makes them ideal candidates for testing deviations from classical gravity and searching for imprints of quantum gravity fluctuations. This section reviews recent advances in gravitational wave detection and explores potential sources of quantum gravity fluctuations in interferometers, discusses the capabilities of next-generation detectors such as the upcoming GQuEST experiment [235, 236], Cosmic Explorer (CE) [137, 291], and the Einstein Telescope (ET) [193], and examines how interferometry connects to theoretical predictions of quantum gravity.

Advances in Gravitational Wave Detection

The direct detection of gravitational waves by the Laser Interferometer Gravitational Wave Observatory (LIGO) in 2015 marked a milestone in observational physics [13], confirming a key prediction of general relativity. Since then, the LIGO-Virgo-KAGRA (LVK) network has detected numerous gravitational wave events [7, 8, 9, 10, 11, 106], including mergers of binary black holes and neutron stars. These

detections have provided insights into astrophysical processes and tested general relativity in the strong-field regime.

Gravitational wave interferometers operate by using laser light to measure tiny changes in the relative lengths of perpendicular arms. A passing gravitational wave alters the proper distance between test masses, creating a phase shift in the laser beams traveling along the arms. The remarkable sensitivity of these detectors has been made possible through advances in quantum optics, seismic isolation, and mirror coating technology. Squeezed vacuum states have been implemented to reduce quantum shot noise, while cryogenic cooling and improved suspension systems continue to push the limits of detection [237, 220, 234, 235, 317, 321].

As current-generation detectors approach their fundamental noise limits, researchers are beginning to explore whether additional, unexplained sources of noise could be present, potentially arising from quantum fluctuations of spacetime itself. If such fluctuations exist, they may introduce a new type of signal in interferometric data, providing an indirect way to probe quantum gravity.

Detection of Stochastic Gravitational Wave Background

A stochastic gravitational wave background (SGWB) refers to a persistent, random gravitational-wave signal arising from the superposition of many independent and unresolved sources. Unlike transient events such as individual black hole mergers, the SGWB forms a diffuse, continuous background of gravitational radiation that permeates the Universe. Its detection would not only confirm theoretical predictions but also provide a unique window into both the population statistics of astrophysical sources and the high-energy processes of the early Universe [226, 98].

The SGWB can arise from two broad classes of sources: astrophysical and cosmological. Astrophysical sources involve gravitational waves emitted throughout cosmic history by processes such as compact binary coalescences, core-collapse supernovae, and rapidly rotating neutron stars. Among these, the dominant contribution in the frequency band of current ground-based detectors is expected to come from the unresolved mergers of binary black holes and binary neutron stars. While nearby mergers are detected as individual events, the distant and numerous ones blend together into a stochastic signal [276, 15]. At lower frequencies, supermassive black hole binaries—formed during galaxy mergers—contribute significantly to the SGWB and are being actively studied through pulsar timing array experiments [19].

Cosmological sources of the SGWB are rooted in the early Universe. These include relic gravitational waves from inflation, phase transitions such as the electroweak transition, and the dynamics of hypothetical objects like cosmic strings. Inflationary models predict a background arising from quantum fluctuations of spacetime, stretched to cosmic scales during rapid expansion [43]. First-order phase transitions, if they occurred, could have generated gravitational waves through bubble collisions and turbulence in the primordial plasma [43]. Cosmic strings, if they exist, could continuously emit gravitational radiation through oscillating loops, contributing to a broadband SGWB [60]. Detection of a cosmological SGWB would yield profound insights into high-energy physics and the Universe’s earliest moments [98].

Detecting the SGWB is inherently challenging due to its random and persistent nature. The key strategy involves cross-correlating the outputs of spatially separated gravitational wave detectors to identify common signals buried in otherwise uncorrelated noise [98]. Ground-based interferometers like LIGO and Virgo operate in the tens to thousands of hertz range and use this technique to search for an SGWB primarily from stellar-mass binary mergers [15]. At nanohertz frequencies, pulsar timing arrays monitor the arrival times of pulses from millisecond pulsars across the sky, searching for the distinctive correlation pattern indicative of a gravitational-wave background. Recently, these efforts have yielded the first compelling evidence for an SGWB, likely sourced by supermassive black hole binaries [19]. In the future, space-based detectors like LISA will explore intermediate frequency bands and may uncover both astrophysical and cosmological backgrounds [43, 30].

The stochastic gravitational wave background represents both a challenge and an opportunity: its detection requires precise instrumentation and long observation times, but its potential to reveal hidden aspects of our Universe—from the life cycles of compact objects to the physics of the Big Bang—makes it one of the most exciting frontiers in gravitational wave astronomy [98].

Detection of Gravitational Wave Memory Effect

The gravitational wave memory effect is a distinctive and lasting prediction of general relativity: it describes a phenomenon in which spacetime undergoes a permanent deformation after the passage of a gravitational wave. Unlike the familiar oscillatory stretching and squeezing caused by standard gravitational waves, the memory effect leaves a net displacement between freely falling test particles that were initially at rest relative to each other. This “memory” encodes how the energy and momentum

radiated by astrophysical events can leave behind a subtle but permanent imprint on the geometry of spacetime.

There are two main types of memory: linear memory, arising from the change in the matter configuration of a system (such as mass ejection in a supernova) [243, 117], and nonlinear (Christodoulou) memory, which is purely gravitational in origin and results from the self-interaction of gravitational waves themselves [99, 100, 242]. The nonlinear memory effect is a remarkable consequence of the nonlinearity of Einstein’s equations: gravitational waves carry energy, and that energy flux generates further curvature, producing a net change in the gravitational field [99, 100]. In compact binary coalescences—such as binary black hole or binary neutron star mergers—the nonlinear memory effect is expected to accompany the merger and ringdown phase as a slow, non-oscillatory rise in the strain signal.

Detecting this effect is a frontier goal in gravitational wave astronomy. The amplitude of memory signals is typically an order of magnitude smaller than the oscillatory component of the waveform, and their characteristic rise time is much longer, placing them predominantly at low frequencies, close to or below the sensitivity limits of current ground-based detectors like LIGO and Virgo [143, 215]. This poses a significant technical challenge, as these detectors are designed to be most sensitive in the ~ 30 – 300 Hz range, whereas memory contributes primarily below ~ 10 Hz. Nevertheless, several strategies are being pursued to make detection feasible.

One promising approach is stacking the memory signals from multiple binary merger events. While the memory from any single merger is small and likely undetectable, combining the signals coherently from tens or hundreds of events can improve the signal-to-noise ratio. This method takes advantage of the fact that the memory waveform is slowly varying and predictable, enabling constructive integration over a large number of detections [268]. With the increasing catalog of mergers detected by the LVK network, this technique is becoming increasingly powerful.

In addition, the prospect of next-generation gravitational wave observatories significantly enhances the outlook for memory detection. Ground-based detectors like Cosmic Explorer [137, 291] and the Einstein Telescope [136, 304] are being designed with improved low-frequency sensitivity, potentially allowing them to observe the memory effect from individual loud events. Meanwhile, space-based interferometers such as LISA will be particularly well-suited for detecting memory from supermassive black hole mergers, where the memory amplitude is expected to be much larger and more easily separated from instrument noise due to the longer

timescales involved [196].

Beyond the technical and observational aspects, the gravitational wave memory effect is deeply intertwined with the asymptotic symmetries of spacetime, specifically the BMS group, which governs the gravitational field at null infinity. Recent theoretical work has shown that memory can be understood as a classical manifestation of spontaneously broken BMS supertranslations, with direct links to conserved charges and soft graviton theorems in quantum field theory [298, 188, 183, 189, 259, 257, 182, 185, 244]. These connections elevate the memory effect from a subtle general relativity prediction to a central feature of the gravitational infrared structure, with implications that bridge classical and quantum gravity.

Detection of Potential Quantum Gravity Fluctuations as Noise Sources in Interferometers

The possibility that quantum gravity effects manifest as a novel source of background in interferometric measurements has become an intriguing area of investigation [313, 328, 329, 219]. Some theoretical models [313, 314, 328, 41, 312, 219] propose that spacetime fluctuations at microscopic scales could accumulate over macroscopic distances, leading to detectable signals in laser interferometry experiments. Unlike conventional sources of noise, which can be mitigated through improved engineering, noise originating from quantum fluctuations in vacuum spacetime would be an inherent property of spacetime itself, setting a fundamental limit on precision measurement.

One class of models suggests that vacuum energy fluctuations in quantum gravity induce metric perturbations that ultimately affect the propagation of light [313, 314, 41, 329, 219]. These fluctuations could alter the interference pattern of laser beams, producing correlations in detector signals. Another approach considers that metric fluctuations might introduce non-local correlations in space and time [47, 88, 87, 89], leading to signatures distinguishable from classical noise sources.

Additionally, some theories [41, 329, 324, 39] propose that spacetime itself may exhibit quantum coherence properties, modifying the way light propagates in interferometers. If spacetime possesses an intrinsic quantum structure at extremely small scales, it could induce subtle fluctuations that accumulate over the laser beam's travel time, ultimately resulting in a measurable phase shift in interferometric measurements. These effects would be encoded in the phase space of causal diamonds, providing a link between interferometry and quantum gravity predictions.

Next-Generation Gravitational Wave Detectors

Although current interferometers have already demonstrated remarkable sensitivity, the next generation of detectors will push these limits further, potentially reaching the regime necessary to detect quantum gravity fluctuations. The proposed Cosmic Explorer (CE) and Einstein Telescope (ET) will improve strain sensitivity by more than an order of magnitude, possibly reaching levels of 10^{-25} or lower [137, 291, 304]. These improvements will be achieved through increased arm lengths, cryogenic cooling of mirrors to reduce thermal noise, and enhanced quantum optical techniques [237, 220, 317].

The upcoming GQuEST experiment [236] aims to empirically investigate models of quantum gravity by utilizing an ultra-sensitive tabletop laser interferometer. Building upon technologies developed for LIGO [107] and the Fermilab Holometer [97], the GQuEST detector seeks to surpass the standard quantum limit by employing photon-counting techniques [235]. This approach enables the detection of minuscule fluctuations in spacetime, potentially revealing quantum gravity effects. Cosmic Explorer [291], planned for deployment in the United States, will feature 40 km arms, significantly longer than the 4 km arms of LIGO, allowing for greater sensitivity to high-frequency gravitational waves. The Einstein Telescope [304], to be built underground in Europe, will adopt a triangular configuration with 10 km arms, designed to operate in both high-frequency and low-frequency modes. These detectors will not only enhance our ability to observe astrophysical events but may also be sensitive enough to reveal subtle signals arising from quantum fluctuations in spacetime itself.

If quantum gravity introduces an additional stochastic background, next-generation interferometers could isolate and characterize this signal. The key challenge lies in distinguishing background signals from quantum spacetime fluctuations amid instrumental and environmental noise. Nonetheless, if such a signal were detected, it would open an unprecedented experimental window into the quantum nature of spacetime, offering insights that enrich and complement theoretical progress.

Connecting Interferometry to Theoretical Predictions of Quantum Gravity

Laser interferometers offer a unique platform for testing certain predictions of quantum gravity. Theoretical models [313, 314, 328, 41, 329, 312, 219, 324, 39] suggest that quantum fluctuations of spacetime could introduce measurable deviations in high-precision optical systems, making interferometry a promising avenue for ex-

perimental tests.

One way to establish this connection is through the study of causal diamonds [313, 41, 324, 75], which provide a framework for analyzing quantum fluctuations in finite regions of spacetime. If these fluctuations influence the travel time of light or introduce subtle correlations between distant points, they could leave signatures in interferometric phase shifts. Moreover, some theories [313, 314, 219, 324, 39] suggest that spacetime fluctuations at small scales could lead to deviations from the classical geodesic deviation equation, potentially measurable with next-generation detectors.

Another key connection arises from the study of soft graviton modes and BMS symmetries, which suggest that gravitational memory effects in asymptotic infinity could introduce new, non-local correlations in gravitational wave signals [184, 191, 190]. If these effects are present, they would also be potentially observable in interferometers operating at low noise levels.

By systematically exploring these ideas, this dissertation aims to develop testable predictions for how quantum gravity fluctuations might manifest in laser interferometry. By integrating theoretical modeling with experimental sensitivity analysis, we aim to pinpoint observables through which fundamental physics can be tested and explored experimentally.

1.3 Scope and Contributions of This Dissertation

The central goal of this dissertation is to develop theoretical models that describe how quantum gravity fluctuations may manifest at observable scales and to explore their potential detectability in next-generation laser interferometers. Although quantum gravity has traditionally been studied as a purely theoretical endeavor, the extraordinary sensitivity of modern gravitational wave detectors offers a novel avenue for experimental investigation. By combining insights from string theory, general relativity, quantum mechanics, statistical mechanics, and precision interferometry, this dissertation aims to bridge the gap between fundamental theory and empirical science.

The first part of this dissertation is dedicated to developing a theoretical framework for understanding quantum fluctuations in gravitational systems. We begin by exploring how concepts from statistical mechanics, such as Brownian motion and the fluctuation-dissipation theorem, provide a foundation for studying quantum fluctuations in spacetime. We then analyze the connection between gravity and fluid

dynamics, investigating how gravitational shockwaves and near-horizon dynamics encode information about the quantum structure of spacetime. We also employ the covariant phase space formalism to investigate the role of asymptotic symmetries—particularly horizon-type BMS symmetries—in understanding gravitational fluctuations and their associated phase space degrees of freedom. A central contribution of this dissertation is the development of a quantum mechanical description for causal diamonds, offering a first-principles approach to studying gravitational degrees of freedom within quantum mechanics.

The second part of this dissertation investigates how quantum gravity fluctuations could give rise to detectable signatures in high-precision interferometric experiments. Although existing gravitational-wave detectors such as LIGO and Virgo have achieved remarkable sensitivity, upcoming next-generation detectors, such as the GQuEST experiment, the Cosmic Explorer, and the Einstein Telescope, will push these limits even further. These detectors may be capable of detecting signal sources that arise from quantum gravity effects, offering empirical evidence of Planck-scale physics. This dissertation explores the potential of laser interferometers to detect deviations from classical predictions by examining how quantum fluctuations may alter light propagation and create novel correlations in detector signals. By developing a theoretical framework to analyze these effects, we offer testable predictions that could inform future experimental endeavors.

Finally, the dissertation concludes with a complementary investigation of classical gravitational wave physics. Chapter 6 introduces a model for the stochastic gravitational wave memory background (SGWMB) sourced by supermassive binary black hole mergers. Building on the non-linear gravitational wave memory effect and the structure of BMS symmetries, this chapter develops a statistical framework for the accumulation of memory signals over cosmic time, characterizing the resulting background as a Brownian-like process with a $1/f^2$ strain spectrum. We further assess the detectability of this SGWMB with future space-based detectors such as LISA. While distinct in origin from the quantum gravity models discussed earlier, this classical background highlights the rich variety of gravitational wave signatures accessible to interferometric observatories and underscores the broader theme of this dissertation: that gravitational wave experiments can serve as powerful probes of both classical and quantum gravitational phenomena.

The key contributions of this dissertation are summarized as follows:

1. Theoretical Models of Quantum Fluctuations in Gravity

- Extend statistical mechanics concepts, such as the fluctuation-dissipation theorem, to gravitational systems.
- Establish a fluid/gravity correspondence framework for causal diamonds in AdS and Minkowski spacetimes and analyze hydrodynamical properties associated with causal horizons in response to quantum fluctuations.
- Investigate gravitational shockwaves as quantum sources of near-horizon fluctuations.
- Develop a quantum mechanics description of causal diamonds in Minkowski spacetime and identify conserved charges that govern their time evolution.

2. Implications for High-Precision Interferometry

- Analyze potential quantum gravity fluctuations as a stochastic background in interferometers.
- Identify concrete observables from quantum gravity effects that could be observed in interferometric experiments.
- Evaluate the feasibility of detecting quantum gravity fluctuations in next-generation detectors.

3. Modeling and Detectability of the Stochastic Gravitational Wave Memory Background

- Construct a theoretical framework for the SGWMB sourced by supermassive binary black hole mergers.
- Model the SGWMB as a Brownian-type process composed of step-function strain profiles, and derive its spectral and energy density characteristics.
- Incorporate astrophysical merger rates and redshift-dependent diffusion to assess the evolution and accumulation of the memory background across cosmic time.
- Evaluate the detectability of the SGWMB in the millihertz band with future space-based interferometers such as LISA, and identify key challenges related to non-Gaussianity and anisotropies in the source population.

By synthesizing these contributions, this dissertation aims to provide a comprehensive framework for understanding how quantum and classical gravitational phenomena may leave detectable imprints in current and future gravitational wave experiments. Although direct detection of quantum gravity remains an ambitious goal, this work lays the groundwork for future theoretical and observational developments that could bring us closer to uncovering the quantum nature of spacetime, while also enriching our understanding of classical gravitational memory and its astrophysical implications.

The remainder of this dissertation is structured as follows.

- **Chapter 2: Stochastic Description of Near-Horizon Fluctuations in Rindler-AdS**

We study quantum spacetime fluctuations near light-sheet horizons associated with a Rindler wedge in AdS spacetime, in the context of AdS/CFT. In particular, we solve the vacuum Einstein equation near the light-sheet horizon, augmented with the Ansatz of a quantum source smeared out in a Planckian width along one of the light-cone directions. Such a source, whose physical interpretation is of gravitational shockwaves created by vacuum energy fluctuations, alters the Einstein equation to a stochastic partial differential equation taking the form of a Langevin equation. By integrating fluctuations along the light sheet, we find an accumulated effect in the round-trip time of a photon to traverse the horizon of the Rindler wedge that depends on both the d -dimensional Newton constant $G_N^{(d)}$ and the AdS curvature L , in agreement with previous literature utilizing different methods.

- **Chapter 3: Rindler Fluids from Gravitational Shockwaves**

We study a correspondence between gravitational shockwave geometry and its fluid description near a Rindler horizon in Minkowski spacetime. Utilizing the Petrov classification that describes algebraic symmetries for Lorentzian spaces, we establish an explicit mapping between a potential fluid and the shockwave metric perturbation, where the Einstein equation for the shockwave geometry is equivalent to the incompressibility condition of the fluid, augmented by a shockwave source. Then we consider an Ansatz of a stochastic quantum source for the potential fluid, which has the physical interpretation of shockwaves created by vacuum energy fluctuations. Under such circumstances, the Einstein equation, or equivalently, the incompressibility condition

for the fluid, becomes a stochastic differential equation. By smearing the quantum source on a stretched horizon in a Lorentz-invariant manner with a Planckian width (similarly to the membrane paradigm), we integrate fluctuations near the Rindler horizon to find an accumulated effect of the variance in the round-trip time of a photon traversing the horizon of a causal diamond.

- **Chapter 4: The Quantum Mechanics of a Spherically Symmetric Causal Diamond in Minkowski Spacetime**

We construct the phase space of a spherically symmetric causal diamond in $(d + 2)$ -dimensional Minkowski spacetime. Utilizing the covariant phase space formalism, we identify the relevant degrees of freedom that localize to the d -dimensional bifurcate horizon and, upon canonical quantization, determine their commutators. On this phase space, we find two Iyer-Wald charges. The first of these charges, proportional to the area of the causal diamond, is responsible for shifting the null time along the horizon and has been well-documented in the literature. The second charge is much less understood, being integrable for $d \geq 2$ only if we allow for field-dependent diffeomorphisms and is responsible for changing the size of the causal diamond.

- **Chapter 5: Quantum Gravity Background in Next-Generation Gravitational Wave Detectors**

We study the effects of geotropic vacuum fluctuations in quantum gravity on next-generation terrestrial gravitational wave detectors. If the VZ effect proposed in Ref. [314], as modeled in Refs. [328, 219], appears in the upcoming GQuEST experiment, we show that it will be a large background for astrophysical gravitational wave searches in observatories like Cosmic Explorer and the Einstein Telescope.

- **Chapter 6: Stochastic Gravitational Wave Memory Background of Supermassive Binary Black Hole Mergers and Its Detection in LISA**

We construct a classical model of the SGWMB sourced by supermassive binary black hole mergers and investigate its potential observability in future space-based detectors. This chapter begins by reviewing the mathematical framework of stochastic gravitational wave backgrounds and the gravitational memory effect, particularly in relation to BMS symmetries. We then derive the SGWMB as a Brownian-type process composed of step-function memory signals from individual mergers, leading to a characteristic $1/f^2$ strain spectrum and a corresponding f -linear energy density. By incorporating cos-

mological merger rates and redshift-dependent diffusion effects, we analyze the accumulation of memory across cosmic time. Finally, we assess the detectability of the SGWMB by comparing its predicted energy density to the sensitivity curve of LISA and discuss challenges such as non-Gaussianity and anisotropies in the source distribution.

- **Chapter 7: Summary and Outlook**

We summarize the key results and discuss future directions for testing quantum gravity through high-precision measurement techniques.

Chapter 2

STOCHASTIC DESCRIPTION OF NEAR-HORIZON
FLUCTUATIONS IN RINDLER-ADS

2.1 Introduction

The quantum mechanical description of gravity is one of the most elusive questions in physics. An important tool towards understanding the ultimate theory of quantum gravity is the AdS/CFT correspondence. In this chapter, we aim to study the dynamics of gravity in the region of AdS spacetime near light sheets shown in Fig. 2.1. In particular, we seek to understand how spacetime fluctuations alter the trajectory of a photon in the d -dimensional bulk. Ref. [313] found a fluctuation in the round-trip time, $T_{r.t.}$, of a photon traveling from the AdS boundary to the Ryu-Takayanagi (RT) surface Σ_{d-2} in the bulk having area $A(\Sigma_{d-2})$ and back to the boundary:

$$\frac{\Delta T_{r.t.}^2}{T_{r.t.}^2} = \frac{2}{(d-2)} \sqrt{\frac{4G_N^{(d)}}{A(\Sigma_{d-2})}}. \quad (2.1)$$

The boundary of a causal diamond created by light sheets is defined by a Rindler horizon, which has a non-zero temperature and entropy, similar to a black hole event horizon. The calculation of Ref. [313] (as well as Refs. [314, 41]) operated through the analogue between the boundary of the Rindler wedge and a black hole horizon, utilizing techniques developed in, *e.g.*, [91, 195]. In AdS/CFT, the modular Hamiltonian K and its fluctuations ΔK obey an area law similar to a black hole horizon [313, 261, 246, 118]

$$\langle K \rangle = \langle \Delta K^2 \rangle = \frac{A(\Sigma_{d-2})}{4G_N^{(d)}} = S_{ent.}, \quad (2.2)$$

where $S_{ent.}$ is the entanglement entropy. Further, the metric, if restricting to only the part of the spacetime covered by the Rindler wedge shown in Fig. 2.1, can be parameterized in terms of the *topological* black hole:

$$ds^2 = -f(\rho)d\tau^2 + \frac{d\rho^2}{f(\rho)} + \frac{\rho^2}{L^2}d\Sigma_{d-2}^2 \quad \text{with} \quad f(\rho) = \frac{\rho^2}{L^2} - 1, \quad (2.3)$$

where L is the AdS radius, the radial coordinate ρ ranges from $L \leq \rho < \infty$. Ref. [329], based on the calculations of Ref. [314, 313, 41], proposed a dictionary

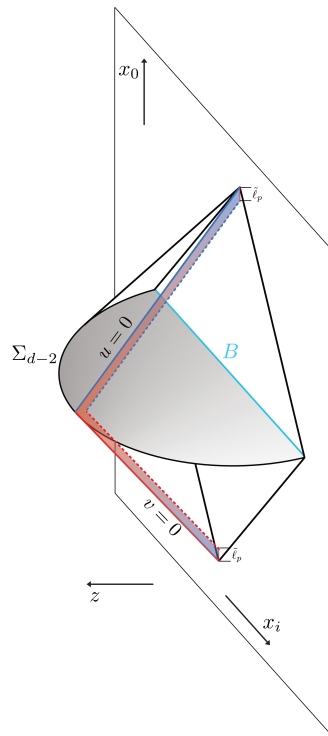


Figure 2.1: Depiction of the causal diamond in AdS space anchored at the boundary. The red solid line traces out the light signal emitted from the boundary to a point in the bulk on the Ryu-Takayanagi surface labeled by Σ_{d-2} , while the blue solid line represents the light reflected from the point in the bulk and received at the boundary. The dashed lines represent the smearing of the light-sheet horizon. The red and blue shaded region represents quantum gravity induced fluctuations of the light trajectory.

between the horizons of causal diamonds (in common spacetimes such as AdS and Minkowski) and black hole horizons.

It has long been known that black hole horizons have a hydrodynamic description, known as the fluid/gravity correspondence [116, 269, 252]. The fluid/gravity correspondence was made more precise in the context of AdS/CFT, where the hydrodynamics of a strongly interacting fluid (*e.g.*, quark-gluon plasma) on the asymptotic boundary of a lower-dimensional spacetime is described by gravitational dynamics on a black brane in the bulk of AdS [266, 267, 211, 212]. These works inspired an extensive literature studying a hydrodynamic effective description of gravity, *e.g.*, [51, 271, 62, 59, 251, 114]. Further, Refs. [71, 70] studied the dynamics of gravity in flat spacetime with a cut-off surface, showing that the Einstein Equation in vacuum reduces to a Navier-Stokes equation in one lower spacetime dimension.

Here, we utilize an effective fluid description of gravity at the horizon of the Rindler Wedge in AdS shown in Fig. 2.1 to understand and re-cast the result Eq. (2.1). In particular, we will study the Einstein equation near the boundary defined by null sheets in Fig. 2.1. The hydrodynamic behavior of the metric becomes apparent when the vacuum Einstein equation in the near-horizon limit is augmented with an *Ansatz* that the Einstein equation has a quantum source:

$$\begin{aligned} \left(\frac{d-2}{L^2} - \nabla_{\perp}^2\right) \langle h_{uu}(u, \mathbf{x}_{\perp}) h_{uu}(u', \mathbf{x}'_{\perp}) \rangle &= 8\pi G_N^{(d)} \frac{\delta(u-u')}{2\pi \tilde{\ell}_p} \delta^{d-2}(\mathbf{x}_{\perp} - \mathbf{x}'_{\perp}), \\ \left(\frac{d-2}{L^2} - \nabla_{\perp}^2\right) \langle h_{vv}(v, \mathbf{x}_{\perp}) h_{vv}(v', \mathbf{x}'_{\perp}) \rangle &= 8\pi G_N^{(d)} \frac{\delta(v-v')}{2\pi \tilde{\ell}_p} \delta^{d-2}(\mathbf{x}_{\perp} - \mathbf{x}'_{\perp}). \end{aligned} \quad (2.4)$$

Here, u , v are light-cone coordinates, while \mathbf{x}_{\perp} are the $(d-2)$ remaining transverse spatial directions. The left-hand side is derived from the vacuum Einstein Equation in AdS in the near-horizon limit, while the right-hand side is a quantum noise term, an *Ansatz* motivated by the membrane paradigm. In particular, a gravitationally coupled ultra-local quantum noise term, $\delta^d(x-x')$, is reduced on one of the light-cone directions by smearing one of the light-cone delta functions with a Planckian width $\tilde{\ell}_p$ across a membrane (or black-brane) at the light-sheet horizon. This smearing is depicted as a red/blue band in Fig. 2.1. When we solve this equation to obtain the fluctuation in the photon round-trip traversal time, we will reproduce Eq. (2.1), provided that the width of the black-brane $\tilde{\ell}_p$ is the reduced Planck-scale, which we discuss below.

Note that the quantum source on the right-hand side of Eq. (2.4) now appears like an energetic particle that creates a gravitational shockwave, as proposed by Dray-'t Hooft [126]. Such shockwaves were recently shown in Ref. [312] to generate the modular relations in Eq. (2.2), creating a self-consistent physical picture. The quantum noise term in Eq. (2.4) turns the Einstein equation into a Langevin-type equation

$$\langle \dot{X}(\tau) \dot{X}(\tau') \rangle = \langle F(\tau) F(\tau') \rangle, \quad (2.5)$$

where $\langle F(\tau) F(\tau') \rangle = 2\mathcal{D}\delta(\tau - \tau')$ is a noise term with the diffusion coefficient \mathcal{D} characterizing the scale of interaction, and we have integrated Eq. (2.4) over the $(d-2)$ directions transverse to the lightcone coordinates. Here $X(\tau)$ is a position variable identified with $X(\tau) = \int^{\tau} h_{\tau\tau}(\tau') d\tau'$, where $\tau = u(v)$ on the lower (upper) half of the causal diamond, and the two-point of $\eta(\tau)$ describes a stochastic noise that drives a random walk. Consequently, the classical Einstein equation becomes a stochastic differential equation, where the *quantum uncertainty* in spacetime itself

undergoes a random walk, with the correlations in the $(d - 2)$ transverse directions given by the Green function of the transverse Laplacian.

A “smeared-out” horizon is quite analogous to the notion of a stretched horizon, which is a time-like hypersurface Planckian separated from the true horizon first proposed by Damour [116]. Later Refs. [269, 252] showed that the properties of a black hole horizon can be mapped to those on the stretched horizon. In the present context, we will smear out the horizon by a “reduced Planck length” previously identified in Refs. [312, 41, 329]:

$$\tilde{\ell}_p^2 \sim \frac{\ell_p^{d-2}}{L^{d-4}}. \quad (2.6)$$

In four dimensions, the reduced Planck length corresponds to simply the Planck length, $\tilde{\ell}_p \sim \ell_p \equiv \sqrt{8\pi G_N}$.¹ In a general number of dimensions, the length scale in Eq. (2.6) was identified as the fundamental length scale of ’t Hooft commutation relations in any number of dimensions [312]. $\tilde{\ell}_p \sim L/\sqrt{S_{ent}}$ in Eq. (2.6) was also identified in Ref. [41] as the decoherence scale of nested causal diamonds, each of which have S_{ent} degrees-of-freedom. We will find that positing a causal diamond with a stretched horizon of width given by Eq. (2.6) allows us to reproduce Eq. (2.1), the main result of Ref. [313].

Lastly, we comment that while the square-root behavior of the variance $\Delta T_{r,t}^2$ in Eq. (2.1) is perhaps somewhat perplexing from a scattering amplitude or naïve EFT perspective, it is, however, characteristic of random walk behavior in hydrodynamics, where fluctuations take a typical form

$$\Delta T_{r,t}^2 \sim \tilde{\ell}_p^2 \mathcal{N}, \quad (2.7)$$

where $\tilde{\ell}_p$ is the UV time scale of the hydrodynamic theory (normally associated to the diffusion coefficient, as discussed in Ref. [329]), and $\mathcal{N} = L/\tilde{\ell}_p$ is the number of steps in the random walk over the round-trip time.

The outline of this chapter is as follows. In Sec. 2.2 we set the stage by reviewing the background geometry. In Sec. 2.3, we study the gravitational perturbations to the background geometry and show that the Einstein equation in near-horizon limit reduces to an equation relating metric fluctuations and gravitational shockwaves. In Sec. 2.4, we solve this equation with a source term derived from the t’Hooft

¹In $d > 4$, the Planck length is reduced by the IR scale L to a scale smaller than ℓ_p , suggesting to us that in $d > 4$ there is actually no cumulative IR effect of the quantum fluctuations of spacetime.

commutation relations. Then we use the solution to calculate the uncertainty in photon round-trip time. Finally, in Sec. 2.5, we discuss implications of our results and point to a few future directions. Throughout this chapter, we will use $8\pi G_N^{(d)} = \ell_p^{d-2}$ for the gravitational constant and Planck length in d dimensions.

2.2 Preliminaries: Background Geometry

As discussed in the introduction, we consider the geometric setup in Fig. 2.1. A photon is emitted from the boundary into the bulk of d -dimensional AdS space, reflected by a “mirror” on the RT surface in the bulk, and finally received on the boundary. We briefly review three coordinates used throughout this chapter, Poincaré, Eddington-Finkelstein (EF), and Kruskal–Szekeres. The first (and most standard) will be useful for interpreting the results in terms of the observable time delay. The EF coordinates are closely related to topological-black hole coordinates introduced in Eq. (2.3), and are useful as an intermediate step to derive equations of motion governing the dynamics of near-horizon metric fluctuations. Finally, the Kruskal–Szekeres coordinates are the curved space analog of the light-cone metric. The light-cone metric is used extensively to study the effects of spacetime fluctuations of a causal diamond in Minkowski space in Refs. [314, 312], and a natural generalization to curved spacetime is provided by the Kruskal–Szekeres coordinates. We now proceed to briefly summarize these three coordinate systems, as useful for our discussion.

From Topological Black Hole to Poincaré Metric

While the topological black hole metric described in Sec. 2.1 is suitable to study the interior of the bulk causal diamond, there is also a causal diamond with spherical symmetry on the boundary, such that the interferometer could also be viewed as being on the (suitably regularized) boundary. The Poincaré metric describes the near boundary region of the d -dimensional AdS space:

$$ds^2 = \frac{L^2}{z^2} (dz^2 - dx_0^2 + \delta_{ab} dx^a dx^b) \quad \text{for } a, b = 1, \dots, d-2. \quad (2.8)$$

A causal diamond in AdS is illustrated in Fig. 2.1, in which the blue line denoted by B is the finite spherical entangling surface on the boundary, described by the inequality $\sum_i x_i^2 \leq L^2$. The full interior of the causal diamond satisfies the inequality [313]

$$L^2 - z^2 - \sum_i x_i^2 + x_0^2 \geq 2L|x_0|. \quad (2.9)$$

The transformation between the Poincaré and topological black hole metrics is given in Refs. [91, 313], which we do not repeat since the details are not important for the purpose of this chapter.

From Topological Black Hole to Kruskal–Szekeres Metric

Our interest is in the dynamics of spacetime fluctuations near the light front of Rindler-AdS space. The light front coincides with the horizon of the topological black hole metric, where Eq. (2.3) becomes singular, and it becomes desirable to perform a coordinate transformation to overcome the apparent pathology of Eq. (2.3). We transform the topological black hole metric into the Eddington-Finkelstein (EF) metric as an intermediate step, defining the tortoise coordinate ρ_*

$$\rho_* \equiv \int^\rho \frac{d\rho'}{f(\rho')} = \frac{L}{2} \ln \frac{\rho - L}{\rho + L}, \quad (2.10)$$

where $f(\rho) = \rho^2/L^2 - 1$. Then we define two new coordinates U and V

$$V \equiv \tau + \rho_* \quad \text{and} \quad U \equiv \tau - \rho_*. \quad (2.11)$$

In terms of U and V , the original topological black hole metric in Eq. (2.3) becomes

$$ds^2 = -f(\rho)dV^2 + 2dVd\rho + \left(\frac{\rho}{L}\right)^2 d\Sigma_{d-2}^2, \quad (\text{EF-ingoing}) \quad (2.12)$$

$$ds^2 = -f(\rho)dU^2 - 2dUd\rho + \left(\frac{\rho}{L}\right)^2 d\Sigma_{d-2}^2. \quad (\text{EF-outgoing}) \quad (2.13)$$

The metric $d\Sigma_{d-2}^2$ in the transverse space is given by

$$d\Sigma_{d-2}^2 = d\chi^2 + \sinh^2\left(\frac{\chi}{L}\right) d\Omega_{d-3}^2. \quad (2.14)$$

The form of Eq. (2.14) plays an important role in determining the angular correlation functions of uncertainty in the photon traversal time. We will discuss angular correlations in detail in Sec. 2.4. Both metrics above are non-singular at the horizon. While Eq. (2.12) describes the trajectories of particles on the upper half of the causal diamond in Fig. 2.1, Eq. (2.13) describes the trajectories of particles on the lower half.

Following Refs. [23, 241], we define the “light-cone” coordinates in Rindler-AdS space

$$u = -Le^{-U/L} = -L\sqrt{\frac{\rho - L}{\rho + L}}e^{-\tau/L}, \quad v = Le^{V/L} = L\sqrt{\frac{\rho - L}{\rho + L}}e^{\tau/L}, \quad (2.15)$$

where the second equality relates u and v to the topological black hole coordinates (τ, ρ) . Rindler-AdS space in the Kruskal-Szekeres metric becomes

$$ds^2 = -\frac{4L^4 dudv}{(L^2 + uv)^2} + \left(\frac{L^2 - uv}{L^2 + uv}\right)^2 d\Sigma_{d-2}^2. \quad (2.16)$$

An advantage of the Kruskal–Szekeres metric is that the “light-cone time” u and v are proportional to the *physical time* of a photon traveling inside an interferometer located on the (regularized) boundary at $z = z_c$. The proportionality constant turns out to be (L/z_c) [313], the conformal factor of the Poincaré metric. In summary, the elapsed lightcone time in traversing the lower (upper) causal diamond is $\Delta u = L$ ($\Delta v = L$), and the physical time $T_{r.t.} \approx 2L^2/z_c$.

Our main task is to determine how spacetime fluctuations would alter the classical traversal time of the light beams; to do so, we start with studying metric perturbations about the Rindler-AdS background geometry in the subsequent section.

2.3 Near Horizon Metric Perturbations

Given the background geometry in Sec. 2.2, our goal is to study fluctuations on top of this background, and how they will give rise to a potentially observable effect in an interferometer experiment. Spacetime fluctuations are encapsulated by metric perturbations. Because these fluctuations are small in amplitude, we utilize the linearized Einstein equations to study the dynamics of the perturbed metric.

The vacuum Einstein equations for AdS_d spacetime reads

$$G_{MN} \equiv R_{MN} - \frac{1}{2}g_{MN}R + \Lambda g_{MN} = 0, \quad (2.17)$$

where $M, N = 1, \dots, d$ are the indices of AdS_d bulk spacetime, and $\Lambda = -(d-1)(d-2)/2L^2$ is the cosmological constant. All the metrics in Secs. 2.1 and 2.2 are solutions to the vacuum Einstein equations.

We are interested in metric fluctuations in the near-horizon region of Rindler-AdS space, so it is most convenient to use the EF coordinates. Metric perturbations along the past (future) light front are described by Eq. (2.13) (Eq. (2.12)). We choose to study metric fluctuations along the past light front, which corresponds to using the EF-outgoing metric. A completely analogous analysis applies for the future light front. The perturbed metric along the past light front is given by

$$ds^2 = -f(\rho)dU^2 - 2dUd\rho + \left(\frac{\rho}{L}\right)^2 d\Sigma_{d-2}^2 + H_{UU}dU^2 + 2H_{U\rho}dUd\rho + H_{\rho\rho}d\rho^2 + \dots, \quad (2.18)$$

where (\dots) denotes H_{ab} , $a, b = 1, \dots, d-2$ in the transverse space.

The perturbed metric in Eq. (2.18) solves the linearized Einstein equation for $|H_{MN}| \ll 1$, which in AdS space is given by [211, 212]

$$\delta G_{MN}^{(1)} \equiv R_{MN}^{(1)} + \frac{d-1}{L^2} H_{MN} = 0, \quad (2.19)$$

where the perturbed Ricci tensor $R_{MN}^{(1)}$ satisfies [266]

$$R_{MN} = R_{MN}^{(0)} + R_{MN}^{(1)} + \dots = -\frac{(d-1)}{L^2} (g_{MN}^{(0)} + H_{MN}). \quad (2.20)$$

Here, $g_{MN}^{(0)}$ denotes the background metric. Next, we expand the perturbations as a power series in the near-horizon region [23, 58]

$$H_{MN} = H_{MN}^{(0)} + H_{MN}^{(1)} \left(\frac{r-L}{L} \right) + \dots, \quad (2.21)$$

and $H_{MN}^{(0)}$ can be written as

$$H_{MN}^{(0)}(U, \mathbf{x}_\perp) = \int \frac{d\omega}{2\pi} h_{MN}(\mathbf{x}_\perp) e^{-i\omega U}, \quad (2.22)$$

where \mathbf{x}_\perp denotes the coordinates in the transverse space, and ω is the frequency conjugate to U . Following the procedure in Refs. [58, 23], one can show that the UU -component of the linearized Einstein equation describes the Dray-'t Hooft shockwave perturbation in Refs. [126, 282]. Substituting Eq. (2.22) into Eq. (2.19), we find the UU -component of Eq. (2.19) to be [23, 58]

$$\begin{aligned} & \frac{d-2}{L^2} \left[1 + L \left(4\pi T - i\omega - \frac{3}{L} \right) \right] h_{UU}^{(0)} - \nabla_\perp^2 h_{UU}^{(0)} \\ & - \frac{i\omega + 2\pi T}{L} X = 0, \end{aligned} \quad (2.23)$$

where

$$T = \frac{f'(\rho)}{4\pi} \Big|_{\rho=L} = \frac{1}{2\pi L} \quad (2.24)$$

is the Hawking temperature. The variable X denotes all $h_{MN}^{(0)}$ coupled to $h_{UU}^{(0)}$ via Eq. (2.19). In general, the exact form of X is quite complicated. For instance, Ref. [23] has computed the form of X in AdS₄ to be

$$\begin{aligned} X \stackrel{d=4}{=} & 2 \coth(\chi/L) h_{U\chi}^{(0)} + i\omega L \left(\text{csch}^2(\chi/L) h_{\theta\theta}^{(0)} + h_{\chi\chi}^{(0)} \right) \\ & + 2 \text{csch}^2(\chi/L) \frac{\partial h_{U\theta}^{(0)}}{\partial \theta} + 2L \frac{\partial h_{U\chi}^{(0)}}{\partial \chi}. \end{aligned} \quad (2.25)$$

Fortunately, the precise form of X will not be relevant for the purposes of this chapter.

Eq. (2.23) thus imposes a constraint relating $h_{UU}^{(0)}$ to other metric perturbation components. However, when $\omega = \omega_\star = i2\pi T$, the second line of Eq. (2.23) vanishes altogether. The resulting equation takes on the same form of the partial differential equation describing metric perturbations due to gravitational shockwaves [126, 282]. As pointed out in Ref. [58], the point $\omega_\star = i2\pi T$ is very special, as $2\pi T$ is also known as the *Lyapunov exponent*: $2\pi T = \lambda_{\max}$, which characterizes chaotic behavior in a quantum system [283, 274, 285, 59]. Following the argument of Refs. [58, 23], one deduces that at the point $\omega_\star = i2\pi T$, $h_{UU}^{(0)}$ decouples from the rest of $h_{MN}^{(0)}$ and becomes an *independent* scalar degree of freedom which satisfies the equation

$$\left(\frac{d-2}{L^2} - \nabla_\perp^2\right)h_{UU}^{(0)} = 0. \quad (2.26)$$

The solution to this equation is readily obtained by setting $\nabla_\perp^2 h_{UU}^{(0)} = -k_\perp^2 h_{UU}^{(0)}$, with k_\perp^2 being the eigenvalue of the transversal Laplacian operator. Therefore, Eq. (2.26) is reduced to an algebraic equation

$$\frac{d-2}{L^2} + k_\perp^2 = 0. \quad (2.27)$$

We can re-write Eq. (2.27) by substituting $\omega_\star = i2\pi T = L^{-1}$ into the expression

$$\omega_\star = iDk_\perp^2, \quad D = \frac{L}{d-2} = \frac{v_B}{2\pi T}, \quad (2.28)$$

so it resembles the dispersion relation arising from a diffusive system. The diffusivity D characterizes the so-called energy diffusion [58], because the metric perturbation is in the UU -component. The factor of $1/(d-2) = v_B$ has been shown [23, 262] to be the *butterfly velocity* in Rindler-AdS space. The butterfly velocity characterizes the speed of information propagating in a system with a horizon (*e.g.*, a black hole), and it is closely related to the propagation of gravitational shockwaves and quantum chaos [283, 281, 301, 285]. Furthermore, Ref. [170] studying an AdS₅ black-brane obtained a similar diffusive dispersion with the same Lyapunov exponent, but with a different v_B . In fact, several recent works [57, 56, 59, 58] have shown that energy diffusion phenomenon is quite universal in various holographic systems, which all have the same Lyapunov exponent, but with a geometry-dependent v_B .

So far our discussions have been completely classical. Eq. (2.26) also describes classical gravitational shockwaves [126, 23, 58, 170] if we add a source, where the

right-hand side is $8\pi G_N T_{UU} \sim \ell_p^{d-2} \frac{\delta(U-U_0)}{2\pi\tilde{\ell}_p} \delta^{d-2}(\mathbf{x}_\perp - \mathbf{x}_\perp^0)$ for a classical shockwave stress-energy tensor propagating at $x_0 = (U_0, \mathbf{x}_\perp^0)$ with momentum $p_\nu = \frac{1}{2\pi\tilde{\ell}_p}$. It is, however, possible to also consider quantum sources. In particular, we focus on a quantum source from vacuum energy fluctuations, motivated by the 't Hooft commutation relations [5, 2]. In particular, Ref. [312] showed that vacuum fluctuations in Minkowski space, fixed by the 't Hooft commutation relations, give rise to the modular fluctuations in Eq. (2.2). In the following, we will utilize this result and apply it to Rindler-AdS space, by adding a quantum source to the vacuum Einstein equation Eq. (2.26) of size fixed by the 't Hooft commutation relations. In so doing, we will reproduce quantum fluctuations in the round-trip photon travel time in Eq. (2.1).

Quantum Sources from the 't Hooft Commutation Relation

We will ultimately be interested in studying Eq. (2.26) in the presence of shockwaves from quantum fluctuations. In particular, these quantum fluctuations are motivated by the commutation relations proposed in Ref. [312], which are written in light-cone coordinates (u, v) . Thus, we will transform the EF coordinates (U, ρ) of Eq. (2.26) to the light-cone (u, v) Kruskal–Szekeres metric, taking $h_{UU} \rightarrow h_{uu}$, where we suppress the superscript henceforth. Because u and U are related via Eq. (2.15), it is straightforward to see that in the Kruskal–Szekeres metric, Eq. (2.26) is

$$\left(\frac{d-2}{L^2} - \nabla_\perp^2\right)h_{uu} = 0. \quad (2.29)$$

Due to vacuum energy fluctuations, the right hand side of Eq. (2.29) is replaced with some stress-energy tensor T_{uu} .

Here we will assume that T_{uu} captures the quantum nature of the fluctuations. This is the *Ansatz* of this chapter that differs from other literature, which further will be crucial for obtaining the fluctuation in the round-trip photon traversal time obtained in Ref. [313]. In particular, we make use of a commutation relation (closely related to those proposed by 't Hooft) at *unequal* times [312]

$$[T_{uu}(x), h_{vv}(x')] = i\delta^d(x - x'), \quad (2.30)$$

where x denotes the coordinates in Rindler-AdS $_d$ space, written in light-cone coordinates. The d -dimensional delta function can be factorized into three parts

$$\delta^d(x - x') = \frac{1}{2}\delta(u - u_0)\delta(v - v_0)\delta^{d-2}(\mathbf{x}_\perp - \mathbf{x}'_\perp), \quad (2.31)$$

where u_0 and v_0 denote the location of the bifurcate horizon, and $\delta^{d-2}(\mathbf{x}_\perp - \mathbf{x}'_\perp)$ is the $(d-2)$ -dimensional delta function in the transverse space. Note that the additional factor of $1/2$ comes from the normalization condition for the delta function in the Kruskal-Szekeres metric. Imposing the commutation relation in Eq. (2.30) implies that h_{uu} and h_{vv} are no longer classical metric perturbations, but have been promoted to quantum operators. By further imposing the linearized Einstein equation on Eq. (2.30), we obtain an operator equation

$$\left(\frac{d-2}{L^2} - \nabla_\perp^2\right)[h_{uu}(u, \mathbf{x}_\perp), h_{vv}(v, \mathbf{x}'_\perp)] = \frac{i}{2}\ell_p^{d-2}\delta(u-u_0)\delta(v-v_0)\delta^{d-2}(\mathbf{x}_\perp - \mathbf{x}'_\perp). \quad (2.32)$$

Note that the transverse Laplacian acts only on $h_{uu}(u, \mathbf{x}_\perp)$, and not the coordinates marked with a prime in $h_{vv}(v, \mathbf{x}'_\perp)$. Eq. (2.32) then implies that

$$[h_{uu}(u, \mathbf{x}_\perp), h_{vv}(v, \mathbf{x}'_\perp)] = \frac{i}{2}\ell_p^{d-2}\delta(u-u_0)\delta(v-v_0)f(\mathbf{x}_\perp; \mathbf{x}'_\perp), \quad (2.33)$$

where $\ell_p^{d-2} = 8\pi G_N^{(d)}$, and $f(\mathbf{x}_\perp; \mathbf{x}'_\perp)$ is the Green function that satisfies

$$\left(\frac{d-2}{L^2} - \nabla_\perp^2\right)f(\mathbf{x}_\perp; \mathbf{x}'_\perp) = \delta^{d-2}(\mathbf{x}_\perp - \mathbf{x}'_\perp). \quad (2.34)$$

Since T_{uu} is a stochastic source in vacuum, this implies that $\langle h_{uu} \rangle$ and $\langle h_{vv} \rangle$ vanish, where $\langle \dots \rangle$ denotes the expectation value of any minimum uncertainty state. However, the variance $\langle h_{uu}^2 \rangle$ and $\langle h_{vv}^2 \rangle$ are non-vanishing by the virtue of the Robertson uncertainty relation in quantum mechanics

$$\langle h_{uu}^2 \rangle \langle h_{vv}^2 \rangle = \left| \frac{1}{2i} \langle [h_{uu}, h_{vv}] \rangle \right|^2 = \left(\frac{\ell_p^{d-2}}{4} \right)^2 [\delta(u-u_0)\delta(v-v_0)f(\mathbf{x}_\perp; \mathbf{x}'_\perp)]^2. \quad (2.35)$$

Two important comments are in order.

- (1) Formally, the 't Hooft commutation relations were formulated on the horizon of a black hole. In the present context, that would imply Eq. (2.35) is evaluated at the bifurcate horizon, which is located at $u_0 = v_0 = 0$. However, according to Refs. [41, 329], the light beam in an interferometer system passes through a series of causal diamonds. Specifically, the maximal causal diamond in Fig. 2.1 is foliated by a sequence of nested causal diamonds. Each of the adjacent causal diamonds is separated by a length scale, called the *decoherence length* $\tilde{\ell}_p$, given in Eq. (2.6). Subsequent causal diamonds separated by a distance larger than

$\tilde{\ell}_p$ become *statistically independent* [41]. A schematic of the nested causal diamonds is shown in Fig. 2.2. Along the past light front, we keep v fixed, while u varies along the trajectory; along the future light front, the opposite holds. From the viewpoint of nested causal diamonds, a light beam traveling along the past light front will experience a series of statistically independent fluctuations. Along the past (future) null trajectory, where the clock is u (v), one can define the variance $\langle h_{uu}^2 \rangle \equiv \langle h_{uu}(u, \mathbf{x}_\perp) h_{uu}(u', \mathbf{x}'_\perp) \rangle$ ($\langle h_{vv}^2 \rangle \equiv \langle h_{vv}(v, \mathbf{x}_\perp) h_{vv}(v', \mathbf{x}'_\perp) \rangle$), where u' (v') denotes the location of the bifurcate horizons of each nested causal diamond.

- (2) We postulate the past (future) light front will be smeared out by $\tilde{\ell}_p$, which operationally means the delta function which localizes the light front at v_0 (u_0), $\delta(v - v_0) = \delta(v)$ ($\delta(u - u_0) = \delta(u)$) will be replaced by a regularized delta function of Planckian width. This is quite similar to the implementation of a stretched horizon for a black hole in Refs. [302, 281, 301]. In the present case, we implement the “smearing” of the light front by regularizing $\delta(v)$ with a Poisson kernel of a Lorentzian width $\tilde{\ell}_p$:

$$\delta(v) = \lim_{\tilde{\ell}_p \rightarrow 0} \frac{2}{\pi} \frac{\tilde{\ell}_p}{\tilde{\ell}_p^2 + v^2} \approx \frac{2}{\pi \tilde{\ell}_p} \quad \text{along the past light front } v \rightarrow 0. \quad (2.36)$$

These points are illustrated in Fig. 2.2, where the broadening of the delta function along the past and future light front is shown as a shaded red/blue gradient. Note that our final result for the fluctuations in the photon round-trip traversal time may depend on the precise form of the delta-function regularization by an $\mathcal{O}(1)$ number, but can be absorbed into an $\mathcal{O}(1)$ (dimensionless) coefficient by matching the present hydrodynamic result to the earlier result in Eq. (2.1). The regularization scheme thus will not impact the overall physical picture since the dimensionful scales match between the present hydrodynamic calculation and the result of Ref. [313].

In summary, Eq. (2.35) together with Eq. (2.36), at a *fixed point* on the past or future null horizon, implies a non-vanishing two-point function of h_{uu} and h_{vv} given by

$$\langle h_{uu}(u, \mathbf{x}_\perp) h_{uu}(u', \mathbf{x}'_\perp) \rangle = \frac{\ell_p^{d-2}}{2\pi \tilde{\ell}_p} \delta(u - u') f(\mathbf{x}_\perp; \mathbf{x}'_\perp), \quad (2.37)$$

$$\langle h_{vv}(v, \mathbf{x}_\perp) h_{vv}(v', \mathbf{x}'_\perp) \rangle = \frac{\ell_p^{d-2}}{2\pi \tilde{\ell}_p} \delta(v - v') f(\mathbf{x}_\perp; \mathbf{x}'_\perp). \quad (2.38)$$

In the next section, we study how these fundamental commutators can be evolved to give the integrated uncertainty in the light traversal time.

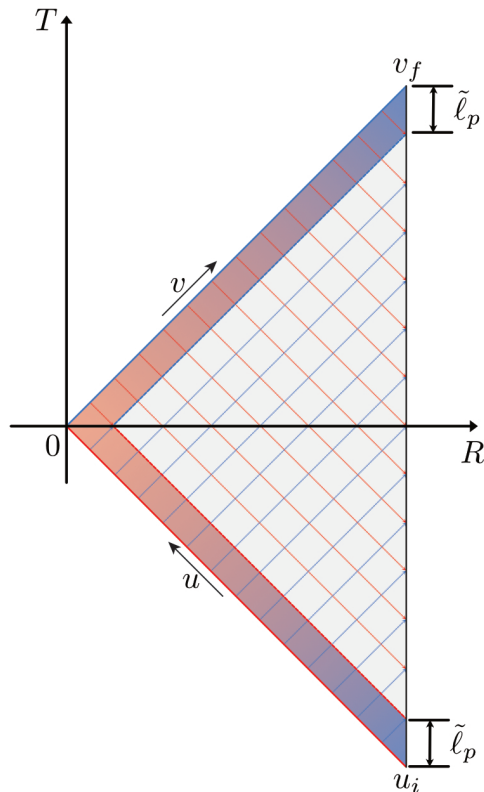


Figure 2.2: The causal diamond in Rindler-AdS space is foliated with a series of nested causal diamonds. The separation between two adjacent diamonds is the decoherence length $\tilde{\ell}_p$. Each nested causal diamond intersects with the past (future) light front at a bifurcate horizon along the past (future) light front. The highlighted region corresponds to the near-light-sheet region of spacetime, where quantum fluctuations cause a probe photon to undergo a random walk.

2.4 Uncertainty in Photon Traversal Time From Near-horizon Quantum Fluctuations

In the previous section, we have argued that vacuum energy fluctuations in the near-horizon region give rise to non-vanishing variance of the metric perturbations, Eqs. (2.37) and (2.38). The equations that govern the two-point function of h_{uu} and h_{vv} are shown in Eq. (2.4). Note that the two-point functions of metric perturbations themselves are not observables in an interferometer system. To connect the equations above to a quantity more directly connected to the observable, we first define two “light-ray” operators as in Ref. [312]:

$$X^v = v + \int^u du' h_{uu}(u', \mathbf{x}_\perp), \quad (2.39)$$

$$X^u = u + \int^v dv' h_{vv}(v', \mathbf{x}_\perp). \quad (2.40)$$

Ref. [312] has demonstrated that the 't Hooft commutation relations in Eq. (2.30) applied on the bifurcate horizon implies a commutation relation of X^u and X^v :

$$[X^u(\mathbf{x}_\perp), X^v(\mathbf{x}'_\perp)] = i\ell_p^{d-2} f(\mathbf{x}_\perp; \mathbf{x}'_\perp). \quad (2.41)$$

Presently, we are interested in obtaining the accumulated uncertainty along the light sheet. This uncertainty is computed from solving the following equations:

$$\left(\frac{d-2}{L^2} - \nabla_\perp^2\right) \langle \partial_u X^v(u, \mathbf{x}_\perp) \partial_{u'} X^v(u', \mathbf{x}'_\perp) \rangle = \frac{\ell_p^{d-2}}{2\pi\tilde{\ell}_p} \delta(u-u') \delta^{d-2}(\mathbf{x}_\perp - \mathbf{x}'_\perp), \quad (2.42)$$

$$\left(\frac{d-2}{L^2} - \nabla_\perp^2\right) \langle \partial_v X^u(v, \mathbf{x}_\perp) \partial_{v'} X^u(v', \mathbf{x}'_\perp) \rangle = \frac{\ell_p^{d-2}}{2\pi\tilde{\ell}_p} \delta(v-v') \delta^{d-2}(\mathbf{x}_\perp - \mathbf{x}'_\perp). \quad (2.43)$$

Eqs. (2.42) and (2.43) look similar to a Langevin equation that describes random motion of a particle suspending in a dissipative fluid [214]. Recall that in statistical mechanics, the one-dimensional Langevin equation is a stochastic differential equation which takes on the form (for a massless particle) of Eq. (2.5). Besides the spatial response in the transverse plane, we can clearly identify quantities derived from gravitational shockwave dynamics in Eqs. (2.42) and (2.43) with the dynamics of a microscopic particle in a fluid subjected to a random force. In particular, we find the following identifications:

$$\begin{aligned} \dot{X}(\tau, \mathbf{x}_\perp) &= \begin{cases} \partial_u X^v(u, \mathbf{x}_\perp) & \text{past light front,} \\ \partial_v X^u(v, \mathbf{x}_\perp) & \text{future light front.} \end{cases} \\ \langle F(\tau, \mathbf{x}_\perp) F(\tau', \mathbf{x}'_\perp) \rangle &\sim \begin{cases} \delta(u-u') f(\mathbf{x}_\perp - \mathbf{x}'_\perp) & \text{past light front,} \\ \delta(v-v') f(\mathbf{x}_\perp - \mathbf{x}'_\perp) & \text{future light front.} \end{cases} \end{aligned} \quad (2.44)$$

We now compute the observable from Eqs. (2.42) and (2.43). An appropriate observable in an interferometer is the total time delay of a light beam traversing the whole causal diamond. This time-delay is measured on the boundary in the Poincaré metric: $T_{r,t} = Lx_0/z_c$. To compute the total time delay, we need to integrate over all *local* (and statistically uncorrelated at distinct spacetime points) fluctuations

generated by the quantum uncertainty in Eqs. (2.42) and (2.43):

$$\begin{aligned} \left(\frac{d-2}{L^2} - \nabla_{\perp}^2 \right) \langle X^v(\mathbf{x}_{\perp}) X^v(\mathbf{x}'_{\perp}) \rangle &= \frac{\ell_p^{d-2} \delta^{d-2}(\mathbf{x}_{\perp} - \mathbf{x}'_{\perp})}{2\pi \tilde{\ell}_p} \int_{u_i}^0 du \int_{u_i}^0 du' \delta(u - u') \\ &= -\frac{\ell_p^{d-2}}{2\pi \tilde{\ell}_p} u_i \delta^{d-2}(\mathbf{x}_{\perp} - \mathbf{x}'_{\perp}), \end{aligned} \quad (2.45)$$

$$\begin{aligned} \left(\frac{d-2}{L^2} - \nabla_{\perp}^2 \right) \langle X^u(\mathbf{x}_{\perp}) X^u(\mathbf{x}'_{\perp}) \rangle &= \frac{\ell_p^{d-2} \delta^{d-2}(\mathbf{x}_{\perp} - \mathbf{x}'_{\perp})}{2\pi \tilde{\ell}_p} \int_0^{v_f} dv \int_0^{v_f} dv' \delta(v - v') \\ &= \frac{\ell_p^{d-2}}{2\pi \tilde{\ell}_p} v_f \delta^{d-2}(\mathbf{x}_{\perp} - \mathbf{x}'_{\perp}). \end{aligned} \quad (2.46)$$

The integration limits in Eqs. (2.45) and (2.46) are:

$$v_f = -u_i = L. \quad (2.47)$$

Notice that these equations already exhibit the random-walk behavior, shown in Eq. (2.7), proposed in Refs. [314, 41, 329], where the total uncertainty in a length operator accumulates linearly with the size of the causal diamond (which here is given by u_i, v_f).

We first consider the case in which the full symmetry of the transverse space is respected (corresponding to the s -wave mode), in order to directly compare with Eq. (2.1). To extract this information from our analysis (which includes the transverse response), we thus (i) take the operator $\nabla_{\perp}^2 \rightarrow 0$ in the left-hand side of Eqs. (2.45), (2.46), and (ii) integrate $\delta^{d-2}(\mathbf{x}_{\perp} - \mathbf{x}'_{\perp})$ over the area and then divide by the area of Σ_{d-2} in the right-hand side of Eqs. (2.45), (2.46):

$$\begin{aligned} (i) : \frac{d-2}{L^2} - \nabla_{\perp}^2 &\rightarrow \frac{d-2}{L^2}, \\ (ii) : \delta^{d-2}(\mathbf{x} - \mathbf{x}'_{\perp}) &\rightarrow \frac{1}{A(\Sigma_{d-2})} \int \delta^{d-2}(\mathbf{x} - \mathbf{x}') d\Sigma_{d-2} = \frac{1}{A(\Sigma_{d-2})}. \end{aligned} \quad (2.48)$$

In an interferometer, the quantity related to the observable is the round-trip time of a light beam measured by a clock on the boundary located at $z = z_c$ [313]:

$$T_{r.t.} = \frac{L}{z_c} (v_f - u_i) \approx \frac{L}{z_c} (2L). \quad (2.49)$$

Fluctuations of $T_{r.t.}$ are captured by the two-point function in Eqs. (2.45) and (2.46), which is now found to be:

$$\begin{aligned} \frac{\Delta T_{r.t.}^2}{T_{r.t.}^2} &\equiv \frac{1}{T_{r.t.}^2} (\langle X^v(\mathbf{x}_{\perp}) X^v(\mathbf{x}'_{\perp}) \rangle + \langle X^u(\mathbf{x}_{\perp}) X^u(\mathbf{x}'_{\perp}) \rangle) \\ &= \frac{1}{2(d-2)} \left(\frac{L}{\tilde{\ell}_p} \right) \frac{1}{S_{ent.}}. \end{aligned} \quad (2.50)$$

Here we have used the definition of the entanglement entropy $S_{ent.} \equiv A(\Sigma_{d-2})/4G_N^{(d)}$ with $8\pi G_N^{(d)} = \ell_p^{d-2}$. Comparing our result in Eq. (2.50) with that from Ref. [313] (shown in Eq. (2.1)) allows us to determine $\tilde{\ell}_p$ as

$$\tilde{\ell}_p = \frac{L}{4\sqrt{S_{ent.}}}. \quad (2.51)$$

This is the same length scale first identified, through independent and complementary means, in Refs. [312, 41, 329] and quoted in Eq. (2.6). In particular, Ref. [312] identified $\tilde{\ell}_p$ as the relevant uncertainty scale appearing in the commutation relation Eq. (2.41), giving a physical interpretation to the width of the stretched horizon we have employed here. The dependence of the uncertainty scale on the dimensionful scales ℓ_p , L can be parametrically seen by noting that $f(\mathbf{x}_\perp, \mathbf{x}'_\perp) \sim L^{4-d}$ (as can be seen from Eq. (2.34) and which we will write out explicitly below), such that that right-hand side of the uncertainty relation Eq. (2.41) has a dimensionful scaling as $\ell_p^{d-2}/L^{d-4} \sim \tilde{\ell}_p^2$. Even more precisely, Eq. (2.51) agrees to a factor of 4 (which can be attributed to uncertainty due to the regularization procedure employed here) with that predicted in Refs. [41, 329].

Angular Correlations of Photon Traversal Time Fluctuations

The form of the expressions in Eqs. (2.45) and (2.46) allows us to now also extract the angular correlations, via $f(\mathbf{x}_\perp; \mathbf{x}'_\perp)$, which as the Green function of the transversal Laplacian in (2.34) becomes

$$\left[\frac{d-2}{L^2} - \frac{\partial^2}{\partial \chi^2} - (d-3) \coth\left(\frac{\chi}{L}\right) \frac{1}{L} \frac{\partial}{\partial \chi} - \frac{1}{L^2 \sinh^2(\chi/L)} \nabla_{\mathbf{S}^{d-3}}^2 \right] f(\mathbf{x}_\perp; \mathbf{x}'_\perp) \quad (2.52)$$

$$= \delta^{d-2}(\mathbf{x}_\perp - \mathbf{x}'_\perp),$$

where the Laplacian operator on the transverse space $\Sigma_{d-2} \cong \mathbf{H}^{d-2}$ is given by Ref. [104] and $\nabla_{\mathbf{S}^{d-3}}^2$ denotes the Laplacian on a $(d-3)$ -dimensional unit-sphere. In the following, we consider an interferometer setup in which the two end mirrors are located at χ and χ' . In other words, the two interferometer arms pick out two particular directions in the χ -coordinate of the transverse space, while leaving the residual subspace \mathbf{S}^{d-3} invariant. Therefore, we can neglect the term $\nabla_{\mathbf{S}^{d-3}}^2$ in Eq. (2.52). Spherical symmetry implies that the solution of Eq. (2.52) depends only on the geodesic distance in Σ_{d-2} , which is given by [23, 104]

$$\xi(\mathbf{x}_\perp; \mathbf{x}'_\perp) \equiv \cosh^{-1} \left(\cosh\left(\frac{\chi}{L}\right) \cosh\left(\frac{\chi'}{L}\right) - \sinh\left(\frac{\chi}{L}\right) \sinh\left(\frac{\chi'}{L}\right) \cos \gamma \right), \quad (2.53)$$

where γ is the polar angle subtended by the two interferometer arms. To further simplify the problem we consider the case in which L is sufficiently large compared to ξ such that the term $(d-2)/L^2$ can be neglected. Eq. (2.52) then reduces to

$$-\frac{\partial^2 f(\mathbf{x}_\perp; \mathbf{x}'_\perp)}{\partial \chi^2} - \frac{(d-3)}{L} \coth\left(\frac{\chi}{L}\right) \frac{\partial f(\mathbf{x}_\perp; \mathbf{x}'_\perp)}{\partial \chi} = \delta^{d-2}(\mathbf{x}_\perp - \mathbf{x}'_\perp). \quad (2.54)$$

The solution to Eq. (2.54) is found in Ref. [104] to be

$$f(\mathbf{x}_\perp; \mathbf{x}'_\perp) = \frac{1}{\Omega_{d-3} L^{d-4}} f(\Sigma; \Sigma'). \quad (2.55)$$

where $f(\Sigma; \Sigma')$ is given in terms of the hypergeometric function [104, 23]

$$f(\Sigma; \Sigma') = \frac{1}{(d-3) \cosh^{d-3} \xi} {}_2F_1\left(\frac{d-3}{2}, \frac{d-2}{2}; \frac{d-1}{2}; \frac{1}{\cosh^2 \xi}\right). \quad (2.56)$$

In the limit where the hyperboloid \mathbf{H}^{d-2} looks locally Euclidean, $f(\Sigma; \Sigma')$ reduces to the familiar result in Euclidean space [104]:

$$f(\Sigma; \Sigma') \approx \begin{cases} \ln \frac{L}{|\chi - \chi'|} & \text{for } d = 4, \\ \left(\frac{L}{|\chi - \chi'|}\right)^{4-d} & \text{for } d \geq 5. \end{cases} \quad (2.57)$$

Because the Green function $f(\mathbf{x}_\perp; \mathbf{x}'_\perp) \sim L^{4-d}$, it receives a conformal rescaling on the (regularized) boundary at $z = z_c$ in the Poincaré metric

$$f(\mathbf{x}_\perp; \mathbf{x}'_\perp) \xrightarrow{z=z_c} \left(\frac{L}{z_c}\right)^{4-d} f(\mathbf{x}_\perp; \mathbf{x}'_\perp). \quad (2.58)$$

Accounting for the conformal factor (L/z_c) properly, and using Eq. (2.45) together with (2.46), we find the fluctuations $\Delta T_{r.t.}^2$ to be

$$\begin{aligned} \Delta T_{r.t.}^2(\mathbf{x}_\perp; \mathbf{x}'_\perp) &\equiv \left(\frac{L}{z_c}\right)^2 (\langle X^v(\mathbf{x}_\perp) X^v(\mathbf{x}'_\perp) \rangle + \langle X^u(\mathbf{x}_\perp) X^u(\mathbf{x}'_\perp) \rangle) \\ &= \left(\frac{L}{z_c}\right)^2 \left(\frac{2L^3}{\tilde{\ell}_p}\right) \left[\frac{\ell_p^{d-2}}{2\pi \Omega_{d-3} L^{d-2} (L/z_c)^{d-3}} \right] f(\Sigma; \Sigma') \\ &= \left(\frac{L}{z_c}\right)^2 8L^2 \frac{1}{\sqrt{S_{ent.}}} f(\Sigma; \Sigma'). \end{aligned} \quad (2.59)$$

In evaluating the second line, we substituted the area of the transverse space $A(\Sigma_{d-2}) \approx \Omega_{d-3} L^{d-2} (L/z_c)^{d-3}$ (for $z_c \rightarrow 0$) and used the definition of the entanglement entropy again, while in the third line we have used the scale precisely identified in Eq. (2.51). Thus, the relative uncertainty of photon round trip time, with angular correlations, is

$$\frac{\Delta T_{r.t.}^2}{T_{r.t.}^2}(\mathbf{x}_\perp; \mathbf{x}'_\perp) = \frac{2}{\sqrt{S_{ent.}}} f(\Sigma; \Sigma'). \quad (2.60)$$

2.5 Summary and Discussion

In this chapter, we have shown that vacuum energy fluctuations in AdS space, with a quantum noise term motivated by commutation relations presented in Ref. [312] and shown in Eqs. (2.30) and (2.41), give rise to hydrodynamic behavior for the fluctuations of the spacetime geometry. In particular, we demonstrated that the near-horizon fluctuations of a finite causal diamond is a diffusive process that captures “random walk” characteristics in time (but with transverse spatial correlations) of quantum spacetime fluctuations. We further analyzed the effect of these fluctuations on the traversal time of photons traveling from the boundary and reflecting off a mirror in the bulk, confirming the previous result of Ref. [313] despite taking a computationally complementary route. An important step in our reasoning was to focus only on the hydrodynamics on the stretched horizon of a causal diamond, distinct from the usual fluid/gravity correspondence that proposes a duality between the bulk gravitational perturbations and boundary hydrodynamics.

There are many interesting future directions to pursue. First, one could carry out a similar type of analysis in Minkowski space. Second, one could seek to understand the underlying origins of these vacuum fluctuations from shockwave geometries. Finally, one could utilize theoretical tools such as out-of-time-order correlators (OTOCs) that describe fast-scrambling systems and quantum chaos to study the connection between hydrodynamics and shockwave geometries. We look forward to further developments in these formal aspects and its groundwork for future observational tests.

RINDLER FLUIDS FROM GRAVITATIONAL SHOCKWAVES

3.1 Introduction

Almost fifty years ago, Damour [115] first connected general relativity to fluid dynamics by demonstrating that when perturbations fall into a black hole horizon, the spacetime near the horizon behaves like a fluid. This idea led to the conception of the membrane paradigm [306, 252, 135, 132, 166], in which the fluid resides on a stretched horizon, a timelike hypersurface very close to the actual black hole horizon. Later on, the discovery of the AdS/CFT correspondence formalized a version of fluid/gravity duality in which the fluid arises as an effective description in the long distance, low frequency regime of the dual gauge theory on the AdS boundary [265, 266, 211, 210, 289, 52, 139].

More recently, substantial progress was made in studying fluid/gravity duality on a cutoff surface in flat Rindler spacetime [71, 70, 108, 109, 224, 264]. The flat space cutoff approach to fluid/gravity duality formulates the map between the Einstein and Navier-Stokes equations in a precise manner. In particular, Refs. [70, 108, 264] showed that the fluid is defined in terms of the extrinsic curvature of a cutoff hypersurface outside of the horizon. This cutoff surface is equipped with a flat induced metric. As in [70], in the leading order hydrodynamic expansion, the constraint equation from the Einstein tensor becomes the incompressibility condition

$$\partial_i v^i = 0. \quad (3.1)$$

Here v^i is the i -component of the fluid velocity. Furthermore, the next leading order constraint Einstein equation becomes the incompressible Navier-Stokes equation [70]

$$\partial_\tau v_i - r_c \partial^2 v_i + \partial_i P + v^j \partial_j v_i = 0. \quad (3.2)$$

Thus the cutoff surface fluid/gravity duality relates Einstein gravity, which governs nonlinear gravitational interactions, to the incompressible Navier-Stokes equations, which are an effective description of classical fluids.

In this chapter, we aim to study the connection between gravitational shockwave spacetimes and their fluid descriptions. Gravitational shockwave geometries were studied first by Dray and 't Hooft [126] when they considered ultra-relativistic

matter falling into a black hole. More recently, [112, 169, 312, 191] have studied shockwaves in flat spacetimes on the quantum level. Rewriting these gravitational shockwaves on the fluid side of fluid/gravity duality will allow us to consider quantum shocks as a fluid source.

Technically, we match gravitational shockwaves to their dual fluids by using their Petrov type. Since the shockwave geometries we consider are Petrov type N, their fluid dual must correspond to a spacetime of the same type. As shown in [206], potential fluids with $v_i = \nabla_i \phi$ have dual geometries of Petrov type N. Since Petrov Type N spacetimes only allow one degree of freedom, we map between the cutoff fluid formalism and shockwave geometries by identifying the fluid potential with the shockwave metric via

$$\phi = \beta r H_{uu}. \quad (3.3)$$

Here ϕ is the fluid potential and H_{uu} characterizes the metric fluctuations due to a shockwave. By choosing β carefully, we find an exact mapping such that the Einstein equation for the shockwave geometries is precisely the incompressibility condition in Eq. (3.1) with the right hand side replaced by the shockwave stress-energy tensor. Solving this differential equation allows us to constrain the pressure term in the next leading order Navier-Stokes equation.

Since we map the shockwaves to potential fluids, the next major goal of our chapter is to study the effects of quantum fluctuations on potential fluids. In the leading order hydrodynamic expansion, we keep the left hand side of the incompressibility equation unchanged, while replacing the right hand side with a quantum noise term. This Ansatz is motivated by a set of commutation relations first studied by 't Hooft [5, 2] in the context of black hole perturbations, and later developed by [312] and [191] for flat spacetime. Such fluctuations alter the classical fluid (Einstein) equation to a stochastic differential equation, resembling the form of a first order Langevin equation, which describes Brownian motion of a massless particle [324]. Quantum uncertainty arises from a Brownian particle undergoing random walk in a stochastic background [41, 329].

We argue in a similar fashion as in [324] that spacetime fluctuations give rise to a “smeared out” horizon, analogous to a stretched horizon [115]. However, our present chapter utilizes the cutoff surface fluid approach to devise a Lorentz invariant method to smear out the horizon. We will impose the condition that the cutoff surface intersects with the boundary of a causal diamond at a distance of the reduced Planck length $\tilde{\ell}_p$ [41, 329, 312]. In four-dimensional spacetime, the

reduced Planck length is simply the Planck length $\tilde{\ell}_p = \ell_p$. Positioning such a cutoff surface allows us to compute the variance of photon traversal time measured by a free-falling observer on the boundary of the causal diamond

$$\Delta T_{r.t.}^2 \sim 2L\ell_p f(\mathbf{x}, \mathbf{x}'). \quad (3.4)$$

Here $f(\mathbf{x}, \mathbf{x}')$ is the transverse response function, which is a unique feature to the shockwave geometries, and is absent in classical Brownian motion. Eq. (3.4) is consistent with the result from previous calculations [313, 314, 41, 329, 324] done via different means.

The outline of this chapter is as follows. In Sec. 3.2 we review the cutoff fluid formalism in flat spacetime. In Sec. 3.3 we compute the Petrov classification for the shockwave spacetime and the fluid metric, respectively, and we show that the shockwave metric is mapped to the potential of a potential flow in hydrodynamics. In Sec. 3.4, we solve the incompressibility equation with a source term posited from the 't Hooft commutation relations, and use the solution to compute the uncertainty in photon traversal time. In Sec. 3.5, we summarize our results and point to some future directions. Throughout this chapter, we use $8\pi G_N = \ell_p^2 = \kappa^2$.

3.2 Rindler Fluids in Einstein Gravity

In this section we review the fluid/gravity correspondence on a cutoff surface of Minkowski space. Following [71, 70, 108, 109], we develop the duality by first performing coordinate transformations to introduce a constant fluid velocity and constant pressure. These transformations produce the “seed” metric, which is just Minkowski space in unusual coordinates. Then, we allow the fluid velocity and pressure to vary slowly with both the x^i and τ coordinates; allowing for higher-order corrections in the hydrodynamic parameter then produces the true fluid dual metric. Resolving the Einstein equations for this more general metric, we find the constraint Einstein equations can be written as conservation equations for the Brown-York stress tensor. Writing these conservation equations explicitly, the first and second-order equations become incompressibility and the Navier-Stokes equations, respectively. Following this review, we additionally review the specific case of potential fluids for later use.

Geometric Setup

We will work throughout in ingoing Eddington-Finkelstein coordinates

$$ds^2 = -(\alpha r)d\tau^2 + 2d\tau dr + \delta_{ij}dx^i dx^j, \quad (3.5)$$

where i, j indicate the transverse directions and thus run from $1 \dots d - 2$ (these correspond to the 2 transverse directions in $d = 4$). α corresponds to the constant proper acceleration of a Rindler observer at fixed r . Our formulation most closely follows [108, 109, 133].

Our fluid will live on a timelike hypersurface called Σ_c . We choose this surface to be $r = r_c$; its induced metric γ_{ab} is

$$ds^2|_{\Sigma_c} = \gamma_{ab} dx^a dx^b = -(\alpha r_c) d\tau^2 + \delta_{ij} dx^i dx^j. \quad (3.6)$$

Here a, b are spacetime indices on Σ_c , so they run over τ as well as i, j . Note that this metric is flat.

Starting from this background geometry, we introduce a constant pressure by shifting r ; since we want to keep the induced metric fixed, we must also rescale τ . The transformation is

$$r \rightarrow r + \frac{1}{\alpha p^2} - r_c, \quad \tau \rightarrow \sqrt{\alpha r_c} p \tau. \quad (3.7)$$

This coordinate transformation shifts the position of the Rindler horizon from $r_h = 0$ to $r_h = r_c - \frac{1}{\alpha p^2}$.

We then introduce a constant fluid velocity by performing the boost

$$\sqrt{\alpha r_c} \tau \rightarrow -u_a x^a, \quad x^i \rightarrow x^i - u^i \sqrt{\alpha r_c} \tau + (1 + \gamma)^{-1} u^i u_j x^j, \quad (3.8)$$

where $\gamma = (1 - v^2/(\alpha r_c))^{-1/2}$, and we set the fluid four-velocity vector u_a to a constant.

Thus we arrive at the ‘seed’ metric for a relativistic fluid, given by

$$ds^2 = -2p u_a dx^a dr + [\gamma_{ab} - \alpha p^2 (r - r_c) u_a u_b] dx^a dx^b. \quad (3.9)$$

As noted above, so far this metric is just a rewriting of Minkowski space in fancy coordinates. However, we can already begin to study the constant ‘fluid’ on the cutoff surface. To characterize the physics on the cutoff surface, we introduce the Brown-York stress-energy tensor [73]

$$\kappa^2 T_{ab} = (K \gamma_{ab} - K_{ab}), \quad (3.10)$$

where $\kappa^2 = 8\pi G_N$. Here, $K_{ab} = \frac{1}{2} \mathcal{L}_n \gamma_{ab}$ is the extrinsic curvature on Σ_c , and $K = K_{ab} \gamma^{ab}$ is its trace. Here, \mathcal{L}_n is the Lie derivative along the unit normal vector n^μ on the cutoff surface Σ_c .

For the seed metric in Rindler spacetime (3.9), the Brown-York stress tensor on the cutoff surface has a form of the perfect fluid in equilibrium with a vanishing energy density:

$$\kappa^2 T_{ab} = \alpha p h_{ab}, \quad (3.11)$$

where $h_{ab} = \gamma_{ab} + u_a u_b$ is the metric of a spacelike hypersurface orthogonal to the velocity vector u_a but still embedded in Σ_c . Since the pressure is constant, there is no time evolution of the momentum density of the fluid. Due to the vanishing energy density, the divergence of the momentum density is vanishing as well by the continuity equation. Thus, the Brown-York stress tensor (3.11) for the seed metric describes the equilibrium fluid that does not flow as seen by a comoving observer with u^a . Thus this background seed metric is equivalent to a somewhat boring fluid.

Before we introduce slow variations in order to consider more interesting fluids, we note that the Brown-York stress-energy tensor T_{ab} is not equivalent to the external matter stress-energy tensor $\mathcal{T}_{\mu\nu}$. The matter stress-energy tensor serves the role of sourcing the geometry, whereas the Brown-York stress-energy tensor describes the properties of a hypersurface within the geometry. More specifically, the Brown-York stress tensor provides a useful prescription for computing the energy and momentum density of a cutoff surface within a gravitational system. In the present case, the Brown-York stress tensor relates the energy and momentum on a cutoff surface Σ_c to the energy and moment of a fluid. We also note that for the simple fluid (3.11), the spacetime stress-energy tensor $\mathcal{T}_{\mu\nu}$ is clearly zero, since the spacetime is just empty Minkowski space. By contrast, the fluid does have a nonzero Brown-York tensor as we have shown.

The Hydrodynamic Limit and Near-Horizon Expansion

In order to obtain non-constant fluids, the next step is to perturb the seed metric (3.9) by allowing the fluid degrees of freedom u_a, p to depend on (τ, x^i) , following the procedure in [108, 109, 264]. Then, near-equilibrium solutions $g_{\mu\nu}^{(n)}$ ($n = 0, 1, 2, \dots$) can be constructed order-by-order in the relativistic gradient expansion. However, in this work we are interested in the non-relativistic hydrodynamic limit since it agrees with the near-horizon expansion [70, 206], and we will be working in the near-horizon regime for the Rindler shockwaves below.

Accordingly, in terms of the nonrelativistic fluid velocity v_i , and the nonrelativistic

pressure P , we have

$$u_a = \frac{1}{\sqrt{\alpha r_c - v^2}} (-\alpha r_c, v_i), \quad p = (\alpha r_c - 2P)^{-1/2}, \quad (3.12)$$

where the relativistic velocity is normalized so $u_a u^a = -1$. The equivalent of the relativistic gradient expansion becomes explicitly the hydrodynamic scaling

$$v_i \sim \mathcal{O}(\epsilon), \quad P \sim \mathcal{O}(\epsilon^2), \quad \partial_i \sim \mathcal{O}(\epsilon), \quad \partial_\tau \sim \mathcal{O}(\epsilon^2). \quad (3.13)$$

Using this non-relativistic scaling, and further solving the non-constraint Einstein equations order-by-order, we construct the non-relativistic fluid metric given in Appendix (78). Although the full fluid-dual geometry is quite complicated, with its metric given by (78) up to $\mathcal{O}(\epsilon^3)$, we are mainly interested in the lowest order expansion of (78):¹

$$\begin{aligned} ds^2 = & -(\alpha r) d\tau^2 + 2d\tau dr + \delta_{ij} dx^i dx^j \\ & - 2\left(1 - \frac{r}{r_c}\right) v_i dx^i d\tau - 2\frac{v_i}{\alpha r_c} dx^i dr + \mathcal{O}(\epsilon^2). \end{aligned} \quad (3.14)$$

As noted above, the fluid behavior is described via the Brown-York stress tensor (3.10) and its conservation equations. Explicitly in terms of the non-relativistic fluid metric, we obtain [70]²

$$\begin{aligned} \kappa^2 T_{ab} dx^a dx^b = & \frac{\alpha v^2}{\sqrt{\alpha r_c}} d\tau^2 - \frac{2\alpha v_i}{\sqrt{\alpha r_c}} dx^i d\tau \\ & + \frac{\alpha}{\sqrt{\alpha r_c}} dx^i dx_i + \frac{P\delta_{ij} + v_i v_j}{r_c \sqrt{\alpha r_c}} dx^i dx^j \\ & - \frac{2\partial_{(i} v_{j)}}{\sqrt{\alpha r_c}} dx^i dx^j + \mathcal{O}(\epsilon^3), \end{aligned} \quad (3.15)$$

where details of the derivation are included in Appendix A1.

Since the constraint Einstein equations on Σ_c match the conservation equations for the Brown-York tensor, we find³

$$\nabla^b T_{ab}|_{\Sigma_c} = -2n^\mu \mathcal{T}_{a\mu}. \quad (3.16)$$

¹We ignore $\mathcal{O}(\epsilon^2)$ and higher order terms presently because we anticipate the relation between the fluid-dual metric in just the leading order of hydrodynamic expansion (3.14) and the shockwave geometry that solves the linearized Einstein equation. This point will become clear in section 3.3.

²We used the symmetrization $X_{(i} Y_{j)} = \frac{1}{2} (X_i Y_j + X_j Y_i)$.

³This is the Gauss-Codazzi equation including the integration constant in r [264]. We set the integration constant to zero by imposing the Brown-York stress tensor to be conserved when we consider the source-free situation.

As before, n^μ is the unit normal vector (79) to the cutoff surface Σ_c . The spacetime stress-energy tensor $\mathcal{T}_{a\mu}$ provides the nonzero source for Einstein's equations, and we again wish to differentiate it from the Brown-York tensor we introduced in Sec. 3.2.

In Section 3.3, we are interested in the spacetime stress-energy tensor $\mathcal{T}_{\mu\nu}$ due to an ultra-relativistic source, also known as the gravitational shockwave. Before turning on the external sources, we now review the fluid behavior when no source is present, that is, when $\mathcal{T}_{\mu\nu} = 0$. At $\mathcal{O}(\epsilon^0)$, T_{ab} is constant, and the Einstein equations are satisfied trivially. At $\mathcal{O}(\epsilon^2)$, we obtain the incompressibility condition [70]

$$\nabla^a T_{\tau a} = 0 \quad \Longleftrightarrow \quad G_{\tau\tau} = \frac{\alpha}{2} \partial^i v_i = 0. \quad (3.17)$$

In writing out (3.17), we have identified the conservation of the Brown-York tensor at $\mathcal{O}(\epsilon^2)$ with the Einstein tensor $G_{\tau\tau}$ at the same order [264]. We note that other components of the Einstein tensor vanish identically at the current order.

In a similar fashion, we compute the conservation equation of the Brown-York tensor at $\mathcal{O}(\epsilon^3)$, and we obtain the incompressible Navier-Stokes equation [70]

$$\nabla^a T_{ia} = 0 \quad \Longleftrightarrow \quad G_{\tau i} = -\frac{1}{2r_c} \left(\partial_\tau v_i - r_c \partial^2 v_i + \partial_i P + v_j \partial^j v_i \right) = 0, \quad (3.18)$$

which is equivalent to the vacuum constraint Einstein equation $G_{\tau i} = 0$ evaluated at the same order [264].

Later, when we add sources to the Einstein equations, these constraint equations will instead become (3.16), adding sources to the fluid equations. In section 3.3, we will see how a nonzero $\mathcal{T}_{\mu\nu}$ coming from gravitational shockwaves influences the fluid on Σ_c .

Potential Fluids Before considering shockwave spacetimes, we review potential fluids. The class of fluids known as potential fluids satisfies

$$v_i = \partial_i \phi. \quad (3.19)$$

These fluids are also known as irrotational, since they have zero vorticity. In our four-dimensional gravity (dual to a 2+1 dimensional fluid), the vorticity is $\partial_x v_y - \partial_y v_x = 0$, since gradients are curl-free.

For a source-free potential fluid, the incompressibility condition (3.17) yields [206]

$$\nabla^a T_{0a} = 0 \quad \Longrightarrow \quad \partial^2 \phi = 0. \quad (3.20)$$

In this case, the incompressible Navier-Stokes equation (3.18) implies the expression of the pressure in terms of ϕ

$$\nabla^a T_{ia} = 0 \quad \implies \quad \partial_i P = -\partial_i \partial_\tau \phi - \partial^j \phi \partial_i \partial_j \phi. \quad (3.21)$$

Rindler to Light Cone Coordinates Lastly, we review the coordinate transformation between the background to the fluid/gravity dual metrics, and light cone coordinates. We review this relationship because both the fluid-dual metrics, and the shockwave metrics we study in the next section, are perturbations away from Minkowski space. However in the fluid case we work in ingoing Eddington-Finkelstein coordinates (3.5), while in the shockwave case the background is written in light cone coordinates.

For the shockwave, the background is Minkowski spacetime in light-cone coordinates $u = T + Z$, $v = T - Z$ where (T, Z) are Minkowski global coordinates, with metric

$$ds^2 = -dudv + \delta_{ij} dx^i dx^j. \quad (3.22)$$

Here again i, j indicate the transverse directions. The coordinate transformation

$$u = \sqrt{\frac{r_c}{\alpha}} e^{\alpha\tau/2} \quad \text{and} \quad v = -\frac{4r}{\sqrt{\alpha r_c}} e^{-\alpha\tau/2} \quad (3.23)$$

yields the line element of Rindler spacetime (3.5). Thus, Eq. (3.23) is the zeroth order coordinate transformation between the fluid metric (3.14) and shockwave metric (3.24). In the next section, we construct the relation at the next order, between the perturbed geometries.

3.3 Near Horizon Fluids from Gravitational Shockwaves

In this section, we establish the relation between the near-horizon fluids constructed in section 3.2 and the gravitational shockwaves in [24]. We first briefly review the shockwave geometry and the external source from the shockwave. Then, we consider how the fluid equations deforms in the presence of an external source. With those two setups constructed, we find the connection between the fluids and shockwaves by using their Petrov classifications.

Gravitational shockwave geometry

The gravitational shockwave geometry was originally proposed by Aichelburg and Sexl [24] to describe gravitational radiation from a massless point particle. The

Aichelburg-Sexl metric is given by [126, 312] with Minkowski spacetime in the light-cone coordinates (3.22).

If we consider a fast particle falling towards the future horizon, the uu -component of the metric is perturbed, which produces the shockwave geometry

$$ds^2 = -dudv + H_{uu}du^2 + \delta_{ij}dx^i dx^j. \quad (3.24)$$

Here H_{uu} is given by

$$H_{uu}(u, x^i) = p_u \kappa^2 \delta(u - u_0) f(\mathbf{x}; \mathbf{x}'), \quad (3.25)$$

where p_u is the constant momentum of the shock, u_0 denotes the location of the shockwave, and $f(\mathbf{x}; \mathbf{x}')$ is the Green's function of the transverse Laplacian operator:

$$-\partial^2 f(\mathbf{x}; \mathbf{x}') = \delta^2(\mathbf{x} - \mathbf{x}'). \quad (3.26)$$

In fact, Eq. (3.26) is equivalent to the Einstein equation, which is exactly solvable in this case. Only the uu component of the Einstein equation $G_{\mu\nu} = \kappa^2 \mathcal{T}_{\mu\nu}$ is nontrivial. Explicitly, this component becomes

$$-\frac{1}{2} \partial^2 H_{uu} = \kappa^2 \mathcal{T}_{uu}, \quad (3.27)$$

where \mathcal{T}_{uu} is the only non-vanishing component of the shockwave stress-energy tensor. For H_{uu} as in (3.25), we have

$$\mathcal{T}_{uu} = \frac{1}{2} p_u \delta(u - u_0) \delta^2(\mathbf{x} - \mathbf{x}'). \quad (3.28)$$

The shockwave geometry can be described in a different gauge, which involves an off-diagonal component with transverse and longitudinal directions. The metric in this gauge is

$$ds^2 = -dudv + \partial_i X^v du dx^i + \delta_{ij} dx^i dx^j \quad (3.29)$$

where we introduced the shockwave degree of freedom X^v

$$X^v(u, v, x^i) = v + \int_0^u du' H_{uu}(u', x^i). \quad (3.30)$$

Now, we have the shockwave geometry sourced by the external matter stress-energy tensor \mathcal{T}_{uu} . In the next section, we will construct a fluid-dual geometry with the same external source in order to make a connection between shockwaves and fluids.

Near Horizon Fluids with External Sources

Just as the stress-energy tensor \mathcal{T}_{uu} in (3.28) sources the shockwave geometry with nonzero H_{uu} , in fluid-dual geometries an external stress-energy tensor can be thought of as a sourcing the fluid dynamics. We anticipate that in the leading order of hydrodynamic expansion the fluid-dual metric given by Eq. (3.14) can be mapped to the shockwave geometry given by Eq. (3.24). In anticipation of this match, we first add a non-zero external source \mathcal{T}_{uu} to the fluid equations (3.16), generalizing the fluid/gravity setup in [70] beyond vacuum solutions.

Since the shockwave metric and fluid metric use different coordinate systems, we need to find the components of $\mathcal{T}_{\mu\nu}$ from (3.28) in (τ, r, x^i) coordinates. Since the only non-vanishing component of $\mathcal{T}_{\mu\nu}$ in (u, v, x^i) coordinates is \mathcal{T}_{uu} , under the background coordinate transformation (3.23) we find that the only non-vanishing component in (τ, r, x^i) coordinates is $\mathcal{T}_{\tau\tau}$, given by

$$\mathcal{T}_{\tau\tau} = \frac{\alpha r_c}{4} e^{\alpha\tau} \mathcal{T}_{uu}. \quad (3.31)$$

In Sec. 3.2, we showed that the conservation Eq. (3.16) of the Brown-York stress tensor at order $O(\epsilon^2)$ is equivalent to the incompressibility condition of the dual fluid (3.17). However, in the presence of a gravitational shockwave, the incompressibility condition instead becomes

$$\nabla^a T_{\tau a}|_{\Sigma_c} = -2n^\mu \mathcal{T}_{\tau\mu} \quad \Longrightarrow \quad \partial^i v_i = \frac{1}{2} \kappa^2 r_c e^{\alpha\tau} \mathcal{T}_{uu}, \quad (3.32)$$

where we have additionally made use of the unit normal as explicitly given in (79).

At $O(\epsilon^3)$, the conservation Eq. (3.16) of the Brown-York stress tensor is given by

$$\nabla^a T_{ia}|_{\Sigma_c} = -2n^\mu \mathcal{T}_{i\mu} \quad \Longrightarrow \quad \partial_\tau v_i - r_c \partial^2 v_i + v_j \partial^j v_i + \partial_i P + v_i \partial^j v_j - r_c \partial_i \partial^j v_j = 0. \quad (3.33)$$

There is no contribution from the external source since the only non-vanishing component of $\mathcal{T}_{\mu\nu}$ in (τ, r, x^i) coordinates is $\mathcal{T}_{\tau\tau}$. However, the equation is not equivalent to the incompressible Navier-Stokes equation (3.18); instead, it has acquired one further term: $r_c \partial_i \partial^j v_j$, since incompressibility is broken.

Potential Fluids If we assume a potential fluid of the form $v_i = \partial_i \phi$, the conservation equation of the Brown-York stress tensor in the leading order (3.32) becomes

$$\nabla^a T_{\tau a}|_{\Sigma_c} = -2n^\mu \mathcal{T}_{\tau\mu} \quad \Longrightarrow \quad \partial^2 \phi = \frac{1}{2} \kappa^2 r_c e^{\alpha\tau} \mathcal{T}_{uu}. \quad (3.34)$$

Upon examining Eq. (3.34) closely with the Einstein equation of the shockwave geometry (3.27), we are tempted to believe that the two geometries are equivalent, at least in the leading order of hydrodynamic expansion. Specifically, we compare Eqs. (3.34) and (3.27) term by term

$$\partial^2 \phi = \frac{1}{2} \kappa^2 r_c e^{\alpha\tau} \mathcal{T}_{uu} \quad \stackrel{?}{\iff} \quad -\frac{1}{2} \partial^2 H_{uu} = \kappa^2 \mathcal{T}_{uu} \quad (3.35)$$

and deduce a relation between H_{uu} and ϕ to be

$$\phi = -\frac{r_c}{4} e^{\alpha\tau} H_{uu}. \quad (3.36)$$

While this may suggest a mapping between a potential fluid and the shockwave metric, it does not guarantee the two metrics are diffeomorphic. The most reassuring way to see whether two spacetimes are equivalent is to construct an explicit diffeomorphism that maps one to the other. However, in our case, finding such a diffeomorphism is quite difficult (considering the form of the fluid metric (3.14)), if not impossible. Thankfully, there is a more straightforward method to connect the shockwave geometry with the potential fluid, because both geometries have Weyl tensors that exhibit explicit algebraic speciality [293, 206]. In Sec. 3.3, we utilize the Petrov classification to find a correspondence between the shockwave and potential fluid geometries, thereby substantiating our claim in Eq. (3.36).

Last but not least, at $O(\varepsilon^3)$, the conservation equation (3.33) becomes

$$\nabla^a T_{ia}|_{\Sigma_c} = -2n^\mu \mathcal{T}_{i\mu} \quad \implies \quad \partial_\tau \partial_i \phi - 2r_c \partial_i \partial^2 \phi + \partial_i P + \partial_j \phi \partial^j \partial_i \phi + \partial_i \phi \partial^2 \phi = 0. \quad (3.37)$$

Eqs. (3.32) and (3.33) determine fluid dynamics on the cutoff surface when we have added the shockwave stress-energy tensor \mathcal{T}_{uu} as an external source. Since the shockwave geometry (3.29) and the fluid-dual geometry are both perturbations away from Minkowski spacetime, when we set them to have the same external source, we expect that they are two equivalent geometries in different gauges. In the next section, we establish the explicit connection between the shockwave metric and the fluid-dual metric.

Petrov Classification Connecting Fluids with Shockwaves

In this section, we derive the relation between the near-horizon fluid metric (3.14) and the shockwave metric (3.24). Instead of finding the complicated diffeomorphism between them, we will adopt the virtue of the Newman-Penrose formalism to link the

shockwave degrees of freedom into the fluid story. We will follow the conventions of [293] throughout.

The Newman-Penrose formalism will allow us to calculate the Petrov classification of our spacetimes. The Petrov classification categorizes spacetimes according to the multiplicities of the principal null directions of the Weyl tensor C_{abcd} . Principal null directions k^μ are null vectors satisfying

$$k_{[\mu}C_{\nu]\rho\sigma}k_{\delta]}k^\rho k^\sigma = 0. \quad (3.38)$$

All four-dimensional spacetimes have four principal null vectors. Spacetimes with four distinct principal null vectors for the Weyl tensor are not algebraically special; they are said to be of Petrov type I. If two principal null directions coincide, then the spacetime is Petrov type II. If the four principal nulls coincide in pairs, then the spacetime is type D. If all four principal null directions coincide, then the spacetime is type N.

Moreover, if the spacetime is type N, the geometry is determined by only one degree of freedom as we will see explicitly in this section. As we will review below, both the shockwave metric and the metric dual to a potential fluid are type N, so we can match them by matching the single degree of freedom.

We begin with the shockwave metric, defining the complex coordinates

$$z = x + iy, \quad \bar{z} = x - iy, \quad (3.39)$$

where we are now explicitly restricting to four-dimensional spacetime. Then, the shockwave metric (3.24) becomes

$$ds^2 = -dudv + H_{uu}(u, z, \bar{z})du^2 + dzd\bar{z}. \quad (3.40)$$

In the Newman-Penrose formalism, the metric is rewritten in terms of a null tetrad, $(k_\mu, l_\mu, m_\mu, \bar{m}_\mu)$. Explicitly, $g_{\mu\nu} = -l_{(\mu}n_{\nu)} + m_{(\mu}\bar{m}_{\nu)}$. For the shockwave geometry, we will use the null tetrad

$$m^\mu \partial_\mu = \sqrt{2}\partial_z, \quad \bar{m}^\mu \partial_\mu = \sqrt{2}\partial_{\bar{z}}, \quad l^\mu \partial_\mu = \sqrt{2}\partial_u - \sqrt{2}H_{uu}\partial_v, \quad k^\mu \partial_\mu = \sqrt{2}\partial_v. \quad (3.41)$$

Here k^μ is a principal null direction since it satisfies (3.38). Indeed, since k^μ obeys the condition

$$C_{\mu\nu\rho\sigma}k^\sigma = 0, \quad (3.42)$$

it is a 4-fold repeated principal null vector, so the shockwave geometry is type N. Importantly, when the null tetrad is chosen so that the first vector in the null tetrad is itself a 4-fold repeated principal null, the Weyl scalars $\Psi_i, i = 0, \dots, 4$ take on a special form, namely $\Psi_0 = \Psi_1 = \Psi_2 = \Psi_3 = 0, \Psi_4 \neq 0$.

In the tetrad formalism, these Weyl scalars contain all the information in the Weyl tensor. In general,

$$\begin{aligned}\Psi_0 &\equiv C_{\mu\nu\rho\sigma} k^\mu m^\nu k^\rho m^\sigma, & \Psi_1 &\equiv C_{\mu\nu\rho\sigma} k^\mu l^\nu k^\rho m^\sigma, & \Psi_2 &\equiv C_{\mu\nu\rho\sigma} k^\mu m^\nu \bar{m}^\rho l^\sigma \\ \Psi_3 &\equiv C_{\mu\nu\rho\sigma} k^\mu l^\nu \bar{m}^\rho l^\sigma, & \Psi_4 &\equiv C_{\mu\nu\rho\sigma} \bar{m}^\mu l^\nu \bar{m}^\rho l^\sigma.\end{aligned}\tag{3.43}$$

These scalars do depend on the choice of null tetrad, but if there is any null tetrad in which only Ψ_4 is nonzero, then the spacetime must be type N.

For fluid dual metrics, the non-relativistic fluid geometry (78) is algebraically special, specifically of type II, as first shown in [70]. More recently, [206] showed that two special types of fluid have higher algebraic speciality. For a constant vorticity fluid, the fluid-dual metric is type D, while for a potential fluid it is type N.

Since both the fluid-dual metric for a potential fluid, and the shockwave geometry (3.24), are type N, their Weyl tensors are described by the single degree of freedom Ψ_4 (in a tetrad choice where all other components are zero). Indeed, a potential fluid is described by only the scalar ϕ , while a shockwave is described by the single function H_{uu} , so we should not be too surprised that they are both type N.

In order to relate the shockwave geometry (3.24) and the fluid metric (3.14), we will choose a tetrad for each where only Ψ_4 is nonzero. If two Petrov type N geometries actually represent the same spacetime, then if tetrads are chosen so that all other Ψ_i vanish, the Ψ_4 's for the two geometries must match up to an overall scaling.

For the shockwave metric (3.24), the non-vanishing Weyl scalar is given by

$$\Psi_4 = 2\partial_{\bar{z}}\partial_{\bar{z}}H_{uu}(u, z, \bar{z}).\tag{3.44}$$

For the fluid metric (3.14) dual to a potential fluid, the tetrad can be chosen so the non-vanishing Weyl scalar is given by [206]

$$\Psi_4 = \frac{2}{r}\partial_{\bar{z}}\partial_{\bar{z}}\phi(\tau, z, \bar{z}).\tag{3.45}$$

Indeed, we find that we can relate the potential fluid ϕ to the shockwave metric component H_{uu} by equating these two Ψ_4 's, up to an overall scale β :

$$\phi = \beta r H_{uu}.\tag{3.46}$$

Note that we have one more constraint when we relate the fluid degrees of freedom with the shockwave one: the leading-order conservation equation of the Brown-York stress tensor (3.32) should be consistent with the Einstein equation (3.27). This additional constraint enables us to determine the overall scaling ambiguity β . Inserting (3.46) into the leading-order fluid equation (3.32), we obtain

$$\beta r \partial^2 H_{uu} = \frac{1}{2} \kappa^2 r_c e^{\alpha\tau} \mathcal{T}_{uu}. \quad (3.47)$$

By judiciously choosing the value of β to be

$$\beta = -\frac{r_c e^{\alpha\tau}}{4r} = \frac{u}{v}, \quad (3.48)$$

we discover that $O(\varepsilon^2)$ conservation equation in the fluid-dual metric matches exactly with the shockwave equation of motion (3.27).

In terms of the shockwave degree of freedom X^v (3.30), the conservation equations of the Brown-York stress tensor become

$$O(\varepsilon^2): \quad -\frac{1}{2} \partial^2 \partial_u X^v = \kappa^2 \mathcal{T}_{uu} \quad (3.49)$$

$$O(\varepsilon^3): \quad \alpha u^2 \partial_i \partial_u^2 X^v + 2\alpha u \partial_i \partial_u X^v - 4r_c u \partial_i \partial_u \partial^2 X^v \approx \frac{8}{\alpha u} \partial_i P \quad (3.50)$$

In the second line, we have used $\partial_\tau H_{uu} = \frac{\alpha}{2} u \partial_u H_{uu}$, since $\partial_v H_{uu} = 0$. Additionally, we have ignored terms with X_v appearing twice. Regardless, the $O(\varepsilon^3)$ equation here has no contribution from the stress-energy tensor sourced by the shockwave, as we already anticipated in (3.37). Note that the $O(\varepsilon^2)$ equation contributes to the third term in the $O(\varepsilon^3)$ equation, leading to

$$O(\varepsilon^3): \quad 2e^{-\alpha\tau/2} P \approx \sqrt{\frac{r_c}{\alpha}} \partial_\tau^2 X^v + \frac{\sqrt{\alpha r_c}}{2} \partial_\tau X^v + 2(\kappa r_c)^2 e^{\alpha\tau/2} \mathcal{T}_{uu}, \quad (3.51)$$

where we used (τ, r, x^i) coordinates, and the external source \mathcal{T}_{uu} for the shockwave (3.40) is given by (3.28). Note that we have omitted nonlinear coupling terms in (3.50) and (3.51). Because time derivatives do not act on the nonlinear coupling terms, coordinate transformation from (u, v, x^i) to (τ, r, x^i) coordinates leave them invariant.

So far, all of the calculations are performed at the classical level. However, by instead promoting our source to a quantum operator, we will find a structure quite similar to [312, 324]. Specifically, we introduce quantum light-ray operators associated with the shockwave degrees of freedom and impose the t'Hooft commutation relation.

Our goal is to study the two-point correlation functions on the cutoff hypersurface Σ_c , which is timelike and boost invariant. In the next section, we will thus generalize the spacetime fluctuations on the null hypersurface [312] to a timelike hypersurface, by utilizing the cutoff fluid approach that we constructed in the previous sections.

3.4 Spacetime Fluctuations from Quantum Sources

In this section, we explore how spacetime fluctuations from quantum sources influence the behavior of fluids living on Σ_c . In particular, we will utilize the 't Hooft commutation relations [5] to modify the classical incompressibility equation to a stochastic differential equation. Then we follow the procedure in [324] to solve the differential equation and compute the variance in photon traversal time.

Our critical assumption is that due to vacuum energy fluctuations, \mathcal{T}_{uu} is no longer the stress-energy tensor of a classical shockwave. Rather, \mathcal{T}_{uu} encapsulates features of quantum fluctuations. We first utilize a commutation relation between H_{vv} and \mathcal{T}_{uu} , in close analogy to those proposed by 't Hooft [312, 324]:

$$[\mathcal{T}_{uu}(x), H_{vv}(x')] = i\delta^4(x - x'), \quad (3.52)$$

where x denotes coordinates in full spacetime dimensions. In writing Eq. (3.52) we have assumed that \mathcal{T}_{uu} and H_{vv} are quantum operators.

Here we have introduced an additional degree of freedom H_{vv} , which classically lives only on the past horizon. Although it is true that along either the future or past light front, only H_{uu} or H_{vv} is non-vanishing classically, in the present case \mathcal{T}_{uu} and H_{vv} act as quantum mechanical conjugate operators, as discussed in Refs. [312, 191]. Their commutation relation (3.52) is formally evaluated at the bifurcate horizon. Nevertheless, we can heuristically argue [41, 329, 324] that a single causal diamond is foliated by a series of nested causal diamonds (see Fig. 3.1), each separated by a microscopic length scale $\tilde{\ell}_p$, known as the decoherence length. Beyond this length scale, the subsequent diamonds become uncorrelated [41, 329, 324]. This argument allows us to identify a series of bifurcate horizons along the future and past light front, enabling us to introduce H_{vv} as an ultra local quantum degree-of-freedom. Crucially, the notion of a nested causal diamond gives rise to an accumulated quantum uncertainty in the photon traversal time [41, 329, 324]. Next, we proceed to compute this uncertainty in detailed steps.

Applying the commutator (3.52), we immediately discover that the classical shockwave equation of motion (3.27), or equivalently, the incompressibility equation for

Because \mathcal{T}_{uu} is stochastic, it naturally implies that $\langle H_{uu} \rangle$ and $\langle H_{vv} \rangle$ vanish. However, the variance $\langle H_{uu}^2 \rangle$ (similarly for $u \rightarrow v$) in general does not vanish. To compute the variance, we invoke the Robertson uncertainty principle [312, 324]

$$\langle H_{uu}^2 \rangle \langle H_{vv}^2 \rangle \geq \left| \frac{1}{2i} \langle [H_{uu}, H_{vv}] \rangle \right|^2 = \left(\frac{\ell_p^2}{2} \right)^2 [\delta(u - u_0) \delta(v - v_0) f(\mathbf{x}; \mathbf{x}')]^2. \quad (3.55)$$

Assuming that both are minimum uncertainty states, then the quantities $\langle H_{uu}^2 \rangle$ and $\langle H_{vv}^2 \rangle$ are equal:

$$\langle H_{uu}^2 \rangle = \langle H_{vv}^2 \rangle = \frac{\ell_p^2}{2} \delta(u - u_0) \delta(v - v_0) f(\mathbf{x}; \mathbf{x}'). \quad (3.56)$$

In order to further evaluate $\langle H_{uu}^2 \rangle$ and $\langle H_{vv}^2 \rangle$, we follow the heuristic argument of nested causal diamonds and statistical independence once again. This line of reasoning follows precisely the logic presented in details in Refs. [41, 324], and we will not reproduce it in this chapter.

However, one crucial distinction sets our current chapter apart from [324]. With the help of the cutoff fluid approach, we implement a ‘‘smeared-out’’ horizon (Fig. 3.1), using Σ_c so we can regularize the appropriate delta function in a manifestly Lorentz invariant manner. The first step in our regularization procedure is to transform the lightcone coordinates (u, v, x^i) into the ingoing coordinates (τ, r, x^i) naturally adapted to describe Σ_c . The two-dimensional delta function in the (u, v) coordinates are written explicitly in the (τ, r) coordinates as

$$\delta(\tau(u) - \tau_0) = \frac{\delta(u - u_0)}{|\tau'(u)|} = \frac{\alpha u}{2} \delta(u - u_0), \quad (3.57)$$

$$\delta(r - r_0) = \delta\left(-\frac{\alpha uv}{4} - r_0\right) = \delta(\alpha uv/4 + r_0) = \frac{4}{\alpha u} \delta(v - v_0), \quad (3.58)$$

where $\tau'(u) = \partial\tau/\partial u$. The function $\delta(\tau - \tau_0)$ keeps track of the causal development of an observer traversing on Σ_c , while $\delta(r - r_0)$ sets the width of the cutoff surface Σ_c . Therefore, we will replace $\delta(r - r_0)$ with a suitably regularized kernel. After first rescaling the argument of $\delta(r - r_0)$ we obtain

$$\delta(r - r_0) = \delta\left(\frac{\alpha uv}{4} + r_0\right) = \frac{4}{\alpha} \delta\left(uv + \frac{4r_0}{\alpha}\right). \quad (3.59)$$

Next, we regularize the delta function with a Poisson kernel⁴

$$\delta\left(uv + \frac{4r_0}{\alpha}\right) = \lim_{\epsilon \rightarrow 0} \frac{2}{\pi} \frac{\epsilon}{\epsilon^2 + (uv + 4r_0/\alpha)^2} \approx \frac{2}{\pi} \frac{1}{\epsilon}. \quad (3.60)$$

⁴The delta function can be represented by various kernels, but choosing the Poisson kernel allows us to keep consistency with the previous work [324].

In obtaining the last quantity, we have evaluated Eq. (3.60) on Σ_c , where $r_0 = r_c$ and uv satisfies the relation

$$uv|_{\Sigma_c} = -\frac{4r_c}{\alpha}. \quad (3.61)$$

The parameter ϵ represents the width of $\delta(uv + 4r_c/\alpha)$. In order to satisfy the Lorentz invariance condition, a particularly convenient candidate⁵ for ϵ is that $\epsilon = 4r_c/\alpha$. Setting $\epsilon = 4r_c/\alpha$ gives us

$$\frac{4}{\alpha}\delta\left(uv + \frac{4r_c}{\alpha}\right) \approx \frac{2}{\pi r_c}. \quad (3.62)$$

Now we have all the ingredients to evaluate $\langle H_{uu}^2 \rangle$. First, we apply the definition of the ‘‘light ray’’ operator (3.30) as in [312, 324], and perform a coordinate transformation to the ingoing Rindler coordinates (τ, r, x^i)

$$\begin{aligned} \langle H_{uu}^2 \rangle &\equiv \langle \partial_u X^v(u, \mathbf{x}) \partial_{u'} X^v(u', \mathbf{x}') \rangle \\ &= \left\langle \left(\frac{\partial \tau}{\partial u} \right) \partial_\tau X^v(\tau, \mathbf{x}) \left(\frac{\partial \tau'}{\partial u'} \right) \partial_{\tau'} X^v(\tau', \mathbf{x}') \right\rangle \\ &= \frac{4}{\alpha r_c} e^{-\alpha(\tau+\tau')/2} \langle \partial_\tau X^v(\tau, \mathbf{x}) \partial_{\tau'} X^v(\tau', \mathbf{x}') \rangle, \end{aligned} \quad (3.63)$$

where we have used $\partial\tau/\partial u = 2/(\alpha u)$ and the explicit relation between u and τ (3.23).

In the next step, we substitute in the delta function of the ingoing Rindler time τ (3.57), as well as the regularized delta function of the radial coordinate r in terms of a Poisson kernel of a width $\pi r_c/2$ (3.62)

$$\langle \partial_\tau X^v(\tau, \mathbf{x}) \partial_{\tau'} X^v(\tau', \mathbf{x}') \rangle = \frac{\ell_p^2 \alpha r_c}{8\pi r_c} e^{\alpha(\tau+\tau')/2} \delta(\tau - \tau') f(\mathbf{x}; \mathbf{x}'). \quad (3.64)$$

Eq. (3.64) takes on the form of a first order Langevin equation. Although the factor of r_c seems to cancel out between the chosen delta function regularization scheme and the coordinate transformation between u and τ , we will soon discover that another hidden factor of r_c will show up once we relate the ingoing Rindler time τ back to the Minkowski global time T relevant for a laboratory observer.

⁵There is an $O(1)$ number uncertainty in choosing ϵ ; however, this number can be absorbed into a redefinition of the reduced Planck length $\tilde{\ell}_p$. Also note that this ϵ is independent of the hydrodynamic expansion parameter ϵ .

In order to compute the two-point correlation function of X^v , we integrate both sides of (3.64) over τ' and τ readily to obtain

$$\begin{aligned}\langle X^v(\mathbf{x})X^v(\mathbf{x}')\rangle &= \frac{\ell_p^2 \alpha r_c}{8\pi r_c} f(\mathbf{x}; \mathbf{x}') \int_{\tau_i}^{\tau_f} d\tau \int_{-\infty}^{\tau} d\tau' e^{\alpha(\tau+\tau')/2} \delta(\tau - \tau') \\ &= \frac{\ell_p^2}{8\pi} \left(\frac{\alpha \Delta u^2}{r_c} \right) f(\mathbf{x}; \mathbf{x}'),\end{aligned}\tag{3.65}$$

where the Lorentz invariant combination α/r_c will be fixed in terms of the size of the causal diamond and the scale of quantum fluctuations shortly. The quantity

$$\Delta u^2 \equiv \frac{r_c}{\alpha} (e^{\alpha\tau_f} - e^{\alpha\tau_i})\tag{3.66}$$

denotes the square of the total elapsed coordinate time in u according to the coordinate transformation (3.23). The light cone coordinate⁶ u is related to Minkowski coordinates (T, Z) via $u = T + Z$. We immediately see that the elapsed time $\Delta u = \Delta T$ for an observer at a fixed location, *e.g.* $Z = L$. Photon traversal time measured by a free falling observer on the boundary of a causal diamond of size L is

$$\Delta T_{r.t.} = 2L = \Delta u\tag{3.67}$$

in the absence of any spacetime fluctuations.

Quantum fluctuations give rise to a ‘‘smeared-out’’ horizon, Σ_c , represented by the green curve Fig. 3.1. This cutoff surface intersects with the boundary of the causal diamond at a distance $\tilde{\ell}_p$ from either bottom or top of the diamond. As in Refs. [41, 329, 312, 324], $\tilde{\ell}_p$ characterizes the scale of quantum fluctuations. From Fig. 3.1, it is clear that the Minkowski global time difference between the light front and Σ_c is $\delta T = \tilde{\ell}_p$. This implies that $\delta u = \tilde{\ell}_p$ for $Z = L$. Moreover, $\delta v = \delta u = \tilde{\ell}_p$ by symmetry. We choose to evaluate the uncertainty at the future tip of the diamond, at which future light ray intersects with the worldline of a free-falling observer at $Z = L$. These constraints along with Eq. (3.61) imply that

$$\frac{4r_c}{\alpha} = -(u_f - \delta u)(v_f - \delta v) \approx u_f \delta v \approx 2L\tilde{\ell}_p,\tag{3.68}$$

where $(u_f, v_f) = (2L, 0)$ corresponds to the location at the top of the diamond. Putting Eq. (3.68) back into Eq. (3.65) gives us the final answer:

$$\langle X^v(\mathbf{x})X^v(\mathbf{x}')\rangle = \frac{\ell_p^2}{\pi} \left(\frac{L}{\tilde{\ell}_p} \right) f(\mathbf{x}; \mathbf{x}').\tag{3.69}$$

⁶Note that our convention of the light-cone coordinates differs from [324]. As a result, (u, v) directions in Fig. 3.1 are flipped, compared to the corresponding figure in [324].

Since X^v and X^u are related via time-reversal symmetry $X^v \leftrightarrow X^u$, we immediately write down the two-point function of $\langle X^u(\mathbf{x})X^u(\mathbf{x}') \rangle$

$$\langle X^u(\mathbf{x})X^u(\mathbf{x}') \rangle = \frac{\ell_p^2}{\pi} \left(\frac{L}{\tilde{\ell}_p} \right) f(\mathbf{x}; \mathbf{x}'). \quad (3.70)$$

The total time delay is the sum of Eqs. (3.69) and (3.70)

$$\begin{aligned} \Delta T_{r.t.}^2(\mathbf{x}; \mathbf{x}') &\equiv \langle X^v(\mathbf{x})X^v(\mathbf{x}') \rangle + \langle X^u(\mathbf{x})X^u(\mathbf{x}') \rangle \\ &= 2 \frac{\ell_p^2}{\pi} \left(\frac{L}{\tilde{\ell}_p} \right) f(\mathbf{x}; \mathbf{x}'). \end{aligned} \quad (3.71)$$

In four dimensions, there is no distinction between $\tilde{\ell}_p$ and ℓ_p [329, 312]; in other words, $\tilde{\ell}_p \cong \ell_p$, and Eq. (3.71) reduces to

$$\Delta T_{r.t.}^2(\mathbf{x}; \mathbf{x}') \stackrel{d=4}{=} \frac{2\ell_p L}{\pi} f(\mathbf{x}; \mathbf{x}'). \quad (3.72)$$

This equation is the main result of this section, and it is consistent with the findings from past literature [314, 313, 41, 329, 312, 324] that used different and complementary means. Note that the variance in the photon traversal time (3.72) has an overall scaling dependence on both UV (ℓ_p) and IR (L) scales. This kind of UV/IR mixing is most frequently encountered in the context of Brownian motion [144]. The hallmark of Brownian motion is that the variance of a Brownian particle depends on two quantities: 1) a diffusion coefficient D , an inter-molecular length scale proportional to the mean free path between collisions, and 2) total time elapsed t , usually set by laboratory measurement, takes on a macroscopic scale. In our case, we have found that quantum fluctuations near the light front of a Minkowski causal diamond also exhibit Brownian-like behavior. This result offers an exciting new avenue to test quantum fluctuations in gravity using precise laser interferometer measurement [313, 74].

3.5 Summary and Outlook

We have studied the relation between fluid and shockwave geometries, showing via Petrov classification that a potential fluid contains the same physical information as a shockwave geometry. We then proceeded to add a source to the fluid equation. The stress energy source is quantum in nature, with an amplitude given by a fundamental uncertainty in spacetime. We solved the equation of motion for spacetime and found an uncertainty in light travel time that depends both on the UV scale (a Planck length), as well as the light-crossing time of the causal diamond.

We hope the relation between the shockwave and potential fluid dual geometries will allow for direct calculation in the sourced potential fluid itself, *e.g.* of the two point function for the potential fluid, including its dependence on time and transverse directions. Although technically more difficult, extending beyond the transverse planar limit should allow for understanding the angular dependence within finite causal diamonds. Ideally we could also use the fluctuation-dissipation theorem to compute the fluid diffusion constant from the quantum source. We leave these and other extensions to future work.

A1 Appendix: Derivation of the Brown-York Stress Tensor

In this appendix, we derive the Brown-York stress tensor in the non-relativistic hydrodynamic expansion (3.15).

To end up with this result, we first describe the near-equilibrium fluid metric by allowing the fluid variables u_a, p to depend on (τ, x^i) [108, 109, 264]. In the derivative expansion⁷, the zeroth order seed metric is written as

$$ds^2 = -2p(x)u_a(x)dx^a dr + [\gamma_{ab} - \alpha p^2(x)(r - r_c)u_a(x)u_b(x)] dx^a dx^b, \quad (73)$$

where x denote (τ, x^i) .

In this work, we are interested in the non-relativistic hydrodynamic limit, which agrees with the near-horizon expansion [70, 206]

$$v_i \sim \mathcal{O}(\epsilon), \quad P \sim \mathcal{O}(\epsilon^2), \quad \partial_i \sim \mathcal{O}(\epsilon), \quad \partial_\tau \sim \mathcal{O}(\epsilon^2). \quad (74)$$

In order to do that, consider the non-relativistic expansion of the pressure and four-velocity

$$p = \frac{1}{\sqrt{\alpha r_c - 2P}} \approx \frac{1}{\sqrt{\alpha r_c}} + \frac{P}{(\alpha r_c)^{3/2}} + \mathcal{O}(\epsilon^4), \quad (75)$$

$$u_0 = \frac{-\alpha r_c}{\sqrt{\alpha r_c - v^2}} \approx \sqrt{\alpha r_c} \left(1 + \frac{v^2}{2\alpha r_c} \right) + \mathcal{O}(\epsilon^4), \quad (76)$$

$$u_i = \frac{v_i}{\sqrt{\alpha r_c - v^2}} \approx \frac{v_i}{\sqrt{\alpha r_c}} + \mathcal{O}(\epsilon^3). \quad (77)$$

Here, v_i is the non-relativistic fluid velocity in the transverse direction, and $v^2 \equiv v^i v_i$. P is the non-relativistic pressure of the fluid on Σ_c . We perform the non-relativistic hydrodynamic expansion in terms of the parameter ϵ , which keeps track of the

⁷The derivative expansion is defined as an order of different scaling $\tilde{\epsilon}$ such that $\partial_r \sim \mathcal{O}(1)$, $\partial_a \sim \mathcal{O}(\tilde{\epsilon})$.

scaling of various quantities. Combining these and expanding the metric in power of ϵ , the resulting metric becomes [70, 206]

$$\begin{aligned}
ds^2 = & -(\alpha r)d\tau^2 + 2d\tau dr + \delta_{ij}dx^i dx^j \\
& - 2\left(1 - \frac{r}{r_c}\right)v_i dx^i d\tau - 2\frac{v_i}{\alpha r_c}dx^i dr \\
& + \left(1 - \frac{r}{r_c}\right)\left[(v^2 + 2P)d\tau^2 + \frac{v_i v_j}{\alpha r_c}dx^i dx^j\right] + \left(\frac{v^2}{\alpha r_c} + \frac{2P}{\alpha r_c}\right)d\tau dr \\
& - \frac{(r^2 - r_c^2)}{\alpha r_c}\partial^2 v_i dx^i d\tau + \mathcal{O}(\epsilon^3).
\end{aligned} \tag{78}$$

The unit normal vector on Σ_c is given by [70]

$$n^\mu \partial_\mu = \frac{1}{\sqrt{\alpha r_c}}\partial_\tau + \sqrt{\alpha r_c}\left(1 - \frac{P}{\alpha r_c}\right)\partial_r + \frac{v^i}{\sqrt{\alpha r_c}}\partial_i + \mathcal{O}(\epsilon^3), \tag{79}$$

and after a short computation, we obtain the extrinsic curvature $K_{ab} = \frac{1}{2}\mathcal{L}_n\gamma_{ab}$ on Σ_c [70]

$$\begin{aligned}
K_{ab}dx^a dx^b = & -\frac{\alpha\sqrt{\alpha r_c}}{2}d\tau^2 + \frac{\alpha v_i}{\sqrt{\alpha r_c}}dx^i d\tau - \frac{\alpha(v^2 + P)}{2\sqrt{\alpha r_c}}d\tau^2 \\
& - \frac{\alpha(v_i v_j - 2r_c\partial_{(i}v_{j)})}{2(\alpha r_c)^{3/2}}dx^i dx^j + \mathcal{O}(\epsilon^3).
\end{aligned} \tag{80}$$

Evaluating the Brown-York stress tensor defined in (3.10), we obtain the Eq. (3.15)

$$\begin{aligned}
\kappa^2 T_{ab}dx^a dx^b = & \frac{\alpha v^2}{\sqrt{\alpha r_c}}d\tau^2 - \frac{2\alpha v_i}{\sqrt{\alpha r_c}}dx^i d\tau + \frac{\alpha}{\sqrt{\alpha r_c}}dx^i dx_i \\
& + \frac{P\delta_{ij} + v_i v_j}{r_c\sqrt{\alpha r_c}}dx^i dx^j - \frac{2\partial_{(i}v_{j)}}{\sqrt{\alpha r_c}}dx^i dx^j + \mathcal{O}(\epsilon^3).
\end{aligned} \tag{81}$$

Chapter 4

THE QUANTUM MECHANICS OF A SPHERICALLY
SYMMETRIC CAUSAL DIAMOND IN MINKOWSKI
SPACETIME

4.1 Introduction

Enormous conceptual progress has been made to unite gravity and quantum mechanics, and horizons have played a crucial role in these developments. In the presence of a horizon, there is a fairly universal notion of entropy, with the covariant entropy bound stating that the maximal entropy of any quantum state within a horizon is bounded above by $A/4G_N$, where A is the area of the horizon. This bound takes the same form as the Bekenstein-Hawking entropy. These results can be shown for conformal field theories with a gravity dual [278, 91], and it has been argued that they apply much more broadly to causal diamonds in maximally symmetric spacetimes [203, 313, 41]. However, outside of the context of AdS/CFT, comparatively few computational tools are available to analyze the quantum mechanics of causal horizons created by lightsheets.

Despite this difficulty, it is essential to understand the role of quantum mechanics in the study of causal diamonds in Minkowski spacetime, which serves as an excellent approximation of the spacetime accessible by laboratory experiments. Fortunately, there has been much research into the algebra of observables of black hole horizons and, more generally, Killing horizons [85, 82, 86, 288, 84, 287, 83, 80, 81], and it has been argued that many of the tools developed are also applicable to the study of causal horizons [41]. More recently, research along this direction has further been developed from the perspective of asymptotic symmetries [209, 180, 120, 134, 121, 181, 131, 176, 171, 17, 122, 18, 190], the covariant phase space formalism [93, 94, 95, 101, 102, 270], and von Neumann algebras [125, 140, 103]. In many of these works, a Hamiltonian charge corresponding to the area of the horizon has been obtained [82, 288, 84, 120, 121, 131, 122, 93, 94, 190].

In this chapter, we consider a relatively simple setup involving a spherically symmetric causal diamond in $(d+2)$ -dimensional Minkowski spacetime.¹ The simplicity of

¹Related analyses similar in spirit, but involving instead Jackiw–Teitelboim gravity, were done in [178, 174].

this spacetime allows us to straightforwardly construct the symplectic form, which we invert to obtain the quantum commutators. Furthermore, we derive the associated Iyer-Wald Hamiltonian charges [201]. One such charge is the area operator, which generates shifts in null time along the horizon. This is also the boost generator, which has been associated with the vacuum modular Hamiltonian of the system, and has been previously studied in similar contexts [203, 94]. However, we discover that by allowing for field-dependent diffeomorphisms, a second (integrable) charge exists, which generates shifts in the global time coordinate and causes the causal diamond to shrink or expand. This pair of charges fully characterizes the quantum mechanics of a spherically symmetric causal diamond, and it would be extremely interesting to explore the observational implications of both charges, as well as their fluctuations, which we leave for future work.

In this chapter, we first construct a coordinate system that describes a causal diamond in Minkowski spacetime. We then derive the symplectic form and quantum commutators associated to the causal diamond via the covariant phase space formalism. Finally, we compute the two families of Iyer-Wald charges and elaborate on their physical significance.

4.2 Parametrization of the Causal Diamond

In retarded coordinates, the metric of $(d + 2)$ -dimensional Minkowski spacetime is given by²

$$ds^2 = -d\tilde{u}^2 - 2 d\tilde{u} d\tilde{r} + \tilde{r}^2 d\Omega_d^2, \quad (4.1)$$

where $\tilde{u} = \tilde{t} - \tilde{r}$ is the retarded time coordinate and $d\Omega_d^2$ is the round metric of the unit S^d . We consider a spherically symmetric causal diamond of size L , defined by $|\tilde{t} + L| + \tilde{r} \leq L$. In retarded coordinates this is given by $-2L \leq \tilde{u} \leq -2\tilde{r}$. The past and future null boundaries \mathcal{H}^\pm of the diamond are respectively given by $\tilde{u} = -2L$ and $\tilde{u} = -2\tilde{r}$. The bifurcate horizon \mathcal{B} is given by $\tilde{r} = L$ and $\tilde{u} = -2L$, which is the intersection between \mathcal{H}^+ and \mathcal{H}^- . We are interested in fluctuations of the causal diamond that arise from spherically symmetric (large) diffeomorphisms. To this end, we consider a coordinate transformation of the form

$$\tilde{u} = -2\Phi_0(u), \quad \tilde{r} = \Phi(u, r). \quad (4.2)$$

²Alternatively, we could have worked with advanced time instead. However, as we will see, the degrees of freedom completely localizes to the bifurcate horizon \mathcal{B} , and hence both coordinate choices are equivalent.

A diffeomorphism of this form ensures that level sets of u are the same as those of \tilde{u} and, therefore, null. We require u to increase to the future and r to increase inwards, so we take $\partial_u \Phi_0 < 0$ and $\partial_r \Phi < 0$. The new coordinates cover the entire interior of the diamond as long as $\Phi \leq \Phi_0 \leq L$. The past horizon \mathcal{H}^- is given by $u = u_-$ where

$$\Phi_0(u_-) = L. \quad (4.3)$$

We require that the future null boundary \mathcal{H}^+ of the diamond be given by $r = 0$, which implies

$$\Phi_0(u) = \lim_{r \rightarrow 0} \Phi(u, r). \quad (4.4)$$

The bifurcate horizon \mathcal{B} is then located at $r = 0$, $u = u_-$. Note that \mathcal{H}^+ is a Cauchy slice for the causal diamond, and the following symplectic analysis will be carried out on this surface.

In the new coordinates, the metric Eq. (4.1) takes the form

$$\begin{aligned} ds^2 = & -2\kappa(u, r)r e^{2\beta(u, r)} du^2 + 2e^{2\beta(u, r)} du dr \\ & + \Phi(u, r)^2 d\Omega_u^2, \end{aligned} \quad (4.5)$$

where

$$\begin{aligned} e^{2\beta(u, r)} &= 2\partial_u \Phi_0(u) \partial_r \Phi(u, r), \\ \kappa(u, r) &= \frac{\partial_u (\Phi_0(u) - \Phi(u, r))}{r \partial_r \Phi(u, r)}. \end{aligned} \quad (4.6)$$

Although this metric resembles the Gaussian null coordinates used near null hypersurfaces, Eq. (4.5) describes the entire causal diamond. For reference, a spacetime diagram of the causal diamond is shown in Fig. 4.1.

4.3 Derivation of the Symplectic Form

We proceed to construct the symplectic form for the spherically symmetric causal diamond, via the use of the covariant phase space formalism [113, 216, 201, 316]. We vary the Einstein-Hilbert action, isolate the boundary term, and then integrate the latter over a Cauchy slice Σ to obtain the pre-symplectic potential (e.g., see [90]). The result is³

$$\tilde{\Theta}_\Sigma[g; \delta g] = \frac{1}{16\pi G_N} \int_\Sigma d\Sigma_\mu (g^{\nu\rho} \delta\Gamma_{\nu\rho}^\mu - g^{\mu\nu} \delta\Gamma_{\nu\rho}^\rho), \quad (4.7)$$

³The tilde emphasizes that Eq. (4.7) is the *pre*-symplectic potential rather than the symplectic potential, as the corresponding *pre*-symplectic form $\tilde{\Omega}$ may not be invertible. The tilde is dropped once we gauge-fix in Eq. (4.17) and Eq. (4.20), which renders $\tilde{\Omega}$ invertible.

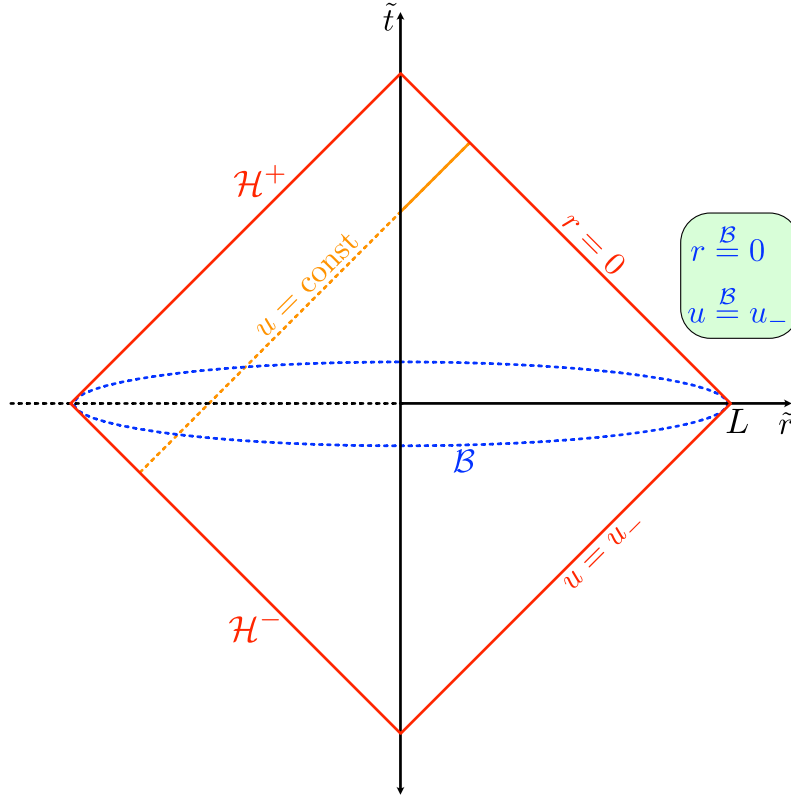


Figure 4.1: A causal diamond of radius L with null boundaries shown as solid red line. The blue dashed ellipse represents the d -dimensional bifurcation surface, while the constant u hypersurface is represented by the orange line.

where $d\Sigma_\mu$ is the surface element on Σ . For the special case where $\Sigma = \mathcal{H}^+$, the surface element is given by⁴

$$d\Sigma_\mu = -\delta_\mu^r \Phi^d e^{2\beta} du d\Omega_d, \quad (4.8)$$

where $d\Omega_d$ is the volume form on S^d . We derive in the Supplementary Material that given the definition

$$\varphi(u, r) \equiv \Phi(u, r)^d, \quad (4.9)$$

the pre-symplectic potential is given by

$$\tilde{\Theta}_{\mathcal{H}^+}[g; \delta g] = \frac{\Omega_d}{8\pi G_N} (\log |\partial_u \varphi| - \beta) \delta \varphi|_{\mathcal{B}} + \delta(\dots), \quad (4.10)$$

⁴The negative sign in Eq. (4.8) arises from the fact our normal vector is outward-pointing, and this is in the direction of decreasing r , since r increases as we move *into* the causal diamond along constant u rays.

where $\Omega_d = \frac{2\pi^{\frac{d+1}{2}}}{\Gamma(\frac{d+1}{2})}$ is the volume of S^d . We note that the pre-symplectic potential localizes entirely on the bifurcate horizon \mathcal{B} with no contribution from the rest of \mathcal{H}^+ . The reason is that in our rather simplistic setup, all metric fluctuations arise due to diffeomorphisms, and it was shown in [201] that such contributions are a boundary term. The $\delta(\dots)$ denotes the total variational terms that do not contribute to the pre-symplectic form, and are neglected henceforth.⁵

The pre-symplectic form is given by

$$\begin{aligned} \tilde{\Omega}[g; \delta_1 g, \delta_2 g] &= \delta_1 \tilde{\Theta}_\Sigma[g; \delta_2 g] - \delta_2 \tilde{\Theta}_\Sigma[g; \delta_1 g] \\ &\quad - \tilde{\Theta}_\Sigma[g; [\delta_1, \delta_2]g], \end{aligned} \quad (4.11)$$

where we dropped the subscript Σ on $\tilde{\Omega}$ since we will eventually see the symplectic form is independent of Σ . It then follows from Eq. (4.10) that

$$\tilde{\Omega}[g; \delta_1 g, \delta_2 g] = \frac{\Omega_d}{8\pi G_N} \delta(\log |\partial_u \varphi| - \beta) \wedge \delta\varphi|_{\mathcal{B}}, \quad (4.12)$$

where we define the notation $\delta a \wedge \delta b \equiv \delta_1 a \delta_2 b - \delta_2 a \delta_1 b$. Furthermore, observing that

$$(\log |\partial_u \varphi| - \beta)|_{\mathcal{B}} = \left(\log \frac{\Phi_0^{d-1} d}{2} + \frac{1}{2} \log \frac{2\partial_u \Phi_0}{\partial_r \Phi} \right) \Big|_{\mathcal{B}}, \quad (4.13)$$

we can use the antisymmetry of the wedge product to obtain

$$\tilde{\Omega}[g; \delta_1 g, \delta_2 g] = \frac{1}{8\pi G_N} \delta\mu \wedge \delta A, \quad (4.14)$$

where

$$A \equiv \Omega_d \varphi|_{\mathcal{B}} = \Omega_d \Phi^d|_{\mathcal{B}}, \quad \mu = \frac{1}{2} \log \frac{2\partial_u \Phi}{\partial_r \Phi} \Big|_{\mathcal{B}}. \quad (4.15)$$

To elevate this to the symplectic form, we demand invertibility and therefore need to perform a small gauge fixing. This is done in the Supplementary Material, and we obtain

$$\beta(u, r) = 0, \quad \kappa(u, r) = \kappa_0, \quad (4.16)$$

where κ_0 is a spacetime constant, and

$$\Phi(u, r) = L - \frac{1}{2\kappa_0} e^{\kappa_0 u + \alpha} - r e^{-\kappa_0 u - \alpha}, \quad (4.17)$$

⁵The pre-symplectic potential in fact has further ambiguities arising from possible corner terms, as explained in Section 1.3.3 of [110]. However, due to spherical symmetry, all such local and covariant corner terms are total variations that do not affect the symplectic form.

where α is another spacetime constant. We also note that in this gauge, u is the proper time for a uniformly accelerating observer at $r = (2\kappa_0)^{-1}$, with their proper acceleration $a = \kappa_0$ and whose future Rindler horizon is \mathcal{H}^+ . The Unruh temperature experienced by this observer is therefore

$$T = \frac{\kappa_0}{2\pi}. \quad (4.18)$$

We now evaluate the symplectic form in this gauge. From the definitions Eq. (4.15), it follows that

$$A = \Omega_d L^d, \quad \mu = \kappa_0 u_- + \alpha. \quad (4.19)$$

From Eqs. (4.3), (4.4), and (4.17), it follows that $u_- = -\infty$, which implies that μ , and therefore $\tilde{\Omega}$, is generically formally divergent. In the Supplementary Material, we show that $\tilde{\Omega}$ can be made finite and invertible by assuming that κ_0 is non-dynamical on the phase space and is instead fixed in terms of L

$$\kappa_0 \equiv \kappa_0(L). \quad (4.20)$$

With this assumption, the symplectic form reduces to

$$\Omega[g; \delta_1 g, \delta_2 g] = \frac{1}{8\pi G_N} \delta\alpha \wedge \delta A. \quad (4.21)$$

Inverting Eq. (4.21), we immediately arrive at the Poisson bracket

$$\{\alpha, A\} = -8\pi G_N. \quad (4.22)$$

Upon canonical quantization, we promote the Poisson bracket to a quantum commutator so that

$$[\alpha, A] = -8\pi i G_N. \quad (4.23)$$

4.4 Hamiltonian Charges

We now derive the Iyer-Wald Hamiltonian charges corresponding to horizon-preserving diffeomorphisms of the causal diamond. Recall that for a generic diffeomorphism generated by a vector field ξ^μ , the Iyer-Wald Hamiltonian charge H_ξ is obtained from the symplectic form via the variational equation [201]

$$\delta H_\xi = \Omega[\phi; \delta\phi, \delta_\xi\phi]. \quad (4.24)$$

This is merely Hamilton's equation expressed in terms of the covariant symplectic form. The slash on the left-hand side indicates that the right-hand side might not be a total variation, and hence H_ξ may not exist. If H_ξ does exist, Eq. (4.24) is integrable, and the charge is obtained by inverting the variation.

We consider diffeomorphisms that preserve the form of our metric Eq. (4.5), with β gauge-fixed to $\beta = 0$ and $\kappa(u, r) = \kappa_0$. This amounts to requiring the following conditions on the vector field ξ^μ generating the diffeomorphism:

$$\mathcal{L}_\xi g_{uu} = O(r), \quad \mathcal{L}_\xi g_{ur} = \mathcal{L}_\xi g_{rr} = 0. \quad (4.25)$$

Symmetries of this or related forms have been studied numerous times in the literature, most famously by Bondi, van der Burg, Metzner, and Sachs [64, 280, 279] in the context of asymptotically flat spacetimes. More recently, asymptotic symmetries of null surfaces have been the subject of significant study [82, 84, 120, 121, 95, 93, 94, 171, 17, 122, 18, 190]. In our case, we also require that ξ^μ preserves the spherical symmetry of the diamond, which significantly simplifies our calculation. The resultant set of allowed diffeomorphisms is generated by

$$\xi^\mu = (f(u), -r\partial_u f(u), \vec{0}), \quad (4.26)$$

where $f(u)$ is any smooth function of u . Under an infinitesimal diffeomorphism $x^\mu \rightarrow x^\mu + \xi^\mu$, we have

$$\begin{aligned} \delta_\xi \kappa_0 = -\lambda_\kappa &\implies \kappa_0 \partial_u f + \partial_u^2 f = \lambda_\kappa \\ &\implies f(u) = c_1 + c_2 e^{-\kappa_0 u - \alpha} + \frac{\lambda_\kappa u}{\kappa_0}, \end{aligned} \quad (4.27)$$

where c_1, c_2 are some undetermined constants and λ_κ is an infinitesimal parameter. If we further fix

$$c_1 = \lambda_\alpha - \frac{\lambda_\kappa}{\kappa_0^2}, \quad c_2 = -2\lambda_L, \quad (4.28)$$

for infinitesimal parameters λ_α and λ_L , then the diffeomorphism generated by ξ^μ yields

$$\delta_\xi \kappa_0 = -\lambda_\kappa, \quad \delta_\xi L = -\lambda_L, \quad \delta_\xi \alpha = -\kappa_0 \lambda_\alpha. \quad (4.29)$$

Recall that we require $\kappa_0 \equiv \kappa_0(L)$ in order for the symplectic form Eq. (4.21) to be finite, which implies

$$\lambda_\kappa = \kappa_0'(L) \lambda_L. \quad (4.30)$$

Comparing this with the field Φ given in Eq. (4.17), we immediately see that λ_α parametrizes the shift in null time u , whereas λ_L parametrizes the change in the size of the causal diamond L . Thus, the most general symmetry preserving the geometry of a spherically symmetric causal diamond is parametrized by λ_L and λ_α . We now construct the Iyer-Wald charges that correspond to the two diffeomorphisms above.

First, let us construct the charge where $\lambda_\alpha \neq 0$ but $\lambda_L = 0$. This is the charge that generates null time shifts in u but keeps L fixed. Using Eq. (4.24) with the symplectic form Eq. (4.21), we obtain

$$\begin{aligned} \delta H_\alpha &= -\frac{1}{8\pi G_N} \delta_\xi \alpha \delta A \\ &= \delta \left(\frac{\lambda_\alpha \Omega_d d}{8\pi G_N} \int_0^L dL' \kappa_0(L') L'^{d-1} \right), \end{aligned} \quad (4.31)$$

where we used Eq. (4.19) and Eq. (4.29). We conclude that the first charge is

$$H_\alpha = \frac{\Omega_d d}{8\pi G_N} \int_0^L dL' \kappa_0(L') L'^{d-1}, \quad (4.32)$$

where we normalized the charge H_α to exclude λ_α . When there are no other length scales in the theory, dimensional analysis implies that κ_0 takes the form $\kappa_0(L) = C/L$ for some dimensionless constant C independent of L . In this case, the charge above is given by⁶

$$H_\alpha = \frac{d}{d-1} \frac{\Omega_d}{8\pi G_N} C L^{d-1} = \frac{d}{d-1} \frac{\kappa_0(L)}{2\pi} \frac{A}{4G_N}. \quad (4.33)$$

Identifying $\kappa_0(L)/2\pi$ with the Unruh temperature of an accelerating observer (see Eq. (4.18)) and associating an entropy $S = A/4G_N$ to the causal diamond, we find a version of the Smarr formula for causal diamonds:

$$\frac{d-1}{d} H_\alpha = TS. \quad (4.34)$$

From Eq. (4.32), we can also reproduce a version of the first law for causal diamonds, namely⁷

$$\delta H_\alpha = \frac{\Omega_d d}{8\pi G_N} \kappa_0(L) L^{d-1} \delta L = \frac{\kappa_0(L)}{2\pi} \delta \left(\frac{A}{4G_N} \right) = T \delta S. \quad (4.35)$$

⁶In three dimensions ($d = 1$), we have $H_\alpha = \frac{C}{4G_N} \log L$.

⁷Notice that because the vector generating shifts in u is timelike, the energy measured by the accelerating observer is $E = -H_\alpha$, which implies that the temperature associated to causal diamonds is negative. This is consistent with the results of [203, 94].

Note that H_α generates time translations in u , which is the proper time of a uniformly accelerating observer. Therefore, we conclude that H_α is in fact the generator of boosts that preserve the causal diamond and is also the vacuum modular Hamiltonian of the causal diamond (see e.g., [54, 55]).

Next, we construct the second charge where $\lambda_\alpha = 0$ but $\lambda_L \neq 0$. Using Eq. (4.24) with the symplectic form Eq. (4.21), we obtain

$$\delta H_L = \frac{1}{8\pi G_N} \delta\alpha \delta_\xi A = -\frac{\lambda_L \Omega_d d}{8\pi G_N} L^{d-1} \delta\alpha, \quad (4.36)$$

where we again used Eq. (4.19) and Eq. (4.29). Because $\delta L \neq 0$ in general, the above equation is not a total variation, which implies that the charge is not integrable.⁸ However, for the special case where we consider a field-dependent diffeomorphism and fix

$$\lambda_L = \frac{G_N \epsilon}{L^{d-1}}, \quad (4.37)$$

where ϵ is an infinitesimal parameter, $\lambda_L L^{d-1}$ becomes a constant on phase space. Thus, the charge becomes integrable and is given by

$$H_L = -\frac{\Omega_d d}{8\pi} \alpha, \quad (4.38)$$

where we normalized the charge to exclude ϵ . As we previously mentioned, this charge generates a shift in the size of the causal diamond L , but the shifts are field-dependent, given by Eq. (4.37). However, the change in the area of the diamond is field-independent and is given by

$$\delta_\xi A = -\Omega_d L^{d-1} \lambda_L d = -\Omega_d G_N d, \quad (4.39)$$

where we used (4.37).

There are some interesting observations regarding H_L . We note that while H_L generates shifts in the size of the causal diamond, it additionally generates shifts in the global Minkowski time \tilde{t} . To see this, note that under the diffeomorphism generated by ξ^μ with $\lambda_\alpha = 0$, we have

$$\begin{aligned} \Phi \rightarrow \Phi + \delta_\xi \Phi = L - \lambda_L - \frac{1}{2(\kappa_0 - \lambda_\kappa)} e^{(\kappa_0 - \lambda_\kappa)u + \alpha} \\ - r e^{-(\kappa_0 - \lambda_\kappa)u - \alpha}. \end{aligned} \quad (4.40)$$

⁸The exception to this is if $d = 1$ and we are in a three-dimensional spacetime, which was observed in [121]. In that case $L^{d-1} = 1$ and there are no obstructions to writing down the charge.

Recalling that Minkowski time is given by $\tilde{t} = \tilde{u} + \tilde{r}$, we have to linear order in the variation using Eq. (4.2)

$$\tilde{t} \rightarrow \tilde{t} + \lambda_L + \lambda_\kappa \left(\frac{1}{2\kappa_0^2} e^{\kappa_0 u + \alpha} (1 - \kappa_0 u) - r u e^{-\kappa_0 u - \alpha} \right), \quad (4.41)$$

implying that \tilde{t} indeed shifts under the action by H_L . In fact, at the bifurcate horizon \mathcal{B} , the second term in the above expression vanishes as $u = -\infty$ and $r = 0$, and we have $\tilde{t} \rightarrow \tilde{t} + \lambda_L$. Furthermore, recalling that the future boundary \mathcal{H}^+ is located at $\tilde{u} + 2\tilde{r} = 0$, it is straightforward to check that \mathcal{H}^+ remains invariant under the action by H_L . On the other hand, the past horizon \mathcal{H}^- is located at $\tilde{u} = -2L$, and this shifts under \mathcal{H}^- to $\tilde{u} = -2L + 2\lambda_L$. In practice, this occurs by shifting the location of the bifurcation surface while keeping the top of the diamond fixed, thereby creating a “nesting” of causal diamonds (see Fig. 4.2) [41, 329, 324, 39]. Thus, while H_α generates null time translations, H_L acts like a dilatation operator (while keeping \mathcal{H}^+ invariant). We can easily compute the commutation relation of the two charges using Eq. (4.23) to obtain

$$[H_\alpha, H_L] = -\frac{i}{8\pi} \kappa_0(L) \Omega_d d. \quad (4.42)$$

4.5 Conclusion

In this chapter, we considered the quantum mechanics of a spherically symmetric causal diamond in $(d+2)$ -dimensional spacetime. We constructed the symplectic form associated with the causal diamond, which localizes to the codimension-2 bifurcate horizon at the corner and also derived two physically relevant Hamiltonian charges using the Iyer-Wald prescription. The first charge H_α shifts the null time u and is proportional to the area of the causal diamond. This is the vacuum modular Hamiltonian and has been extensively studied in the literature in a variety of contexts [54, 55, 91, 41, 312, 202, 203]. However, there is an interesting second charge H_L , which changes the size of the causal diamond, and it exists only if field-dependent diffeomorphisms (for $d \geq 2$) are allowed. Because our setup is simple enough to directly relate the original Minkowski spacetime to our Gaussian null coordinates, we can deduce that H_L equivalently shifts the global Minkowski time.

There are many natural future directions to explore. Perhaps first and foremost is to relax the spherical symmetry assumption. Many previous works have considered the full asymptotic symmetry algebra of generic null surfaces [82, 84, 120, 121, 95, 93, 94, 171, 122, 17, 18, 270, 190], but have obtained differing results due to the

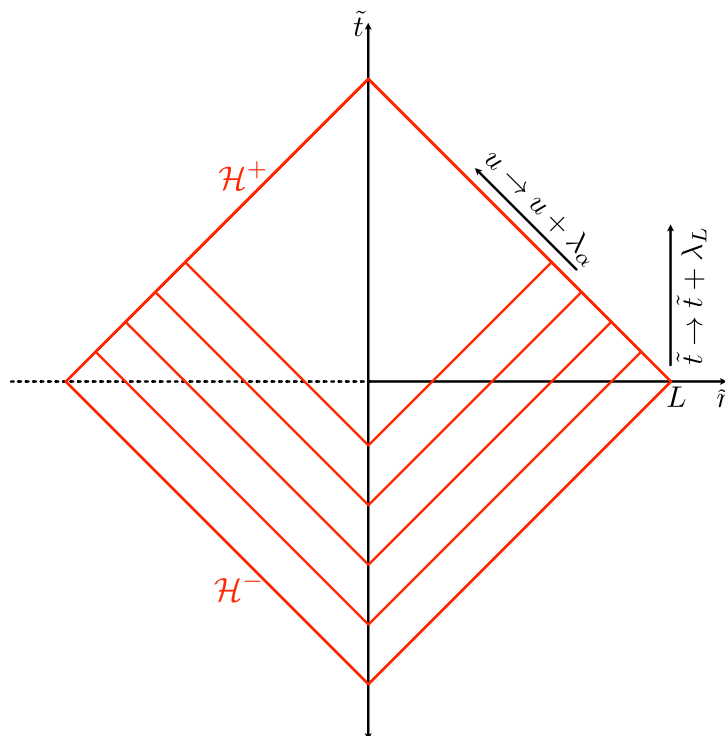


Figure 4.2: Pictorial depiction of a series of “nested” causal diamonds. Charge H_α generates translation in null time $u \mapsto u + \lambda_\alpha$, whereas charge H_L generates shift in the size of the diamond, which corresponds to, at the bifurcate horizon \mathcal{B} , a translation in Minkowski time $\tilde{t} \mapsto \tilde{t} + \lambda_L$.

choice of boundary conditions, charge integrability, and a variety of other challenges. Moreover, many of these works did not allow for field-dependent diffeomorphisms (notable exceptions are [171, 18, 270, 190] and references therein), which we have shown are essential for the existence of the second charge that generates shifts in the area of the bifurcation surface. To our knowledge, no analysis has been carried out to study this charge or its higher modes in a more general environment. It would be extremely interesting to understand whether the algebra of these higher modes admits a central extension, as well as to explore the observational consequences of the two charges.

B1 Appendix: Derivation of the Pre-symplectic Potential

In this section, our goal is to derive the pre-symplectic potential for the metric Eq. (4.5) and obtain Eq. (4.10). We begin by recalling Eq. (4.7) and Eq. (4.8), which

immediately implies

$$\begin{aligned}\tilde{\Theta}_{\mathcal{H}^+}[g; \delta g] &= -\frac{1}{16\pi G_N} \int_{\mathcal{H}^+} du d\Omega_d e^{2\beta} \Phi^d \left[g^{\mu\nu} (\delta\Gamma_{\mu\nu}^r) - g^{\mu r} (\delta\Gamma_{\lambda\mu}^\lambda) \right] \\ &= -\frac{1}{16\pi G_N} \int_{\mathcal{H}^+} du d\Omega_d \varphi \left[2\delta\Gamma_{ur}^r + \frac{e^{2\beta}}{\varphi^{\frac{2}{d}}} \gamma^{ab} \delta\Gamma_{ab}^r - \delta\Gamma_{\lambda u}^\lambda \right],\end{aligned}\quad (43)$$

where we defined

$$\varphi(u, r) \equiv \Phi(u, r)^d. \quad (44)$$

Evaluating the variations of the Christoffel symbols, the integrand of Eq. (43) becomes

$$\begin{aligned}\varphi \left[2\delta\Gamma_{ur}^r + \frac{e^{2\beta}}{\varphi^{\frac{2}{d}}} \gamma^{ab} \delta\Gamma_{ab}^r - \delta\Gamma_{\lambda u}^\lambda \right] &= -2\varphi\delta\kappa + 2\partial_u\varphi\delta\beta - 2\left(\frac{1}{d} - 1\right)\frac{1}{\varphi}\partial_u\varphi\delta\varphi \\ &\quad - 2\partial_u\delta\varphi - 2\varphi\partial_u\delta\beta + \mathcal{O}(r).\end{aligned}\quad (45)$$

Now, recall that the pre-symplectic form is defined as

$$\tilde{\Omega}[g; \delta_1 g, \delta_2 g] = \delta_1 \tilde{\Theta}_\Sigma[g; \delta_2 g] - \delta_2 \tilde{\Theta}_\Sigma[g; \delta_1 g] - \tilde{\Theta}_\Sigma[g; [\delta_1, \delta_2]g], \quad (46)$$

so by the antisymmetry of δ_1 and δ_2 , terms that are total variations in the pre-symplectic potential will not contribute to the pre-symplectic form, thereby allowing us to ignore such terms. Thus, we can rewrite Eq. (45) as

$$\begin{aligned}\varphi \left[2\delta\Gamma_{ur}^r + \frac{e^{2\beta}}{\varphi^{\frac{2}{d}}} \gamma^{ab} \delta\Gamma_{ab}^r - \delta\Gamma_{\lambda u}^\lambda \right] &= \left[2\kappa + 4\partial_u\beta - 2\left(\frac{1}{d} - 1\right)\frac{1}{\varphi}\partial_u\varphi \right] \delta\varphi \\ &\quad - 2\partial_u(\delta\varphi\beta) + \delta(\dots) + \mathcal{O}(r),\end{aligned}\quad (47)$$

where $\delta(\dots)$ indicate terms that are total variations. Substituting this back into Eq. (43) and dropping the $\mathcal{O}(r)$ terms since $r \rightarrow 0$ on \mathcal{H}^+ , we see that the pre-symplectic potential is given by

$$\begin{aligned}\tilde{\Theta}_{\mathcal{H}^+}[g; \delta g] &= -\frac{\Omega_d}{16\pi G_N} \int_{u_-}^{u_+} du \left\{ \left[2\kappa + 4\partial_u\beta - 2\left(\frac{1}{d} - 1\right)\frac{1}{\varphi}\partial_u\varphi \right] \delta\varphi - 2\partial_u(\delta\varphi\beta) \right\} \\ &\quad + \delta(\dots),\end{aligned}\quad (48)$$

where we integrated over the angular directions to obtain the volume of the unit d -sphere Ω_d , and u_\pm indicates the integration limits of the future horizon \mathcal{H}^+ . We can further simplify this by substituting it in Eq. (4.6) to obtain

$$\tilde{\Theta}_{\mathcal{H}^+}[g; \delta g] = -\frac{\Omega_d}{8\pi G_N} \int_{u_-}^{u_+} du \left[\partial_u \log |\partial_u \varphi| \delta\varphi - \partial_u(\delta\varphi\beta) \right] + \delta(\dots). \quad (49)$$

We now note the first term in the integrand of Eq. (49) can be written as

$$\begin{aligned}\partial_u \log |\partial_u \varphi| \delta \varphi &= \partial_u (\log |\partial_u \varphi| \delta \varphi) - \log |\partial_u \varphi| \partial_u \delta \varphi \\ &= \partial_u (\log |\partial_u \varphi| \delta \varphi) + \delta(\cdots),\end{aligned}\quad (50)$$

which means we can further simplify Eq. (49) to be

$$\tilde{\Theta}_{\mathcal{H}^+}[g; \delta g] = \frac{\Omega_d}{8\pi G_N} (\log |\partial_u \varphi| - \beta) \delta \varphi \Big|_{u=u_-} + \delta(\cdots), \quad (51)$$

where we carried out the u integral, and noted that $\varphi(u_+) = \Phi(u_+, 0)^d = 0$ since by definition ($u = u_+, r = 0$) is at the top of causal diamond, which corresponds to $\tilde{r} = 0$, and hence $\Phi(u_+, 0) = 0$ by Eq. (4.2). This is precisely Eq. (4.10).

B2 Appendix: Promotion of the Pre-symplectic Form to Symplectic Form

In this section, we show how to gauge-fix so that the pre-symplectic form Eq. (4.14), reproduced here for convenience as

$$\tilde{\Omega}[g; \delta_1 g, \delta_2 g] = \frac{1}{8\pi G_N} \delta \mu \wedge \delta A, \quad (52)$$

becomes invertible and hence the symplectic form Eq. (4.21). First, note that the pre-symplectic form written in the form Eq. (4.12) does not depend on β independently, but rather depend on the linear combination $\log |\partial_u \varphi| - \beta$ at \mathcal{B} . Hence, we can choose to gauge-fix β , and since the symplectic form is independent of the value of β away from \mathcal{B} , we choose the simplest choice, namely

$$\beta = 0. \quad (53)$$

Recalling from Eq. (4.6) the definition of β , and we have upon setting $\beta = 0$ in Eq. (4.6) the equality

$$\Phi(u, r) = \Phi_0(u) + \frac{r}{2\partial_u \Phi_0(u)}. \quad (54)$$

Using Eq. (4.6) and Eq. (54), we similarly derive

$$\kappa(u, r) = \frac{\partial_u^2 \Phi_0(u)}{\partial_u \Phi_0(u)}. \quad (55)$$

Next, we note that the pre-symplectic form only depends on $\kappa(u_-, 0)$, which means it does not matter how κ changes as a function of u and r . This allows to further gauge-fix so that $\kappa(u, r) \equiv \kappa_0$ is independent of u and r and therefore a spacetime constant. In this case, we solve Eq. (55) to obtain

$$\Phi(u, r) = L - \frac{1}{2\kappa_0} e^{\kappa_0 u + \alpha} - r e^{-\kappa_0 u - \alpha}, \quad (56)$$

where L is the radius of the causal diamond, and α an arbitrary spacetime constant. Note that in our original Bondi coordinates Eq. (4.1), the bifurcate horizon \mathcal{B} is located at $\tilde{u} = -2L$ and $\tilde{r} = L$, or equivalently at $u = u_-$ and $r = 0$. The coordinate transformation Eq. (4.2) suggests that \mathcal{B} is located at

$$\tilde{r} = L = \Phi(u_-, 0) = \Phi_0(u_-). \quad (57)$$

Comparing this to Eq. (56), we see that \mathcal{B} , which also corresponds to the past boundary of \mathcal{H}^+ , is located at $u_- = -\infty$. We can also determine u_+ by using $\Phi(u_+, 0) = 0$, which yields

$$u_+ = \frac{1}{\kappa_0} (\log(2\kappa_0 L) - \alpha). \quad (58)$$

Recalling Eq. (4.15), we see from Eq. (56) that

$$A = \Omega_d L^d, \quad \mu = \lim_{u \rightarrow u_-} (\alpha + \kappa_0 u) = \alpha + \kappa_0 u_-. \quad (59)$$

Because $u_- = -\infty$, μ is formally divergent. Furthermore, from (59), it appears that there are three degrees of freedom, namely L , α , and κ_0 . Since the phase space is even-dimensional, it must be the case that not all three degrees of freedom are independent. We can resolve both issues if we assume $\kappa_0 = \kappa_0(L)$, so that κ_0 depends purely on L and is not an independent degree of freedom. In this case, κ_0 is still a spacetime constant as it is independent of u , r , and we have $\delta\kappa_0 = \kappa'(L)\delta L$. By the antisymmetry of the wedge product, the divergent term vanishes, and we are left with⁹

$$\Omega[g; \delta_1 g, \delta_2 g] = \frac{1}{8\pi G_N} \delta\alpha \wedge \delta A. \quad (60)$$

We have dropped the tilde on Ω as the above expression is invertible, and this is precisely Eq. (4.21).

⁹Another common choice in the literature has been to take κ_0 to be a fixed constant on the phase space, such that $\delta\kappa_0 = 0$ (e.g., see [120, 121, 131, 134]), which corresponds to the case of an isolated horizon.

QUANTUM GRAVITY BACKGROUND IN NEXT-GENERATION GRAVITATIONAL WAVE DETECTORS

5.1 Introduction

Bridging the gap between theory and experiment in the study of quantum gravity is at the forefront of research in physics. Although the effects of quantum gravity are ordinarily expected to appear on unobservably-small scales of order the Planck length, $l_p = \sqrt{8\pi G\hbar/c^3} \sim 10^{-34}$ m, recent works [313, 314, 328, 41, 174, 312, 324] have shown that this naive effective field theory (EFT) reasoning may not capture the complete physical picture. Instead, Refs. [313, 314] showed, using standard holographic techniques, that spacetime fluctuations accumulate from the UV into the IR to produce an effect that scales with the size L of the physical system. In particular, in flat spacetime, the trajectories of photons in an interferometer of length L enclose a finite spacetime region known as a causal diamond. The geometric fluctuations induced by entropic fluctuations within the causal diamond, or “geotropic fluctuations,” manifest as uncertainty in the arm length of the interferometer, as measured by the photon travel time, with a variance that scales as

$$\langle \Delta L^2 \rangle \sim l_p L. \quad (5.1)$$

Additionally, these fluctuations exhibit long-range transverse correlations which enable observation. This result has proven to be theoretically robust, having been confirmed with several distinct theoretical approaches in Refs. [328, 41, 174, 312, 324], such that the geotropic fluctuations are observed in flat Minkowski, dS, and AdS spacetimes. For a summary of all of these works, see Ref. [329].

More recently, Ref. [219], building upon the work of Ref. [328], developed a *model* of these geotropic fluctuations in terms of bosonic degrees of freedom coupled to the metric. The model is designed to capture the most prominent features of the theory developed in Refs. [313, 314, 41, 174, 324, 312], while being local and allowing for the explicit computation of the gauge-invariant interferometer observable. It features a scalar field ϕ , the “pixellon”, a breathing mode corresponding to spacetime fluctuations of the (spherically symmetric) volume of spacetime under observation. This model allows for the calculation of the power spectral density (PSD)

of geotropic fluctuations in spherically-symmetric configurations, in particular for traditional L-shaped interferometers such as LIGO [234] and LISA [37].

Ref. [219] also compared the PSD of the pixellon model to the strain sensitivities of several current and future gravitational wave (GW) detectors, namely LIGO/Virgo [234], Holometer [96], GEO600 [305], and LISA [37]. These experiments either produced modest constraints on the pixellon model (in the cases of LIGO and Holometer) or were not sensitive to the model (in the cases of GEO600 and LISA). There are several general reasons for this. For large instruments such as LISA, we expect a reduced signal as the geotropic strain scales parametrically as $h = \frac{\Delta L}{L} \sim \sqrt{\frac{l_p}{L}}$. On the other hand, existing terrestrial experiments typically have poorer strain sensitivities near the relatively high frequency $\omega_{\text{peak}} \sim \frac{1}{L}$ at which the pixellon signal achieves its peak. In this chapter, we build upon this previous work and survey the landscape of next-generation GW detectors, characterizing their sensitivity to geotropic fluctuations as modeled by the pixellon. We also consider these experiments in the context of the upcoming GQuEST experiment [236], which explicitly seeks to measure the geotropic signal. Note that in this chapter we assume the pixellon is a good *physically equivalent* description of the geotropic fluctuations predicted by the VZ effect [313, 314, 41, 174, 324, 329, 312]. As discussed above, while it has been shown that the pixellon model reproduces important features of the VZ effect (such as the angular correlations), the physical equivalence in all aspects of the interferometer observable has not been shown, and is the subject of ongoing, first-principles calculations. We plan to update observational signatures as the theoretical modeling captures more aspects of the first-principles calculations.

With this caveat in mind, the chapter is organized as follows. In Sec. 5.2, we briefly summarize the pixellon model of Refs. [328, 219]. In Sec. 5.3, we review a variety of proposed GW detectors following Ref. [20], and discuss their potential sensitivity to the geotropic signal. In Sec. 5.4, we extend the calculation of the pixellon PSD in Ref. [219] to more general interferometer-like experiments, particularly for those with geometries other than the traditional L-shape, and for optically-levitated sensors. In Sec. 5.5, we then apply the results to specific experiments and compare the geotropic signal to the expected strain sensitivities of these experiments. Finally, in Sec. 5.6, we collect our results and discuss their implications for the future of GW observation.

In anticipation of our main result, in Fig. 5.1, we plot the predicted pixellon signal alongside the strain sensitivities of two prominent next-generation GW detectors:

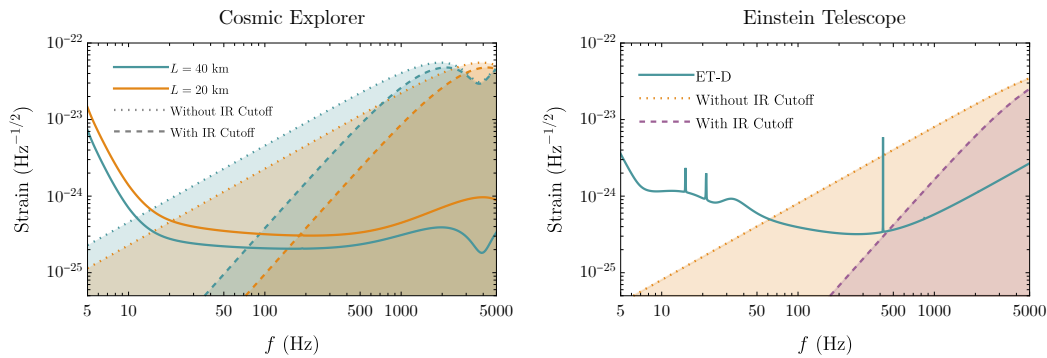


Figure 5.1: Pixellon strain (dashed and dotted lines) overlaid with the strain sensitivities for CE [291] and ET [193] (solid lines). For CE, we have included both designs with arm lengths $L = 20$ km (orange lines) and $L = 40$ km (blue lines). The dotted lines give the pixellon strain from Eq. (5.35) computed without an IR cutoff, and the dashed lines give the same quantity including the IR cutoff from Eq. (5.28). The pixellon strain is computed with the benchmark value $\alpha = 1$.

Cosmic Explorer (CE) [137, 291] and the Einstein Telescope (ET) [193]. From these plots, we find a typical geontropic signal exceeds the strain sensitivities of these detectors by two orders of magnitude over a wide range of frequencies. As such, the signal represents a large stochastic background which, if present, would imply a reevaluation of the future of GW astronomy. Moreover, we will show that of the experiments considered in this chapter, only CE and ET will have better sensitivity to the geontropic signal than GQuEST, which is a nearer-term apparatus than CE and ET.

5.2 Pixellon Model

In this section, we review the pixellon model proposed in Refs. [328, 219] to model the geontropic fluctuations of the spherical entangling surface bounding an interferometer, which is also a specialization of the dilaton model studied in Refs. [41, 174] to causal diamonds in 4-d flat spacetime. Before proceeding, we emphasize that while we expect the pixellon model to reproduce a number of the salient features of the effect proposed in Refs. [313, 314, 312, 41], the physical equivalence between the model and the complete theory remains to be shown. Demonstrating this physical equivalence will be crucial for claiming a decisive test of the VZ effect. More specifically, Ref. [219] considered a breathing mode of the metric associated with the spacetime volume probed by the interferometer,

$$ds^2 = -dt^2 + (1 - \phi)(dr^2 + r^2 d\Omega^2), \quad (5.2)$$

where ϕ is a bosonic scalar field,

$$\phi(x) = l_p \int \frac{d^3\mathbf{p}}{(2\pi)^3} \frac{1}{\sqrt{2\omega(\mathbf{p})}} \left(a_{\mathbf{p}} e^{ip \cdot x} + a_{\mathbf{p}}^\dagger e^{-ip \cdot x} \right), \quad (5.3)$$

and satisfies the dispersion relation of a sound mode,

$$\omega = c_s |\mathbf{p}|, \quad c_s = \sqrt{\frac{1}{3}}. \quad (5.4)$$

The dispersion relation in Eq. (5.4) and the normalization factor l_p in Eq. (5.3) were derived from plugging the metric in Eq. (5.2) into the linearized Einstein-Hilbert action [219]. The creation and annihilation operators ($a_{\mathbf{p}}^\dagger, a_{\mathbf{p}}$) satisfy the standard commutation relation,

$$\left[a_{\mathbf{p}_1}, a_{\mathbf{p}_2}^\dagger \right] = (2\pi)^3 \delta^{(3)}(\mathbf{p}_1 - \mathbf{p}_2). \quad (5.5)$$

Instead of being a vacuum state, ϕ is thermal with a nontrivial thermal density matrix ρ_{pix} [328, 219]:

$$\rho_{pix} = \frac{1}{\mathcal{Z}} \exp \left[-\beta \int \frac{d^3\mathbf{p}}{(2\pi)^3} (\epsilon_{\mathbf{p}} - \mu) a_{\mathbf{p}}^\dagger a_{\mathbf{p}} \right], \quad (5.6)$$

$$\mathcal{Z} = \prod_{\mathbf{p}} \frac{1}{1 - e^{-\beta(\epsilon_{\mathbf{p}} - \mu)}}, \quad (5.7)$$

where $\epsilon_{\mathbf{p}}$ is the energy of the pixellon mode of momentum \mathbf{p} , and μ is the chemical potential counting the background degrees of freedom. In this case, the pixellon modes ϕ have an occupation number given by the standard bosonic statistics, *i.e.*,

$$\begin{aligned} \text{Tr} \left(\rho_{pix} a_{\mathbf{p}_1}^\dagger a_{\mathbf{p}_2} \right) &= (2\pi)^3 \sigma_{pix}(\mathbf{p}_1) \delta^{(3)}(\mathbf{p}_1 - \mathbf{p}_2), \\ \sigma_{pix}(\mathbf{p}) &= \frac{1}{e^{\beta(\epsilon_{\mathbf{p}} - \mu)} - 1}. \end{aligned} \quad (5.8)$$

To further simplify the occupation number $\sigma_{pix}(\mathbf{p})$, Refs. [328, 219] used that in flat spacetime, the modular Hamiltonian K inside a causal diamond satisfies [313, 41]

$$\langle K \rangle \sim \langle \Delta K^2 \rangle \sim \frac{A(\Sigma)}{l_p^2}, \quad (5.9)$$

and similar results in AdS were found in Refs. [314, 118, 246]. Since the number of gravitational degrees of freedom \mathcal{N} inside the causal diamond is given by

$$\mathcal{N} \equiv \langle K \rangle, \quad (5.10)$$

the energy fluctuation per degree of freedom is given by [328, 219]

$$\beta(\epsilon_{\mathbf{p}} - \mu) \equiv \beta\omega(\mathbf{p}) \sim \frac{\sqrt{\langle \Delta K^2 \rangle}}{\langle K \rangle} \sim \frac{l_p}{L}. \quad (5.11)$$

If one uses Eq. (5.11), identifies $\omega(\mathbf{p}) \sim \frac{1}{L}$, and expands $\sigma_{\text{pix}}(\mathbf{p})$ in Eq. (5.8) to leading order in $\frac{l_p}{L}$, one finds

$$\sigma_{\text{pix}}(\mathbf{p}) = \frac{a}{l_p \omega(\mathbf{p})}, \quad (5.12)$$

where a is a dimensionless number, to be fixed by experiment. In Eq. (5.11), $\beta \sim l_p$ corresponds to the local temperature of the near-horizon region probed by the light beams. Comparing the pixellon model here to Refs. [313, 314, 328] and incorporating ϕ as a sound mode [*i.e.*, Eq. (5.4)], Ref. [219] fixed $a = c_s^2/(2\pi)$, which corresponds to $\beta = 2\pi l_p/c_s^2$. Defining

$$\alpha \equiv \frac{2\pi}{c_s^2} a, \quad (5.13)$$

we obtain the theory-motivated benchmark for detection $\alpha \sim 1$.

In Ref. [219], the pixellon model was used to compute the auto-correlation function of length fluctuations of a single Michelson interferometer with length L and separation angle θ . It was found that the peak of the signal is at $\omega L \sim 1$ with an overall amplitude $\sqrt{\langle \Delta L^2 \rangle} \sim \sqrt{l_p L}$. Moreover, the angular correlations from the pixellon model match well with the predictions of Refs. [313, 312] from shockwave geometry. The peak frequency $\omega_{\text{peak}} \sim \frac{1}{L}$ is consistent with both the identification $\omega(\mathbf{p}) \sim \frac{1}{L}$ made by Eq. (5.12) and the pixellon mode being a breathing mode controlling the size of the spherical entangling surface bounding the interferometer. From this typical frequency and the strain's amplitude, one can directly see that for a general detector probing a causal diamond of size L , we need a strain sensitivity $\sqrt{S_h(f)} \lesssim \sqrt{\omega_{\text{peak}} \langle \Delta L^2 \rangle} \sim \sqrt{l_p} \sim 10^{-23} \text{ Hz}^{-1/2}$ near the frequency $\omega_{\text{peak}} \sim \frac{1}{L}$, where $S_h(f)$ is the one-sided noise strain defined in Eq. (5.34). Most current interferometers, especially those aiming for GW detection, do not have such good strain sensitivity near the free spectral range, which is a higher frequency than is probed by many interferometers. Thus, we would first like to investigate whether other types of high-frequency GW detectors, besides the next-generation interferometers, can potentially detect geotropic signals.

5.3 High-Frequency GW Detectors

This section follows the review in Ref. [20] to investigate a broad class of high-frequency GW detectors with various operating principles. To understand how

the detection of geotropic fluctuations fits in this landscape, we first discuss the proposed scientific goals of these high-frequency GW detectors. Most current proposals intend to probe astrophysical objects in unexplored limits, or test quantum gravity near highly curved spacetime. In contrast, the effect considered in Refs. [313, 314, 328, 41, 174, 312, 329, 219, 324] and this work fills the gap of examining quantum gravity in flat spacetime. Moreover, the necessary sensitivity and frequency range are within the same regime as other science cases, so utilizing these detectors for geotropic signals is natural. In the second half of this section, we examine these detectors' suitabilities for measuring geotropic fluctuations and argue that interferometer-like experiments are the most optimal.

Sources of High-frequency GWs

Since the successful detection of GWs by the LIGO-Virgo collaboration [13], there have been continuous efforts to improve the sensitivity of GW detectors at higher frequencies. One direct motivation for this is to study extreme astrophysical objects in limits or environments which cannot be reached by current GW detectors. For example, the merger of sub-solar mass primordial BHs of 10^{-9} – $10^{-1} M_{\odot}$ can emit GWs with frequencies of 10 – 10^9 kHz [20]. For neutron stars (NSs), the remnant hot, high-density matter after their merger can generate GWs at either ~ 1 – 4 kHz [128] for a BH remnant or $\gtrsim 6$ kHz [286, 38] for an NS remnant [16]. These high-frequency GWs provide opportunities to study different phases of matter predicted by quantum chromodynamics in a high-density finite-temperature environment [45]. At larger scales, high-frequency GW detectors will assist in learning about GWs emitted by the thermal plasma of the early universe [157] (1 – 100 GHz), the stochastic GW background generated by primordial BHs [31] (10 – 10^{10} THz), cosmic strings [207] (1 – 10^6 kHz), and other events at cosmological scales [20].

One vital application of these high-frequency GW detectors is to explore quantum gravity, the central focus of this work. Standard tests of quantum gravity using GWs focus on examining the properties of quantum BHs against their classical counterparts. For example, GW detections have been used to test the no-hair theorem [197], stating that any classical stationary BH (a solution to the Einstein-Maxwell equation) is characterized only by its mass, charge, and angular momentum [241]. Still, quantum gravity might dress BHs with hair [163, 50]. The spectrum of GWs can also serve as a test of the horizon's existence [231, 127], where quantum gravity can modify the structure of the near-horizon geometry [162], either drastically via a "firewall" hiding all quantum effects [29], or smoothly with the quantum effects

extending over some distance around the BH [161].

Unlike these standard tests, the series of works in Refs. [313, 314, 328, 41, 174, 312, 329, 219, 324] instead focus on perturbations of the near-horizon geometry of causal diamonds in flat spacetime due to quantum gravity, which the pixellon models as an effective description. As introduced in Secs. 2.1 and 5.2 and shown in detail in Sec. 5.5, the length fluctuations induced by the pixellon in an L-shaped interferometer of length L have a size of $\sqrt{\langle \Delta L^2 \rangle} \sim \sqrt{l_p L}$ and a peak frequency at $\omega L \sim 1$, corresponding to a PSD with an amplitude of $\sim \sqrt{c l_p}$. For an interferometer, or, more generally, a causal diamond with characteristic size $L \sim 10 \text{ m} - 10 \text{ km}$, we need a strain sensitivity of $\sim 10^{-23} \text{ Hz}^{-1/2}$ at the peak frequencies of $\frac{1}{L} \sim \text{kHz} - \text{MHz}$, which is within the target sensitivity of many high-frequency GW detectors. Thus, these high-frequency GW detectors planned for various purposes can also be used to test quantum gravity in flat spacetime, which motivates our following investigation.

Detectors for High-frequency GWs

Interferometers

The most natural GW detectors to consider are the next-generation interferometers, such as CE [137, 291], ET [136], and NEMO [16], for which the pixellon model was designed to describe the geotropic fluctuations. Although CE and ET are not usually considered high-frequency detectors but instead broadband detectors, they can access frequencies of a few kHz, which are near their free spectral range. For a single interferometer, the causal diamond is naturally defined by the light beams traveling between the mirrors, with its size equal to the interferometer's arm length. Perturbations to the spherical entangling surface bounding the interferometer are then controlled by the pixellon mode. Although the metric in Eq. (5.2) is not spherically symmetric due to the nontrivial angular dependence of $\phi(x)$, its spatial part is conformal to the metric of a 3-ball, adapting to the spherical symmetry of an interferometer.

The pixellon model and the procedure to compute length fluctuations can be extended to alternative configurations of Michelson interferometers, such as the triangular configuration of ET. In Ref. [219], the PSD and the angular correlations of a single L-shaped interferometer with an arbitrary separation angle were computed. In Sec. 5.4, we further show that the previous results can be extended to multiple interferometers if we consistently correlate pixellons in different causal diamonds. The cross-correlations of different interferometers can then be studied, becoming

a smoking gun signature of geotropic signals. Another advantage of studying cross-correlations between detectors is that the cross spectrum of a correlated noise background between different detectors can be detected at a level much lower than their individual independent noise spectra [28].

One fundamental barrier for an interferometer to reach the high-frequency regime is the quantum shot noise of lasers (or the high uncertainty of the laser’s phase quadrature). The most direct solution to this limitation is to increase the laser power P_{arm} , since the PSD of the quantum noise at high frequencies is proportional to $P_{\text{arm}}^{-1/2}$ [232], which is the approach adopted by NEMO [16]. However, increasing laser power is technically challenging, with issues such as the parametric instability of the mirrors’ motion due to energy transfer from the light beams [138] or the thermal deformation of the mirrors [137, 72].

Besides increasing laser power, one can also inject squeezed vacuum into the dark port of the interferometer, leading to a reduced phase uncertainty at the cost of sacrificing the sensitivity at low frequencies [137]. Nonetheless, Refs. [220, 317] recently proposed that one can connect a quantum parametric amplifier to the interferometer to stabilize the “white-light cavity” design in Ref. [237], such that the sensitivity at kHz frequencies can be increased without sacrificing the bandwidth.

In addition, for detecting a stochastic background like the geotropic signal, which is spatially correlated for two physically overlapping interferometers, a cross-correlation method can be established for each individual detector to dig under shot noise [233]. This allows us to achieve a better sensitivity than each detector’s noise budget for detecting gravitational waves.

Another way to circumvent quantum shot noise is using photon counting instead of the standard homodyne readout [235]. Such a readout will be implemented in a proposed 5 m tabletop interferometer being commissioned by Caltech and Fermilab under the Gravity from the Quantum Entanglement of Space-Time (GQuEST) collaboration [236], which will explicitly target geotropic fluctuations. By employing photon counting and thereby beating the standard quantum limit, GQuEST will be able to place constraints on α substantially more efficiently in terms of integration time than it would with only a homodyne readout. For a detailed examination of the advantages of photon counting, see Ref. [235]. As GQuEST is a tabletop-sized experiment, it will also be capable of probing the angular correlations of the geotropic fluctuations by adjusting its arm angle. Moreover, it is conceived to be a nearer-term instrument than third generation GW detectors such as CE and ET. As

such, should the geontropic signal be detected with GQuEST, this information can be incorporated into the design and planning of future GW detectors, whose strain sensitivities to astrophysical signals might be limited by a geontropic background.

Optically-levitated Sensors

Besides interferometers, there are other high-frequency GW detectors that operate like an interferometer, such as the optically-levitated sensor described in Refs. [33, 21]. The optically-levitated sensor functions by trapping a dielectric sphere or microdisk in an anti-node of an optical cavity (see Fig. 5.6) [33]. One can also build a Michelson interferometer from optically-levitated sensors by inserting the sensors in each arm's cavity (see Fig. 5.7) [21]. As illustrated in Sec. 5.5, one optically-levitated sensor can be effectively treated as two aligned interferometer arms, where the longer arm has the same length ℓ_m as the cavity. The shorter arm has length x_s , the distance to a chosen anti-node of the trapping field. The optically-levitated sensor measures the differential distance change $\delta\ell_m - \delta x_s$, the correlations of which are similar to an interferometer of length $L = \ell_m - x_s$, but not identical since the two arms have to be treated separately. Moreover, as depicted in Fig. 5.7, there are two causal diamonds enclosing the shorter and longer arms, respectively. In Sec. 5.4, we show how to consistently correlate these multiple causal diamonds.

Levitated sensors achieve their gain in sensitivity by making the test masses respond resonantly to gravitational waves whose frequencies match the test masses' natural oscillation frequency in the trapping potential. In the devices considered by Refs. [33, 21], sensitivities are mainly constrained by the thermal noise due to heating of the sensor by the scattering light [21]. The development of techniques to reduce the thermal noise of an optically-trapped object in many other contexts thus allows a better strain sensitivity for the optically-levitated sensor at high frequencies compared to an interferometer [33]. It was further found in Ref. [21] that by using stacked disks as the sensor, the thermal noise due to photon recoiling can be further reduced. In addition, the high-frequency performance of the levitated sensor is further enhanced by its tunability. Indeed, the experiment achieves its peak strain sensitivity when the trapped object is resonantly excited at the trapping frequency, which is widely tunable via laser intensity [21]. In Sec. 5.5, we will compare the PSD of length fluctuations measured by the optically-levitated sensor to its predicted strain sensitivity from Ref. [21].

Inverse-Gertsenshtein Effect and Other Experiments

Apart from interferometer-like experiments, there are other high-frequency GW detectors with different working principles. One major class of such experiments uses the inverse-Gertsenshtein effect, which converts gravitons to electromagnetic (EM) waves [156]. For most of these experiments, strong static magnetic fields of several Tesla are used to convert gravitons into photons [20]. Many of these experiments have been designed to detect ultralight axion dark matter, which can also couple to the EM fields, such as the ones using microwave cavities (*e.g.*, ADMX [44], HAYSTAC [326], and SQMS [160]) or pickup circuits (*e.g.*, ABRACADABRA [205] and SHAFT [167]) to receive the signal. Refs. [130, 49, 119] found that some of these experiments might be sensitive to high-frequency GWs, especially when the geometry of the detector reflects the spin-2 nature of gravitons. For example, Ref. [119] found that a figure-8 pickup circuit has a much larger sensitivity than a circular loop. For microwave cavities, if the resonant cavity modes have the same spatial profile as the effective current generated by the inverse-Gertsenshtein effect, there is also a boost of the signal [49].

The pixellon model considered in Refs. [328, 219] and this work can be, in principle, used to compute the inverse-Gertsenshtein effect since geotropic fluctuations manifest themselves as metric fluctuations, *i.e.*, Eq. (5.2). However, in most available calculations, the response to GWs has only been calculated in the transverse-traceless (TT) gauge or the proper detector frame. Moreover, some of these calculations were not careful with gauge invariance. It was recently shown in Ref. [49] that if one incorporates all the physical effects (such as circuits' motion due to coordinate transformation), the observables, such as current density, are gauge invariant. Nonetheless, this proof was done by explicitly computing the observables in these two specific frames without incorporating all possible coordinate transformations.

Such a calculation is usually sufficient for GW detections, but not geotropic fluctuations. First, since geotropic fluctuations have a typical wavelength of the system's size, the long wavelength assumption of the expansion used in the proper detector frame doesn't apply. Second, geotropic fluctuations are not solutions to the vacuum linearized Einstein equations. They cannot be transformed into the TT gauge, despite Eq. (5.2) being similar to TT gauge, where only light propagation needs to be considered. Thus, one has to be more generous with the frame choices and show that the observables in this type of experiment are invariant under all possible gauge transformations, as Ref. [219] demonstrated for length fluctuations

in interferometers.

A more fundamental question is whether the pixellon model is appropriate for describing this type of experiment, especially those using microwave cavities. The pixellon model was designed to effectively describe gravitational perturbations of the spherical entangling surface bounding the interferometer, a spatial slice of the causal diamond defined by the light beams. Within the cavity, there is no freely propagating photon, so the detector doesn't probe the near-horizon geometry of any causal diamond. In this case, the pixellon model might not be a good effective description, and geotropic fluctuations might be negligible since they are driven by near-horizon dynamics [41]. Note that the photon counting technique in Ref. [235] also detects the excess photons generated by gravitational perturbations. However, this readout is still embedded in a Michelson interferometer, so there is a well-defined causal diamond.

Besides the experiments above, other types of high-frequency GW detectors are discussed in Ref. [20], such as the bulk acoustic wave devices [165], which operate like a resonant mass bar [319] and measure the vibration of piezoelectric materials due to passing GWs. Similarly, GWs can also deform microwave cavities, which couple different resonant cavity modes and can be detected [92]. There are also experiments utilizing the coupling between GWs and electron spin, where the collective electron spin excitations or magnons of ferromagnetic crystals due to GWs are measured [198, 199]. Since no causal diamond is being probed in all of these experiments, geotropic signals might be minimal. For this reason, for the rest of this work, we focus on these interferometer-like experiments and calculate their sensitivity to the pixellon model.

5.4 Extension of the Pixellon Model to Multiple Interferometers

In this section, we extend the calculation in Ref. [219] of the auto-correlation of a single interferometer's length fluctuations to the cross-correlation of two interferometer-like detectors, which may have different arm lengths and origins.

As shown in Ref. [219], for the metric in Eq. (5.2), the only nonzero component in the $t - r$ sector of the metric is h_{rr} , so we only need to consider light propagation when computing length fluctuations. For a light beam sent at time $t - L$ from the origin \mathbf{x} along the direction \mathbf{n} , the total time delay $T(t, \mathbf{n})$ of a round trip is given

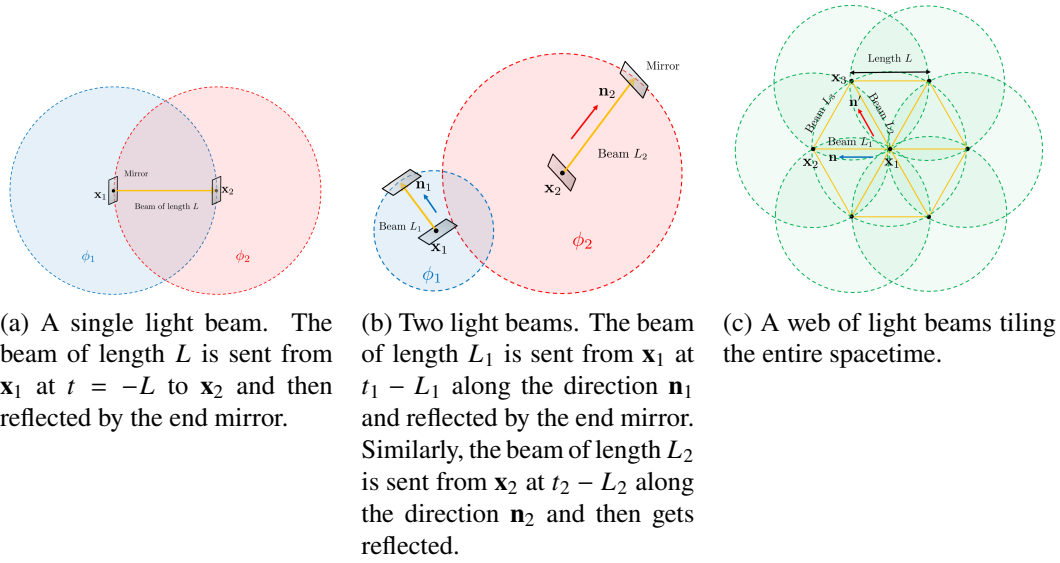


Figure 5.2: Plots of spherical entangling surfaces or spatial slices of the causal diamonds bounding different configurations of light beams. The shaded circles represent entangling surfaces, each of which is associated with a pixellon model. For all the figures above, we have projected the spherical entangling surface to the plane of the light beams.

by ¹

$$T(t, \mathbf{x}, \mathbf{n}) = 2L - \frac{1}{2} \int_0^L dr [\phi(x) + \phi(x')],$$

$$x \equiv (t - L + r, \mathbf{x} + r\mathbf{n}), \quad x' \equiv (t + L - r, \mathbf{x} + r\mathbf{n}). \quad (5.14)$$

Notice that although Eq. (5.14) has an explicit dependence on the origin \mathbf{x} , the auto-correlation function of T or its fluctuations doesn't depend on \mathbf{x} , as shown in Ref. [219] and Eq. (5.32). This indicates that geotropic fluctuations are physical, since they don't depend on the choice of coordinates.

Next, let us consider two light beams sent at times $t_1 - L_1$ and $t_2 - L_2$ from positions \mathbf{x}_1 and \mathbf{x}_2 along directions \mathbf{n}_1 and \mathbf{n}_2 , respectively, as depicted in Fig. 5.2b. We also assume the lengths of the two beams without any geotropic fluctuations to be L_1 and L_2 , respectively. Then the correlation function of the length fluctuations δT of these two beams is

$$C(\Delta t, \Delta \mathbf{x}, \mathbf{n}_{1,2}) \equiv \left\langle \frac{\delta T(t_1, \mathbf{x}_1, \mathbf{n}_1) \delta T(t_2, \mathbf{x}_2, \mathbf{n}_2)}{4L_1 L_2} \right\rangle,$$

$$\Delta t \equiv t_1 - t_2, \quad \Delta \mathbf{x} \equiv \mathbf{x}_1 - \mathbf{x}_2, \quad (5.15)$$

¹We have corrected a typo in Ref. [219], where the sign before the integral should be minus.

where we have defined $\delta T(t, \mathbf{x}, \mathbf{n}) = T(t, \mathbf{x}, \mathbf{n}) - 2L$ with $T(t, \mathbf{x}, \mathbf{n})$ given in Eq. (5.14). Here, we have assumed that the origins of the light beams enter the cross-correlation function only via their difference $\Delta \mathbf{x}$, so it is independent of the choice of coordinates. We will see this assumption is true in Eq. (5.27).

Since these two light beams are enclosed by two different causal diamonds as shown in Fig. 5.2b, their length fluctuations are separately described by two pixellon models with the metric in Eq. (5.2) centered at \mathbf{x}_1 and \mathbf{x}_2 , respectively. To distinguish these two pixellon models, we assign $\phi_1(x)$ and $\phi_2(x)$ to the first and the second beams, respectively. Within each pixellon model, the length fluctuations are still described by Eq. (5.14), so

$$C(\Delta t, \Delta \mathbf{x}, \mathbf{n}_{1,2}) = \frac{1}{16L_1L_2} \int_0^{L_1} dr_1 \int_0^{L_2} dr_2 \langle (\phi_1(x_1) + \phi_1(x'_1)) (\phi_2(x_2) + \phi_2(x'_2)) \rangle, \quad (5.16)$$

which is in a similar form as Eq. (32) of Ref. [219]. For convenience, let us define

$$C(x_1, x_2) = \langle (\phi_1(x_1) + \phi_1(x'_1)) (\phi_2(x_2) + \phi_2(x'_2)) \rangle. \quad (5.17)$$

To evaluate $C(x_1, x_2)$, we first need to compute $\langle \phi_1(x_1) \phi_2(x_2) \rangle$, where x_1 and x_2 are in two different causal diamonds. From Eqs. (5.3) and (5.4), we notice that both ϕ_1 and ϕ_2 satisfy the wave equation, as constrained by the linearized Einstein-Hilbert action [219]. Thus, ϕ_1 has translational symmetry, *i.e.*, $\phi_1(y) = e^{-ip \cdot (x-y)} \phi_1(x)$ classically, and similarly for ϕ_2 . This implies that although the metric in Eq. (5.2) effectively describes the length fluctuations of a finite-size interferometer, nothing prevents us from propagating the pixellon field $\phi(x)$ to places outside the interferometer. This is also consistent with the fact that ϕ has modes with long wavelengths, as imposed by Eq. (5.12). Thus, ϕ_1 is well-defined in the causal diamond of ϕ_2 , and vice versa.

To derive a precise relation between ϕ_1 and ϕ_2 , let us consider a single light beam sent from \mathbf{x}_1 at $t = -L$ to \mathbf{x}_2 , as depicted in Fig. 5.2a. To compute the round-trip time delay, one can either use the pixellon model centered at \mathbf{x}_1 with the pixellon ϕ_1 , or the one centered at \mathbf{x}_2 with the pixellon ϕ_2 . For the former case, we set the origin of the coordinates at \mathbf{x}_1 and align the x -axis with the outgoing light beam, so the shift of the round-trip time delay δT_1 is given by Eq. (5.14),

$$\begin{aligned} \delta T_1 &= -\frac{1}{2} \int_0^L dr [\phi_1(x) + \phi_1(x')] , \\ x_1 &= (-L + r, r\hat{\mathbf{x}}) , \quad x'_1 = (L - r, r\hat{\mathbf{x}}) , \end{aligned} \quad (5.18)$$

where the first and second terms correspond to the time delay of the outgoing and ingoing light beams, respectively.

For the latter case, we set the origin at \mathbf{x}_2 and align the x -axis with the ingoing light beam. Notice the ingoing beam here is the outgoing beam for the pixellon model at \mathbf{x}_1 , and vice versa. Then, δT_2 is given by

$$\begin{aligned}\delta T_2 &= -\frac{1}{2} \int_{-L}^0 dr [\phi_2(x) + \phi_2(x')] , \\ x_2 &= (r, r\hat{\mathbf{x}}), \quad x'_2 = (-r, r\hat{\mathbf{x}}),\end{aligned}\tag{5.19}$$

where the first and second terms correspond to the time delay of the ingoing and outgoing light beams, respectively. One can further make a change of variables $\tilde{r} = r + L$ and shift the coordinates, $\mathbf{x} \rightarrow \mathbf{x} + L\hat{\mathbf{x}}$, such that

$$\begin{aligned}\delta T_2 &= -\frac{1}{2} \int_0^L dr [\phi_2(x) + \phi_2(x)] , \\ x_2 &= (-L + r, r\hat{\mathbf{x}}), \quad x'_2 = (L - r, r\hat{\mathbf{x}}),\end{aligned}\tag{5.20}$$

where we have replaced the symbol \tilde{r} with r at the end. Since $\delta T_1 = \delta T_2$, Eqs. (5.18) and (5.20) indicate that $\phi_1 = \phi_2$.

This relation between $\phi_{1,2}$ does not hold only for these two causal diamonds, but rather the entire spacetime. One can easily see this by tiling the entire spacetime with light beams of the same length L as depicted in Fig. 5.2c. One can repeat the same argument above for every segment of this web of null rays to relate the pixellon models centered at any two adjacent endpoints. Since all of these null rays are connected, one can easily show a universal ϕ across the entire spacetime within the pixellon model. Thus, there is no need to distinguish ϕ in different causal diamonds.

On the other hand, this does not indicate that we can avoid using separate pixellon models for different light beams. The metric in Eq. (5.2) is designed to effectively describe the geotropic fluctuations of any causal diamond located at the origin of the local coordinates picked out by the metric. Thus, the light beams not propagating in the radial direction in these local coordinates cannot be described by the associated pixellon model. Furthermore, the argument of gauge invariance of the calculations in Ref. [219] does not hold for these non-radial light beams, since the angular directions of the metric were ignored in the proof. Nonetheless, one can always find another causal diamond in which the originally non-radial light beam becomes

radial, *e.g.*, the causal diamond located at the endpoints of this beam. For example, in Fig. 5.2c, the beams L_1 and L_2 can be described by the pixellon model centered at \mathbf{x}_1 , but not the beam L_3 , although it is in the same causal diamond of the beams $L_{1,2}$. Instead, one should compute the length fluctuations of the beam L_3 using the pixellon models at \mathbf{x}_2 or \mathbf{x}_3 .

One might also worry, in this case, whether the length fluctuations at \mathbf{x}_1 have multiple inconsistent descriptions dependent on the causal diamond we choose, particularly with respect to their angular correlations. For example, since the dominant modes of pixellons are low- l modes [219], the pixellon model at \mathbf{x}_2 constrains the fluctuations at \mathbf{x}_1 to be mostly along \mathbf{n} . However, if one uses the pixellon model at \mathbf{x}_3 , the fluctuations at \mathbf{x}_1 are mainly along \mathbf{n}' . This is not a contradiction in the pixellon model since light beams in different directions are probing different ‘‘polarizations’’ of pixellons, which control different local entangling surfaces. If one goes to the causal diamond at \mathbf{x}_1 , the pixellon model consistently predicts that most fluctuations are along the radial direction, so fluctuations along both \mathbf{n} and \mathbf{n}' can potentially be excited. When the light beam is sent along one of these directions, the spherical symmetry is broken by exciting fluctuations mainly in this specific direction.

In this case, to compute the correlation of any two beams as depicted in Fig. 5.2b, we use the metric in Eq. (5.2) centered at \mathbf{x}_1 for beam L_1 and the one at \mathbf{x}_2 for beam L_2 , but do not distinguish ϕ in these two metrics. Thus, Eq. (5.17) becomes

$$C(x_1, x_2) = \langle (\phi(x_1) + \phi(x'_1))(\phi(x_2) + \phi(x'_2)) \rangle. \quad (5.21)$$

Using Eq. (5.3), we get

$$\begin{aligned} C(x_1, x_2) &= 4l_p^2 \int \frac{d^3 \mathbf{p}_1}{(2\pi)^3} \int \frac{d^3 \mathbf{p}_2}{(2\pi)^3} \frac{1}{\sqrt{4\omega_1(\mathbf{p}_1)\omega_2(\mathbf{p}_2)}} \\ &\quad \cos[\omega_1(L_1 - r_1)] \cos[\omega_2(L_2 - r_2)] \left[\langle a_{\mathbf{p}_1} a_{\mathbf{p}_2}^\dagger \rangle \right. \\ &\quad \left. e^{-i[\omega_1 t_1 - \omega_2 t_2 - \mathbf{p}_1 \cdot (\mathbf{x}_1 + r_1 \mathbf{n}_1) + \mathbf{p}_2 \cdot (\mathbf{x}_2 + r_2 \mathbf{n}_2)]} + c.c. \right], \\ &= 4l_p^2 \int \frac{d^3 \mathbf{p}}{(2\pi)^3} \frac{\sigma_{\text{pix}}(\mathbf{p})}{2\omega(\mathbf{p})} \cos[\omega(L_1 - r_1)] \\ &\quad \cos[\omega(L_2 - r_2)] \left[e^{-i\omega \Delta t + i\mathbf{p} \cdot \delta \mathbf{x}} + c.c. \right], \end{aligned} \quad (5.22)$$

where we have defined

$$\delta \mathbf{x} \equiv \Delta \mathbf{x} + r_1 \mathbf{n}_1 - r_2 \mathbf{n}_2. \quad (5.23)$$

Plugging the occupation number in Eq. (5.12), the correlation function of the length fluctuations is given by

$$\begin{aligned}
& C(\Delta t, \Delta \mathbf{x}, \mathbf{n}_{1,2}) \\
&= \frac{al_p}{8L_1L_2} \int_0^{L_1} dr_1 \int_0^{L_2} dr_2 \int \frac{d^3\mathbf{p}}{(2\pi)^3} \frac{1}{\omega^2(\mathbf{p})} \\
&\quad \cos[\omega(L_1 - r_1)] \cos[\omega(L_2 - r_2)] e^{-i\omega\Delta t + i\mathbf{p}\cdot\delta\mathbf{x}},
\end{aligned} \tag{5.24}$$

where we have dropped the *c.c.* term and hereafter assume for simplicity that the complex conjugate is included implicitly.

Eq. (5.24) is very similar to Eq. (41) of Ref. [219], except that $\delta\mathbf{x}$ also contains the difference between the origins of the two light beams. Evaluating the angular part of the momentum integral, we have

$$\begin{aligned}
& C(\Delta t, \Delta \mathbf{x}, \mathbf{n}_{1,2}) \\
&= \frac{al_p}{16\pi^2 c_s^3 L_1 L_2} \int_0^{L_1} dr_1 \int_0^{L_2} dr_2 \int_0^\infty d\omega \\
&\quad \cos[\omega(L_1 - r_1)] \cos[\omega(L_2 - r_2)] \\
&\quad \text{sinc}[\omega\mathcal{D}(r_{1,2}, \Delta \mathbf{x}, \mathbf{n}_{1,2})/c_s] e^{-i\omega\Delta t},
\end{aligned} \tag{5.25}$$

with

$$\mathcal{D}(r_{1,2}, \Delta \mathbf{x}, \mathbf{n}_{1,2}) = |\delta\mathbf{x}|. \tag{5.26}$$

The PSD $\tilde{C}(\omega, \Delta \mathbf{x}, \mathbf{n}_{1,2})$ is then given by

$$\begin{aligned}
& \tilde{C}(\omega, \Delta \mathbf{x}, \mathbf{n}_{1,2}) \\
&= \frac{al_p}{8\pi c_s^3 N} \int_0^{L_1} dr_1 \int_0^{L_2} dr_2 \cos[\omega(L_1 - r_1)] \\
&\quad \cos[\omega(L_2 - r_2)] \text{sinc}[\omega\mathcal{D}(r_{1,2}, \Delta \mathbf{x}, \mathbf{n}_{1,2})/c_s],
\end{aligned} \tag{5.27}$$

where we have absorbed the normalization L_1L_2 into N . We make this redefinition for convenience since in certain experiments discussed later, PSDs similar to Eq. (5.27) appear but with $N \neq L_1L_2$. If we also insert an IR cutoff $\omega^2(\mathbf{p}) \rightarrow \omega^2(\mathbf{p}) + \omega_{\text{IR}}^2$ in Eq. (5.24) similar to Ref. [313], it was found in Ref. [219] that

$$\tilde{C}(\omega, \Delta \mathbf{x}, \mathbf{n}_{1,2}) \rightarrow \frac{\omega^2}{\omega^2 + \omega_{\text{IR}}^2} \tilde{C}(\omega, \Delta \mathbf{x}, \mathbf{n}_{1,2}). \tag{5.28}$$

In the case that the two arms have the same length L , Ref. [219] fixed $\omega_{\text{IR}} = \frac{1}{L}$, which gave a better agreement with the angular correlations predicted in Refs. [313, 312].

One direct application of the results above is to compute the cross-correlation of length fluctuations across two different interferometers. Let the origins of two interferometers be at $\mathbf{x}_{I,II}$, respectively. For the interferometer at \mathbf{x}_I , let its two arms be along the directions $\mathbf{n}_{1,2}$ with length L_I . Similarly, let the two arms of the interferometer at \mathbf{x}_{II} be along the directions $\mathbf{n}_{3,4}$ with length L_{II} . Define $\mathcal{T}(\mathbf{x}, t)$ to be the difference of length fluctuations of two arms within a single interferometer at position \mathbf{x} , the light beams of which are sent at time t . Then the cross-correlation of the time difference across two arms is

$$\begin{aligned} C_{\mathcal{T}}(\Delta t, \Delta \mathbf{x}, \mathbf{n}_{I,II}) &\equiv \left\langle \frac{\mathcal{T}_I(\mathbf{x}_I, t_1) \mathcal{T}_{II}(\mathbf{x}_2, t_2)}{4L_I L_{II}} \right\rangle, \\ \mathcal{T}_I(\mathbf{x}_I, t_1) &= \delta T(t_I, \mathbf{x}_I, \mathbf{n}_2) - \delta T(t_I, \mathbf{x}_I, \mathbf{n}_1), \\ \mathcal{T}_{II}(\mathbf{x}_{II}, t_2) &= \delta T(t_{II}, \mathbf{x}_{II}, \mathbf{n}_4) - \delta T(t_{II}, \mathbf{x}_{II}, \mathbf{n}_3), \end{aligned} \quad (5.29)$$

where $\mathbf{n}_I = (\mathbf{n}_1, \mathbf{n}_2)$, $\mathbf{n}_{II} = (\mathbf{n}_3, \mathbf{n}_4)$, and $\Delta \mathbf{x} = \mathbf{x}_I - \mathbf{x}_{II}$ such that

$$\begin{aligned} &\tilde{C}_{\mathcal{T}}(\omega, \Delta \mathbf{x}, \mathbf{n}_{I,II}) \\ &= \tilde{C}(\omega, \Delta \mathbf{x}, \mathbf{n}_{1,3}) + \tilde{C}(\omega, \Delta \mathbf{x}, \mathbf{n}_{2,4}) \\ &\quad - \tilde{C}(\omega, \Delta \mathbf{x}, \mathbf{n}_{1,4}) - \tilde{C}(\omega, \Delta \mathbf{x}, \mathbf{n}_{2,3}). \end{aligned} \quad (5.30)$$

The equation above generally contains complicated geometric factors, and the integral within Eq. (5.25) cannot be easily evaluated for a generic geometry. Thus, we consider several specific configurations in the next section.

5.5 Interferometer-like Experiments

In this section, we apply the results of Sec. 5.4 to several types of interferometer-like experiments: a single L-shaped interferometer (*e.g.*, LIGO [234], CE [137, 291], NEMO [16]), the equilateral triangle configuration of multiple interferometers (*e.g.*, LISA [37], ET [193]), and optically-levitated sensors [33, 21].

Single L-shaped Interferometer

Ref. [219] calculated the auto-correlation of length fluctuations in an L-shaped interferometer due to geotropic fluctuations. In this case, we have $\mathbf{x}_I = \mathbf{x}_{II}$ and $\mathbf{n}_I = \mathbf{n}_{II}$, so we can set the origin of the coordinates to coincide with the beam splitter of the interferometer. Furthermore, we can align the x - y plane with the plane of the interferometer and choose the x -axis to be along the first arm of the interferometer. Then the whole configuration is determined by the separation angle θ between two arms. In this case, the first two terms are the same in Eq. (5.30) and

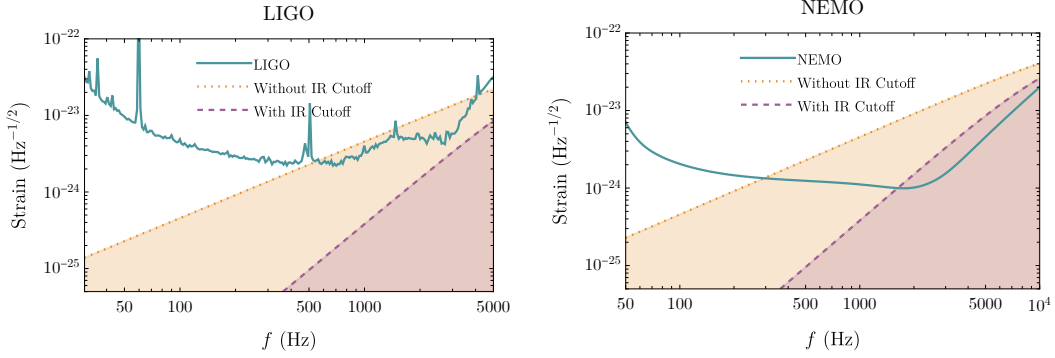


Figure 5.3: Pixellon strain (dashed and dotted lines) overlaid with the strain sensitivities for LIGO [234] and NEMO [222] (solid lines). The LIGO data was obtained from the Livingston detector, and the NEMO data omits suspension thermal noise. The dotted lines give the pixellon strain from Eq. (5.35) computed without an IR cutoff, and the dashed lines give the same quantity including the IR cutoff from Eq. (5.28). We again compute the pixellon strain with $\alpha = 1$.

similarly for the last two terms, so Eq. (5.30) reduces to

$$\tilde{C}_{\mathcal{T}}(\omega, \theta) = 2\tilde{C}(\omega, 0) - 2\tilde{C}(\omega, \theta), \quad (5.31)$$

which is consistent with Eq. (45) of Ref. [219]. The spectrum $\tilde{C}(\omega, \theta)$ is given by Eq. (5.27) after setting $L_1 = L_2 = L$, where L is the length of the interferometer, *i.e.*,

$$\begin{aligned} \tilde{C}(\omega, \theta) = \frac{al_p}{8\pi c_s^3 L^2} \int_0^L dr_1 \int_0^L dr_2 \operatorname{sinc} [\omega \mathcal{D}(r_1, r_2, \theta)/c_s] \\ \cos [\omega(L - r_1)] \cos [\omega(L - r_2)], \end{aligned} \quad (5.32)$$

where the distance factor \mathcal{D} is now completely determined by r_1 , r_2 , and θ ,

$$\mathcal{D}(r_1, r_2, \theta) = \sqrt{r_1^2 + r_2^2 - 2r_1 r_2 \cos \theta}. \quad (5.33)$$

To compare against the strain sensitivity of real experiments, one needs to first convert Eq. (5.32) to the one-sided noise strain S_h defined by Refs. [245, 96]

$$\sqrt{S_h(f)} = \sqrt{2 \int_{-\infty}^{\infty} \left\langle \frac{\Delta L(\tau)}{L} \frac{\Delta L(0)}{L} \right\rangle e^{-2\pi i f \tau} d\tau}, \quad (5.34)$$

which has units of $\text{Hz}^{-1/2}$. In many of these interferometers, Fabry-Pérot cavities are used to increase the sensitivity, in which light travels multiple round trips. By converting the strain sensitivity to the phase sensitivity, Ref. [219] showed that the

geotropic signal does accumulate in Fabry-Pérot cavities since the output is linear in the phase shift of the light. Thus, it is legitimate to compare our PSD to the strain sensitivity of these experiments. From Eqs. (5.29) and (5.34), Ref. [219] found that

$$\sqrt{S_h(f)} = \sqrt{2\tilde{C}_T(\omega, \theta)}. \quad (5.35)$$

Nonetheless, the signal's shape is determined by the geometry of one light-crossing. For example, we expect that the signal peak is at $\omega L \sim 1$, where L is the length of the interferometer instead of the total distance traveled across multiple light-crossings.

Using Eqs. (5.31)–(5.32), Ref. [219] computed the PSD of the pixellon model in several L-shaped interferometers (Holometer [96], GEO-600 [305], and LIGO [234]) and one set of interferometers in LISA [37], and compared the signal to their strain sensitivities. It was found that GEO-600 and LISA are unlikely to detect geotropic fluctuations due to their relatively low peak sensitivity (at $\omega L \sim 1$), while LIGO and Holometer respectively constrain the α -parameter to be $\alpha \lesssim 3$ and $\alpha \lesssim 0.7$ (with an IR cutoff), and $\alpha \lesssim 0.1$ and $\alpha \lesssim 0.6$ (without an IR cutoff) at 3σ significance. Note that the LIGO sensitivity data that we have used here and in Ref. [219] is that from Ref. [234] with the quantum shot noise removed (*i.e.*, the gray curve in Fig. 2 of Ref. [234]) by the quantum-correlation technique in Ref. [233]. Nonetheless, this technique only removes the expectation value of the shot noise but not its variance [321], limiting the extent to which we can dig under the shot noise. More specifically, with a frequency band of Γ and an integration time of T , we expect the noise suppression factor to be $\sim (\Gamma T)^{1/4}$ in amplitude—or until the next underlying noise is revealed. In the particular case of LIGO, that underlying noise includes coating and suspension thermal noise at low frequencies, and laser noise at high frequencies. Further studying these underlying noise sources in LIGO can in principle put more stringent upper limits on the geotropic noise.

Besides the GW detectors above, there are other future L-shaped interferometers to be considered but not included in Ref. [219]. The most important ones are the third-generation GW detectors: CE [137, 291] and ET [193]. CE is a ground-based broadband GW detector using dual-recycled Fabry-Pérot Michelson interferometers with perpendicular arms. CE will have two sites with several potential designs: a 20 km interferometer paired with a 40 km interferometer, or a pair of 20 km or 40 km interferometers. As largely a scale-up of Advanced LIGO [137], CE will operate at room temperature with a fused-silica coating of mirrors to reduce thermal noise, and degenerate optical parametric amplifiers injecting squeezed light with low phase uncertainty to reduce quantum noise (shot noise) at high frequency [310].

ET is an equilateral triangle configuration of three independent nested detectors, each of which contains two dual-recycled Fabry-Pérot Michelson interferometers with arms of length 10 km (plotted in Fig. 5.4) for low- and high-frequency detections, respectively. ET will be built underground to reduce seismic noise. Cryogenic systems are used to reduce thermal noise by cooling the optical systems to 10–20 K at low frequency, while squeezed light (frequency-dependent) is also inserted to reduce quantum noise at high frequency [136].

As briefly discussed in Sec. 2.1 and shown in Fig. 5.1, for the benchmark value $\alpha = 1$, the PSD of the geotropic signal overwhelms the strain sensitivity of CE and ET by about two orders of magnitude for $f \sim 1$ kHz. For CE, we have considered both the interferometers of length 20 km and 40 km. For ET, we have computed the auto-correlation of a single interferometer within the entire configuration. A study of the cross-correlation of different interferometers is carried out in Sec. 5.5.

Besides ET and CE, another next-generation GW detector is NEMO [16], a Michelson interferometer with perpendicular Fabry-Pérot arms of length 4 km. Although with less sensitivity than the full third-generation detectors in general, NEMO is important for testing technological developments to be used in the third-generation detectors while making interesting scientific discoveries, such as understanding the compositions of NSs. Due to its interest in binary NS mergers, NEMO specializes in high-frequency events with its optimal sensitivity at $f \sim 1\text{--}4$ kHz [16]. As plotted in Fig. 5.3, within the optimal sensitivity of NEMO, the geotropic signal exceeds the strain sensitivity by about one order of magnitude. Thus, the geotropic signal must be constrained before these next-generation GW detectors can detect other high-frequency events. For future detectors, we have compared the geotropic signal with their design sensitivities, without considering removal of shot noise via the quantum-correlation approach—even though at high frequencies, where the constraints for geotropic noise are the best, these detectors are limited by shot noise. It can be anticipated that at these frequencies, these detectors’ shot noise dominates over other types of noise by a significant factor. In this way, these detectors are capable of putting much more stringent bounds on the geotropic α parameter.

Equilateral Triangle Configurations

In this subsection, we consider configurations of multiple interferometers with certain geometries. For GW detections, these different geometries are helpful in retrieving the polarization of GWs. One important configuration is the equilateral

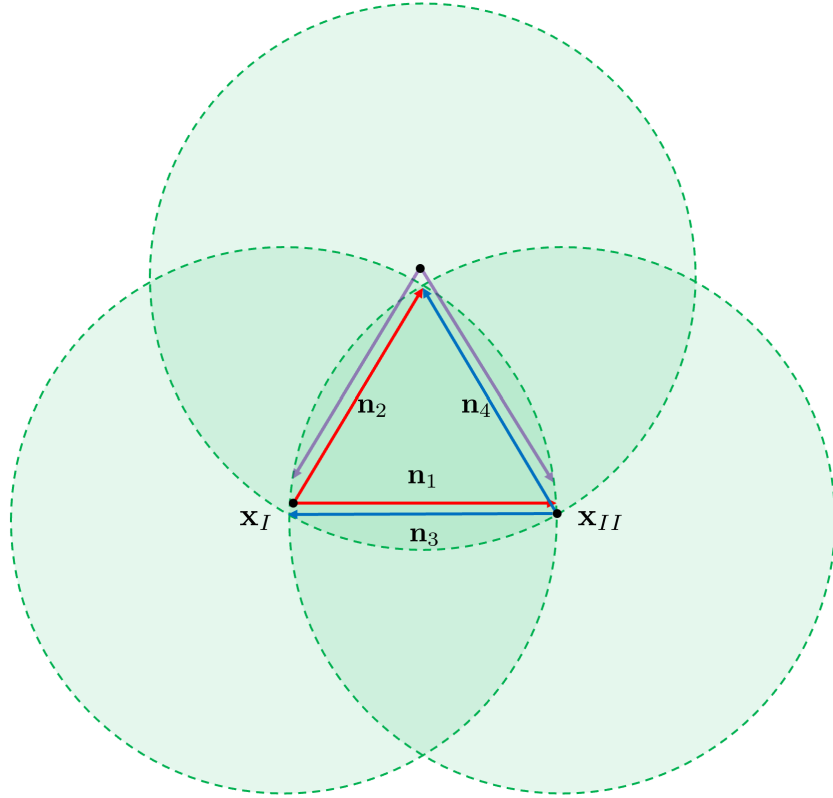


Figure 5.4: Setup of ET. The red, blue, and purple rays correspond to the three detectors in ET, where we have only shown one of the two interferometers within each detector. We choose not to plot the mirrors at the endpoints of the light beams for simplicity.

triangle configuration of three interferometer arms, such as LISA [37], or three partially overlapping independent detectors, such as ET [193], as shown in Fig. 5.4. For LISA, the signals of different arms can be time shifted and linearly combined to form virtual Michelson interferometers [153, 30]. Nonetheless, as found in Ref. [219] and discussed in Sec. 5.5, LISA is not promising for detecting geotropic signals, so we will focus on the specific configuration of ET.

In this subsection, we will study the cross-correlation of multiple detectors of ET. For stochastic wave backgrounds with completely random radiation, a single detector cannot distinguish the background from random instrumental noise within a short observing time unless the sources distribute anisotropically [304]. However, since the ET detectors occupy the same spatial region, geotropic fluctuations modeled by the pixellons are correlated between them. Assuming that the noises of different ET detectors are largely uncorrelated, cross-correlating multiple ET detectors allows us to dig under the noise with a suppression factor $\sim (\Gamma T)^{1/4}$, or until a correlated

noise background is reached [276, 304]. By contrast, the single-detector quantum-correlation technique discussed in Sec. 5.5 only allows us to dig under the shot noise, and it will be limited by non-quantum noise sources of a single detector. This motivates the calculation of cross-correlations of different detectors within configurations of interferometers, such as ET.

Let us consider one set of two interferometers across different detectors within ET, *e.g.*, the red and blue detectors in Fig. 5.4, and pick the origin of coordinates at the origin of the red detector \mathbf{x}_1 . Let us also pick the x - y plane to be the plane of the interferometers, with the x -axis along \mathbf{n}_1 . In this case,

$$\begin{aligned} \mathbf{x}_I = 0, \quad \mathbf{x}_{II} = L\hat{\mathbf{x}}, \quad \mathbf{n}_1 = \hat{\mathbf{x}}, \quad \mathbf{n}_2 = \frac{1}{2}\hat{\mathbf{x}} + \frac{\sqrt{3}}{2}\hat{\mathbf{y}}, \\ \mathbf{n}_3 = -\hat{\mathbf{x}}, \quad \mathbf{n}_4 = -\frac{1}{2}\hat{\mathbf{x}} + \frac{\sqrt{3}}{2}\hat{\mathbf{y}}. \end{aligned} \quad (5.36)$$

Here, we have assumed that the arms along the same line completely overlap with each other (*i.e.*, the arms along \mathbf{n}_1 and \mathbf{n}_3). In reality, there is a finite separation between these arms, which can be dealt with via the general procedure in Sec. 5.4. Then one can compute $\mathcal{D}(r_{i,j}, \Delta\mathbf{x}, \mathbf{n}_{i,j})$ for all the combinations in Eq. (5.30), *i.e.*,

$$\begin{aligned} \mathcal{D}_{13}(r_1, r_2) &= |r_1 + r_2 - L|, \\ \mathcal{D}_{24}(r_1, r_2) &= \frac{1}{2}\sqrt{(2L - r_1 - r_2)^2 + 3(r_1 - r_2)^2}, \\ \mathcal{D}_{14}(r_1, r_2) &= \frac{1}{2}\sqrt{(2L - 2r_1 - r_2)^2 + 3r_2^2}, \\ \mathcal{D}_{32}(r_1, r_2) &= \mathcal{D}_{14}(r_1, r_2). \end{aligned} \quad (5.37)$$

Here, we have defined $\mathcal{D}_{ij}(r_1, r_2)$ such that r_1 is the integration variable along the arm with direction \mathbf{n}_i , and r_2 is the integration variable along the arm with direction \mathbf{n}_j . Plugging Eq. (5.37) into Eq. (5.30), we get

$$\begin{aligned} \tilde{C}_{\mathcal{T}}(\omega) &= \frac{al_p}{8\pi c_s^3 L} \int_0^L dr_1 \int_0^L dr_2 \\ &\quad \cos[\omega(L - r_1)] \cos[\omega(L - r_2)] \\ &\quad \{ \text{sinc}[\omega\mathcal{D}_{13}(r_1, r_2)/c_s] + \text{sinc}[\omega\mathcal{D}_{24}(r_1, r_2)/c_s] \\ &\quad - 2 \text{sinc}[\omega\mathcal{D}_{14}(r_1, r_2)/c_s] \}, \end{aligned} \quad (5.38)$$

the result of which is plotted in Fig. 5.5.

Besides the equilateral triangle configuration of ET, one can compute the response of other geometries of interferometers to the pixellon model following the procedure

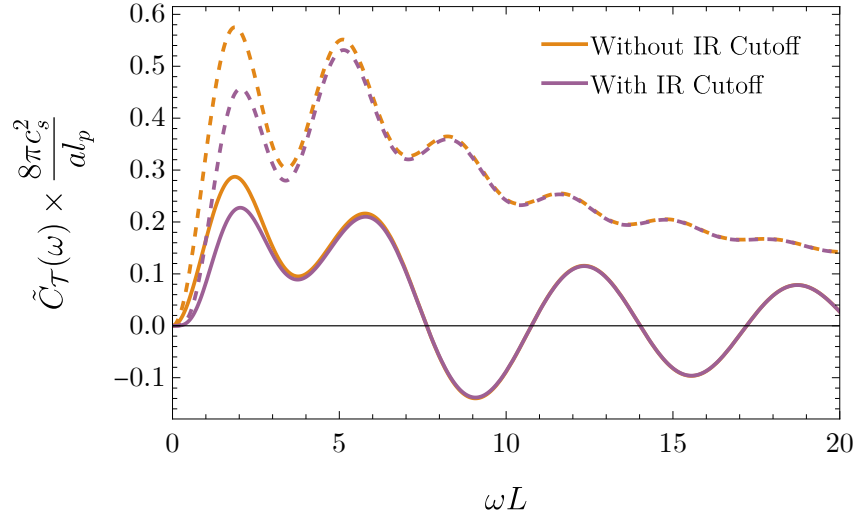


Figure 5.5: The PSD $\tilde{C}_{\mathcal{T}}(\omega)$ of the cross-correlation function of two sets of interferometers within a triangular configuration like ET [Eq. (5.38), solid lines], together with the corresponding auto-correlation $\tilde{C}_{\mathcal{T}}(\omega, \theta = \frac{\pi}{3})$ of a single interferometer within this configuration [Eq. (5.31), dashed lines].

in Sec. 5.4. For example, one can consider two or multiple interferometers with the same length located at the same origin but rotated from each other by certain angles as depicted in Ref. [153]. There are even more complicated geometries, such as the twin 3D interferometers that will be built at Cardiff University [315]. The authors in Ref. [315] claimed that the angular correlations of geotropic fluctuations, as discussed in detail in Refs. [313, 328, 312, 219], especially the transverse correlations due to the low- ℓ modes, can be probed by this geometry. While, in principle, the geotropic signal can be computed for such a complicated interferometer geometry, the pixellon model may not adequately encapsulate the underlying physics of the VZ effect. Further, first-principles calculations of geotropic fluctuations assume a simple causal diamond radiating outward from a beam splitter. One major feature of the twin 3D interferometers in Ref. [315] is that the interferometer arms are bent at mirrors MM_A and MM_B (see Fig. 1 of Ref. [315]), so the causal diamond of the whole apparatus is distorted. The bent-arm configuration explicitly breaks spherical symmetry, which the previous calculations [328, 219] relied on. Specifically, the pixellon metric in Eq. (5.2) captures metric fluctuations only along interferometer arms that extend radially outward from a beam splitter. One can decompose the bent interferometer arms into segments of straight arms, and, assuming the pixellon model pertains to such a causal diamond, attempt to apply the pixellon model to each segment by choosing *local* coordinates centered at the beam splitter, MM_A , and

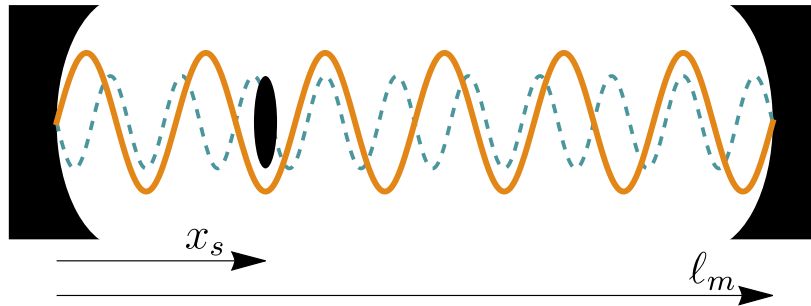


Figure 5.6: Schematic diagram of the optically-levitated sensor as described in Refs. [33, 21]. A dielectric sphere or microdisk is trapped in an anti-node of an optical cavity (solid orange). A second laser (dashed blue) is used to cool the sensor and read out its position. Transverse motion is cooled by additional lasers (not shown).

MM_B , respectively. However, the major obstacle for this procedure is that at MM_A (or MM_B) there does not exist a closed causal diamond, because light continues to traverse past MM_A (or MM_B) until it reaches EM_A (or EM_B) or the beam splitter. Since the calculations in Refs. [328, 219] require a closed causal diamond such that the observable computed is manifestly gauge invariant, one first needs to ascertain whether the procedures in Ref. [219] for computing gauge-invariant quantities are still valid when piecing together these non-closed causal diamonds. Due to these complications, we do not attempt to apply the pixellon model to the Cardiff experiment, as we believe that an accurate prediction for such bent-arm configurations will require a more direct, first-principles calculation requiring better theoretical control than current technology allows. In the next subsection, we focus on another interferometer-like experiment, the optically-levitated sensor.

Optically-levitated Sensor

In this subsection, we study the response of the optically-levitated sensor in Refs. [33, 21] to geontropic fluctuations described by the pixellon model. To understand the working principle of the optically-levitated sensor, let us first consider its response to GWs following Ref. [33], working in the local Lorentz frame with origin at the input mirror. Let the unperturbed distance between the optical cavity mirrors be ℓ_m , and the unperturbed distance from the input mirror to the sensor in its trap minimum be x_s . Under a passing GW perpendicular to the cavity with strain h , the proper distances to the mirror and sensor are both shifted,

$$\delta x_s = \frac{1}{2} h x_s, \quad \delta \ell_m = \frac{1}{2} h \ell_m. \quad (5.39)$$

The new position of the trap minimum can be found from the condition

$$k_t(\ell'_m - x'_{\min}) = k_t(\ell_m - x_{\min}) = \left(n + \frac{1}{2}\right)\pi, \quad (5.40)$$

where n is an integer, and k_t is the wavenumber of the trapping laser. The shift of the trap minimum is then given by $\delta x_{\min} = \ell'_m - \ell_m = \delta \ell_m$. Here, we have assumed that the trapping laser has a constant frequency inside the cavity. Thus, the sensor is displaced from its trap minimum by an amount given in Ref. [33] as

$$\Delta X \equiv \delta x_s - \delta x_{\min} = \frac{1}{2}h(x_s - \ell_m) + \mathcal{O}(h^2). \quad (5.41)$$

This displacement will result in an oscillatory driving force on the sensor. If the GW frequency matches the trapping frequency ω_0 of the sensor, the driving force will resonantly excite the sensor. The corresponding oscillations can then be measured. When $x_s \ll \ell_m$, the effect of the GW is maximized.

For the pixellon model, the response of the optically-levitated sensor can be calculated similarly. In our case, δx_s and $\delta \ell_m$ are given by

$$\delta x_s = -\frac{1}{4} \int_0^{x_s} dr [\phi(x) + \phi(x')], \quad (5.42)$$

$$\delta \ell_m = -\frac{1}{4} \int_0^{\ell_m} dr [\phi(y) + \phi(y')], \quad (5.43)$$

where

$$\begin{aligned} x &= (t_x - x_s + r, r\mathbf{n}), & x' &= (t_x + x_s - r, r\mathbf{n}), \\ y &= (t_\ell - \ell_m + r, r\mathbf{n}), & y' &= (t_\ell + \ell_m - r, r\mathbf{n}), \end{aligned} \quad (5.44)$$

and the start times of each beam are chosen to be $t_x - x_s$ and $t_\ell - \ell_m$. Note the additional factor of $\frac{1}{2}$ as compared to Eq. (5.14), since the lengths ℓ_m and x_s are one-half of the corresponding round-trip time delays when there are no geotropic fluctuations. Within a single arm, since there is only a single beam measuring the position of the sensor, we can choose

$$t_x = t + x_s, \quad t_\ell = t + \ell_m \quad (5.45)$$

such that the start times of the beam probing the sensor and the end mirror are the same. Notice that, in general, two independent pixellon models should be used for the shorter and longer arms. Nevertheless, since both spherical entangling surfaces are located at the same origin, as depicted in Fig. 5.7, and the pixellon fields ϕ are universal across these two causal diamonds as discussed in Sec. 5.4, the forms of

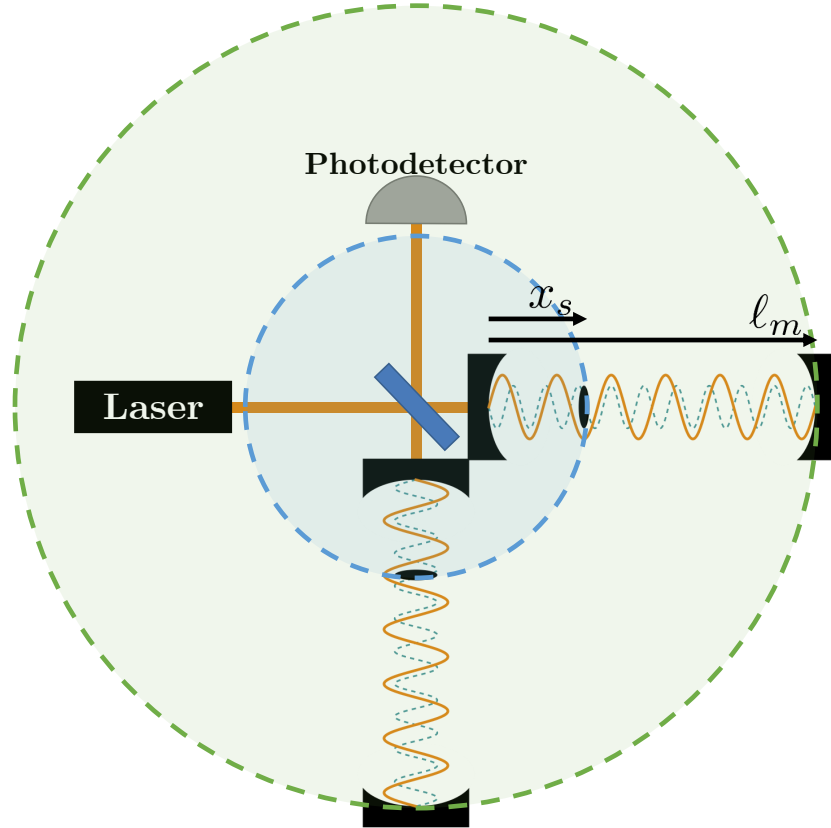


Figure 5.7: Two levitated sensors inserted into the Fabry-Pérot cavities of a Michelson interferometer, as described in Ref. [21]. The entangling surfaces corresponding to the two arms of length x_s and ℓ_m are marked by the blue and green shaded circles, respectively. Note that this diagram ignores the distances between the beam splitter and the input mirrors of the two cavities.

Eqs. (5.42) and (5.43) are very similar. This is consistent with the fact that the metric in Eq. (5.2) is spatially conformal.

The displacement of the levitated sensor from its trap minimum is then given by

$$\Delta X = -\frac{1}{4} \int_0^{x_s} dr [\phi(x) + \phi(x')] + \frac{1}{4} \int_0^{\ell_m} dr [\phi(y) + \phi(y')]. \quad (5.46)$$

Note that Eq. (5.46) is similar, but not identical to, the round-trip time of a photon traveling from position x_s to ℓ_m , *i.e.*,

$$\begin{aligned} \Delta X|_{x_s \leftrightarrow \ell_m} &= \frac{1}{4} \int_{x_s}^{\ell_m} dr [\phi(y) + \phi(y')], \\ y &= (t - \ell_m + r, r\mathbf{n}), \quad y' = (t + \ell_m - r, r\mathbf{n}). \end{aligned} \quad (5.47)$$

Using Eq. (5.47) instead of Eq. (5.46) would give a PSD identical to Eq. (5.32) with length $L = \ell_m - x_s$.

We can then define the correlation function of ΔX as

$$C^{\Delta X}(\Delta t, \theta) \equiv \left\langle \frac{\Delta X(t_1, \mathbf{n}_1) \Delta X(t_2, \mathbf{n}_2)}{(\ell_m - x_s)^2} \right\rangle, \quad (5.48)$$

where the unit vectors \mathbf{n}_i parameterize the orientations of the two levitated sensor arms, and the angle θ between them is given by $\cos(\theta) = \mathbf{n}_1 \cdot \mathbf{n}_2$. The difference between the beam start times is $\Delta t \equiv t_1 - t_2$. Note that the normalization of $C^{\Delta X}$ assumes that the characteristic length of the system is $\ell_m - x_s$, as per the above discussion. Using Eq. (5.46), we find that

$$\begin{aligned} C^{\Delta X}(\Delta t, \theta) &= \frac{1}{16(\ell_m - x_s)^2} \left[\int_0^{x_s} dr_1 \int_0^{x_s} dr_2 C(x_1, x_2) \right. \\ &\quad - \int_0^{x_s} dr_1 \int_0^{\ell_m} dr_2 C(x_1, y_2) - \int_0^{\ell_m} dr_1 \int_0^{x_s} dr_2 C(y_1, x_2) \\ &\quad \left. + \int_0^{\ell_m} dr_1 \int_0^{\ell_m} dr_2 C(y_1, y_2) \right], \end{aligned} \quad (5.50)$$

where $C(x, y)$ is defined in Eq. (5.21). The first and last terms above are correlations between the arms with the same length (either $L = x_s$ or $L = \ell_m$). In contrast, the second and third terms correlate arms with different lengths, *i.e.*, the arm of $L = x_s$ with the arm of $L = \ell_m$.

Following a similar calculation as the one to obtain Eq. (5.27), we find the two-sided PSD $\tilde{C}^{\Delta X}(\omega, \theta)$ as

$$\begin{aligned} \tilde{C}^{\Delta X}(\omega, \theta) &= [\tilde{C}^{\Delta X}(\omega, x_1, x_2) + \tilde{C}^{\Delta X}(\omega, y_1, y_2) \\ &\quad - 2\tilde{C}^{\Delta X}(\omega, x_1, y_2)], \end{aligned} \quad (5.51)$$

where the first two terms are given by Eq. (5.27) with $N = (\ell_m - x_s)^2$ and $\mathcal{D}(r_1, r_2, \theta) = \sqrt{r_1^2 + r_2^2 - 2r_1 r_2 \cos(\theta)}$. The last term, which corresponds to the correlation between the arms of length $L = x_s$ and $L = \ell_m$, carries an additional geometrical factor of $\cos[\omega(\ell_m - x_s)]$ due to the difference in the sizes of the causal diamonds, *i.e.*,

$$\begin{aligned} &\tilde{C}^{\Delta X}(\omega, x_1, y_2) \\ &= \frac{al_p}{8\pi c_s^3 (\ell_m - x_s)^2} \int_0^{x_s} dr_1 \int_0^{\ell_m} dr_2 \cos[\omega(x_s - r_1)] \\ &\quad \cos[\omega(\ell_m - r_2)] \cos[\omega(\ell_m - x_s)] \text{sinc}[\omega \mathcal{D}(r_1, r_2, \theta)/c_s]. \end{aligned} \quad (5.52)$$

We can also define $\tilde{C}_{\mathcal{T}}^{\Delta X}(\omega, \theta)$ as in Eq. (5.31) via

$$\tilde{C}_{\mathcal{T}}^{\Delta X}(\omega, \theta) = 2 [\tilde{C}^{\Delta X}(\omega, 0) - \tilde{C}^{\Delta X}(\omega, \theta)]. \quad (5.53)$$

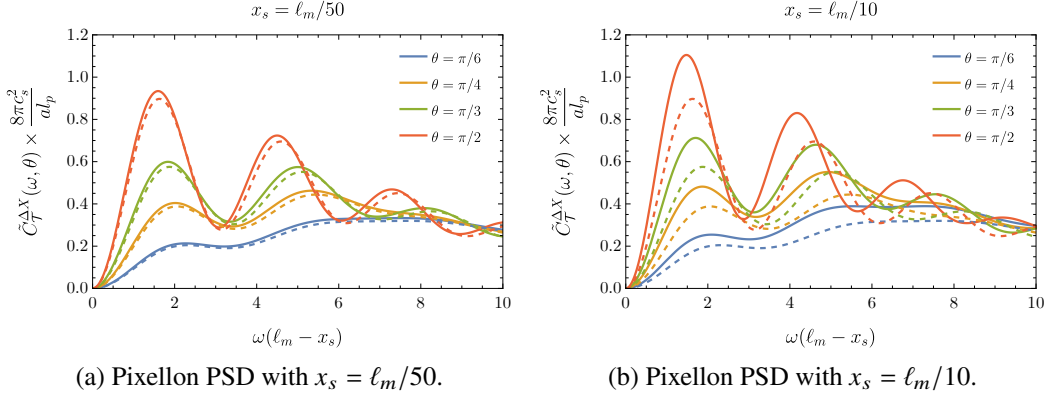


Figure 5.8: Pixellon PSD $\tilde{C}_{\mathcal{T}}^{\Delta X}(\omega, \theta)$ as it would appear in an optically-levitated sensor [Eq. (5.53), solid lines] shown alongside the PSD of an ordinary L-shaped interferometer $\tilde{C}_{\mathcal{T}}(\omega, \theta)$ [Eq. (5.31), dashed lines]. We take the length of the L-shaped interferometer to be $L = \ell_m - x_s$. All PSDs are computed without an IR cutoff.

In the limit $x_s \rightarrow 0$, only the second term in Eq. (5.51) is nonzero, corresponding to the length fluctuations of an interferometer of size $L = \ell_m$. Thus, the levitated sensor can be treated as an ordinary interferometer when x_s is sufficiently small. This is confirmed by Fig. 5.8a, where we plot the interferometer PSD from Eq. (5.32) against the levitated sensor PSD from Eq. (5.51), setting $x_s = \ell_m/50$ and neglecting the IR cutoff for the purpose of demonstration. The interferometer PSD is given by the dashed lines, whereas the levitated sensor PSD is given by the solid lines. We can see that, as expected, the PSDs of these two different types of experiments are very similar in the limit of small x_s . In Fig. 5.8b, we show a similar comparison but instead pessimistically set $x_s = \ell_m/10$. For this larger value of x_s , the PSD for the levitated sensor becomes somewhat larger in magnitude compared to that of the ordinary interferometer, but retains a similar shape. In the limit of $\omega \rightarrow 0$, we have

$$\tilde{C}_{\mathcal{T}}^{\Delta X}(\omega, \theta) = \frac{al_p}{48\pi c_s^5} \omega^2 (l_m + x_s)^2 (1 - \cos \theta) + \mathcal{O}(\omega^4). \quad (5.54)$$

From the scaling $\tilde{C}_{\mathcal{T}}^{\Delta X}(\omega, \theta) \propto (l_m + x_s)^2$, one can see the increase of signal as x_s increases, which is a result of treating the system as two sets of causal diamonds. However, we expect the above treatment to break down beyond the limit of $x_s \ll l_m$. We emphasize that this calculation is not intended to be fully rigorous, but rather seeks to provide a heuristic description of the pixellon model in a levitated sensor experiment. Nevertheless, we continue to expect that the levitated sensor will behave similarly to an L-shaped interferometer in the limit of small x_s .

Next, let us compare the PSD found above to the predicted strain sensitivity of optically-levitated sensor experiments. The thermal-noise-limited minimum detectable strain of the optically-levitated sensor at temperature T_{CM} is given by Refs. [33, 21] as

$$h_{\text{limit}} = \frac{4}{\omega_0^2 \ell_m} \sqrt{\frac{k_B T_{\text{CM}} \gamma_g b}{M} \left[1 + \frac{\gamma_{\text{sc}} + R_+}{N_i \gamma_g} \right]} H(\omega_0), \quad (5.55)$$

where ω_0 is the trapping frequency, γ_g is the gas-damping coefficient, γ_{sc} is the scattered photon-recoil heating rate, b is the bandwidth, M is the mass of the sensor, and $N_i = k_B T_{\text{CM}} / \hbar \omega_0$ is the mean initial phonon occupation number. The cavity response function is $H(\omega) = \sqrt{1 + (2\mathcal{F}/\pi)^2 \sin^2(\omega \ell_m / c)}$, where \mathcal{F} is the finesse of the cavity. Detailed expressions for all of these quantities can be found in Refs. [33, 21].

The peak frequency response of the experiment occurs at the trapping frequency ω_0 , at which oscillations of the levitated sensor are resonantly enhanced. The trapping frequency can be widely tuned via the laser intensity [21]. Thus, the sensitivity curve for the levitated sensor can be obtained by continuously varying the locus of the sensitivity curve for each fixed value of ω_0 , as given by Eq. (5.55).

In Fig. 5.9, we plot the strain sensitivity of the levitated sensor experiment from Ref. [21] (with a sensor consisting of a stack of dielectric disks) against the PSD of the pixellon model from Eqs. (5.51)–(5.53). In Fig. 5.9b, we additionally include an IR cutoff $\omega_{\text{IR}} = 1/L$ as in Eq. (5.28), where we take the characteristic length of the system to be $L = \ell_m - x_s$. This choice comes from the comparison of the displacement ΔX with the length fluctuations of an interferometer of size $\ell_m - x_s$, as discussed with relation to Eq. (5.47). Note that Ref. [21] uses a 300 kHz upper bound for their sensitivity curves, citing limitations of power absorption by the suspended sensor. From these plots, we observe that the levitated sensor would only be competitive for detecting the geontropic signal at $\ell_m \gtrsim 100$ m. At the time of writing, a 1 m prototype of this experiment is under construction, and a 100 m device is at the concept stage [20, 21]. That these proposed levitated sensor experiments are not competitive for constraining the pixellon model is expected: their reach in frequency is such that $\omega \ell_m \ll 1$, whereas the pixellon signal is expected to peak at $\omega \ell_m \sim 1$. Finally, let us note that, although the levitated sensors do not move along geodesics, but instead have amplified non-geodesic movements, the same amplification factors are applied to motion induced by the noisy thermal force. In this way, because the device is limited by thermal noise [20, 21], comparing the

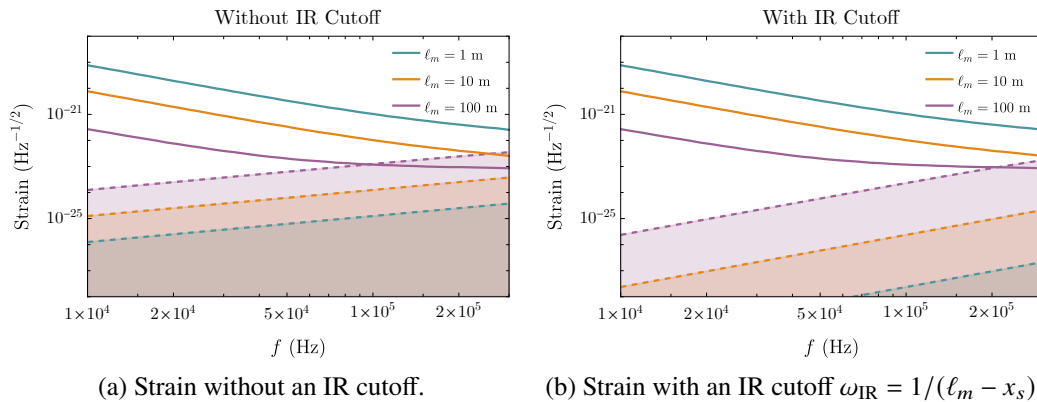


Figure 5.9: The pixellon strain (dashed lines) overlaid with the predicted strain sensitivity for a stacked-disk levitated sensor (solid lines), as given by Fig. 3 of Ref. [21]. The color coding corresponds to the size ℓ_m of the levitated sensor. The pixellon strain is computed from Eq. (5.53), and we set $x_s = \ell_m/10$ throughout.

displacement (5.46) and the thermal strain (5.55), as if there were no trapping, still leads to the correct thermal-noise-limited sensitivity.

5.6 Conclusions

We have considered the effect of the geotropic signal, from the VZ effect proposed in Refs. [313, 314, 41, 174, 312], specifically as modeled in Refs. [328, 219], on next-generation terrestrial GW detectors. We have found that if GQuEST observes spacetime fluctuations from the pixellon, Cosmic Explorer and the Einstein Telescope will have a large background to astrophysical sources from vacuum fluctuations in quantum gravity with which to contend. On the other hand, LISA and other lower-frequency devices are insensitive to this signal. Note that in making these predictions we have assumed the physical equivalence of the pixellon model with the VZ effect for interferometer observables, the proof of which is still the subject of ongoing first-principles calculations. Even so, given how large the geotropic signal is expected to be in future GW observatories, our results may inform optimal designs for GW observatories, whether searching for quantum or classical sources of GWs.

STOCHASTIC GRAVITATIONAL WAVE MEMORY BACKGROUND OF SUPERMASSIVE BINARY BLACK HOLE MERGERS AND ITS DETECTION IN LISA

6.1 Introduction

Gravitational waves (GWs) were first predicted by Einstein in 1916 as ripples in spacetime emanating from accelerating masses. For decades they eluded direct detection due to their tiny effects. Indirect evidence emerged in the 1970s with the Hulse-Taylor binary pulsar, whose shrinking orbit matched energy loss to GWs as predicted by general relativity [248]. A century after Einstein’s prediction, advanced laser interferometers achieved the first direct GW observation in 2015: the LIGO detectors recorded the inspiral and merger of two $\sim 30M_{\odot}$ black holes (event GW150914), heralded as “the first direct detection of gravitational waves and the first observation of a binary black hole merger” [13]. This discovery opened the era of gravitational-wave astronomy, soon confirmed by additional binary black hole and neutron star merger detections in subsequent years [7, 105, 8, 9, 10, 11]. These successful observations established GWs as a powerful new messenger for astrophysics and cosmology.

Beyond discrete events, one expects a persistent stochastic gravitational wave background (SGWB) formed by the superposition of countless unresolved sources across the universe [14]. In essence, the SGWB is a gravitational-wave analog of a diffuse background noise, with contributions from myriad processes: *e.g.*, mergers of compact binaries at high redshift, core-collapse supernovae, rapidly spinning neutron stars, cosmic strings, and even quantum fluctuations from the early universe’s inflationary epoch [14]. By definition, individual waves in a SGWB cannot be distinguished; instead the background is described statistically. Typically, the SGWB is assumed to be *isotropic* (the same intensity coming from all sky directions), *stationary* (statistical properties constant in time), and *Gaussian* (signal amplitudes following a normal distribution due to many independent overlaps) [26, 98]. Under these assumptions (also usually taking it to be unpolarized), the SGWB can be characterized by a power spectrum or energy density spectrum $\Omega_{\text{gw}}(f)$, and searched for via cross-correlation of detector signals [26, 28]. Detecting a SGWB would have

profound implications: it would reveal the integrated history of GW sources and potentially reveal new physics (*e.g.*, relic GWs from the early universe) beyond what is accessible with individual events. In fact, the worldwide network of ground-based detectors has placed stringent upper limits on an isotropic SGWB in the 10–1000 Hz band, while very recently the nanohertz frequency realm has yielded the first exciting hints of a stochastic background signal. In particular, pulsar timing array experiments have reported evidence for a common-spectrum low-frequency stochastic background consistent with GWs from a cosmological population of merging supermassive black hole binaries [19]. This development strongly suggests that an astrophysical SGWB exists, and motivates searches in other frequency bands for analogous signals.

Another subtle prediction of general relativity, and one especially relevant to this work, is the gravitational wave memory effect. Gravitational-wave memory refers to the permanent displacement or relative velocity change left in test masses after a burst of gravitational radiation has passed. Unlike the oscillatory “strain” of a typical GW, the memory is a non-oscillatory DC offset – a lasting imprint on spacetime. Early theoretical work by Zel’dovich and Polnarev [322] pointed out the possibility of such one-time shifts from gravitational radiation. Later, Christodoulou demonstrated that GR’s nonlinear dynamics in fact predict a significant memory effect: gravitational waves from astronomical sources have a nonlinear effect on laser interferometers, with the signature being a permanent displacement of test masses after the passage of a GW [99, 100]. This so-called “nonlinear memory” (also known as the Christodoulou memory) adds to the smaller linear memory contributions from emitted mass or momentum flux. Fundamentally, GW memory is tied to the changing flux of energy–momentum carried by the waves: as a system emits gravitational waves, it can undergo a net recoil, and the spacetime metric does not return to exactly its pre-wave state. In modern understanding, memory is deeply connected to the symmetries of asymptotically flat spacetime. In particular, the permanent offset is associated with a Bondi-Metzner-Sachs (BMS) supertranslation—an asymptotic symmetry transformation—induced by the passage of waves. Equivalently, the memory effect can be viewed as the sourcing of very low-frequency (“soft”) gravitons that carry information about the total energy radiated [64, 298, 295, 243, 242]. This connection, elucidated through studies of infrared gravitational physics, underscores that GW memory is rooted in conserved quantities and symmetry principles of GR.

Experimentally, detecting the GW memory effect is challenging because the memory’s strain amplitude is typically much smaller than the main oscillatory waveform of a given event [215, 194, 168, 300, 196]. To date, no direct observation of memory has been achieved. The first LIGO/Virgo detections of stellar-mass binary mergers were not sensitive enough to confidently measure the tiny permanent shift left behind by those events. Advanced data analyzes [215, 194, 300, 196] have been developed to search for memory by stacking multiple signals or looking for subtle low-frequency trends, but with current detectors, it is expected that single event memory is at or below the noise floor [168]. In the pulsar timing domain, a passing GW burst with memory would produce a characteristic change in pulsar pulse arrival times; though PTA projects have sought this signature from potential supermassive black hole mergers, the event rates for such dramatic “memory bursts” are estimated to be very low [175, 111, 318]. In short, observing memory likely requires either an extremely nearby or catastrophic event or the accumulation of many events. This latter approach leads naturally to the idea of a stochastic background of memory signals, wherein numerous memory-producing events over cosmic time superpose to yield a persistent random metric perturbation. Just as the incoherent sum of many small GW bursts can form a SGWB, so too many memory steps could form a stochastic gravitational wave memory background (SGWMB).

The concept of a SGWMB arising especially from frequent supermassive black hole binary (SMBH) coalescences has recently gained attention [78, 66]. Each time a massive binary black hole merges, it emits a burst of gravitational waves and a non-reversible memory step in the spacetime metric. Over the history of the universe, countless SMBH mergers (especially at high redshift) would cumulatively generate a random series of these metric steps. The resulting SGWMB can be thought of as a sort of “random walk” or Brownian motion in the GW strain: successive memory jumps add up in a diffusive manner [325, 78, 330, 66]. Theoretical work by Zhao and Cao [325] provided the first detailed analysis of such a memory-generated background, showing that it has a distinctive spectral character. In the limit that many memory events overlap, the SGWMB strain power spectral density scales inversely with frequency (approximately $S_h(f) \propto 1/f^2$), corresponding to a red-colored noise spectrum. Equivalently, the fractional energy density $\Omega_{\text{gw}}(f)$ of the memory background grows with frequency, since memory contributes more power at lower frequencies. Notably, the amplitude of this memory background is determined predominantly by the global merger rate of black holes [325, 66]. This implies that measuring the SGWMB could directly inform us about the population

of merging SMBHs in the universe. Moreover, because the memory signals accumulate linearly, rather than oscillating and averaging down, the SGWMB provides a new avenue to detect the memory effect statistically. It has been argued that a SGWMB provides a new means to detect gravitational wave memory [325]. In other words, even if individual memory bursts are too weak to detect on their own, their collective imprint might be observable as a low-frequency stochastic signal, offering both a confirmation of the memory effect and a probe of cosmological BH merger dynamics. One caveat is that a memory background may violate some of the usual SGWB assumptions (*e.g.*, it may be non-Gaussian or anisotropic if only a limited number of sources contribute at a given time), complicating detection strategies. These issues, as well as the expected magnitude of the SGWMB relative to other backgrounds, are active areas of research.

Given these theoretical developments, the impending launch of next-generation GW observatories adds timely urgency to the study of the SGWMB. In particular, the Laser Interferometer Space Antenna (LISA)—a space-based GW detector scheduled for the 2030s—will be sensitive in the millihertz frequency band, perfectly suited for observing signals from $\sim 10^4$ – $10^8 M_\odot$ black hole binaries [30]. LISA consists of three spacecraft in a triangular formation with millions of kilometers arm-length, designed to detect GWs in the 0.1 mHz to 0.1 Hz range. This mHz band is expected to be richly populated with sources: massive black hole mergers, extreme mass-ratio inspirals, galactic binaries, and possibly a stochastic background from the early universe [40]. Importantly, LISA should individually observe many SMBH merger events which are of significant interest for GW memory production. It will also have the capability to search for a diffuse background in its band. A memory background from numerous SMBH mergers, if it exists at a detectable level, would manifest as an additional low-frequency noise component in LISA’s data. Being a space mission, LISA offers long observation times and is free from terrestrial seismic noise at low frequencies, making it ideal for capturing the slowly accumulating memory effect. Indeed, studies indicate that space-based detectors are ideal to detect the gravitational wave memory background corresponding to supermassive binary black holes [30, 196]. A detection, or even a constraint of the SGWMB by LISA would be profoundly informative: it would confirm a novel general relativistic effect on cosmic scales, test the BMS symmetry predictions, and provide insight into the cosmic merger history and environments of SMBHs. Given that pulsar timing arrays are now observing a stochastic signal at nHz frequencies and ground-based interferometers continue to improve at ~ 100 Hz and above, LISA will fill

the crucial mHz gap—potentially allowing us to piece together a full spectrum of gravitational wave backgrounds across 12 orders of magnitude in frequency. In this context, understanding the expected SGWMB from SMBH mergers is both timely and necessary for maximizing LISA’s scientific return.

This chapter is organized as follows. In Sec. 6.2, we present the mathematical foundation of the SGWB. In addition, we review the techniques employed to detect the SGWB. In Sec. 6.3, we give an overview of the BMS symmetry group and explore how it underlies the gravitational wave memory effect through nonlinear dynamics and asymptotic charges. Furthermore, we focus on the gravitational memory effect from a single binary black hole merger, detailing the strain contributions, multipolar decomposition, and numerical relativity results. In Sec. 6.4, we extend this discussion to the SGWMB, treating it as a Brownian accumulation of individual memory steps from numerous supermassive black hole mergers. We derive its spectral density and discuss its deviation from standard SGWB assumptions. In Sec. 6.5, we evaluate the detectability of the SGWMB with LISA, including its expected signal strength and the impact of source resolvability. Finally, in Sec. 6.6, we summarize key findings and outline future directions for theory, modeling, and observational strategies relevant to detecting the memory background in forthcoming gravitational wave missions.

6.2 Stochastic Gravitational Wave Backgrounds: An Overview

In this section, we provide a comprehensive overview of the SGWB, including both its theoretical underpinnings and the techniques used to detect it. We begin with a mathematical description of the SGWB, including its standard statistical assumptions and formal definitions of key quantities such as the strain power spectral density, characteristic strain, and spectral energy density. We then review the primary methods used across different gravitational wave observatories to search for a SGWB, focusing on ground-based interferometers, PTAs, and space-based detectors. Finally, we briefly introduce the concept of anisotropies in the SGWB and how directional dependence can be probed using spherical harmonic decomposition. This overview sets the stage for deeper analysis of memory-induced backgrounds and their observational prospects in subsequent sections.

Mathematical Foundations of the SGWB

Gravitational wave backgrounds are described as small metric perturbations $h_{ij}(t, \mathbf{x})$ superposed from many independent sources. We work in the transverse-traceless

(TT) gauge, where the metric perturbation has only spatial components and is traceless. In this gauge one can expand h_{ij} as a superposition of plane waves traveling in various directions. For a wave propagating from direction $\widehat{\Omega}$ (a unit vector on the sky) with polarization A (where $A = +, \times$ in general relativity), we write the plane-wave expansion as [26, 28, 98]

$$h_{ij}(t, \mathbf{x}) = \sum_{A=+, \times} \int_{-\infty}^{\infty} df \int_{S^2} d^2\widehat{\Omega} h_A(f, \widehat{\Omega}) e_{ij}^A(\widehat{\Omega}) e^{2\pi i f(t - \widehat{\Omega} \cdot \mathbf{x}/c)}, \quad (6.1)$$

where $e_{ij}^A(\widehat{\Omega})$ are the polarization basis tensors for plus and cross modes, defined with respect to two unit vectors $\widehat{\mathbf{m}}, \widehat{\mathbf{n}}$ orthogonal to $\widehat{\Omega}$ so that $\widehat{\Omega}, \widehat{\mathbf{m}}, \widehat{\mathbf{n}}$ form an orthonormal triad [26, 98]. For example, one convenient choice is $e_{ij}^+(\widehat{\Omega}) = \widehat{\mathbf{m}}_i \widehat{\mathbf{m}}_j - \widehat{\mathbf{n}}_i \widehat{\mathbf{n}}_j$ and $e_{ij}^\times(\widehat{\Omega}) = \widehat{\mathbf{m}}_i \widehat{\mathbf{n}}_j + \widehat{\mathbf{n}}_i \widehat{\mathbf{m}}_j$. With this choice of the basis, $e_{ij}^A e^{A', ij} = 2\delta^{AA'}$.

Because a SGWB results from an incoherent superposition of many independent sources, it is typically modeled as a *stationary, Gaussian* random process that is *isotropic* on the sky and *unpolarized* on average [28, 276, 98, 208]. These assumptions mean, respectively, that the statistical properties of $h_{ij}(t)$ do not change in time, the Fourier components follow a Gaussian distribution (by the central limit theorem, if many random sources contribute) [308, 311, 327], the background has no preferred direction, and equal power is carried in the two polarization states. Under these standard assumptions, one can characterize the SGWB by the ensemble averages of the Fourier mode amplitudes $h_A(f, \widehat{\Omega})$. In particular, the power spectral density $S_h(f)$ of the background is defined by the ensemble correlation of these Fourier components [26, 28, 98, 240]:

$$\langle h_A^*(f, \widehat{\Omega}) h_{A'}(f', \widehat{\Omega}') \rangle = \frac{\delta^2(\widehat{\Omega}, \widehat{\Omega}')}{4\pi} \frac{\delta_{AA'}}{2} \delta(f - f') S_h(f), \quad (6.2)$$

where $\langle \cdot \rangle$ denotes an ensemble (or time) average, and we use Dirac delta functions to enforce that the only nonzero correlations are for the same frequency ($f = f'$), same sky direction ($\widehat{\Omega} = \widehat{\Omega}'$), and same polarization $A = A'$. The normalization is chosen such that $S_h(f)$ is the double-sided power spectral density (PSD) of the gravitational-wave strain field with units of Hz^{-1} [28, 276]. Intuitively, $S_h(f)$ encodes the spectral distribution of strain power in the SGWB: for any frequency band, $S_h(f) df$ is proportional to the mean squared strain contributed by that band.

Given $S_h(f)$, we can derive the energy density carried by the SGWB. Gravitational waves carry energy and momentum as a form of radiation. In the weak-field limit, the stress-energy tensor of gravitational waves (averaged over many wavelengths) is

given by Isaacson's formula [28, 276, 98, 240],

$$T_{\mu\nu}^{\text{gw}} = \frac{c^4}{32\pi G} \langle \partial_\mu h_{ij} \partial_\nu h^{ij} \rangle. \quad (6.3)$$

In particular, the energy density (energy per unit volume) in GWs is,

$$\rho_{\text{gw}} = T_{00}^{\text{gw}} = \frac{c^4}{32\pi G} \langle \dot{h}_{ij} \dot{h}^{ij} \rangle \quad (6.4)$$

where overdots denote time derivatives. Using the plane-wave expansion and the statistical properties above, one can show that [225, 240]

$$\langle h_{ij}(t) h^{ij}(t) \rangle = 2 \int_{-\infty}^{\infty} df S_h(f) = 4 \int_{f=0}^{f=\infty} d(\ln f) S_h(f), \quad (6.5)$$

i.e. the total mean-squared strain rate is an integral over frequency of $S_h(f)$ weighted by f^2 . Inserting this into the expression for ρ_{gw} and converting the integration variable to $d \ln f$, we obtain the spectral energy density of the SGWB. It is convenient to express this as a dimensionless fraction of the Universe's critical energy density ρ_c , also known as the energy density needed to close the universe [28, 225, 98]. We define $\Omega_{\text{gw}}(f)$ as the fraction of energy density in GWs per logarithmic frequency interval [225, 98, 240]:

$$\Omega_{\text{gw}}(f) \equiv \frac{1}{\rho_c} \frac{d\rho_{\text{gw}}}{d \ln f}, \quad (6.6)$$

so that $\Omega_{\text{gw}}(f) d \ln f$ is the GW energy density (in units of ρ_c) in the band $[f, f+df]$. Using $\rho_c = \frac{3H_0^2}{8\pi G}$, where H_0 is the Hubble expansion rate today, we find the relation between Ω_{gw} and the strain PSD [225, 240]:

$$\Omega_{\text{gw}}(f) = \frac{4\pi^2}{3H_0^2} f^3 S_h(f), \quad (6.7)$$

which is a fundamental quantity describing a SGWB. This $\Omega_{\text{gw}}(f)$ is dimensionless; it directly measures the GW energy content of the universe at frequency f , normalized to the critical density [240]. Often, one also defines the characteristic strain $h_c(f)$ of the background as a dimensionless amplitude representing the strain per unit frequency. A common definition is [225]

$$h_c(f) \equiv \sqrt{2f S_h(f)}. \quad (6.8)$$

The factor of two arises from converting the double-sided power spectral density S_h into its one-sided form, which is the convention used for comparison with the LISA sensitivity curve. In terms of $h_c(f)$, the energy density spectrum takes the

form $\Omega_{\text{gw}}(f) = 2\pi^2 f^2 h_c^2 / (3H_0^2)$. All three quantities $S_h(f)$, $h_c(f)$, and $\Omega_{\text{gw}}(f)$ are used in the literature to characterize stochastic backgrounds; given one of them, the others can be obtained via the above relations.

In summary, $S_h(f)$ describes the strain power spectrum of the SGWB, $h_c(f)$ gives an effective strain amplitude per frequency band, and $\Omega_{\text{gw}}(f)$ describes the contribution of GWs to the universe's energy density at each frequency. For a sense of typical values, a flat spectrum with $\Omega_{\text{gw}}(f) \sim 10^{-9}$ would correspond to an extremely faint dimensionless strain $h_c(f) \sim 10^{-24}$ in the ~ 100 Hz band of ground-based detectors [28, 98, 208].

Detection Strategies and Experiments

A SGWB does not produce a distinct “chirp” or signal in a single detector, but rather a persistent, random strain noise present in the data. Detecting it requires careful statistical analysis to distinguish the SGWB from instrumental noise. Different types of experiments probe the SGWB over a wide range of frequencies, from nanohertz up to kilohertz, using different techniques [26, 28, 276, 240]. We outline the main detection methods used by ground-based interferometers, pulsar timing arrays, and space-based detectors, as well as the cross-correlation techniques that maximize the signal-to-noise ratio (SNR).

Ground-based Interferometers

Ground-based laser interferometers like LIGO and Virgo operate in the high-frequency band and have detected transient GWs from individual astrophysical events [13, 6, 7, 8, 9, 10, 11]. To search for an SGWB, these observatories use multiple detectors and exploit the fact that a stochastic signal would be a common random strain present in all detectors, whereas instrumental noises are largely independent. The basic strategy is to cross-correlate the strain data from two or more spatially separated detectors and look for a correlated signal hidden in the noise [14, 308, 208]. By integrating correlations over long observation times, one can detect an SGWB that is far below the noise level of any single detector.

In practice, if $s_1(t)$ and $s_2(t)$ are the strain time series in two detectors, with $s_i(t) = h(t) + n_i(t)$ being the sum of GW signal and instrument noise, one constructs an estimator Y for the GW energy density by cross-correlating their Fourier components with an optimal filter $Q(f)$ [308]. The optimal filter is chosen to maximize the SNR by weighting each frequency according to the expected SGWB spectrum and the

detectors' noise spectra [28, 229]. For an assumed target spectrum $\Omega_{\text{gw}}(f)$, the optimal filter in frequency space is $Q(f) \propto \frac{\gamma_{12}(f)\Omega_{\text{gw}}(|f|)}{|f|^3 P_1(|f|)P_2(|f|)}$ [229], where $P_1(|f|)$ and $P_2(|f|)$ are the noise power spectral densities of the two detectors, and $\gamma_{12}(|f|)$ is the overlap reduction function. The function $\gamma_{12}(|f|)$, which is dimensionless and bounded between ± 1 , encodes the relative alignment and separation of the two detectors: it is essentially the normalized scalar product of the detector antenna response patterns as a function of GW frequency [308]. For co-located, co-aligned interferometers $\gamma_{12}(|f|) = 1$ at all f , but for separated detectors $\gamma_{12}(|f|)$ can be less than one or even negative at certain frequencies, reducing sensitivity [308]. For example, LIGO's Hanford–Livingston detector pair has $\gamma_{\text{HL}}(f) \approx 0.8$ at low frequencies dropping to negative values above ~ 60 Hz due to their 3000 km separation and relative orientation [308, 14].

After applying the optimal filter, the output cross-correlation statistic Y is an estimator for the amplitude of $\Omega_{\text{gw}}(f)$. One can derive the expected signal-to-noise ratio for a given background spectrum by comparing the expected cross-correlation signal to the variance contributed by noise. For a Gaussian, stationary background and uncorrelated detector noise, the SNR after an observation time T is

$$\text{SNR} = \frac{3H_0^2}{10\pi^2} \sqrt{T} \left(\int_{-\infty}^{\infty} df \frac{\gamma_{12}^2(f)\Omega_{\text{gw}}^2(|f|)}{|f|^6 P_1(|f|)P_2(|f|)} \right)^{1/2}, \quad (6.9)$$

where we have assumed $\Omega_{\text{gw}}(f)$ is the target spectrum being searched for [229]. This expression makes clear that the sensitivity improves with \sqrt{T} and that frequencies at which the detectors have high noise $P_i(f)$ or poor overlap, meaning $\gamma_{12}(f) \approx 0$ contribute little to the SNR [229]. In practice, ground-based SGWB searches integrate the cross-correlation over months or years of data to build up sensitivity [276, 276, 229]. No SGWB has yet been detected in the LIGO–Virgo band; instead, the result of such analyses is typically an upper limit on $\Omega_{\text{gw}}(f)$. For instance, the latest LIGO/Virgo limit is of order $\Omega_{\text{gw}} < 10^{-9}$ in the ~ 20 – 100 Hz band set by the non-observation of a cross-correlation signal above the noise [208]. These limits already constrain some models of cosmological backgrounds and astrophysical populations [240]. In the future, as the detector sensitivities improve and new detectors join the network, there is hope to either detect an astrophysical SGWB or push upper limits low enough to test early-universe models [208, 240].

Pulsar Timing Arrays

At much lower frequencies (10^{-9} to 10^{-7} Hz, corresponding to periods of years to decades), pulsar timing arrays employ a conceptually similar strategy to detect an SGWB, using millisecond pulsars as a galaxy-scale gravitational wave detector. An array of pulsars distributed across the sky is monitored for tiny fluctuations in their pulse arrival times. A passing gravitational wave stretches or shrinks the spacetime between Earth and each pulsar, inducing a characteristic pattern of timing residuals, which deviate from the expected pulse arrival times. While the timing data from a single pulsar contains a stochastic residual that could be due to a GW background or various noise processes, a real SGWB will imprint a distinctive spatial correlation between the timing residuals of different pulsar pairs. This correlation as a function of the angle ξ_{ab} between pulsar a and b on the sky was first derived by Hellings and Downs [192] and given by a curve known as the Hellings–Downs curve that depends only on ξ_{ab} [303, 272, 275]. In the ideal case of an isotropic, unpolarized GW background in general relativity, the correlation between pulsar timing residuals has a monopole and quadrupole angular dependence: it is positive for pulsars separated by large angles and decreases to a small negative value for pulsars nearly coincident on the sky [204, 19]. PTA data analysis searches for this correlated signature in the timing data of many pulsars. Practically, this involves computing the pairwise correlation of timing residual time-series for all pulsar pairs and comparing the measured angular correlation function to the theoretical Hellings–Downs curve. Since each pulsar has various intrinsic noise contributions such as measurement errors, irregularities in pulsar spin, interstellar medium effects, a significant detection requires averaging over a network of many pulsars, analogous to cross-correlating multiple detectors in the LIGO case [247, 19]. The signal is exceedingly small—fractional variations in pulse arrival times of order 10^{-15} —and builds up slowly over years of data. In the past few years, PTA experiments have reported the first strong evidence of a common-spectrum stochastic process with Hellings–Downs spatial correlations, consistent with an SGWB signal [240]. Notably, in 2023 the North American Nanohertz Observatory for Gravitational Waves (NANOGrav) and other PTA collaborations announced the detection of a stochastic common process in pulsar timing data with the expected Hellings–Downs correlation at the $3\text{--}4\sigma$ level [240, 19]. In the coming years, extended observations as well as adding more pulsars will refine these measurements, aiming to confirm the GW nature of the signal unambiguously and potentially begin characterizing the frequency spectrum $\Omega_{\text{gw}}(f)$ in the nHz band.

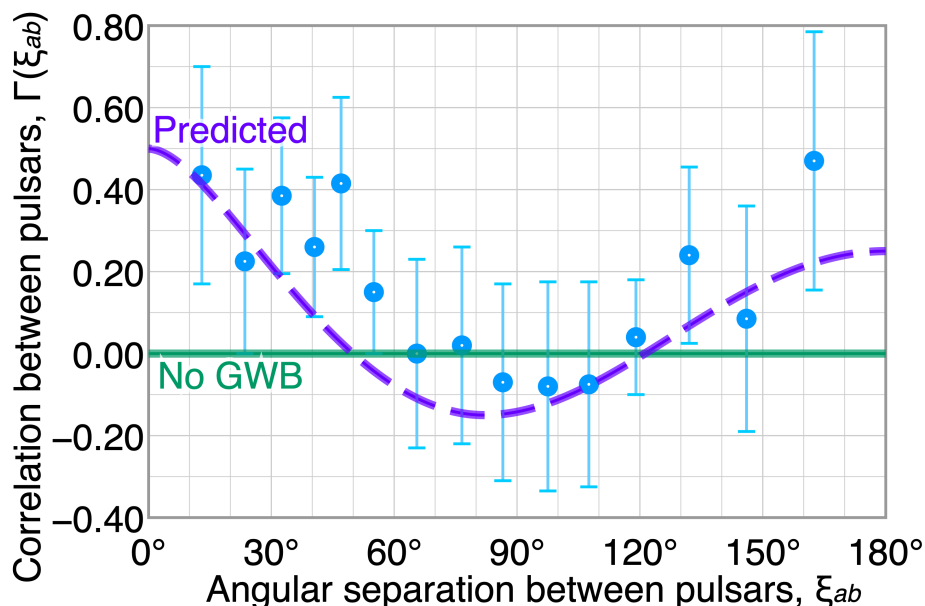


Figure 6.1: Expected Hellings–Downs correlation (purple dashed line) of timing residuals as a function of the angle between two pulsars, compared to recent observations (blue points with error bars) from a pulsar timing array. The green line at zero represents the no-GW hypothesis. A SGWB produces the distinctive quadrupolar correlation pattern shown by the dashed curve [247].

Methodologically, PTAs also use cross-correlation estimators and optimal filtering, but in a somewhat different statistical framework than ground-based interferometers. Rather than a continuous Fourier integration, as done in LIGO analysis, PTA analyses often work with the covariance matrix of pulsar timing residuals across the array and perform a Bayesian or frequentist search for the common cross-correlation pattern [320, 42]. The end result, however, is analogous: by combining many pulsar pair correlations, the analyses strengthen the common SGWB signal and suppress uncorrelated noise. The recent PTA results are an exciting confirmation that the cross-correlation approach—applied now on Galactic scales—can successfully detect a stochastic background.

Space-based Detectors

In the millihertz band (10^{-4} – 10^{-1} Hz), the planned Laser Interferometer Space Antenna (LISA) will open another window onto stochastic backgrounds. LISA, scheduled for launch in the 2030s, will consist of a triangular constellation of spacecraft forming a 2.5-million-km arm-length interferometer in space [30]. This instrument is designed to detect GWs in a frequency range inaccessible from Earth

due to seismic noise and gravity gradient noise at low frequencies [43, 40]. Many cosmological models predict a stochastic background in the millihertz band, for instance, from processes in the early Universe such as phase transitions, cosmic strings, or inflationary relics, and a key science goal of LISA is to search for such signals [43, 30, 40, 240]. Astrophysical backgrounds are also expected, for example from the unresolved confusion noise of many millions of compact binaries in our galaxy and beyond [240].

Detecting a SGWB with LISA will also rely on cross-correlation techniques, although the implementation differs because LISA is a single multi-arm detector rather than multiple independent detectors. However, LISA’s time-delay interferometry (TDI) will produce multiple data streams, sometimes called X , Y , Z or A , E , T channels, that have different response patterns to GWs and noise. By forming appropriate pairs or linear combinations of these TDI channels, one can effectively obtain “synthetic” detectors and apply cross-correlation methods similar to the ground-based case [30]. In fact, analyses have shown that a network of cross-correlated LISA channels, or even a joint analysis of LISA with possible future space detectors, can achieve high sensitivity to isotropic or even anisotropic SGWBs in the mHz band [273, 42]. The formalism developed for ground detectors such as optimal filters, overlap reduction functions, and likelihood analyses has been generalized to the LISA configuration [276, 320]. For example, one can define a noise-orthogonal TDI channel known as the “T” channel that is largely insensitive to GWs and use it as a null stream to check instrument noise, while cross-correlating the others such as “A” and “E” to search for a SGWB [320].

In addition to LISA, other future detectors are being considered. Space-based pulsar timing could one day extend PTA sensitivity by placing radio telescopes in orbit or on the Moon for longer baselines. Even sooner, Doppler tracking of spacecraft (using radio links between Earth and a spacecraft) has been used to probe SGWBs in the microhertz range – for instance, the Cassini mission was used to set limits on an SGWB around 10^{-6} - 10^{-3} Hz [276]. Meanwhile, next-generation ground interferometers such as Einstein Telescope [136] and Cosmic Explorer [137] will dramatically improve sensitivity in the audio band, and combined with LIGO/Virgo/KAGRA they will form a network that could either detect an astrophysical background or constrain it to very low levels. The synergy of all these approaches—ground, space, and pulsar timing—means that the SGWB will be probed over an enormous frequency span, ~ 20 orders of magnitude from nHz

to kHz, in the coming decades [240]. Each window has the potential to reveal different sources from supermassive black hole binaries to inflationary GWs, making SGWB searches a rich interdisciplinary target in gravitational wave astronomy and cosmology.

Directional Dependence and Anisotropies

Gravitational-wave backgrounds need not be perfectly isotropic. In fact, there is strong motivation to study anisotropies in the SGWB – irregularities in the intensity of the background across the sky – because they can carry information about the distribution and motion of GW sources. For example, a stochastic background arising from a foreground of Galactic binaries would be brighter along the Milky Way plane than in other directions [27]. Such anisotropies would cause the correlated signal between detectors to vary with time as the Earth rotates [27]. By observing these modulation patterns, one can infer the multipole moments that characterize the sky distribution of the SGWB [27]. In other words, measuring the directional dependence of a SGWB provides a way to map its angular power distribution, analogous to how anisotropies of the cosmic microwave background are analyzed.

To quantify anisotropy, we define a directional GW energy-density spectrum $\Omega_{\text{gw}}(f, \hat{\Omega})$. This function gives the energy density of the background per unit logarithmic frequency f and per unit solid angle in direction $\hat{\Omega}$ on the sky, normalized by the critical density ρ_c of the Universe. In analogy with the isotropic case, one can write:

$$\Omega_{\text{gw}}(f, \hat{\Omega}) \equiv \frac{1}{\rho_c} \frac{d^3 \rho_{\text{gw}}}{d \ln f d^2 \Omega}. \quad (6.10)$$

Here $d^3 \rho_{\text{gw}}$ is the energy density in GWs in the frequency interval df about f coming from an infinitesimal solid angle $d^2 \Omega$ around direction $\hat{\Omega}$ [27, 271]. Integrating $\Omega_{\text{gw}}(f, \hat{\Omega})$ over all directions recovers the usual (all-sky average) spectrum $\Omega_{\text{gw}}(f)$. If the background is isotropic, $\Omega_{\text{gw}}(f, \hat{\Omega})$ is independent of $\hat{\Omega}$; anisotropies are present when Ω_{gw} varies across the sky.

It is convenient to expand the directional spectrum in spherical harmonics $Y_{\ell m}(\hat{\Omega})$, which form an orthonormal basis on the sky. Thus, one writes the multipole expansion:

$$\Omega_{\text{gw}}(f, \hat{\Omega}) = \sum_{\ell=0}^{\infty} \sum_{m=-\ell}^{\ell} a_{\ell m}(f) Y_{\ell m}(\hat{\Omega}). \quad (6.11)$$

The coefficients $a_{\ell m}(f)$ represent the anisotropy multipole moments of the background at frequency f . The monopole term $\ell = 0$ corresponds to the all-sky average,

and higher ℓ terms encode anisotropic structure on angular scales roughly $\sim 180^\circ/\ell$. In stochastic terms, one often assumes these multipole coefficients are random variables with some angular power spectrum C_ℓ defined by $\langle a_{\ell m}(f) a_{\ell' m'}^*(f) \rangle = C_\ell(f) \delta_{\ell\ell'} \delta_{mm'}$. An angular power spectrum can be estimated as

$$C_\ell(f) = \frac{1}{2\ell + 1} \sum_{m=-\ell}^{\ell} |a_{\ell m}(f)|^2, \quad (6.12)$$

which quantifies the amplitude of anisotropy at multipole ℓ . The set C_ℓ thus characterizes how power in the SGWB is distributed over different angular scales, analogous to the C_ℓ spectrum used for CMB anisotropies. In particular, C_0 is related to the mean background level, C_1 to any dipole, C_2 to quadrupolar structure, and so on.

An anisotropic background influences the cross-correlation signals of detector pairs in a direction-dependent way. The measured correlation between two detectors I and J , which are at locations $\mathbf{x}_I, \mathbf{x}_J$ with respective antenna response patterns $F_I(\hat{\mathbf{\Omega}}, F_J(\hat{\mathbf{\Omega}}))$ can be expressed as an integral over the sky weighted by $\Omega_{\text{gw}}(f, \hat{\mathbf{\Omega}})$. In the frequency domain, the cross-correlation spectral density $S_{IJ}(f)$ is proportional to [27]:

$$S_{IJ}(f) \propto \int_{S^2} d^2\Omega \Omega_{\text{gw}}(f, \hat{\mathbf{\Omega}}) F_I(\hat{\mathbf{\Omega}}) F_J(\hat{\mathbf{\Omega}}) e^{i2\pi f \hat{\mathbf{\Omega}} \cdot (\mathbf{x}_I - \mathbf{x}_J)/c}. \quad (6.13)$$

For an isotropic background, $\Omega_{\text{gw}}(f, \hat{\mathbf{\Omega}}) = \Omega_{\text{gw}}(f)$ is constant over the sky, and the above integral simplifies. In that case one defines the usual overlap reduction function (ORF) $\gamma_{IJ}(f)$, which encapsulates the geometrical sensitivity of the detector pair to a monopole SGWB. The ORF is a known function determined by the baseline separation and detector orientations [27]. If the SGWB is anisotropic, however, different spherical-harmonic components of Ω_{gw} contribute to the correlation. By inserting the expansion for $\Omega_{\text{gw}}(f, \hat{\mathbf{\Omega}})$ into the integral, one finds that each multipole (ℓ, m) produces a term proportional to $a_{\ell m}(f)$, with a corresponding generalized overlap reduction function $\gamma_{IJ}^{\ell m}(f)$ serving as the coupling coefficient [27]. In other words, $\gamma_{IJ}^{\ell m}(f)$ is the response of the I - J baseline to a unit spherical harmonic $Y_{\ell m}$ distribution on the sky. It can be written as the sky integral of the detectors' antenna patterns against the $Y_{\ell m}$ mode [27]:

$$\gamma_{IJ}^{\ell m}(f) = \frac{1}{4\pi} \int_{S^2} d^2\Omega Y_{\ell m}^*(\hat{\mathbf{\Omega}}) F_I(\hat{\mathbf{\Omega}}) F_J(\hat{\mathbf{\Omega}}) e^{i2\pi f \hat{\mathbf{\Omega}} \cdot (\mathbf{x}_I - \mathbf{x}_J)/c}. \quad (6.14)$$

This reduces to the standard $\gamma_{IJ}(f)$ for $\ell = 0$, since $Y_{00} = 1/\sqrt{4\pi}$ is constant. The set of functions $\gamma_{IJ}^{\ell m}(f)$ thus generalizes the overlap reduction function to an anisotropic

background. In practical analyses, one expands the data from correlated detectors in this spherical-harmonic basis, estimating or constraining the coefficients $a_{\ell m}(f)$ by projecting out each mode’s contribution via the known $\gamma_{IJ}^{\ell m}(f)$ [309].

Anisotropic searches for the SGWB are implemented across ground-based interferometers, PTAs, and space-based detectors, each exploiting how time-varying detector orientations or spatial configurations modulate the observed signal. Ground-based interferometers rotate with the Earth, producing sidereal modulations in the cross-correlation signal if anisotropies are present [309, 308, 208]. These modulations are analyzed using spherical harmonic decomposition to reconstruct the directional GW energy distribution. The resulting sky maps allow constraints on angular multipoles $a_{\ell m}(f)$ and corresponding power spectra $C_\ell(f)$.

PTAs use the angular correlation of pulse arrival times across a distributed array of pulsars to probe anisotropy in the nanohertz band. Deviations from the expected Hellings–Downs curve indicate directional structure in the background, which can be expanded in spherical harmonics or Legendre polynomials [154, 303]. Similarly, space-based detectors like LISA exploit orbital motion and multiple interferometry channels to gain directional sensitivity [42, 221]. Across all platforms, anisotropic searches generalize the standard isotropic formalism by including direction-dependent GW energy density $\Omega_{\text{gw}}(f, \hat{\Omega})$ and its coupling to detector baselines via generalized overlap reduction functions $\gamma_{IJ}^{\ell m}(f)$.

6.3 Gravitational Memory and the BMS Symmetry

The gravitational wave memory effect was first predicted in the 1970s as a subtle permanent distortion of spacetime caused by a burst of gravitational radiation. In 1974, Zel’dovich and Polnarev computed the gravitational waves from two masses on hyperbolic flyby orbits and found that the strain h_{ij} does not return to zero at late times—instead, there is a net change in the waveform between the distant past and future [322, 298, 295, 242]. This effect arises because the stress-energy distribution of the system is different after the encounter than before, leading to a different asymptotic gravitational field. Braginsky and Grishchuk later termed this the “memory effect” and clarified its observational meaning as a lasting offset in the separation of test masses after a gravitational wave passes [242]. By 1987, Braginsky and Thorne had derived an explicit formula for the memory produced by a scattering of N particles, showing that the net change in the transverse-traceless strain h_{ij}^{TT} is proportional to the total change in the system’s relativistic momentum

distribution between the incoming and outgoing state [67, 68, 307]. For example, in a simple case of particles with mass M_A and velocity v_A deflected by a collision, they found:

$$\Delta h_{ij}^{TT} = \frac{4}{r} \Delta \sum_{A=1}^N M_A \sqrt{1 - v_A^2} \left(\frac{v_A^i v_A^j}{1 - v_A \cos \theta_A} \right)^{TT}, \quad (6.15)$$

where r is the distance to the observer and θ_A is the angle of each particle's velocity relative to the observer [242]. This “linear” memory effect is now often called the ordinary displacement memory, as it causes a lasting displacement of test particles.

It was long assumed that this linear memory, arising from a change in matter distribution or radiation escaping to infinity, was the full story, until Demetrios Christodoulou made a groundbreaking discovery in 1991. Christodoulou showed that even in the absence of any net mass ejected, gravitational waves themselves carry energy and momentum and can induce an additional nonlinear memory effect [99, 100]. In other words, the spacetime curvature produced by the gravitational wave feed-back on itself, causing a permanent strain offset—a phenomenon now known as the nonlinear memory or null memory [242]. This revealed that gravitational memory is an inherent prediction of full General Relativity, not just an artifact of linearized theory. Subsequent work in the 1990s and 2000s [67, 68, 307, 53] further explored and confirmed the memory effect in various contexts, solidifying that any burst of gravitational radiation – such as from binary black hole mergers or supernovae – should leave behind a small but permanent distortion in the fabric of spacetime. In recent years, attention has also turned to new forms of memory in gravitational theory: notably, a “spin memory” effect was predicted around 2015–2016 [250, 168, 243], arising from the angular momentum carried by gravitational waves.

Physically, the gravitational wave memory effect can be understood as a permanent displacement or relative velocity change of free-falling test masses after a gravitational wave has passed. Imagine a ring of inertial detectors at rest relative to each other far from a source. As a burst of gravitational waves sweeps through, it will distort the ring – stretching and squeezing it—and typically, after the wave has passed, the ring does not return exactly to its original configuration. In the simplest case, the distances between the particles are permanently shifted by a tiny amount. This lasting offset is the hallmark of the memory effect: the spacetime has been “warped” in a way that persists even after the transient gravitational waves are gone. Unlike the oscillatory oscillations of a gravitational wave, which cause an AC

strain, the memory is like a DC offset—a non-oscillatory change in the gravitational field. The effect is extremely small for typical astrophysical sources, with fractional displacements of order 10^{-21} or less for LIGO-accessible events, but it is in principle measurable given sufficiently sensitive detectors or clever measurement techniques. Crucially, this permanent distortion is a genuine physical observable and not merely a gauge artifact. In General Relativity, the memory effect encodes the cumulative momentum flux carried away by the gravitational waves: essentially, the detectors remember the passage of a wave because the spacetime has been left in a different state from it was originally.

There are several distinct types of gravitational memory, characterized by how the relative motion of test particles is affected after the wave passes:

- **Displacement memory:** This is the classic memory effect described above, in which initially co-moving inertial observers end up with a lasting displacement between them but no relative motion at late times. The wave causes a permanent shift in their positions while their relative velocity returns to zero after the wave. This occurs, for example, when a burst of gravitational radiation carries away energy—the remaining field has a lower monopole or different multipole configuration, leading to a net change in the strain field [242]. Displacement memory is sourced by any net change in the stress-energy distribution, including both ordinary memory (from mass motions or ejecta) and nonlinear memory (from gravitational radiation itself) [99, 100, 298]. It manifests as a step-like change in the gravitational wave strain $h(t)$ as $t \rightarrow \infty$. In practical terms, two test masses initially at rest are permanently repositioned relative to each other after the wave.
- **Velocity memory:** In some scenarios, gravitational waves can impart a lasting velocity to test particles, rather than a mere offset. In a velocity memory effect, freely falling particles that start at rest acquire a constant relative velocity after the wave has passed, causing their separation to grow linearly with time [323]. This was noted in analyses of idealized plane-fronted gravitational waves: instead of a permanent displacement, the particles continue drifting apart indefinitely at a small constant speed. Early works by [67, 68, 69] considered this possibility, highlighting that an asymptotic relative velocity change is an alternative signature of memory. Whether displacement or velocity memory occurs depends on the nature of the source and the spacetime geometry of the

wave. For typical bounded sources such as binary mergers that become quiet after the burst, one expects displacement-type memory. On the other hand, an impulsive plane wave or a situation without a return to stationary conditions can produce a velocity memory effect, where the strain asymptotes to zero but with a “kick” imparted to the test masses [323].

- **Spin memory:** The spin memory effect is a more recently recognized type of memory associated with gravitational waves carrying angular momentum. It is related to the magnetic-parity part of the gravitational field perturbation. In technical terms, spin memory is tied to a nonzero change in the time-integral of the magnetic (B -mode) component of the strain, as opposed to the electric (E -mode) component that governs displacement memory [250, 168, 243]. Physically, one way to interpret spin memory is by considering observers with an initial relative motion: unlike displacement memory, which affects observers initially at rest relative to each other, spin memory affects observers that have some initial relative velocity or null separation [242].

Connecting Gravitational Memory with the Bondi–Sachs Framework

To formalize gravitational memory, it is helpful to work in the Bondi–Sachs framework, which provides a convenient description of asymptotically flat spacetimes at null infinity. In Bondi–Sachs coordinates, one uses retarded time u , a radial coordinate r , and angles (θ, ϕ) on the sky. The metric is chosen such that as $r \rightarrow \infty$ one approaches flat Minkowski space, with the coordinates adapted to outgoing radiation. A key feature of this framework is the asymptotic expansion of the metric at large r . For example, the angular part of the metric on a surface of constant u and r can be written as [298]:

$$g_{AB}(u, r, \theta, \phi) = r^2 q_{AB}(\theta, \phi) + r C_{AB}(u, \theta, \phi) + \dots, \quad (6.16)$$

where q_{AB} is the metric of the unit two-sphere and $C_{AB}(u, \theta, \phi)$ is the Bondi shear tensor. The shear C_{AB} represents the leading $\mathcal{O}(1/r)$ deviation of the metric from exact spherical symmetry—essentially it encodes the outgoing gravitational waves at infinity. One often decomposes C_{AB} into radiative modes via spherical harmonics of spin-weight 2, which correspond to the two polarization states of gravitational waves. The Bondi news tensor $N_{AB}(u, \theta, \phi)$ is then defined as the retarded time derivative of the shear:

$$N_{AB}(u, \theta, \phi) \equiv \partial_u C_{AB}(u, \theta, \phi). \quad (6.17)$$

This N_{AB} is essentially the gravitational wave strain rate observed at infinity. Importantly, $N_{AB}(u)$ vanishes in stationary regions of spacetime—if the source is not emitting gravitational waves, the shear is constant in time. If a burst of radiation is emitted, N_{AB} will be non-zero during the transient, and will return to zero after the source has settled down. Einstein’s field equations impose constraint conditions at null infinity relating these quantities to conserved charges. For instance, the Bondi mass aspect $m(u, \theta, \phi)$ evolves according to an energy conservation law:

$$\partial_u m = -\frac{1}{8} N_{AB} N^{AB} + \dots . \quad (6.18)$$

This equation shows that energy carried away by gravitational waves reduces the mass of the system: it is the Bondi mass-loss formula. Similarly, angular momentum aspects are related to angular integrals of N_{AB} and its angular moments [242]. The main point is that in the Bondi–Sachs picture, all the information about outgoing gravitational radiation is encoded in the news N_{AB} , and any permanent effect of that radiation will be encoded in the changes of the shear C_{AB} .

Given these definitions, we can formally define the gravitational memory in this context as the difference in the shear tensor between the final and initial states (before and after the burst of waves). If the spacetime is stationary (no news) in the remote past $u \rightarrow -\infty$ and becomes stationary again at $u \rightarrow +\infty$ after the waves have passed, one can compare the shear in the two regions. The memory is then quantified by

$$\Delta C_{AB} \equiv C_{AB}(u \rightarrow +\infty, \theta, \phi) - C_{AB}(u \rightarrow -\infty, \theta, \phi). \quad (6.19)$$

Equivalently, since $N_{AB} = \partial_u C_{AB}$, the memory can be expressed as the time-integral of the news during the burst:

$$\Delta C_{AB} = \int_{-\infty}^{+\infty} N_{AB}(u, \theta, \phi) du. \quad (6.20)$$

This gauge-invariant quantity ΔC_{AB} encapsulates the permanent strain offset produced by the gravitational waves [298, 295, 242]. In regions where there was no incoming radiation initially and no outgoing radiation finally, ΔC_{AB} completely characterizes the memory effect on the spacetime geometry. For example, for a binary black hole merger, one would find that C_{AB} , which is related to the gravitational waveform, approaches zero as $u \rightarrow -\infty$ and approaches some constant $C_{AB}^{(\infty)}$ as $u \rightarrow +\infty$ after the merger—this constant shear at late time is the gravitational memory encoded in the waveform [242]. In practice, ΔC_{AB} corresponds to the

permanent strain that would be measured by an idealized detector: if one computes the metric perturbation h_{ij} in transverse-traceless gauge far from the source, ΔC_{AB} is directly related to the change in h_{ij} projected onto a sphere's basis between the initial and final states:

$$h \equiv \frac{1}{2} \bar{q}^A \bar{q}^B C_{AB} = \sum_{\ell=2}^{\infty} \sum_{m=-\ell}^{\ell} h_{\ell m}(u) Y_{\ell m}^{(-2)}(\theta, \phi). \quad (6.21)$$

Here, (\bar{q}^A, \bar{q}^B) define the dyads on the two-sphere, and $Y_{\ell m}^{(-2)}(\theta, \phi)$ is the spin-weighted spherical harmonics. Thus, the Bondi–Sachs formalism provides a precise way to calculate memory from the radiative degrees of freedom of the spacetime.

The BMS Symmetry Group and Supertranslations

When studying asymptotically flat spacetimes at null infinity, one finds that the symmetry group of this boundary—the group of transformations that preserve the asymptotic form of the metric—is larger than the familiar Poincaré group of special relativity. Instead, it is the BMS group, first described by Bondi, van der Burg, and Metzner, and independently by Sachs, in 1962 [64, 280, 279]. The BMS group consists of the usual Lorentz transformations together with an infinite-dimensional family of angle-dependent translations, known as supertranslations [298, 295, 242]. In intuitive terms, a supertranslation is a shift of the retarded time coordinate u by an arbitrary function of the angular coordinates:

$$u \rightarrow u' = u + f(\theta, \phi), \quad (6.22)$$

for some smooth function f on the sphere. Unlike a constant time translation, this allows different time offsets in different angular directions. Such transformations preserve the asymptotic flatness of the metric, but they change the labeling of null rays and instantaneous slices of \mathcal{I}^+ . The existence of supertranslations implies that even after one fixes a convenient coordinate system at infinity, there remains a residual coordinate freedom corresponding to these angle-dependent shifts [242]. Physically, the BMS group is the symmetry group of isolated radiating systems: any two such systems that are related by a BMS transformation are indistinguishable as far as the asymptotic gravitational field is concerned, except for the transformation in coordinates [298, 295].

An important consequence of the BMS symmetry is the concept of degenerate vacua in general relativity. In classical field theory without gravity, one expects a unique vacuum state such as Minkowski space which is invariant under the Poincaré group.

However, once supertranslations are included, Minkowski spacetime is no longer invariant under all BMS transformations—applying a non-trivial supertranslation to flat Minkowski space yields a physically equivalent spacetime, but one described in a different coordinate frame that does not globally coincide with the original Minkowski frame [298]. In technical terms, Minkowski space, and more generally any stationary vacuum spacetime at null infinity, can be labeled by a function C_{AB} on the sphere that is pure gauge. A supertranslation with parameter $f(\theta, \phi)$ induces a shift in the shear: $C_{AB} \rightarrow C_{AB} + \delta_f C_{AB}$, where

$$\delta_f C_{AB} = 2D_A D_B f - q_{AB} D^2 f, \quad (6.23)$$

which is precisely the form of a memory-like strain¹. Thus, one can think of each function $f(\theta, \phi)$ as labeling a distinct “vacuum” configuration of the gravitational field at infinity. All these vacua are physically empty and flat, but they differ by a BMS frame—essentially, the relative orientation of the coordinate grid at infinity. They are sometimes described as an infinite degeneracy of Minkowski vacuum states, related by BMS supertranslation symmetries [297, 298, 177, 295].

One of the most important insights about the gravitational memory effect is that it corresponds to a transition between different BMS vacua—in other words, the memory is essentially a BMS supertranslation [298]. This can be understood as follows: consider an isolated system that starts in a stationary configuration at early times, and ends in another stationary configuration at late times after emitting gravitational waves. The initial state can be characterized by some shear $C_{AB}^{(\text{ini.})}$, which can be taken to zero by an appropriate choice of coordinates, and the final state by some $C_{AB}^{(\text{fin.})}$. If there is a non-zero memory $\Delta C_{AB} = C_{AB}^{(\text{fin.})} - C_{AB}^{(\text{ini.})}$, this difference is a stationary shear configuration on the sphere. As noted above, any static shear configuration can be viewed as a pure gauge associated with a supertranslation [242]. This means that the effect of the gravitational wave burst has been to change the spacetime from one BMS frame to another. The gravitational wave has essentially applied a supertranslation to the spacetime.

In concrete terms, if one were to compare the metric of the spacetime before and after the radiation, one could find a coordinate transformation, a particular supertranslation f on the sphere, that relates the two metrics. That supertranslation

¹The expression $\delta_f C_{AB} = 2D_A D_B f - q_{AB} D^2 f$ is the leading-order effect of an infinitesimal supertranslation on the shear. This comes from how the Bondi metric transforms: since u is shifted by $f(\theta, \phi)$, the shear gains a gradient term. Any such pure-gauge C_{AB} , coming from some f , is often called a soft mode of the gravitational field.

is precisely what ΔC_{AB} encodes. Therefore, the memory effect is equivalent to a BMS supertranslation imparted to the system by the passage of radiation [298, 295, 177, 243, 242]. Another way to say this is that the gravitational wave memory is the imprint of the gravitational waves' energy-momentum on the spacetime, manifesting as a shift in the zero of the Bondi coordinate u as a function of angle. This connection was made explicit by Strominger and others in the mid-2010s: they showed that the traditional memory formula can be derived as a consequence of BMS supertranslation symmetry and associated conservation laws at null infinity [297, 188, 183, 189, 298, 244, 177]. In particular, every burst of gravitational waves carries a certain “soft graviton” component, which is associated with a shift in the classical field—the memory—and this is precisely the soft mode associated with a broken BMS symmetry. The initial and final vacua differ by that soft graviton insertion.

This perspective places memory in the context of conservation laws and symmetries. For example, energy conservation at null infinity implies that if energy E is radiated away, the Bondi mass at infinity decreases by E . But in a theory with the BMS group, there is an associated balance law for the supertranslation charge. The supertranslation charge can be thought of as the “net displacement” of the center-of-mass frame at infinity. The memory effect ensures that this balance law is satisfied: the change in the supertranslation charge between the initial and final state is provided exactly by the flux of energy-momentum carried by the news N_{AB} [298, 295].

Observational Prospect

The detection of gravitational memory would have significant implications for both astrophysics and fundamental physics. From an observational standpoint, measuring the memory effect would provide a direct validation of General Relativity's nonlinear dynamics. In particular, observing the Christodoulou memory [99] would confirm that gravity gravitates—*i.e.*, gravitational waves themselves produce a gravitational field—a quintessentially general relativistic phenomenon. It would also test the BMS symmetry of spacetime: a positive detection could be viewed as evidence that the BMS conservation laws (associated with supertranslations) hold in nature, and that the vacuum of gravity is indeed degenerate and can be shaken by radiation. Detecting memory would thus probe the infrared structure of gravity—the realm of long-wavelength (near-zero-frequency) gravitons and their associated symmetries [188, 183, 189, 295, 182, 244].

Experimentally, the memory effect is subtle, because it involves zero-frequency or very low-frequency gravitational strain. Traditional laser interferometric detectors like LIGO and Virgo are AC-coupled and cannot easily measure a direct DC offset in the interferometer arm lengths. Moreover, after a burst passes, the interferometer components tend to gradually drift back to equilibrium due to seismic and suspension damping, potentially masking a small permanent shift. These factors make directly detecting memory with ground-based detectors challenging [107]. Indeed, so far no definitive memory signal has been observed in LIGO/Virgo data. However, novel methods are being pursued: for example, one can look for an effective low-frequency “tail” in the gravitational wave signal or stack the results of many events to boost the signal-to-noise of memory [63]. By statistically combining multiple binary merger events, researchers hope the cumulative memory effect could emerge [325, 66].

Looking ahead, the prospects for detecting memory improve dramatically with planned space-based interferometers. The proposed LISA mission [30], operating in the millihertz band, will observe long-lived signals from massive black hole mergers and other slow, powerful sources. Crucially, LISA will be sensitive to much lower frequencies and will essentially be in free fall, which makes them well-suited to observe the memory effect [196]. Simulations [159, 196] suggest that LISA should detect the displacement memory from massive black hole mergers: the memory step for such events can be a significant fraction of the peak strain, and LISA’s long observation time of the inspiral allows one to measure the wave’s non-zero baseline shift [196]. In addition, LISA might detect memory from the cumulative effect of many smaller sources [325] or even nonlinear gravitational memory from extreme mass-ratio inspirals and bursts [159]. There is also the possibility of observing the spin memory in the waveform of certain events or by networking multiple detectors [158]. Efforts are underway to forecast how a network of next-generation ground detectors such as the Einstein Telescope or Cosmic Explorer and LISA together could measure both the displacement and spin memory effects [242].

6.4 Stochastic Gravitational Wave Memory Background

Although individual GW memory events may be extremely challenging to detect directly, the cumulative effect of many such events over cosmic time can produce a stochastic gravitational-wave memory background (SGWMB). This SGWMB is formed by the superposition of countless memory steps from distant mergers and can be described statistically as a random-walk accumulation of strain in the universe [325, 66]. Each memory-generating merger adds a tiny permanent tensor

perturbation; over billions of years and many sources, these add up in random directions. The result is analogous to Brownian motion: the metric undergoes a slow diffusive evolution as successive memory “kicks” build up. Importantly, this memory background is expected to be subdominant in amplitude compared to the ordinary oscillatory SGWB produced by the inspiral and ringdown waves of the same sources [325]. Nevertheless, the SGWMB represents a unique signal with distinct characteristics that make it worth investigating, especially since detecting it would confirm a fundamental prediction of general relativity’s radiative structure.

Statistical Model and Spectral Characteristics

We model the SGWMB as the sum of discrete step-like strain contributions. Let $\Delta h_i(t)$ represent the memory strain from the i -th merger event, which for simplicity can be idealized as a Heaviside step function $\Theta(t - t_i)$ scaled by the memory amplitude Δh_i . The total strain from memory at time t is then $h_{\text{mem}}(t) = \sum_i \Delta h_i \Theta(t - t_i)$, where t_i are the random occurrence times of mergers. If the merger events occur as a Poisson process with an average rate R , one can show that $h_{\text{mem}}(t)$ behaves like a stochastic process with unbounded variance (a random walk). The mean squared strain grows linearly in time, $\langle [h_{\text{mem}}(t) - h_{\text{mem}}(0)]^2 \rangle = 2Dt$ for large t , where D is an effective diffusion constant proportional to the merger rate and the typical squared memory kick amplitude [325, 66]. In the frequency domain, this leads to a characteristic PSD $S_h(f)$ that falls off as the inverse square of frequency. Quantitatively, one can derive the PSD for one-dimensional Brownian motion by using the Wiener–Khinchin theorem [155]. First, recall that the white noise is a purely random, non-correlated noise which satisfy the following condition:

$$\langle \xi(t_1)\xi(t_2) \rangle = 2D\delta(t_1 - t_2), \quad (6.24)$$

where ξ is a white noise, and $\langle \cdot \rangle$ denotes averaging over different time moments. Note that such signal has no trends, its spectral density is constant, and depends only on the standard deviation of the particular white noise. A Brownian motion, also known as a Wiener process, on the other hand, arises from the accumulation of many white noise perturbations [155]. Mathematically, we let $W(t)$ denote a Brownian motion, which is a sum of the white noise:

$$dW(t) = W(t + dt) - W(t) = \xi(t)dt, \quad (6.25)$$

and

$$W(t) = \int_0^t dW(t') = \int_0^t \xi(t')dt'. \quad (6.26)$$

Since $W(t)$ is a Brownian motion, it satisfies the following important properties

$$\langle W(t) \rangle = 0 \quad \text{and} \quad \langle [W(t) - W(0)]^2 \rangle = 2Dt. \quad (6.27)$$

In other words, $W(t)$ has a probability density function of the normal distribution with mean zero and variance $2Dt$. Another important property for Brownian motion is that

$$\langle W(t)W(s) \rangle = 2D \min(t, s). \quad (6.28)$$

This property can be readily proved by using (6.27) as well as the fact that $W(t) - W(s)$ is independent of $W(s)$. Putting everything together, we compute the double-sided PSD of a Brownian motion

$$\begin{aligned} S_h^{\text{mem}}(f) &\equiv \lim_{T \rightarrow \infty} \frac{1}{T} \int_0^T dt_1 \int_0^T dt_2 e^{i2\pi f(t_1-t_2)} \underbrace{\langle W(t_1)W(t_2) \rangle}_{2D \min(t_1, t_2)} \\ &= \lim_{T \rightarrow \infty} \left\{ \frac{2D}{T} \int_0^T dt_1 \int_0^{t_1} dt_2 e^{i2\pi f(t_1-t_2)} t_2 + \int_0^T dt_1 \int_{t_1}^T dt_2 e^{i2\pi f(t_1-t_2)} t_1 \right\} \\ &= \lim_{T \rightarrow \infty} \frac{D}{(\pi f)^2} \left[1 - \frac{\sin(2\pi f T)}{2\pi f T} \right] \\ &= \frac{D}{(\pi f)^2}. \end{aligned} \quad (6.29)$$

The hallmark of a $1/f^2$ power-law spectrum expected from a Brownian motion process is fundamentally different from the nearly white-noise (f^0) spectrum that would come from a memory-like burst rate that is uncorrelated, because here each event's effect persists indefinitely. Eq. (6.29) can be understood intuitively: the time derivative $\dot{h}_{\text{mem}}(t)$ is a train of delta-function impulses (each memory event induces an impulse in \dot{h}), which has a flat spectrum at low frequencies; integrating \dot{h} to get h then divides the spectrum by f^2 , yielding $S_h^{\text{mem}} \propto 1/f^2$. In such a scenario, the power-law index of the memory background PSD is -2 , independent of the details of the source population [325, 66]. This result is robust and in fact is expected to hold as a generic feature of any SGWMB in general relativity.

From the PSD, one can derive the corresponding characteristic strain spectrum $h_c(f)$ and energy density spectrum $\Omega_{\text{mem}}(f)$. The characteristic strain $h_c(f)$, defined in Eq. (6.8), represents the strain amplitude per logarithmic frequency interval. Substituting $S_h^{\text{mem}}(f)$ from Eq. (6.29) and converting it to the one-sided PSD by

multiplying a factor of two, we obtain:

$$h_c^{\text{mem}}(f) = \sqrt{2fS_h} = \sqrt{\frac{2D}{\pi^2 f}}. \quad (6.30)$$

Thus $h_c(f)$ of the memory background rises toward lower frequencies as $f^{-1/2}$, indicating a very strong low-frequency contribution [325, 66]. In other words, the memory-induced background has a much larger strain at the lowest frequencies than at higher frequencies—a direct consequence of the permanent nature of the memory strain. However, it's important to recognize that in any finite observation, frequencies below about $1/T_{\text{obs}}$, with T_{obs} the observation time, cannot be measured, so the $h_c \propto f^{-1/2}$ growth will eventually saturate in practice.

Recall that the energy density Ω_{gw} for SGWB is given by Eq. (6.6). Furthermore, for a generic SGWB, Ω_{gw} is related to the PSD (6.7), so when we substitute the PSD of a Brownian motion (6.29), we obtain the energy density for SGWMB:

$$\Omega_{\text{mem}} = \frac{4Df}{3H_0^2}. \quad (6.31)$$

Thus, in the low-frequency regime where the memory approximation holds, $\Omega_{\text{mem}}(f)$ grows linearly with frequency [325, 66]. At the lowest accessible frequencies, Ω_{mem} will be suppressed, which reflects the fact that memory carries only a finite total energy—there is no divergent pile-up of energy at zero frequency even though the strain variance grows without bound. The slope $\Omega_{\text{mem}}(f) \propto f$ is shallower than that of the standard astrophysical SGWB from inspiraling compact binaries, which typically scales as $\Omega_{\text{gw}}(f) \propto f^{2/3}$ at low frequencies [225, 325, 78]. This means that the memory background is subdominant at low frequencies, but may become relatively more significant at higher frequencies where its steeper rise begins to catch up. In fact, at sufficiently low frequencies within the observation band, one can anticipate that $\Omega_{\text{mem}}(f)$ will eventually overtake the rising inspiral background, which grows as $f^{2/3}$ more slowly than f —except that the inspiral background itself ceases to grow once binaries start merging. In practice, there will be a transition frequency around the merger regime of the binaries: above this frequency, the ordinary GW background from inspiral/merger waves dominates, while below a certain cutoff frequency, related to the typical merger time scale, the memory-induced f^{-2} spectrum dominates [325]. For supermassive binary black holes (SMBHs), this transition lies in the millihertz range (the boundary between the inspiral-dominated and merger-dominated spectrum for a $\sim 10^6$ – $10^8 M_\odot$ binary is on the order of 10^{-2} – 10^{-3}

Hz) [325, 66]. Crucially, the amplitude of the memory background, the constant diffusion coefficient D , in the above formulas, is set by the cosmic merger rate and typical memory kick size. In fact, detailed calculations find that the strength of the SGWMB is determined entirely by the binary black hole merger rate, largely independent of other astrophysical details [325]. In simple terms, more frequent mergers lead to a higher diffusion constant D and thus a stronger memory background. This implies that an observed $\Omega_{\text{mem}}(f)$ directly encodes information about the population merger rate—a point of great interest for astrophysics.

6.5 Toward Detectability with LISA

Detecting the SGWMB is a formidable challenge, but Ref. [325] claims that near-future space-based interferometers such as LISA offer an excellent opportunity to observe this background. These detectors are sensitive in the low-frequency band ($\sim 10^{-4}$ to 1 Hz) where the memory background is expected to be significant [30, 325, 37, 42]. Moreover, the target sources for these missions are precisely SMBH mergers, which produce the largest memory jumps. In contrast, current ground-based detectors (LIGO, Virgo, KAGRA) operate at higher frequencies ($\gtrsim 10$ Hz) and have shorter observation times, making them ill-suited to detect a slowly accumulating memory background. The quasi-DC nature of memory signals means that ground detectors would see them as an almost step-like offset, which is very hard to extract from instrumental drifts and low-frequency noise. Indeed, it has been estimated that a single memory event in LIGO is undetectable without special analysis techniques, and a statistical memory background in the audio-band would require an impractically large number of merger events. PTAs, on the other hand, probe ultra-low frequencies ($\sim 10^{-9}$ – 10^{-7} Hz) and could in principle observe memory from the most massive black hole mergers as a one-time pulse in pulsar signals. However, such events are exceedingly rare; PTAs might need to wait much longer than a human lifetime to catch a single, sufficiently nearby SMBH memory burst. The stochastic memory background from many smaller events is likely to be buried under the louder ordinary nanohertz GW background and intrinsic pulsar noise [325]. Therefore, neither current ground detectors nor PTAs are expected to detect a SGWMB under realistic scenarios.

Space-based GW observatories fill the sweet spot for SGWMB detection. Their frequency band is low enough that memory signals from SMBH mergers accumulate power, since $h_c \sim f^{-1/2}$ grows toward this band, yet high enough that a large number of such mergers have occurred over cosmic history to contribute to

a detectable background. Furthermore, missions like LISA will operate for years, enabling integration over a long time to build up sensitivity at the lowest frequencies. The anticipated approach to detect a SGWMB is analogous to that for any stochastic background: one would use cross-correlation or auto-correlation analysis of the detector data, looking for the characteristic spectral shape of a SGWMB. Because LISA is essentially a single-detector system with multiple laser links forming one or a few independent data channels, the standard strategy is to use the instrument's multiple channels or pair different detectors to cross-correlate and cancel out instrumental noise. The unique spectral signature of the memory background—a power-law of index -2 in $S_h(f)$ —helps in distinguishing it from other stochastic signals. In practice, one would search for an $\Omega_{\text{gw}}(f)$ that rises $\propto f^1$ at the lowest frequencies, in contrast to, say, a relic cosmological background that might be flat or decreasing toward low f [325, 78, 66].

Specifically, current estimates [325] suggest that a SGWMB from SMBH mergers could be within reach of LISA and its contemporaries. Using fiducial SMBH merger rates from models, on the order of a few per year out to high redshift, the predicted memory background characteristic strain $h_c(f)$ in the LISA band is around 10^{-16} – 10^{-17} at $f \sim 10^{-3}$ Hz, rising toward $\sim 10^{-15}$ at 10^{-4} Hz [325]. These levels are comparable to or somewhat below the projected LISA sensitivity to a stochastic background after $T \sim 4$ – 10 years of integration. In a detailed analysis, Ref. [325] find that for a range of plausible SMBH merger rates, the memory background is actually stronger than the corresponding non-memory background in the LISA band. This is because many of the inspiral signals at mHz frequencies will eventually merge, thereby removing power from the stochastic background as those sources become individually resolvable, whereas the memory from all those mergers accumulates in the low-frequency background. Moreover, the power-law integrated sensitivity curves for LISA, Taiji, and TianQin indicate that a $1/f^2$ spectrum at the expected amplitude would be detectable with a favorable SNR [325]. In fact, taking optimistic merger rate models, the predicted SGWMB could yield $\text{SNR} \gg 1$; Ref. [325] reports SNR values ranging from order unity in pessimistic cases up to hundreds or thousands in the most optimistic scenarios.

It is worth noting that separating the SGWMB from the ordinary gravitational wave background requires careful data analysis. Since LISA is expected to individually resolve the loudest inspiral and merger events, particularly from SMBH, standard practice would involve subtracting the modeled waveforms of these events from the

data. This subtraction necessarily removes not only the oscillatory inspiral-merger-ringdown signal but also the associated memory step, insofar as it is captured by the waveform model. However, residual memory contributions from unresolved or distant mergers—too weak or too numerous to be subtracted individually—will persist, forming a diffuse memory background. Therefore, the SGWMB to be detected by LISA will predominantly consist of memory signals originating from nonresolvable sources.

In the following analysis, we aim to quantitatively assess the claim of Ref. [325] that the SGWMB remains a pronounced background well above LISA’s sensitivity curve. To this end, we first subtract the waveforms of all individually resolvable mergers, thereby removing their associated memory contributions. We then recompute the diffusion coefficient that characterizes the cumulative memory strain from the remaining unresolved events. Using this updated diffusion coefficient, we calculate the revised SGWMB spectrum and plot it against LISA’s sensitivity curve. This procedure allows us to evaluate whether the residual memory background—after accounting for source subtraction—remains detectable by LISA.

Derivation of the Diffusion Coefficient

The goal of this section is to derive the analytical expression for the diffusion coefficient D of the SGWMB, which directly determines the characteristic strain $h_c(f)$, the power spectral density $S_h(f)$, and the energy spectrum density $\Omega_{\text{mem}}(f)$ via Eqs. (6.30), (6.29), and (6.31), respectively. To begin, we first specify the memory strain produced by a single merger event.

Refs. [141, 142, 143] derived an analytical expression for the memory waveform—known as the minimal waveform model—that agrees with numerical relativity simulations [243, 242]. However, due to its complexity and computational cost, we instead adopt the step function model [268, 223, 325, 66], which approximates the memory as an instantaneous strain jump at the merger time:

$$h_{\text{det}}(t) = \Theta(t - t_0) F_+(\theta, \phi, \psi) h_+^{\text{mem}}(z, M, \theta), \quad (6.32)$$

where $\Theta(t - t_0)$ is the Heaviside step function centered at the merger time t_0 , F_+ is the detector antenna response to the + polarization, and h_+^{mem} is the memory strain amplitude. This approximation assumes that the merger timescale is much shorter than the observation timescale.

The antenna pattern F_+ is given by [325]

$$F_+(\theta, \phi, \psi) = -\frac{1}{2}(1 + \cos^2 \theta) \cos 2\phi \cos 2\psi - \cos \theta \sin 2\phi \sin 2\psi, \quad (6.33)$$

and its sky- and polarization-averaged value for LISA is [30]

$$\langle F_+^2 \rangle = \frac{1}{4\pi^2} \int_0^{2\pi} d\phi \int_0^\pi \sin \theta d\theta \int_0^\pi d\psi F_+^2 = \frac{1}{5}. \quad (6.34)$$

Since the memory signal predominantly arises from the + polarization for compact binary mergers [141, 325, 66], it suffices to model the memory strain for the + mode. Specifically, for SMBH mergers, we write

$$h_+^{\text{mem}} = Y_{20}^{(-2)}(\theta, \phi) h_{20}, \quad (6.35)$$

where the spin-weighted spherical harmonic $Y_{20}^{(-2)}(\theta, \phi)$ is [164]

$$Y_{20}^{(-2)}(\theta, \phi) = \sqrt{\frac{15}{32\pi}} \sin^2 \theta, \quad (6.36)$$

with the normalization convention as $\int d\Omega |Y_{20}^{(-2)}|^2 = 1$. The amplitude h_{20} is given by [268, 223, 325]

$$h_{20} = \frac{GM}{c^2 r} \left(0.0969 + 0.0562\chi_{\text{eff}} + 0.0340\chi_{\text{eff}}^2 + 0.0296\chi_{\text{eff}}^3 + 0.0206\chi_{\text{eff}}^4 \right), \quad (6.37)$$

where M is the total mass of the binary, r is the luminosity distance, and $\chi_{\text{eff}} \equiv (m_1\chi_{1z} + m_2\chi_{2z})/M$ is the effective spin parameter.

For simplicity, we restrict to the case of nonspinning SMBHs, for which $\chi_{\text{eff}} = 0$ and Eq. (6.37) reduces to

$$h_{20} = \frac{GM}{c^2 r} \times 0.0969. \quad (6.38)$$

In Fig. 6.2, we compare the step-function model with a full numerical relativity memory waveform [242] for a nonspinning equal-mass binary of total mass $M = 60 M_\odot$ at a distance $r = 10$ Mpc, showing that the step-function approximation captures the key features of the memory signal.

Having established the memory waveform model, we now compute the total gravitational-wave energy density spectrum using the standard formula [12]:

$$\Omega_{\text{mem}}(f) = \frac{f}{\rho c H_0} \int_0^\infty dz \frac{R_{\text{SMBH}}(z) \langle dE_{\text{mem}}/df \rangle}{(1+z)\sqrt{\Omega_\Lambda + \Omega_M(1+z)^3}}. \quad (6.39)$$

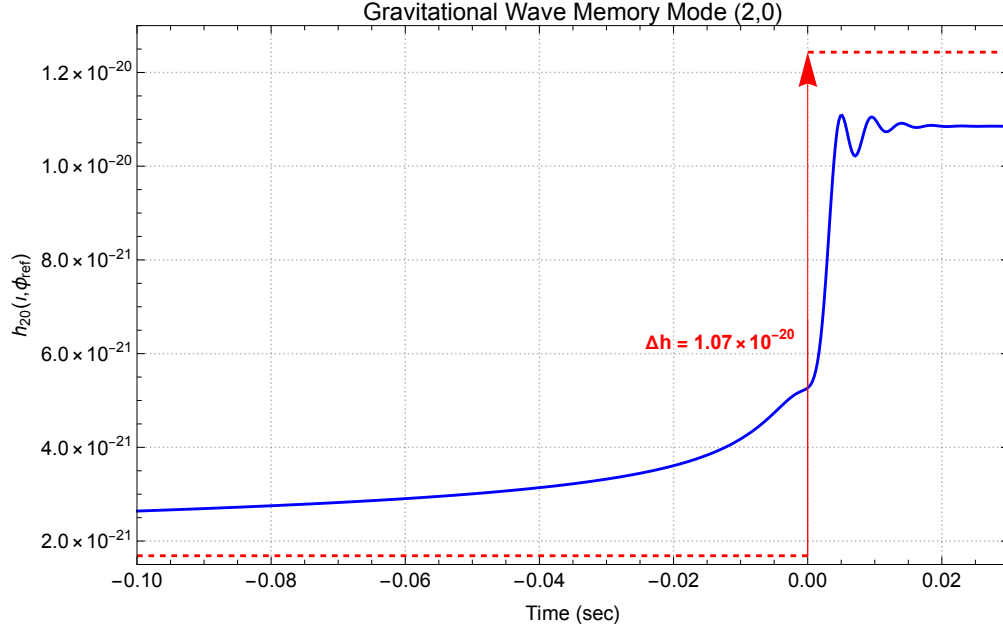


Figure 6.2: Comparison between the numerical relativity waveform h_{20} (blue curve) [242] and the step function model (red dashed line, Eq. (6.38)). Parameters: $\chi_A = \chi_B = 0$, $m_A = m_B$, $M = 60 M_\odot$, $r = 10$ Mpc, incl. angle = 0, $\phi_{\text{ref}} = 0$.

Here $\Omega_M = 0.3$ and $\Omega_\Lambda = 0.7$ are the matter and dark energy density parameters, respectively. $R_{\text{SMBH}}(z)$ denotes the redshift-dependent SMBH merger rate, which we will specify shortly. The ensemble average $\langle \cdot \rangle$ involves integration over the mass and angular distributions: $\langle \cdot \rangle = \int d\theta \sin \theta \int dM g_{\text{SMBH}}(M)$, where $g_{\text{SMBH}}(M)$ is the SMBH mass distribution function, which we will also specify shortly.

Another advantage of employing the step function model is the simplicity of its Fourier transform. Specifically, the Fourier transform of $h(t)$ is

$$\mathcal{F}[\Theta(t)] = \frac{1}{2} \delta(f) + \frac{1}{2\pi i f}. \quad (6.40)$$

Since gravitational wave detectors are insensitive to the extremely low-frequency regime, we can safely neglect the δ -function contribution in the analysis of $\tilde{h}(f)$.

The GWM energy spectrum per unit frequency is given by [263, 66],

$$\frac{dE_{\text{mem}}}{df} = \frac{\pi^2 c^3}{G} d^2(z) (1+z)^2 f^2 |\tilde{h}[f(1+z)]|^2, \quad (6.41)$$

where $d(z)$ is the comoving distance to the source, expressed as

$$d(z) = \frac{c}{H_0} \int_0^z \frac{dz'}{\sqrt{\Omega_\Lambda + \Omega_M(1+z')^3}}. \quad (6.42)$$

Substituting Eqs. (6.32)–(6.42) into the expression for Ω_{mem} , we arrive at an analytical formula for the memory energy density of SGWMB,

$$\Omega_{\text{mem}}(f) = \left(\frac{2\pi G^2 \mathcal{N}^2 \sigma_\theta^2}{3H_0^3 c^3} \right) f \int dM M^2 g_{\text{SMBH}}(M) \int_0^\infty dz \frac{R_{\text{SMBH}}(z)}{(1+z)\sqrt{\Omega_\Lambda + \Omega_M(1+z)^3}}, \quad (6.43)$$

where $\mathcal{N} = 0.0969$ from Eq. (6.38), and the angular factor σ_θ^2 is defined as

$$\sigma_\theta^2 = \int_0^\pi d\theta \sin\theta \left[Y_{20}^{(-2)} \right]^2 = \frac{1}{2\pi}. \quad (6.44)$$

By equating (6.43) with the earlier expression for Ω_{mem} in Eq. (6.31), we can immediately extract the diffusion coefficient D as

$$D = \frac{\pi G^2 \mathcal{N}^2 \sigma_\theta^2}{2H_0 c^3} \int dM M^2 g_{\text{SMBH}}(M) \int_0^\infty dz \frac{R_{\text{SMBH}}(z)}{(1+z)\sqrt{\Omega_\Lambda + \Omega_M(1+z)^3}}. \quad (6.45)$$

In the following section, we will adopt a specific SMBH population model from Ref. [66] to numerically evaluate D , and subsequently determine the corresponding characteristic strain $h_c(f)$ and energy density spectrum $\Omega_{\text{mem}}(f)$. We will then implement a SNR cutoff to exclude individually resolvable merger events from the computation of D , and assess the resulting impact on the residual SGWMB spectrum after resolved sources have been subtracted.

Implementation of the SMBH Population Model

There are several SMBH population models available in the literature. In this work, we adopt the model proposed in [66], as its parameters are clearly specified and its predictions are consistent with the results of Ref. [325].

Table 6.1: SMBH Model Parameters. We use $\mathcal{N}(\mu, \sigma)$ to denote normal distribution, and $\mathcal{U}_{[a,b]}$ to denote the uniform distribution [66].

Parameter	Distribution	Mean Value
$\log_{10} \frac{\dot{n}_0}{(\text{Mpc}^{-3} \text{Gyr}^{-1})}$	$\mathcal{N}(-3, 1)$	-3
α_M	$\mathcal{U}_{[-2,2]}$	0
$\log_{10} \frac{M_*}{M_\odot}$	$\mathcal{U}_{[6.5,8.5]}$	7.5
β_z	$\mathcal{U}_{[0,7]}$	3.5
z_c	$\mathcal{U}_{[0,5]}$	2.5

The population model used in [66] was first outlined in Refs. [239, 238, 292], capturing the key astrophysical features of SMBH mergers while maintaining computational simplicity. In this framework, the redshift-dependent merger rate R_{SMBH}

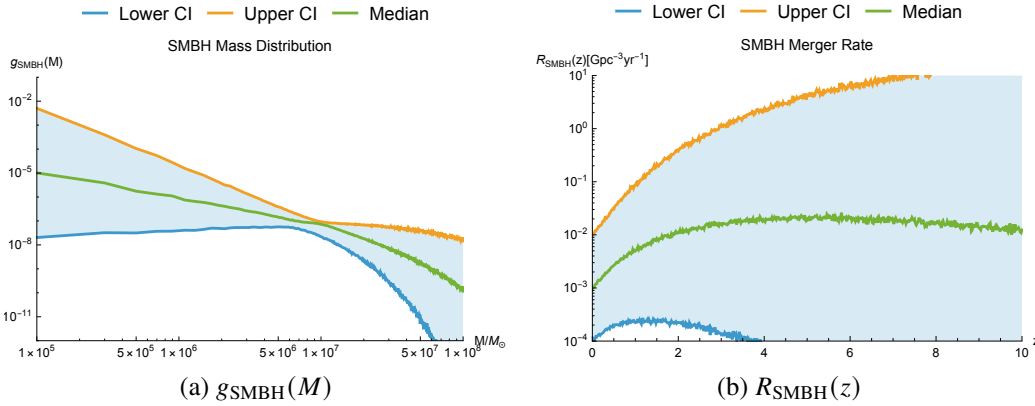


Figure 6.3: Mass probability density function and merger rate for SMBH population model using Eqs. (6.47) and (6.46) are shown. The shaded region denotes the $1\text{-}\sigma$ confidence interval [66].

follows a modified Schechter-like function:

$$R_{\text{SMBH}}(z) = \dot{n}_0 (1+z)^{\beta_z} e^{-z/z_c}, \quad (6.46)$$

where \dot{n}_0 is the local merger density rate measured per unit comoving volume and rest-frame time. The corresponding mass probability distribution $g_{\text{SMBH}}(M)$ is given by

$$g_{\text{SMBH}}(M) = \frac{1}{M} \left(\frac{M}{10^7 M_\odot} \right)^{-\alpha_M} e^{-M/M_*}, \quad (6.47)$$

describing a power law with an exponential cutoff.

A plot of g_{SMBH} and R_{SMBH} with $1\text{-}\sigma$ confidence interval is shown in Fig. 6.4. In this model, the parameters α_M and M_* characterize the shape of the mass distribution $g_{\text{SMBH}}(M)$, while β_z and z_c determine the redshift evolution of the merger rate $R_{\text{SMBH}}(z)$.

By substituting the expressions for the merger rate $R_{\text{SMBH}}(z)$ from Eq. (6.46) and the mass distribution $g_{\text{SMBH}}(M)$ from Eq. (6.47) into the diffusion coefficient formula Eq. (6.45), we compute the resulting SGWMB energy density spectrum $\Omega_{\text{mem}}(f)$. The resulting spectrum is shown in Fig. 6.4a.

Using Eq. (6.30), we also derive the corresponding characteristic strain spectrum $h_c^{\text{mem}}(f)$, which is plotted in Fig. 6.4b.

Both plots reveal substantial variance in the amplitude of $\Omega_{\text{mem}}(f)$ and $h_c^{\text{mem}}(f)$ even within a single population model, suggesting that the SGWMB from SMBH mergers could exhibit significant amplitude fluctuations. This variability indicates

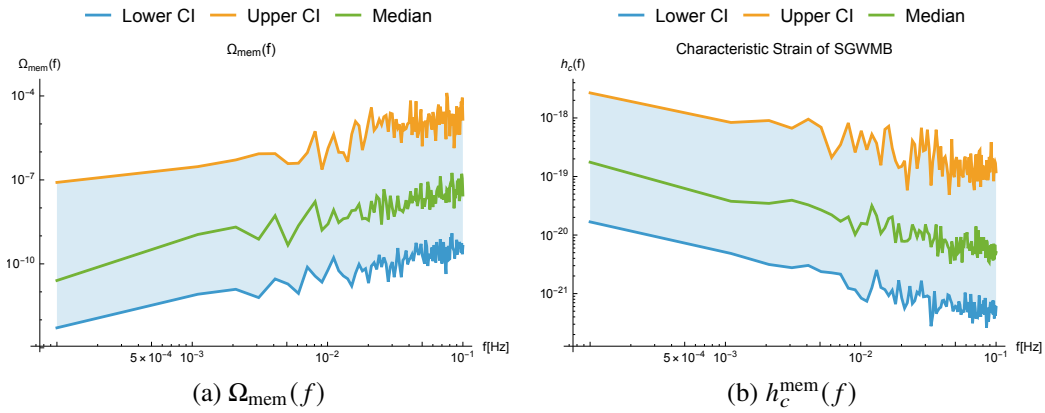


Figure 6.4: Left: SGWMB energy spectrum density Ω_{mem} as a function of frequency along with its $1\text{-}\sigma$ confidence interval. Right: SGWMB characteristic strain h_c^{mem} as a function of frequency along with its $1\text{-}\sigma$ confidence interval.

that, in favorable scenarios, the SGWMB could constitute a prominent background for space-based detectors such as LISA [30, 37, 42].

Recall that LISA achieves peak sensitivity around $f_{\text{peak}} \sim 10^{-2}$ Hz, with a characteristic strain sensitivity approximately $h_c^{(\text{min})} \sim 10^{-20}$ [37]. From Fig. 6.4b, it is evident that the predicted SGWMB lies well above LISA's sensitivity threshold in a substantial fraction of the parameter space, suggesting promising prospects for detection.

However, it is important to note that the analysis above does not account for the subtraction of individually resolvable merger events. In the next section, we incorporate this effect by excluding resolvable sources from the SGWMB computation, recalculating the diffusion coefficient, and reassessing the resulting power spectrum, energy density, and characteristic strain to reevaluate the detectability prospects with LISA.

Subtraction of Individually Memory Resolvable Merger Events

In this section, our objective is to compute the SNR of individual memory jumps from a population of SMBH merger events detectable by LISA. To maintain computational tractability, we adopt the step function model (6.32) rather than the full numerical relativity waveforms.

As a further simplification, we evaluate the merger rate $R_{\text{SMBH}}(z)$ (6.46) and mass distribution $g_{\text{SMBH}}(M)$ (6.47) using the mean values of the parameters listed in the third column of Table 6.1. The resulting distributions, based on these average

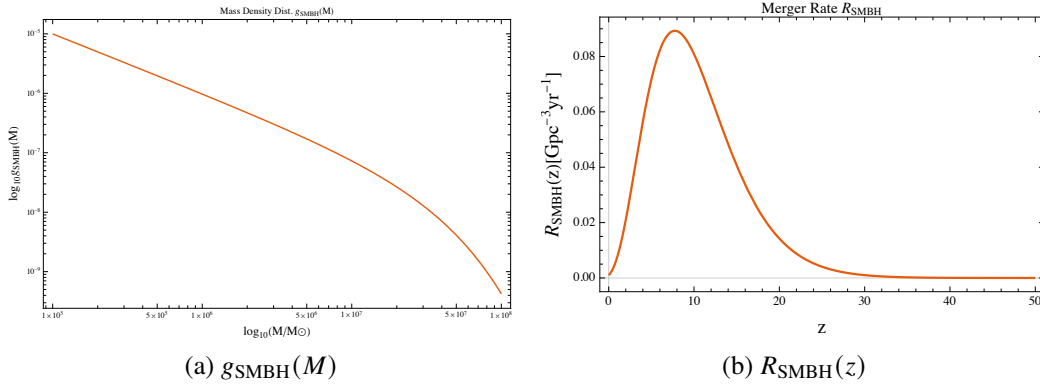


Figure 6.5: Left: SMBH mass distribution $g_{\text{SMBH}}(M)$ computed using the mean parameter values from Table 6.1. Right: SMBH merger rate $R_{\text{SMBH}}(z)$ evaluated using the same set of mean parameters.

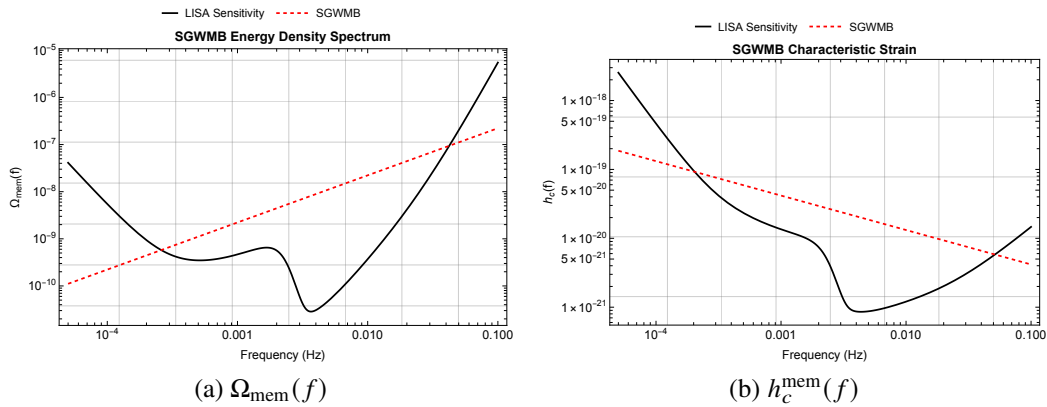


Figure 6.6: Left: SGWMB energy density spectrum (red dashed line) computed using the mean values from the SMBH population model parameters in Table 6.1, shown alongside LISA's sensitivity curve (black solid line). Right: SGWMB characteristic strain (red dashed line) based on the same mean parameter values, plotted against LISA's characteristic noise curve (black solid line).

parameters, are shown in Fig. 6.5.

Using these distributions, we compute the diffusion coefficient D via Eq. (6.45). The corresponding SGWMB energy density spectrum $\Omega_{\text{mem}}(f)$ and characteristic strain $h_c^{\text{mem}}(f)$ are then obtained and plotted against LISA's sensitivity curve, taken from Ref. [30], as shown in Fig. 6.6.

As shown in Fig. 6.6, the SGWMB, under optimistic assumptions, lies well above the sensitivity threshold of LISA in its optimal frequency range. However, since LISA is specifically designed to resolve and detect individual SMBH merger events [37, 42], it is crucial to account for the subtraction of these resolvable events. Af-

ter subtraction, only the residual memory contributions from unresolved or distant mergers—too faint or too numerous to be individually detected—will remain, forming a diffuse memory background.

We now assess whether the residual SGWMB remains detectable by LISA after subtracting individually resolvable sources. As a first step, we recall the SNR formula for a single memory event [141, 142, 143]:

$$\text{SNR} = \left[\int_0^\infty \frac{h_c^2(f) df}{h_n^2(f) f} \right]^{1/2}. \quad (6.48)$$

Here, $h_n(f)$ denotes the sky-averaged root-mean-square (rms) noise amplitude for LISA [141, 30], which is given by

$$h_n(f) = \sqrt{\frac{20}{3} f S_n(f)}, \quad (6.49)$$

where $S_n(f)$ is the one-sided noise power spectral density.

The memory characteristic strain $h_c^{\text{mem}}(f)$ is defined as [141, 142, 143]

$$h_c^{\text{mem}}(f) = 2(1+z)f \left\langle \left| \tilde{h}_+^{\text{mem}}[(1+z)f] \right|^2 \right\rangle^{1/2} \Big|_{r \rightarrow d(z)}, \quad (6.50)$$

where \tilde{h}_+^{mem} is the Fourier transform of the memory waveform. Using Eqs. (6.35)–(6.37) together with the Fourier transform of the step function (6.40), we obtain

$$\tilde{h}_+^{\text{mem}}(f) = Y_{20}^{(-2)}(\theta) \left(\frac{GM}{c^2 r} \times 0.0969 \right) \left(\frac{1}{2\pi i f} \right). \quad (6.51)$$

The bracket in Eq. (6.50) denotes an average over sky position and polarization angles. We adopt a step-function model for the memory waveform, whose Fourier transform scales as f^{-1} . While this approximation is simple and analytically tractable (see Fig. 6.2), it assumes an instantaneous memory jump and neglects finer features of the waveform. In more realistic scenarios, the memory builds up over a short but finite time and is followed by damped oscillations before settling into a constant value. Incorporating a more accurate analytical model, such as those in Refs. [141, 142, 143], would introduce higher-order corrections to the frequency dependence and modify the resulting SNR estimates.

With these expressions, we numerically compute the SNR as a function of the total mass of SMBH M and redshift z . Specifically, we generate a grid of SMBH masses spanning $[10^5, 10^{10}] M_\odot$ and evaluate the SNR for selected redshifts $z = 0.1, 1, 2, 5, 10$. The resulting SNR curves are shown in Fig. 6.7.

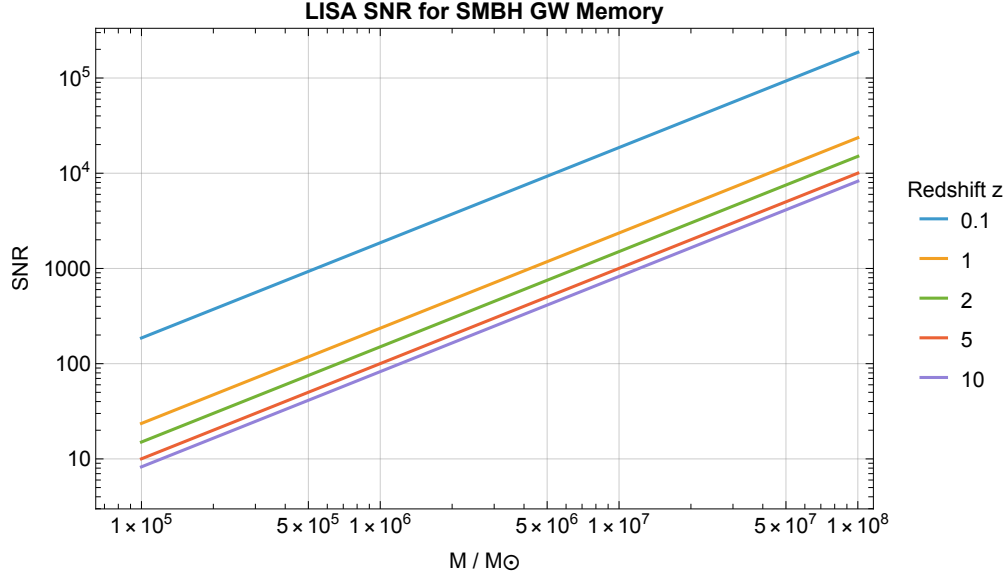


Figure 6.7: Sky- and polarization-averaged SNR of the memory signal for equal-mass, non-spinning SMBHs as a function of the total mass M and redshift z .

To compute the effective diffusion coefficient D_{eff} , we first construct a table of $(M, z, \text{SNR}(M, z))$ values, where M spans a grid from $10^5 M_{\odot}$ to $10^{10} M_{\odot}$, and z ranges from 0.1 to 10. We then assess the impact of selectively removing resolvable merger events based on their SNR by imposing various thresholds. Specifically, we assume that LISA can resolve events with $\text{SNR} > 1000$, $\text{SNR} > 100$, and $\text{SNR} > 10$, respectively, and examine how these criteria affect D_{eff} .

In practice, we implement an SNR cut-off by introducing a threshold Γ_c that separates resolvable from nonresolvable events, and recalculate D_{eff} using the modified expression:

$$D_{\text{eff}} = \frac{\pi G^2 \mathcal{N}^2 \sigma_{\theta}^2}{2H_0 c^3} \int_0^{\infty} dz \int dM M^2 \frac{g_{\text{SMBH}}(M) R_{\text{SMBH}}(z)}{(1+z)\sqrt{\Omega_{\Lambda} + \Omega_M(1+z)^3}} \Theta(\Gamma_c - \text{SNR}(M, z)), \quad (6.52)$$

where Γ_c denotes the SNR threshold, sequentially set to 1000, 100, and 10.

Since $\text{SNR}(M, z)$ is a complicated function of the SMBH mass and redshift, we evaluate the integrals in Eq. (6.52) by discretely summing over the grid of (M, z) values generated earlier. The resulting effective diffusion coefficients D_{eff} for different SNR thresholds are summarized in Table 6.2.

Using the values of D_{eff} from Table 6.2, we recompute the SGWMB energy density spectrum $\Omega_{\text{mem}}(f)$ and characteristic strain $h_c^{\text{mem}}(f)$, retaining only contributions from merger events below the corresponding SNR thresholds Γ_c . These unresolved

Table 6.2: Effective diffusion coefficient D_{eff} under different GW memory SNR thresholds.

D_{eff} (sec^{-1})	GW Memory SNR Threshold
9.5×10^{-42}	None subtracted
3.2×10^{-43}	SNR < 1000
3.9×10^{-45}	SNR < 100
1.4×10^{-47}	SNR < 10

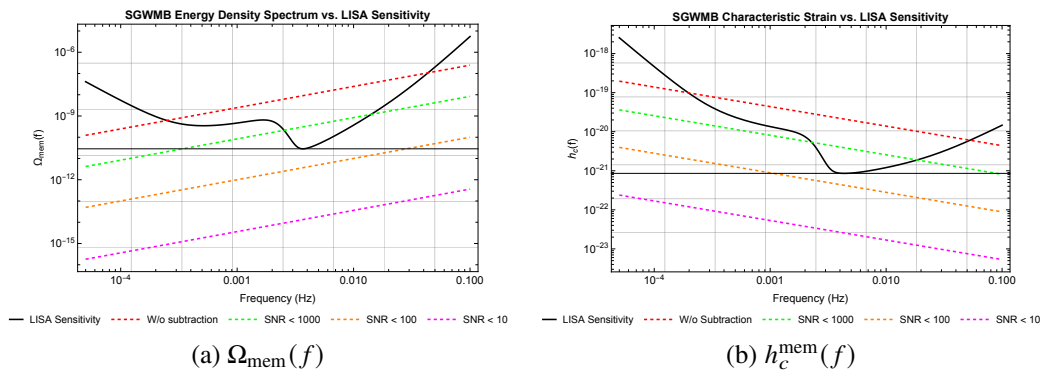


Figure 6.8: Left: SGWMB energy density spectrum under different SNR subtraction thresholds compared to the LISA sensitivity curve (black). The curves correspond to no subtraction (red), and SNR cuts at SNR < 1000 (green), SNR < 100 (orange), and SNR < 10 (magenta), respectively. Right: SGWMB characteristic strain under different SNR subtraction thresholds compared to the LISA sensitivity curve (black). The curves correspond to no subtraction (red), and SNR cuts at SNR < 1000 (green), SNR < 100 (orange), and SNR < 10 (magenta), respectively.

events form a diffuse stochastic background. The resulting spectra are shown in Fig. 6.8.

From Fig. 6.8a and Fig. 6.8b, we find that the detectability of the SGWMB is highly sensitive to the treatment of individually resolvable merger events. Although the background appears prominent if no subtraction is applied, or even if only events with SNR > 1000 are excluded, its amplitude remains above LISA’s sensitivity curve. However, applying a more restrictive threshold of SNR < 100 reduces the background to a level below LISA’s sensitivity, and for SNR < 10, the residual SGWMB becomes well below the detection limit. This indicates that, once high-SNR memory events are properly identified and removed, the remaining nonresolvable background is effectively undetectable by LISA.

These findings revise the conclusions drawn in prior work such as Ref. [325], which predicted that the SGWMB from SMBH mergers would be well above LISA’s sen-

sitivity. Crucially, those studies did not account for the subtraction of individually resolvable memory bursts, and therefore overestimated the amplitude of the residual background. Our analysis shows that although GW memory events from SMBH mergers may statistically resemble a Gaussian process, they do not overlap sufficiently in time to form a truly diffuse background. Instead, these memory bursts are sparse and typically resolvable as individual events in LISA. Once these are subtracted, the remaining SGWMB lies far below the reach of current or foreseeable detector technologies. This underscores the need for careful subtraction modeling when forecasting the observability of stochastic gravitational wave memory signals in future space-based detectors.

6.6 Conclusion and Future Directions

In this chapter, we have investigated the SGWMB arising from SMBH mergers, with a focus on its detectability by future space-based observatories such as LISA. We began by reviewing the necessary theoretical background, including the mathematical foundations of the standard SGWB, the gravitational memory effect, and the role of BMS symmetries in encoding memory in asymptotically flat spacetimes. Building on this foundation, we then focused on the SGWMB, highlighting its origin as a cumulative effect of gravitational memory steps from individual merger events, and deriving its expected f^{-2} PSD characteristics based on a Brownian motion model.

Using a step function approximation for the memory waveform, we modeled the memory strain from individual mergers and computed the energy density spectrum $\Omega_{\text{mem}}(f)$ and characteristic strain $h_c^{\text{mem}}(f)$ associated with the SGWMB. Adopting an SMBH population model from Ref. [66], we explored the distribution of SMBH masses and merger rates across cosmic time, and calculated the diffusion coefficient D that governs the cumulative memory background.

In the absence of source subtraction, the SGWMB from supermassive black hole mergers appears well above LISA's sensitivity curve in the millihertz band, initially suggesting favorable prospects for detection. However, a more realistic treatment must account for the fact that LISA is capable of resolving and subtracting loud individual events. To model this, we computed the SNR of memory bursts across a broad range of SMBH masses and redshifts, and applied thresholds at $\text{SNR} > 1000, 100,$ and 10 to remove the contributions of resolvable events. We then recalculated the effective diffusion coefficient D_{eff} for the residual population of unresolved mergers. This subtraction significantly alters the predicted SGWMB amplitude and plays a

critical role in evaluating its observability in future detectors.

The results show that applying a lenient threshold of $\text{SNR} > 1000$ leads to only modest suppression of the SGWMB, which remains above LISA's sensitivity curve. With a stricter cut at $\text{SNR} > 100$, the background is significantly reduced and falls just below LISA's sensitivity curve throughout its entire frequency band. Finally, under the most conservative condition, excluding all events with $\text{SNR} > 10$, the residual SGWMB falls well below the detection threshold. These results refine earlier highly optimistic projections [325, 66], which did not incorporate a careful subtraction of resolvable memory bursts and consequently overestimated the magnitude of the diffuse background.

Although the detectability of the SGWMB appears limited under these more realistic assumptions, several avenues for future research may alter this conclusion:

- **Improved Source Population Models:** Refining SMBH population models, especially better constraints on merger rates and mass distributions at high redshifts, could modify the expected background amplitude. For instance, a higher-than-expected merger rate or a population of more massive binaries could enhance the SGWMB signal.
- **Waveform Modeling Enhancements:** Incorporating more detailed memory waveform models beyond the step function approximation, including spin effects and higher harmonics, could slightly alter the characteristic strain predictions and might reveal additional detectable features.
- **Detector Design Optimizations:** Future detector designs that enhance low-frequency sensitivity or multi-detector cross-correlation techniques could lower the effective noise floor at millihertz frequencies, improving prospects for detecting a suppressed SGWMB.

In summary, while the SGWMB from nonresolvable SMBH mergers lies below the sensitivity of current-generation space-based detectors, its theoretical importance remains profound. Continued improvements in astrophysical modeling, data analysis techniques, and detector sensitivity technology will be essential to eventually probe this elusive manifestation of gravitational wave memory effect.

Chapter 7

CONCLUSION AND OUTLOOK

The study of quantum gravity remains one of the most fundamental challenges in theoretical physics, requiring a deep integration of quantum mechanics and general relativity. While direct experimental access to Planck-scale physics remains elusive, this dissertation has explored how quantum gravity fluctuations may manifest at observable scales and how they could be probed using next-generation laser interferometers. By developing theoretical models that describe spacetime fluctuations near light-sheet horizons and connecting them to potential experimental signatures, this work contributes to the growing effort to bridge fundamental quantum gravity research with high-precision measurement techniques.

A central theme of this dissertation is the use of hydrodynamic analogies, symmetry principles, gravitational shockwave modeling, and near-horizon dynamics to describe quantum fluctuations in gravity. Through the study of causal diamonds, shockwaves, and horizon BMS-like symmetries, this work offers new insights into the microscopic structure of spacetime and the quantum properties of light-sheet horizons. Additionally, the covariant phase space construction for causal diamonds in Minkowski space presents a first-principles framework for studying quantum degrees of freedom in flat spacetime gravity, providing a promising foundation for future exploration.

Building upon these theoretical developments, this dissertation has also investigated a related experimental phenomenon: the SGWMB arising from the cumulative memory effect of supermassive black hole mergers. After reviewing the standard SGWB, gravitational memory effects, and BMS symmetries, the SGWMB was modeled using a Brownian motion framework. Careful analysis showed that while the SGWMB initially appears above the sensitivity curve of detectors such as LISA, realistic subtraction of individually resolvable merger events significantly suppresses the residual memory background, pushing it below the detection threshold of LISA. This highlights the importance of accounting for source subtraction when assessing the detectability of subtle gravitational phenomena and underscores the need for refined data analysis techniques in future experiments.

The experimental implications of this work suggest that quantum gravity fluctuations—

and memory-induced backgrounds—could introduce fundamental noise sources in interferometric measurements, potentially confounding signals from astrophysical sources in next-generation detectors such as Cosmic Explorer, the Einstein Telescope, and LISA. If such fluctuations or backgrounds are detected, they would offer an unprecedented experimental window into quantum gravity phenomena. Although significant challenges remain in isolating these signatures from instrumental and environmental noise, the potential for interferometry to probe new physics beyond classical general relativity continues to inspire new lines of inquiry.

Moving forward, several directions remain open for exploration. The interplay between gravitational shockwaves, entanglement structures, and stochastic memory effects could offer deeper insights into the information flow across horizons. Additionally, further developing the connection between BMS symmetries, causal diamonds, gravitational memory, and experimental observables may lead to refined predictions for how quantum fluctuations influence spacetime at macroscopic scales. On the experimental side, future technological advances in quantum-limited precision measurements, enhanced gravitational wave detector networks, and novel statistical techniques may improve sensitivity to these elusive signals.

Ultimately, this dissertation takes a step toward making quantum gravity experimentally accessible by identifying potentially observable signatures, proposing new theoretical frameworks, and assessing realistic detectability prospects. Whether through interferometry, holography, or emergent spacetime paradigms, the pursuit of quantum gravity phenomena continues to expand the frontiers of both theory and experiment. As precision gravitational wave detectors advance, they may open an unprecedented window into the quantum nature of spacetime, bringing us closer to uncovering the fundamental principles that govern the universe.

BIBLIOGRAPHY

- [1] Gerard 't Hooft. “Dimensional reduction in quantum gravity”. In: *Conf. Proc. C* 930308 (1993), pp. 284–296. arXiv: [gr-qc/9310026](#).
- [2] Gerard 't Hooft. “Discreteness of Black Hole Microstates”. In: (Sept. 2018). arXiv: [1809.05367 \[gr-qc\]](#).
- [3] Gerard 't Hooft. “Graviton Dominance in Ultrahigh-Energy Scattering”. In: *Phys. Lett. B* 198 (1987), pp. 61–63. doi: [10.1016/0370-2693\(87\)90159-6](#).
- [4] Gerard 't Hooft. “The black hole interpretation of string theory”. In: *Nucl. Phys. B* 335 (1990), pp. 138–154. doi: [10.1016/0550-3213\(90\)90174-C](#).
- [5] Gerard 't Hooft. “The Scattering matrix approach for the quantum black hole: An Overview”. In: *Int. J. Mod. Phys. A* 11.26 (Oct. 1996). arXiv: [gr-qc/9607022](#), pp. 4623–4688. issn: 0217-751X, 1793-656X. doi: [10.1142/S0217751X96002145](#). arXiv: [gr-qc/9607022](#).
- [6] B.P. Abbott et al. (LIGO Scientific Collaboration and Virgo Collaboration). “Binary Black Hole Mergers in the first Advanced LIGO Observing Run”. In: *Physical Review X* 6.4 (2016), p. 041015. doi: [10.1103/PhysRevX.6.041015](#). arXiv: [1606.04856](#).
- [7] B.P. Abbott et al. (LIGO Scientific Collaboration and Virgo Collaboration). “GW151226: Observation of Gravitational Waves from a 22-Solar-Mass Binary Black Hole Coalescence”. In: *Physical Review Letters* 116.24 (2016), p. 241103. doi: [10.1103/PhysRevLett.116.241103](#). arXiv: [1606.04855](#).
- [8] B.P. Abbott et al. (LIGO Scientific Collaboration and Virgo Collaboration). “GW170104: Observation of a 50-Solar-Mass Binary Black Hole Coalescence at Redshift 0.2”. In: *Physical Review Letters* 118.22 (2017), p. 221101. doi: [10.1103/PhysRevLett.118.221101](#). arXiv: [1706.01812](#).
- [9] B.P. Abbott et al. (LIGO Scientific Collaboration and Virgo Collaboration). “GW170608: Observation of a 19-solar-mass Binary Black Hole Coalescence”. In: *The Astrophysical Journal Letters* 851.2 (2017), p. L35. doi: [10.3847/2041-8213/aa9f0c](#). arXiv: [1711.05578](#).
- [10] B.P. Abbott et al. (LIGO Scientific Collaboration and Virgo Collaboration). “GW170814: A three-detector observation of gravitational waves from a binary black hole coalescence”. In: *Physical Review Letters* 119.14 (2017), p. 141101. doi: [10.1103/PhysRevLett.119.141101](#). arXiv: [1709.09660](#).

- [11] B.P. Abbott et al. (LIGO Scientific Collaboration and Virgo Collaboration). “GW170817: Observation of Gravitational Waves from a Binary Neutron Star Inspiral”. In: *Physical Review Letters* 119.16 (2017), p. 161101. doi: [10.1103/PhysRevLett.119.161101](https://doi.org/10.1103/PhysRevLett.119.161101). arXiv: [1710.05832](https://arxiv.org/abs/1710.05832).
- [12] B. P. Abbott et al. “GW150914: Implications for the stochastic gravitational wave background from binary black holes”. In: *Phys. Rev. Lett.* 116.13 (2016), p. 131102. doi: [10.1103/PhysRevLett.116.131102](https://doi.org/10.1103/PhysRevLett.116.131102). arXiv: [1602.03847](https://arxiv.org/abs/1602.03847) [gr-qc].
- [13] B. P. Abbott et al. “Observation of Gravitational Waves from a Binary Black Hole Merger”. In: *Phys. Rev. Lett.* 116.6 (2016), p. 061102. doi: [10.1103/PhysRevLett.116.061102](https://doi.org/10.1103/PhysRevLett.116.061102). arXiv: [1602.03837](https://arxiv.org/abs/1602.03837) [gr-qc].
- [14] B. P. Abbott et al. “Search for the isotropic stochastic background using data from Advanced LIGO’s second observing run”. In: *Phys. Rev. D* 100.6 (2019), p. 061101. doi: [10.1103/PhysRevD.100.061101](https://doi.org/10.1103/PhysRevD.100.061101). arXiv: [1903.02886](https://arxiv.org/abs/1903.02886) [gr-qc].
- [15] R. Abbott et al. “Upper limits on the isotropic gravitational-wave background from Advanced LIGO and Advanced Virgo’s third observing run”. In: *Phys. Rev. D* 104.2 (2021), p. 022004. doi: [10.1103/PhysRevD.104.022004](https://doi.org/10.1103/PhysRevD.104.022004). arXiv: [2101.12130](https://arxiv.org/abs/2101.12130) [gr-qc].
- [16] K. Ackley et al. “Neutron Star Extreme Matter Observatory: A kilohertz-band gravitational-wave detector in the global network”. In: *Publ. Astron. Soc. Austral.* 37 (2020), e047. doi: [10.1017/pasa.2020.39](https://doi.org/10.1017/pasa.2020.39). arXiv: [2007.03128](https://arxiv.org/abs/2007.03128) [astro-ph.HE].
- [17] H. Adami, D. Grumiller, S. Sadeghian, M. M. Sheikh-Jabbari, and C. Zwiikel. “T-Witts from the horizon”. In: *JHEP* 04 (2020), p. 128. doi: [10.1007/JHEP04\(2020\)128](https://doi.org/10.1007/JHEP04(2020)128). arXiv: [2002.08346](https://arxiv.org/abs/2002.08346) [hep-th].
- [18] H. Adami, D. Grumiller, M. M. Sheikh-Jabbari, V. Taghiloo, H. Yavartanoo, and C. Zwiikel. “Null boundary phase space: slicings, news & memory”. In: *JHEP* 11 (2021), p. 155. doi: [10.1007/JHEP11\(2021\)155](https://doi.org/10.1007/JHEP11(2021)155). arXiv: [2110.04218](https://arxiv.org/abs/2110.04218) [hep-th].
- [19] Gabriella Agazie et al. “The NANOGrav 15 yr Data Set: Evidence for a Gravitational-wave Background”. In: *Astrophys. J. Lett.* 951.1 (2023), p. L8. doi: [10.3847/2041-8213/acdac6](https://doi.org/10.3847/2041-8213/acdac6). arXiv: [2306.16213](https://arxiv.org/abs/2306.16213) [astro-ph.HE].
- [20] Nancy Aggarwal et al. “Challenges and opportunities of gravitational-wave searches at MHz to GHz frequencies”. In: *Living Rev. Rel.* 24.1 (2021), p. 4. doi: [10.1007/s41114-021-00032-5](https://doi.org/10.1007/s41114-021-00032-5). arXiv: [2011.12414](https://arxiv.org/abs/2011.12414) [gr-qc].
- [21] Nancy Aggarwal et al. “Searching for New Physics with a Levitated-Sensor-Based Gravitational-Wave Detector”. In: *Phys. Rev. Lett.* 128.11 (2022), p. 111101. doi: [10.1103/PhysRevLett.128.111101](https://doi.org/10.1103/PhysRevLett.128.111101). arXiv: [2010.13157](https://arxiv.org/abs/2010.13157) [gr-qc].

- [22] Ofer Aharony, Steven S. Gubser, Juan Martin Maldacena, Hirosi Ooguri, and Yaron Oz. “Large N field theories, string theory and gravity”. In: *Phys. Rept.* 323 (2000), pp. 183–386. DOI: [10.1016/S0370-1573\(99\)00083-6](https://doi.org/10.1016/S0370-1573(99)00083-6). arXiv: [hep-th/9905111](https://arxiv.org/abs/hep-th/9905111).
- [23] Yongjun Ahn, Viktor Jahnke, Hyun-Sik Jeong, and Keun-Young Kim. “Scrambling in Hyperbolic Black Holes: shock waves and pole-skipping”. In: *JHEP* 10.10 (Oct. 2019). arXiv: 1907.08030, p. 257. ISSN: 1029-8479. DOI: [10.1007/JHEP10\(2019\)257](https://doi.org/10.1007/JHEP10(2019)257). arXiv: [1907.08030 \[hep-th\]](https://arxiv.org/abs/1907.08030).
- [24] P. C. Aichelburg and R. U. Sexl. “On the gravitational field of a massless particle”. In: *General Relativity and Gravitation* 2.4 (1971), pp. 303–312. DOI: [10.1007/BF00758149](https://doi.org/10.1007/BF00758149). URL: <https://doi.org/10.1007/BF00758149>.
- [25] Francesco Alessio and Michele Arzano. “Note on the symplectic structure of asymptotically flat gravity and BMS symmetries”. In: *Phys. Rev. D* 100.4 (2019), p. 044028. DOI: [10.1103/PhysRevD.100.044028](https://doi.org/10.1103/PhysRevD.100.044028). arXiv: [1906.05036 \[gr-qc\]](https://arxiv.org/abs/1906.05036).
- [26] Bruce Allen. “The Stochastic gravity wave background: Sources and detection”. In: *Les Houches School of Physics: Astrophysical Sources of Gravitational Radiation*. Apr. 1996, pp. 373–417. arXiv: [gr-qc/9604033](https://arxiv.org/abs/gr-qc/9604033).
- [27] Bruce Allen and Adrian C. Ottewill. “Detection of anisotropies in the gravitational wave stochastic background”. In: *Phys. Rev. D* 56 (1997), pp. 545–563. DOI: [10.1103/PhysRevD.56.545](https://doi.org/10.1103/PhysRevD.56.545). arXiv: [gr-qc/9607068](https://arxiv.org/abs/gr-qc/9607068).
- [28] Bruce Allen and Joseph D Romano. “Detecting a stochastic background of gravitational radiation: Signal processing strategies and sensitivities”. In: *Physical Review D* 59.10 (1999), p. 102001.
- [29] Ahmed Almheiri, Donald Marolf, Joseph Polchinski, and James Sully. “Black Holes: Complementarity or Firewalls?” In: *JHEP* 02 (2013), p. 062. DOI: [10.1007/JHEP02\(2013\)062](https://doi.org/10.1007/JHEP02(2013)062). arXiv: [1207.3123 \[hep-th\]](https://arxiv.org/abs/1207.3123).
- [30] Pau Amaro-Seoane et al. “Laser Interferometer Space Antenna”. In: (Feb. 2017). arXiv: [1702.00786 \[astro-ph.IM\]](https://arxiv.org/abs/1702.00786).
- [31] Richard Anantua, Richard Easther, and John T. Giblin. “GUT-Scale Primordial Black Holes: Consequences and Constraints”. In: *Phys. Rev. Lett.* 103 (2009), p. 111303. DOI: [10.1103/PhysRevLett.103.111303](https://doi.org/10.1103/PhysRevLett.103.111303). arXiv: [0812.0825 \[astro-ph\]](https://arxiv.org/abs/0812.0825).
- [32] Nima Arkani-Hamed, Monica Pate, Ana-Maria Raclariu, and Andrew Strominger. “Celestial amplitudes from UV to IR”. In: *JHEP* 08 (2021), p. 062. DOI: [10.1007/JHEP08\(2021\)062](https://doi.org/10.1007/JHEP08(2021)062). arXiv: [2012.04208 \[hep-th\]](https://arxiv.org/abs/2012.04208).
- [33] Asimina Arvanitaki and Andrew A. Geraci. “Detecting high-frequency gravitational waves with optically-levitated sensors”. In: *Phys. Rev. Lett.* 110.7 (2013), p. 071105. DOI: [10.1103/PhysRevLett.110.071105](https://doi.org/10.1103/PhysRevLett.110.071105). arXiv: [1207.5320 \[gr-qc\]](https://arxiv.org/abs/1207.5320).

- [34] Abhay Ashtekar, Miguel Campiglia, and Adam Henderson. “Loop Quantum Cosmology and Spin Foams”. In: *Phys. Lett. B* 681 (2009), pp. 347–352. DOI: [10.1016/j.physletb.2009.10.042](https://doi.org/10.1016/j.physletb.2009.10.042). arXiv: [0909.4221](https://arxiv.org/abs/0909.4221) [gr-qc].
- [35] Abhay Ashtekar, Miguel Campiglia, and Alok Laddha. “Null infinity, the BMS group and infrared issues”. In: *Gen. Rel. Grav.* 50.11 (2018), pp. 140–163. DOI: [10.1007/s10714-018-2464-3](https://doi.org/10.1007/s10714-018-2464-3). arXiv: [1808.07093](https://arxiv.org/abs/1808.07093) [gr-qc].
- [36] Alexander Atanasov, Adam Ball, Walker Melton, Ana-Maria Raclariu, and Andrew Strominger. “(2, 2) Scattering and the celestial torus”. In: *JHEP* 07 (2021), p. 083. DOI: [10.1007/JHEP07\(2021\)083](https://doi.org/10.1007/JHEP07(2021)083). arXiv: [2101.09591](https://arxiv.org/abs/2101.09591) [hep-th].
- [37] Stanislav Babak, Martin Hewitson, and Antoine Petiteau. “LISA Sensitivity and SNR Calculations”. In: (2021). DOI: [10.48550/ARXIV.2108.01167](https://doi.org/10.48550/ARXIV.2108.01167). URL: <https://arxiv.org/abs/2108.01167>.
- [38] Luca Baiotti, Bruno Giacomazzo, and Luciano Rezzolla. “Accurate evolutions of inspiralling neutron-star binaries: prompt and delayed collapse to black hole”. In: *Phys. Rev. D* 78 (2008), p. 084033. DOI: [10.1103/PhysRevD.78.084033](https://doi.org/10.1103/PhysRevD.78.084033). arXiv: [0804.0594](https://arxiv.org/abs/0804.0594) [gr-qc].
- [39] Sang-Eon Bak, Cynthia Keeler, Yiwen Zhang, and Kathryn M. Zurek. “Rindler fluids from gravitational shockwaves”. In: *JHEP* 05 (2024), p. 331. DOI: [10.1007/JHEP05\(2024\)331](https://doi.org/10.1007/JHEP05(2024)331). arXiv: [2403.18013](https://arxiv.org/abs/2403.18013) [hep-th].
- [40] John Baker et al. “Space Based Gravitational Wave Astronomy Beyond LISA”. In: *Bull. Am. Astron. Soc.* 51.7 (2019), p. 243. arXiv: [1907.11305](https://arxiv.org/abs/1907.11305) [astro-ph.IM].
- [41] Thomas Banks and Kathryn M. Zurek. “Conformal description of near-horizon vacuum states”. In: *Phys. Rev. D* 104.12 (12 Dec. 2021), p. 126026. DOI: [10.1103/PhysRevD.104.126026](https://doi.org/10.1103/PhysRevD.104.126026). arXiv: [2108.04806](https://arxiv.org/abs/2108.04806) [hep-th]. URL: <https://link.aps.org/doi/10.1103/PhysRevD.104.126026>.
- [42] Nicola Bartolo et al. “Probing anisotropies of the Stochastic Gravitational Wave Background with LISA”. In: *JCAP* 11 (2022), p. 009. DOI: [10.1088/1475-7516/2022/11/009](https://doi.org/10.1088/1475-7516/2022/11/009). arXiv: [2201.08782](https://arxiv.org/abs/2201.08782) [astro-ph.CO].
- [43] Nicola Bartolo et al. “Science with the space-based interferometer LISA. IV: Probing inflation with gravitational waves”. In: *JCAP* 12 (2016), p. 026. DOI: [10.1088/1475-7516/2016/12/026](https://doi.org/10.1088/1475-7516/2016/12/026). arXiv: [1610.06481](https://arxiv.org/abs/1610.06481) [astro-ph.CO].
- [44] C. Bartram et al. “Search for Invisible Axion Dark Matter in the 3.3–4.2 μeV Mass Range”. In: *Phys. Rev. Lett.* 127.26 (2021), p. 261803. DOI: [10.1103/PhysRevLett.127.261803](https://doi.org/10.1103/PhysRevLett.127.261803). arXiv: [2110.06096](https://arxiv.org/abs/2110.06096) [hep-ex].
- [45] Andreas Bauswein et al. “Equation-of-state Constraints and the QCD Phase Transition in the Era of Gravitational-Wave Astronomy”. In: *AIP Conf. Proc.* 2127.1 (2019). Ed. by Ang Li, Bao-An Li, and Furong Xu, p. 020013. DOI: [10.1063/1.5117803](https://doi.org/10.1063/1.5117803). arXiv: [1904.01306](https://arxiv.org/abs/1904.01306) [astro-ph.HE].

- [46] K. Becker, M. Becker, and J. H. Schwarz. *String theory and M-theory: A modern introduction*. Cambridge University Press, Dec. 2006. ISBN: 978-0-511-25486-4, 978-0-521-86069-7, 978-0-511-81608-6. DOI: [10.1017/CB09780511816086](https://doi.org/10.1017/CB09780511816086).
- [47] Jacob Becey, Daniel Carney, and Giacomo Marocco. “Quantum measurements in fundamental physics: a user’s manual”. In: (Nov. 2023). arXiv: [2311.07270](https://arxiv.org/abs/2311.07270) [hep-ph].
- [48] J. D. Bekenstein. “Black holes and the second law”. In: *Lettere al Nuovo Cimento (1971-1985)* 4.15 (1972), pp. 737–740. DOI: [10.1007/BF02757029](https://doi.org/10.1007/BF02757029). URL: <https://doi.org/10.1007/BF02757029>.
- [49] Asher Berlin et al. “Detecting high-frequency gravitational waves with microwave cavities”. In: *Phys. Rev. D* 105.11 (2022), p. 116011. DOI: [10.1103/PhysRevD.105.116011](https://doi.org/10.1103/PhysRevD.105.116011). arXiv: [2112.11465](https://arxiv.org/abs/2112.11465) [hep-ph].
- [50] Emanuele Berti et al. “Testing General Relativity with Present and Future Astrophysical Observations”. In: *Class. Quant. Grav.* 32 (2015), p. 243001. DOI: [10.1088/0264-9381/32/24/243001](https://doi.org/10.1088/0264-9381/32/24/243001). arXiv: [1501.07274](https://arxiv.org/abs/1501.07274) [gr-qc].
- [51] Sayantani Bhattacharyya, Veronika E Hubeny, Shiraz Minwalla, and Mukund Rangamani. “Nonlinear Fluid Dynamics from Gravity”. In: *JHEP* 02 (2008), p. 045. DOI: [10.1088/1126-6708/2008/02/045](https://doi.org/10.1088/1126-6708/2008/02/045). arXiv: [0712.2456](https://arxiv.org/abs/0712.2456) [hep-th].
- [52] Sayantani Bhattacharyya, Shiraz Minwalla, and Spenta R. Wadia. “The Incompressible Non-Relativistic Navier-Stokes Equation from Gravity”. In: *JHEP* 08 (2009), p. 059. DOI: [10.1088/1126-6708/2009/08/059](https://doi.org/10.1088/1126-6708/2009/08/059). arXiv: [0810.1545](https://arxiv.org/abs/0810.1545) [hep-th].
- [53] Lydia Bieri. “An Extension of the Stability Theorem of the Minkowski Space in General Relativity”. In: *J. Diff. Geom.* 86.1 (2010), pp. 17–70. arXiv: [0904.0620](https://arxiv.org/abs/0904.0620) [gr-qc].
- [54] Joseph J. Bisognano and Eyvind H. Wichmann. “On the duality condition for a Hermitian scalar field”. In: *J. Math. Phys.* 16.4 (1975), pp. 985–1007. ISSN: 0022-2488. DOI: [10.1063/1.522605](https://doi.org/10.1063/1.522605). URL: <https://doi.org/10.1063/1.522605>.
- [55] Joseph J. Bisognano and Eyvind H. Wichmann. “On the duality condition for quantum fields”. In: *J. Math. Phys.* 17.3 (1976), pp. 303–321. ISSN: 0022-2488. DOI: [10.1063/1.522898](https://doi.org/10.1063/1.522898). URL: <https://doi.org/10.1063/1.522898>.
- [56] Mike Blake. “Universal Charge Diffusion and the Butterfly Effect in Holographic Theories”. In: *Phys. Rev. Lett.* 117.9 (2016), p. 091601. DOI: [10.1103/PhysRevLett.117.091601](https://doi.org/10.1103/PhysRevLett.117.091601). arXiv: [1603.08510](https://arxiv.org/abs/1603.08510) [hep-th].

- [57] Mike Blake. “Universal Diffusion in Incoherent Black Holes”. In: *Phys. Rev. D* 94 (2016), p. 086014. DOI: [10.1103/PhysRevD.94.086014](https://doi.org/10.1103/PhysRevD.94.086014). arXiv: [1604.01754](https://arxiv.org/abs/1604.01754) [hep-th].
- [58] Mike Blake, Richard A. Davison, Sašo Grozdanov, and Hong Liu. “Many-body chaos and energy dynamics in holography”. In: *JHEP* 10 (2018), p. 035. DOI: [10.1007/JHEP10\(2018\)035](https://doi.org/10.1007/JHEP10(2018)035). arXiv: [1809.01169](https://arxiv.org/abs/1809.01169) [hep-th].
- [59] Mike Blake, Hyunseok Lee, and Hong Liu. “A quantum hydrodynamical description for scrambling and many-body chaos”. In: *JHEP* 10 (2018), p. 127. DOI: [10.1007/JHEP10\(2018\)127](https://doi.org/10.1007/JHEP10(2018)127). arXiv: [1801.00010](https://arxiv.org/abs/1801.00010) [hep-th].
- [60] Jose J. Blanco-Pillado, Ken D. Olum, and Xavier Siemens. “New limits on cosmic strings from gravitational wave observation”. In: *Phys. Lett. B* 778 (2018), pp. 392–396. DOI: [10.1016/j.physletb.2018.01.050](https://doi.org/10.1016/j.physletb.2018.01.050). arXiv: [1709.02434](https://arxiv.org/abs/1709.02434) [astro-ph.CO].
- [61] Stephen J. Blundell and Katherine M. Blundell. *Concepts in Thermal Physics*. OUP Oxford, 2009.
- [62] Jan de Boer, Michal P. Heller, and Natalia Pinzani-Fokeeva. “Effective actions for relativistic fluids from holography”. In: *JHEP* 08 (2015), p. 086. DOI: [10.1007/JHEP08\(2015\)086](https://doi.org/10.1007/JHEP08(2015)086). arXiv: [1504.07616](https://arxiv.org/abs/1504.07616) [hep-th].
- [63] Oliver M. Boersma, David A. Nichols, and Patricia Schmidt. “Forecasts for detecting the gravitational-wave memory effect with Advanced LIGO and Virgo”. In: *Phys. Rev. D* 101.8 (2020), p. 083026. DOI: [10.1103/PhysRevD.101.083026](https://doi.org/10.1103/PhysRevD.101.083026). arXiv: [2002.01821](https://arxiv.org/abs/2002.01821) [astro-ph.HE].
- [64] H. Bondi, M. G. J. van der Burg, and A. W. K. Metzner. “Gravitational waves in general relativity. 7. Waves from axisymmetric isolated systems”. In: *Proc. Roy. Soc. Lond. A* 269 (1962), pp. 21–52. DOI: [10.1098/rspa.1962.0161](https://doi.org/10.1098/rspa.1962.0161).
- [65] Raphael Bousso. “The Holographic principle”. In: *Rev. Mod. Phys.* 74 (2002), pp. 825–874. DOI: [10.1103/RevModPhys.74.825](https://doi.org/10.1103/RevModPhys.74.825). arXiv: [hep-th/0203101](https://arxiv.org/abs/hep-th/0203101).
- [66] Tore Boybeyi, Vuk Mandic, and Alexandros Papageorgiou. “Astrometric deflections from gravitational wave memory accumulation over cosmological scales”. In: *Phys. Rev. D* 110.4 (2024), p. 043047. DOI: [10.1103/PhysRevD.110.043047](https://doi.org/10.1103/PhysRevD.110.043047). arXiv: [2403.07614](https://arxiv.org/abs/2403.07614) [astro-ph.CO].
- [67] V. B. Braginsky and L. P. Grishchuk. “Kinematic Resonance and Memory Effect in Free Mass Gravitational Antennas”. In: *Sov. Phys. JETP* 62 (1985), pp. 427–430.
- [68] V. B. Braginsky and L. P. Grishchuk. “Kinematic Resonance and Memory Effect in Free Mass Gravitational Antennas”. In: *Sov. Phys. JETP* 62 (1985). [*Zh. Eksp. Teor. Fiz.*89,744(1985)], pp. 427–430.

- [69] Vladimir B. Braginsky and Kip S. Thorne. “Gravitational-wave bursts with memory and experimental prospects”. In: *Nature* 327.6118 (1987), pp. 123–125. URL: <https://doi.org/10.1038/327123a0>.
- [70] Irene Bredberg, Cynthia Keeler, Vyacheslav Lysov, and Andrew Strominger. “From Navier-Stokes To Einstein”. In: *JHEP* 07 (2012), p. 146. DOI: [10.1007/JHEP07\(2012\)146](https://doi.org/10.1007/JHEP07(2012)146). arXiv: [1101.2451](https://arxiv.org/abs/1101.2451) [hep-th].
- [71] Irene Bredberg, Cynthia Keeler, Vyacheslav Lysov, and Andrew Strominger. “Wilsonian Approach to Fluid/Gravity Duality”. In: *JHEP* 03 (2011), p. 141. DOI: [10.1007/JHEP03\(2011\)141](https://doi.org/10.1007/JHEP03(2011)141). arXiv: [1006.1902](https://arxiv.org/abs/1006.1902) [hep-th].
- [72] A. F. Brooks et al. “Point absorbers in Advanced LIGO”. In: *Appl. Opt.* 60.13 (2021), pp. 4047–4063. DOI: [10.1364/AO.419689](https://doi.org/10.1364/AO.419689). arXiv: [2101.05828](https://arxiv.org/abs/2101.05828) [physics.ins-det].
- [73] J. David Brown and James W. York Jr. “Quasilocal energy and conserved charges derived from the gravitational action”. In: *Phys. Rev. D* 47 (1993), pp. 1407–1419. DOI: [10.1103/PhysRevD.47.1407](https://doi.org/10.1103/PhysRevD.47.1407). arXiv: [gr-qc/9209012](https://arxiv.org/abs/gr-qc/9209012).
- [74] Mathew W. Bub, Yanbei Chen, Yufeng Du, Dongjun Li, Yiwen Zhang, and Kathryn M. Zurek. “Quantum gravity background in next-generation gravitational wave detectors”. In: *Phys. Rev. D* 108.6 (2023), p. 064038. DOI: [10.1103/PhysRevD.108.064038](https://doi.org/10.1103/PhysRevD.108.064038). arXiv: [2305.11224](https://arxiv.org/abs/2305.11224) [gr-qc].
- [75] Mathew W. Bub, Temple He, Prahar Mitra, Yiwen Zhang, and Kathryn M. Zurek. “Quantum Mechanics of a Spherically Symmetric Causal Diamond in Minkowski Spacetime”. In: *Phys. Rev. Lett.* 134.12 (2025), p. 121501. DOI: [10.1103/PhysRevLett.134.121501](https://doi.org/10.1103/PhysRevLett.134.121501). arXiv: [2408.11094](https://arxiv.org/abs/2408.11094) [hep-th].
- [76] Herbert B. Callen and Theodore A. Welton. “Irreversibility and Generalized Noise”. In: *Phys. Rev.* 83 (1 July 1951), pp. 34–40. DOI: [10.1103/PhysRev.83.34](https://doi.org/10.1103/PhysRev.83.34). URL: <https://link.aps.org/doi/10.1103/PhysRev.83.34>.
- [77] Miguel Campiglia, Rodolfo Gambini, and Jorge Pullin. “Loop quantization of spherically symmetric midi-superspaces : The Interior problem”. In: *AIP Conf. Proc.* 977.1 (2008). Ed. by Alfredo Macias, Claus Lämmerzahl, and Abel Camacho, pp. 52–63. DOI: [10.1063/1.2902798](https://doi.org/10.1063/1.2902798). arXiv: [0712.0817](https://arxiv.org/abs/0712.0817) [gr-qc].
- [78] Zhoujian Cao, Xiaokai He, and Zhi-Chao Zhao. “Gravitational wave memory produced by cosmic background radiation”. In: *Phys. Lett. B* 847 (2023), p. 138313. DOI: [10.1016/j.physletb.2023.138313](https://doi.org/10.1016/j.physletb.2023.138313). arXiv: [2210.17422](https://arxiv.org/abs/2210.17422) [gr-qc].
- [79] Federico Capone, Prahar Mitra, Aaron Poole, and Bilyana Tomova. “Phase Space Renormalization and Finite BMS Charges in Six Dimensions”. In: (Apr. 2023). arXiv: [2304.09330](https://arxiv.org/abs/2304.09330) [hep-th].

- [80] S. Carlip. “Black Hole Entropy from Bondi-Metzner-Sachs Symmetry at the Horizon”. In: *Phys. Rev. Lett.* 120.10 (2018), p. 101301. doi: [10.1103/PhysRevLett.120.101301](https://doi.org/10.1103/PhysRevLett.120.101301). arXiv: [1702.04439](https://arxiv.org/abs/1702.04439) [gr-qc].
- [81] S. Carlip. “Near-horizon Bondi-Metzner-Sachs symmetry, dimensional reduction, and black hole entropy”. In: *Phys. Rev. D* 101.4 (2020), p. 046002. doi: [10.1103/PhysRevD.101.046002](https://doi.org/10.1103/PhysRevD.101.046002). arXiv: [1910.01762](https://arxiv.org/abs/1910.01762) [hep-th].
- [82] Steven Carlip. “Black hole entropy from conformal field theory in any dimension”. In: *Phys. Rev. Lett.* 82 (1999), pp. 2828–2831. doi: [10.1103/PhysRevLett.82.2828](https://doi.org/10.1103/PhysRevLett.82.2828). arXiv: [hep-th/9812013](https://arxiv.org/abs/hep-th/9812013).
- [83] Steven Carlip. “Effective Conformal Descriptions of Black Hole Entropy”. In: *Entropy* 13 (2011), pp. 1355–1379. doi: [10.3390/e13071355](https://doi.org/10.3390/e13071355). arXiv: [1107.2678](https://arxiv.org/abs/1107.2678) [gr-qc].
- [84] Steven Carlip. “Entropy from conformal field theory at Killing horizons”. In: *Class. Quant. Grav.* 16 (1999), pp. 3327–3348. doi: [10.1088/0264-9381/16/10/322](https://doi.org/10.1088/0264-9381/16/10/322). arXiv: [gr-qc/9906126](https://arxiv.org/abs/gr-qc/9906126).
- [85] Steven Carlip. “The Statistical mechanics of the (2+1)-dimensional black hole”. In: *Phys. Rev. D* 51 (1995), pp. 632–637. doi: [10.1103/PhysRevD.51.632](https://doi.org/10.1103/PhysRevD.51.632). arXiv: [gr-qc/9409052](https://arxiv.org/abs/gr-qc/9409052).
- [86] Steven Carlip. “What we don’t know about BTZ black hole entropy”. In: *Class. Quant. Grav.* 15 (1998), pp. 3609–3625. doi: [10.1088/0264-9381/15/11/020](https://doi.org/10.1088/0264-9381/15/11/020). arXiv: [hep-th/9806026](https://arxiv.org/abs/hep-th/9806026).
- [87] Daniel Carney. “Comments on graviton detection”. In: July 2024. arXiv: [2408.00094](https://arxiv.org/abs/2408.00094) [gr-qc].
- [88] Daniel Carney, Valerie Domcke, and Nicholas L. Rodd. “Graviton detection and the quantization of gravity”. In: *Phys. Rev. D* 109.4 (2024), p. 044009. doi: [10.1103/PhysRevD.109.044009](https://doi.org/10.1103/PhysRevD.109.044009). arXiv: [2308.12988](https://arxiv.org/abs/2308.12988) [hep-th].
- [89] Daniel Carney, Manthos Karydas, and Allic Sivaramakrishnan. “Response of interferometers to the vacuum of quantum gravity”. In: (Sept. 2024). arXiv: [2409.03894](https://arxiv.org/abs/2409.03894) [hep-th].
- [90] Sean M. Carroll. *Spacetime and Geometry: An Introduction to General Relativity*. Cambridge University Press, July 2019. ISBN: 978-0-8053-8732-2, 978-1-108-48839-6, 978-1-108-77555-7. doi: [10.1017/9781108770385](https://doi.org/10.1017/9781108770385).
- [91] Horacio Casini, Marina Huerta, and Robert C. Myers. “Towards a derivation of holographic entanglement entropy”. In: *JHEP* 05.5 (Feb. 2011). arXiv: [1102.0440](https://arxiv.org/abs/1102.0440), p. 036. ISSN: 1029-8479. doi: [10.1007/JHEP05\(2011\)036](https://doi.org/10.1007/JHEP05(2011)036). arXiv: [1102.0440](https://arxiv.org/abs/1102.0440) [hep-th].
- [92] C. M. Caves. “MICROWAVE CAVITY GRAVITATIONAL RADIATION DETECTORS”. In: *Phys. Lett. B* 80 (1979), pp. 323–326. doi: [10.1016/0370-2693\(79\)90227-2](https://doi.org/10.1016/0370-2693(79)90227-2).

- [93] Venkatesa Chandrasekaran, Éanna É. Flanagan, and Kartik Prabhu. “Symmetries and charges of general relativity at null boundaries”. In: *JHEP* 11 (2018). [Erratum: *JHEP* 07, 224 (2023)], p. 125. DOI: [10.1007/JHEP11\(2018\)125](https://doi.org/10.1007/JHEP11(2018)125). arXiv: [1807.11499](https://arxiv.org/abs/1807.11499) [[hep-th](#)].
- [94] Venkatesa Chandrasekaran and Kartik Prabhu. “Symmetries, charges and conservation laws at causal diamonds in general relativity”. In: *JHEP* 10 (2019), p. 229. DOI: [10.1007/JHEP10\(2019\)229](https://doi.org/10.1007/JHEP10(2019)229). arXiv: [1908.00017](https://arxiv.org/abs/1908.00017) [[gr-qc](#)].
- [95] Venkatesa Chandrasekaran and Antony J. Speranza. “Anomalies in gravitational charge algebras of null boundaries and black hole entropy”. In: *JHEP* 01 (2021), p. 137. DOI: [10.1007/JHEP01\(2021\)137](https://doi.org/10.1007/JHEP01(2021)137). arXiv: [2009.10739](https://arxiv.org/abs/2009.10739) [[hep-th](#)].
- [96] Aaron Chou et al. “Interferometric Constraints on Quantum Geometrical Shear Noise Correlations”. In: *Class. Quant. Grav.* 34.16 (July 2017), p. 165005. DOI: [10.1088/1361-6382/aa7bd3](https://doi.org/10.1088/1361-6382/aa7bd3). arXiv: [1703.08503](https://arxiv.org/abs/1703.08503) [[gr-qc](#)]. URL: <https://doi.org/10.1088/1361-6382/aa7bd3>.
- [97] Aaron Chou et al. “The Holometer: An Instrument to Probe Planckian Quantum Geometry”. In: *Class. Quant. Grav.* 34.6 (2017), p. 065005. DOI: [10.1088/1361-6382/aa5e5c](https://doi.org/10.1088/1361-6382/aa5e5c). arXiv: [1611.08265](https://arxiv.org/abs/1611.08265) [[physics.ins-det](#)].
- [98] Nelson Christensen. “Stochastic Gravitational Wave Backgrounds”. In: *Rept. Prog. Phys.* 82.1 (2019), p. 016903. DOI: [10.1088/1361-6633/aae6b5](https://doi.org/10.1088/1361-6633/aae6b5). arXiv: [1811.08797](https://arxiv.org/abs/1811.08797) [[gr-qc](#)].
- [99] D. Christodoulou. “Nonlinear nature of gravitation and gravitational wave experiments”. In: *Phys. Rev. Lett.* 67 (1991), pp. 1486–1489. DOI: [10.1103/PhysRevLett.67.1486](https://doi.org/10.1103/PhysRevLett.67.1486).
- [100] D. Christodoulou and S. Klainerman. “The Global nonlinear stability of the Minkowski space”. In: (1993).
- [101] Luca Ciambelli, Laurent Freidel, and Robert G. Leigh. “Null Raychaudhuri: canonical structure and the dressing time”. In: *JHEP* 01 (2024), p. 166. DOI: [10.1007/JHEP01\(2024\)166](https://doi.org/10.1007/JHEP01(2024)166). arXiv: [2309.03932](https://arxiv.org/abs/2309.03932) [[hep-th](#)].
- [102] Luca Ciambelli, Laurent Freidel, and Robert G. Leigh. “Quantum Null Geometry and Gravity”. In: (July 2024). arXiv: [2407.11132](https://arxiv.org/abs/2407.11132) [[hep-th](#)].
- [103] Luca Ciambelli, Jerzy Kowalski-Glikman, and Ludovic Varrin. “Quantum Corner Symmetry: Representations and Gluing”. In: (June 2024). arXiv: [2406.07101](https://arxiv.org/abs/2406.07101) [[hep-th](#)].
- [104] Howard S. Cohl and Ernie G. Kalnins. *Fundamental solution of the Laplacian in the hyperboloid model of hyperbolic geometry*. 2012. DOI: [10.48550/ARXIV.1201.4406](https://doi.org/10.48550/ARXIV.1201.4406). URL: <https://arxiv.org/abs/1201.4406>.

- [105] LIGO Scientific Collaboration and Virgo Collaboration. “An improved analysis of GW150914 using a fully spin-precessing waveform model”. In: *Physical Review X* 6.4 (2016), p. 041014. DOI: [10.1103/PhysRevX.6.041014](https://doi.org/10.1103/PhysRevX.6.041014). arXiv: [1606.01210](https://arxiv.org/abs/1606.01210).
- [106] LIGO Scientific Collaboration and Virgo Collaboration. “GWTC-1: A Gravitational-Wave Transient Catalog of Compact Binary Mergers Observed by LIGO and Virgo during the First and Second Observing Runs”. In: *Physical Review X* 9.3 (2019), p. 031040. DOI: [10.1103/PhysRevX.9.031040](https://doi.org/10.1103/PhysRevX.9.031040). arXiv: [1811.12907](https://arxiv.org/abs/1811.12907).
- [107] The LIGO Scientific Collaboration. “LIGO: the Laser Interferometer Gravitational-Wave Observatory”. In: *Reports on Progress in Physics* 72.7 (June 2009), p. 076901. DOI: [10.1088/0034-4885/72/7/076901](https://doi.org/10.1088/0034-4885/72/7/076901). URL: <https://doi.org/10.1088/0034-4885/72/7/076901>.
- [108] Geoffrey Compere, Paul McFadden, Kostas Skenderis, and Marika Taylor. “The Holographic fluid dual to vacuum Einstein gravity”. In: *JHEP* 07 (2011), p. 050. DOI: [10.1007/JHEP07\(2011\)050](https://doi.org/10.1007/JHEP07(2011)050). arXiv: [1103.3022](https://arxiv.org/abs/1103.3022) [hep-th].
- [109] Geoffrey Compere, Paul McFadden, Kostas Skenderis, and Marika Taylor. “The relativistic fluid dual to vacuum Einstein gravity”. In: *JHEP* 03 (2012), p. 076. DOI: [10.1007/JHEP03\(2012\)076](https://doi.org/10.1007/JHEP03(2012)076). arXiv: [1201.2678](https://arxiv.org/abs/1201.2678) [hep-th].
- [110] Geoffrey Compère and Adrien Fiorucci. “Advanced Lectures on General Relativity”. In: (Jan. 2018). arXiv: [1801.07064](https://arxiv.org/abs/1801.07064) [hep-th].
- [111] J. M. Cordes and F. A. Jenet. “DETECTING GRAVITATIONAL WAVE MEMORY WITH PULSAR TIMING”. In: *The Astrophysical Journal* 752.1 (May 2012), p. 54. DOI: [10.1088/0004-637X/752/1/54](https://doi.org/10.1088/0004-637X/752/1/54). URL: <https://dx.doi.org/10.1088/0004-637X/752/1/54>.
- [112] Andrea Cristofoli. “Gravitational shock waves and scattering amplitudes”. In: *JHEP* 11 (2020), p. 160. DOI: [10.1007/JHEP11\(2020\)160](https://doi.org/10.1007/JHEP11(2020)160). arXiv: [2006.08283](https://arxiv.org/abs/2006.08283) [hep-th].
- [113] C. Crnkovic and E. Witten. “Covariant description of canonical formalism in geometrical theories.” In: *Three Hundred Years of Gravitation*. 1987, pp. 676–684.
- [114] Michael Crossley, Paolo Glorioso, Hong Liu, and Yifan Wang. “Off-shell hydrodynamics from holography”. In: *JHEP* 02 (2016), p. 124. DOI: [10.1007/JHEP02\(2016\)124](https://doi.org/10.1007/JHEP02(2016)124). arXiv: [1504.07611](https://arxiv.org/abs/1504.07611) [hep-th].
- [115] Thibaut Damour. “Black-hole eddy currents”. In: *Phys. Rev. D* 18 (10 Nov. 1978), pp. 3598–3604. DOI: [10.1103/PhysRevD.18.3598](https://doi.org/10.1103/PhysRevD.18.3598). URL: <https://link.aps.org/doi/10.1103/PhysRevD.18.3598>.

- [116] Thibaut Damour. “Quelques proprietes mecaniques, electromagnet iques, thermodynamiques et quantiques des trous noir”. PhD thesis. Paris U., VI-VII, 1979.
- [117] Subhajit Dandapat, Abhimanyu Susobhanan, Lankeswar Dey, A. Gopakumar, Paul T. Baker, and Philippe Jetzer. “Efficient prescription to search for linear gravitational wave memory from hyperbolic black hole encounters and its application to the NANOGrav 12.5-year dataset”. In: *Phys. Rev. D* 109.10 (2024), p. 103018. doi: [10.1103/PhysRevD.109.103018](https://doi.org/10.1103/PhysRevD.109.103018). arXiv: [2402.03472](https://arxiv.org/abs/2402.03472) [[astro-ph.HE](#)].
- [118] Jan De Boer, Jarkko Järvelä, and Esko Keski-Vakkuri. “Aspects of capacity of entanglement”. In: *Phys. Rev. D* 99.6 (6 Mar. 2019), p. 066012. doi: [10.1103/PhysRevD.99.066012](https://doi.org/10.1103/PhysRevD.99.066012). arXiv: [1807.07357](https://arxiv.org/abs/1807.07357) [[hep-th](#)]. URL: <https://link.aps.org/doi/10.1103/PhysRevD.99.066012>.
- [119] Valerie Domcke, Camilo Garcia-Cely, and Nicholas L. Rodd. “Novel Search for High-Frequency Gravitational Waves with Low-Mass Axion Haloscopes”. In: *Phys. Rev. Lett.* 129.4 (2022), p. 041101. doi: [10.1103/PhysRevLett.129.041101](https://doi.org/10.1103/PhysRevLett.129.041101). arXiv: [2202.00695](https://arxiv.org/abs/2202.00695) [[hep-ph](#)].
- [120] Laura Donnay, Gaston Giribet, Hernan A. Gonzalez, and Miguel Pino. “Supertranslations and Superrotations at the Black Hole Horizon”. In: *Phys. Rev. Lett.* 116.9 (2016), p. 091101. doi: [10.1103/PhysRevLett.116.091101](https://doi.org/10.1103/PhysRevLett.116.091101). arXiv: [1511.08687](https://arxiv.org/abs/1511.08687) [[hep-th](#)].
- [121] Laura Donnay, Gaston Giribet, Hernán A. González, and Miguel Pino. “Extended Symmetries at the Black Hole Horizon”. In: *JHEP* 09 (2016), p. 100. doi: [10.1007/JHEP09\(2016\)100](https://doi.org/10.1007/JHEP09(2016)100). arXiv: [1607.05703](https://arxiv.org/abs/1607.05703) [[hep-th](#)].
- [122] Laura Donnay, Gaston Giribet, and Julio Oliva. “Horizon symmetries and hairy black holes in AdS”. In: *JHEP* 09 (2020), p. 120. doi: [10.1007/JHEP09\(2020\)120](https://doi.org/10.1007/JHEP09(2020)120). arXiv: [2007.08422](https://arxiv.org/abs/2007.08422) [[hep-th](#)].
- [123] Laura Donnay, Sabrina Pasterski, and Andrea Puhm. “Asymptotic Symmetries and Celestial CFT”. In: *JHEP* 09 (2020), p. 176. doi: [10.1007/JHEP09\(2020\)176](https://doi.org/10.1007/JHEP09(2020)176). arXiv: [2005.08990](https://arxiv.org/abs/2005.08990) [[hep-th](#)].
- [124] Laura Donnay, Andrea Puhm, and Andrew Strominger. “Conformally Soft Photons and Gravitons”. In: *JHEP* 01 (2019), p. 184. doi: [10.1007/JHEP01\(2019\)184](https://doi.org/10.1007/JHEP01(2019)184). arXiv: [1810.05219](https://arxiv.org/abs/1810.05219) [[hep-th](#)].
- [125] William Donnelly, Laurent Freidel, Seyed Farough Moosavian, and Antony J. Speranza. “Matrix Quantization of Gravitational Edge Modes”. In: *JHEP* 05 (2023), p. 163. doi: [10.1007/JHEP05\(2023\)163](https://doi.org/10.1007/JHEP05(2023)163). arXiv: [2212.09120](https://arxiv.org/abs/2212.09120) [[hep-th](#)].
- [126] Tevian Dray and Gerard 't Hooft. “The gravitational shock wave of a massless particle”. In: *Nuclear Physics B* 253 (1985), pp. 173–188. ISSN: 0550-3213. doi: [https://doi.org/10.1016/0550-3213\(85\)90525-5](https://doi.org/10.1016/0550-3213(85)90525-5).

URL: <https://www.sciencedirect.com/science/article/pii/S0550321385905255>.

- [127] Song Ming Du and Yanbei Chen. “Searching for near-horizon quantum structures in the binary black-hole stochastic gravitational-wave background”. In: *Phys. Rev. Lett.* 121.5 (2018), p. 051105. DOI: [10.1103/PhysRevLett.121.051105](https://doi.org/10.1103/PhysRevLett.121.051105). arXiv: [1803.10947](https://arxiv.org/abs/1803.10947) [gr-qc].
- [128] Fernando Echeverria. “Gravitational-wave measurements of the mass and angular momentum of a black hole”. In: *Phys. Rev. D* 40 (10 Nov. 1989), pp. 3194–3203. DOI: [10.1103/PhysRevD.40.3194](https://doi.org/10.1103/PhysRevD.40.3194). URL: <https://link.aps.org/doi/10.1103/PhysRevD.40.3194>.
- [129] Albert Einstein. *Investigations on the Theory of the Brownian Movement*. Dover Publications, 1956.
- [130] Aldo Ejlli, Damian Ejlli, Adrian Mike Cruise, Giampaolo Pisano, and Hartmut Grote. “Upper limits on the amplitude of ultra-high-frequency gravitational waves from graviton to photon conversion”. In: *Eur. Phys. J. C* 79.12 (2019), p. 1032. DOI: [10.1140/epjc/s10052-019-7542-5](https://doi.org/10.1140/epjc/s10052-019-7542-5). arXiv: [1908.00232](https://arxiv.org/abs/1908.00232) [gr-qc].
- [131] Christopher Eling. “Spontaneously Broken Asymptotic Symmetries and an Effective Action for Horizon Dynamics”. In: *JHEP* 02 (2017), p. 052. DOI: [10.1007/JHEP02\(2017\)052](https://doi.org/10.1007/JHEP02(2017)052). arXiv: [1611.10214](https://arxiv.org/abs/1611.10214) [hep-th].
- [132] Christopher Eling, Itzhak Fouxon, and Yaron Oz. “The Incompressible Navier-Stokes Equations From Membrane Dynamics”. In: *Phys. Lett. B* 680 (2009), pp. 496–499. DOI: [10.1016/j.physletb.2009.09.028](https://doi.org/10.1016/j.physletb.2009.09.028). arXiv: [0905.3638](https://arxiv.org/abs/0905.3638) [hep-th].
- [133] Christopher Eling, Adiel Meyer, and Yaron Oz. “The Relativistic Rindler Hydrodynamics”. In: *JHEP* 05 (2012), p. 116. DOI: [10.1007/JHEP05\(2012\)116](https://doi.org/10.1007/JHEP05(2012)116). arXiv: [1201.2705](https://arxiv.org/abs/1201.2705) [hep-th].
- [134] Christopher Eling and Yaron Oz. “On the Membrane Paradigm and Spontaneous Breaking of Horizon BMS Symmetries”. In: *JHEP* 07 (2016), p. 065. DOI: [10.1007/JHEP07\(2016\)065](https://doi.org/10.1007/JHEP07(2016)065). arXiv: [1605.00183](https://arxiv.org/abs/1605.00183) [hep-th].
- [135] Christopher Eling and Yaron Oz. “Relativistic CFT Hydrodynamics from the Membrane Paradigm”. In: *JHEP* 02 (2010), p. 069. DOI: [10.1007/JHEP02\(2010\)069](https://doi.org/10.1007/JHEP02(2010)069). arXiv: [0906.4999](https://arxiv.org/abs/0906.4999) [hep-th].
- [136] ET steering committee. *ET design report update 2020*. 2020. URL: <https://apps.et-gw.eu/tds/ql/?c=15418>.
- [137] Matthew Evans et al. “A Horizon Study for Cosmic Explorer: Science, Observatories, and Community”. In: (Sept. 2021). arXiv: [2109.09882](https://arxiv.org/abs/2109.09882) [astro-ph.IM].

- [138] Matthew Evans et al. “Observation of Parametric Instability in Advanced LIGO”. In: *Phys. Rev. Lett.* 114.16 (2015), p. 161102. DOI: [10.1103/PhysRevLett.114.161102](https://doi.org/10.1103/PhysRevLett.114.161102). arXiv: [1502.06058](https://arxiv.org/abs/1502.06058) [astro-ph.IM].
- [139] Thomas Faulkner, Hong Liu, and Mukund Rangamani. “Integrating out geometry: Holographic Wilsonian RG and the membrane paradigm”. In: *JHEP* 08 (2011), p. 051. DOI: [10.1007/JHEP08\(2011\)051](https://doi.org/10.1007/JHEP08(2011)051). arXiv: [1010.4036](https://arxiv.org/abs/1010.4036) [hep-th].
- [140] Thomas Faulkner and Antony J. Speranza. “Gravitational algebras and the generalized second law”. In: (May 2024). arXiv: [2405.00847](https://arxiv.org/abs/2405.00847) [hep-th].
- [141] Marc Favata. “Gravitational-wave memory revisited: memory from the merger and recoil of binary black holes”. In: *J. Phys. Conf. Ser.* 154 (2009). Ed. by Alberto Lobo and Carlos F. Sopuerta, p. 012043. DOI: [10.1088/1742-6596/154/1/012043](https://doi.org/10.1088/1742-6596/154/1/012043). arXiv: [0811.3451](https://arxiv.org/abs/0811.3451) [astro-ph].
- [142] Marc Favata. “Nonlinear gravitational-wave memory from binary black hole mergers”. In: *Astrophys. J. Lett.* 696 (2009), pp. L159–L162. DOI: [10.1088/0004-637X/696/2/L159](https://doi.org/10.1088/0004-637X/696/2/L159). arXiv: [0902.3660](https://arxiv.org/abs/0902.3660) [astro-ph.SR].
- [143] Marc Favata. “The gravitational-wave memory effect”. In: *Class. Quant. Grav.* 27 (2010). Ed. by Zsuzsa Marka and Szabolcs Marka, p. 084036. DOI: [10.1088/0264-9381/27/8/084036](https://doi.org/10.1088/0264-9381/27/8/084036). arXiv: [1003.3486](https://arxiv.org/abs/1003.3486) [gr-qc].
- [144] Richard P. Feynman. *The Brownian Movement*. Vol. I. 1964, p. 41.
- [145] Laurent Freidel, Marc Geiller, and Daniele Pranzetti. “Edge modes of gravity. Part I. Corner potentials and charges”. In: *JHEP* 11 (2020), p. 026. DOI: [10.1007/JHEP11\(2020\)026](https://doi.org/10.1007/JHEP11(2020)026). arXiv: [2006.12527](https://arxiv.org/abs/2006.12527) [hep-th].
- [146] Laurent Freidel, Marc Geiller, and Daniele Pranzetti. “Edge modes of gravity. Part II. Corner metric and Lorentz charges”. In: *JHEP* 11 (2020), p. 027. DOI: [10.1007/JHEP11\(2020\)027](https://doi.org/10.1007/JHEP11(2020)027). arXiv: [2007.03563](https://arxiv.org/abs/2007.03563) [hep-th].
- [147] Laurent Freidel, Marc Geiller, and Daniele Pranzetti. “Edge modes of gravity. Part III. Corner simplicity constraints”. In: *JHEP* 01 (2021), p. 100. DOI: [10.1007/JHEP01\(2021\)100](https://doi.org/10.1007/JHEP01(2021)100). arXiv: [2007.12635](https://arxiv.org/abs/2007.12635) [hep-th].
- [148] Laurent Freidel, Roberto Oliveri, Daniele Pranzetti, and Simone Speziale. “Extended corner symmetry, charge bracket and Einstein’s equations”. In: *JHEP* 09 (2021), p. 083. DOI: [10.1007/JHEP09\(2021\)083](https://doi.org/10.1007/JHEP09(2021)083). arXiv: [2104.12881](https://arxiv.org/abs/2104.12881) [hep-th].
- [149] Laurent Freidel, Roberto Oliveri, Daniele Pranzetti, and Simone Speziale. “The Weyl BMS group and Einstein’s equations”. In: *JHEP* 07 (2021), p. 170. DOI: [10.1007/JHEP07\(2021\)170](https://doi.org/10.1007/JHEP07(2021)170). arXiv: [2104.05793](https://arxiv.org/abs/2104.05793) [hep-th].
- [150] Laurent Freidel and Daniele Pranzetti. “Gravity from symmetry: duality and impulsive waves”. In: *Journal of High Energy Physics* 2022.4, 125 (Apr. 2022), p. 125. DOI: [10.1007/JHEP04\(2022\)125](https://doi.org/10.1007/JHEP04(2022)125). arXiv: [2109.06342](https://arxiv.org/abs/2109.06342) [hep-th].

- [151] Laurent Freidel, Daniele Pranzetti, and Ana-Maria Raclariu. “Higher spin dynamics in gravity and $w_{1+\infty}$ celestial symmetries”. In: *Phys. Rev. D* 106.8 (2022), p. 086013. DOI: [10.1103/PhysRevD.106.086013](https://doi.org/10.1103/PhysRevD.106.086013). arXiv: [2112.15573](https://arxiv.org/abs/2112.15573) [hep-th].
- [152] Laurent Freidel, Daniele Pranzetti, and Ana-Maria Raclariu. “Sub-subleading soft graviton theorem from asymptotic Einstein’s equations”. In: *JHEP* 05 (2022), p. 186. DOI: [10.1007/JHEP05\(2022\)186](https://doi.org/10.1007/JHEP05(2022)186). arXiv: [2111.15607](https://arxiv.org/abs/2111.15607) [hep-th].
- [153] A. Freise, S. Chelkowski, S. Hild, W. Del Pozzo, A. Perreca, and A. Vecchio. “Triple Michelson Interferometer for a Third-Generation Gravitational Wave Detector”. In: *Class. Quant. Grav.* 26 (2009), p. 085012. DOI: [10.1088/0264-9381/26/8/085012](https://doi.org/10.1088/0264-9381/26/8/085012). arXiv: [0804.1036](https://arxiv.org/abs/0804.1036) [gr-qc].
- [154] Jonathan Gair, Joseph D. Romano, Stephen Taylor, and Chiara M. F. Mingarelli. “Mapping gravitational-wave backgrounds using methods from CMB analysis: Application to pulsar timing arrays”. In: *Phys. Rev. D* 90.8 (2014), p. 082001. DOI: [10.1103/PhysRevD.90.082001](https://doi.org/10.1103/PhysRevD.90.082001). arXiv: [1406.4664](https://arxiv.org/abs/1406.4664) [gr-qc].
- [155] C. Gardiner. *Stochastic Methods: A Handbook for the Natural and Social Sciences*. Springer Series in Synergetics. Springer Berlin Heidelberg, 2009. ISBN: 9783540866848. URL: <https://books.google.com/books?id=epf8sgEACAAJ>.
- [156] M.E. Gertsenshtein. “Wave Resonance of Light and Gravitational Waves”. In: *Journal of Experimental and Theoretical Physics* 41 (1961), pp. 113–114.
- [157] J. Ghiglieri and M. Laine. “Gravitational wave background from Standard Model physics: Qualitative features”. In: *JCAP* 07 (2015), p. 022. DOI: [10.1088/1475-7516/2015/07/022](https://doi.org/10.1088/1475-7516/2015/07/022). arXiv: [1504.02569](https://arxiv.org/abs/1504.02569) [hep-ph].
- [158] Debodirna Ghosh and Biswajit Sahoo. “Spin-dependent gravitational tail memory in $D = 4$ ”. In: *Phys. Rev. D* 105.2 (2022), p. 025024. DOI: [10.1103/PhysRevD.105.025024](https://doi.org/10.1103/PhysRevD.105.025024). arXiv: [2106.10741](https://arxiv.org/abs/2106.10741) [hep-th].
- [159] Sourath Ghosh, Alexander Weaver, Jose Sanjuan, Paul Fulda, and Guido Mueller. “Detection of the gravitational memory effect in LISA using triggers from ground-based detectors”. In: *Phys. Rev. D* 107.8 (2023), p. 084051. DOI: [10.1103/PhysRevD.107.084051](https://doi.org/10.1103/PhysRevD.107.084051). arXiv: [2302.04396](https://arxiv.org/abs/2302.04396) [gr-qc].
- [160] B. Giacomone et al. “SQMS axion searches based on Q0~10 10 multimode superconducting cavities”. In: (2022). DOI: [10.2172/1896635](https://doi.org/10.2172/1896635).
- [161] Steven B. Giddings. “Black hole information, unitarity, and nonlocality”. In: *Phys. Rev. D* 74 (2006), p. 106005. DOI: [10.1103/PhysRevD.74.106005](https://doi.org/10.1103/PhysRevD.74.106005). arXiv: [hep-th/0605196](https://arxiv.org/abs/hep-th/0605196).

- [162] Steven B. Giddings. “Gravitational wave tests of quantum modifications to black hole structure – with post-GW150914 update”. In: *Class. Quant. Grav.* 33.23 (2016), p. 235010. doi: [10.1088/0264-9381/33/23/235010](https://doi.org/10.1088/0264-9381/33/23/235010). arXiv: [1602.03622](https://arxiv.org/abs/1602.03622) [gr-qc].
- [163] Steven B. Giddings, Jeffrey A. Harvey, J. G. Polchinski, Stephen H. Shenker, and Andrew Strominger. “Hairy black holes in string theory”. In: *Phys. Rev. D* 50 (1994), pp. 6422–6426. doi: [10.1103/PhysRevD.50.6422](https://doi.org/10.1103/PhysRevD.50.6422). arXiv: [hep-th/9309152](https://arxiv.org/abs/hep-th/9309152).
- [164] J. N. Goldberg, A. J. Macfarlane, E. T. Newman, F. Rohrlich, and E. C. G. Sudarshan. “Spin-s Spherical Harmonics and δ ”. In: *Journal of Mathematical Physics* 8.11 (Nov. 1967), pp. 2155–2161. issn: 0022-2488. doi: [10.1063/1.1705135](https://doi.org/10.1063/1.1705135). eprint: https://pubs.aip.org/aip/jmp/article-pdf/8/11/2155/19109311/2155_1_online.pdf. url: <https://doi.org/10.1063/1.1705135>.
- [165] Maxim Goryachev and Michael E. Tobar. “Gravitational Wave Detection with High Frequency Phonon Trapping Acoustic Cavities”. In: *Phys. Rev. D* 90.10 (2014), p. 102005. doi: [10.1103/PhysRevD.90.102005](https://doi.org/10.1103/PhysRevD.90.102005). arXiv: [1410.2334](https://arxiv.org/abs/1410.2334) [gr-qc].
- [166] Eric Gourgoulhon. “A Generalized Damour-Navier-Stokes equation applied to trapping horizons”. In: *Phys. Rev. D* 72 (2005), p. 104007. doi: [10.1103/PhysRevD.72.104007](https://doi.org/10.1103/PhysRevD.72.104007). arXiv: [gr-qc/0508003](https://arxiv.org/abs/gr-qc/0508003).
- [167] Alexander V. Gramolin, Deniz Aybas, Dorian Johnson, Janos Adam, and Alexander O. Sushkov. “Search for axion-like dark matter with ferromagnets”. In: *Nature Phys.* 17.1 (2021), pp. 79–84. doi: [10.1038/s41567-020-1006-6](https://doi.org/10.1038/s41567-020-1006-6). arXiv: [2003.03348](https://arxiv.org/abs/2003.03348) [hep-ex].
- [168] Alexander M. Grant and David A. Nichols. “Outlook for detecting the gravitational-wave displacement and spin memory effects with current and future gravitational-wave detectors”. In: *Phys. Rev. D* 107.6 (2023). [Erratum: *Phys.Rev.D* 108, 029901 (2023)], p. 064056. doi: [10.1103/PhysRevD.107.064056](https://doi.org/10.1103/PhysRevD.107.064056). arXiv: [2210.16266](https://arxiv.org/abs/2210.16266) [gr-qc].
- [169] Finnian Gray, David Kubiznak, Taillte May, Sydney Timmerman, and Erickson Tjoa. “Quantum imprints of gravitational shockwaves”. In: *JHEP* 11 (2021), p. 054. doi: [10.1007/JHEP11\(2021\)054](https://doi.org/10.1007/JHEP11(2021)054). arXiv: [2105.09337](https://arxiv.org/abs/2105.09337) [hep-th].
- [170] Sašo Grozdanov, Koenraad Schalm, and Vincenzo Scopelliti. “Black hole scrambling from hydrodynamics”. In: *Phys. Rev. Lett.* 120.23 (June 2018). arXiv:1710.00921, p. 231601. issn: 0031-9007, 1079-7114. doi: [10.1103/PhysRevLett.120.231601](https://doi.org/10.1103/PhysRevLett.120.231601). arXiv: [1710.00921](https://arxiv.org/abs/1710.00921) [hep-th].
- [171] Daniel Grumiller, Alfredo Pérez, M. M. Sheikh-Jabbari, Ricardo Troncoso, and Céline Zwikel. “Spacetime structure near generic horizons and

- soft hair”. In: *Phys. Rev. Lett.* 124.4 (2020), p. 041601. DOI: [10.1103/PhysRevLett.124.041601](https://doi.org/10.1103/PhysRevLett.124.041601). arXiv: [1908.09833 \[hep-th\]](https://arxiv.org/abs/1908.09833).
- [172] S. S. Gubser, Igor R. Klebanov, and Alexander M. Polyakov. “Gauge theory correlators from noncritical string theory”. In: *Phys. Lett. B* 428.1–2 (May 1998). arXiv:hep-th/9802109, pp. 105–114. ISSN: 03702693. DOI: [10.1016/S0370-2693\(98\)00377-3](https://doi.org/10.1016/S0370-2693(98)00377-3). arXiv: [hep-th/9802109](https://arxiv.org/abs/hep-th/9802109).
- [173] Steven S. Gubser. “AdS / CFT and gravity”. In: *Phys. Rev. D* 63 (2001), p. 084017. DOI: [10.1103/PhysRevD.63.084017](https://doi.org/10.1103/PhysRevD.63.084017). arXiv: [hep-th/9912001](https://arxiv.org/abs/hep-th/9912001).
- [174] Sergei Gukov, Vincent S. H. Lee, and Kathryn M. Zurek. “Near-horizon quantum dynamics of 4D Einstein gravity from 2D Jackiw-Teitelboim gravity”. In: *Phys. Rev. D* 107.1 (2023), p. 016004. DOI: [10.1103/PhysRevD.107.016004](https://doi.org/10.1103/PhysRevD.107.016004). arXiv: [2205.02233 \[hep-th\]](https://arxiv.org/abs/2205.02233).
- [175] Rutger van Haasteren and Yuri Levin. “Gravitational-wave memory and pulsar timing arrays”. In: *Mon. Not. Roy. Astron. Soc.* 401 (2010), p. 2372. DOI: [10.1111/j.1365-2966.2009.15885.x](https://doi.org/10.1111/j.1365-2966.2009.15885.x). arXiv: [0909.0954 \[astro-ph.IM\]](https://arxiv.org/abs/0909.0954).
- [176] Sasha Haco, Stephen W. Hawking, Malcolm J. Perry, and Andrew Strominger. “Black Hole Entropy and Soft Hair”. In: *JHEP* 12 (2018), p. 098. DOI: [10.1007/JHEP12\(2018\)098](https://doi.org/10.1007/JHEP12(2018)098). arXiv: [1810.01847 \[hep-th\]](https://arxiv.org/abs/1810.01847).
- [177] Yuta Hamada, Min-Seok Seo, and Gary Shiu. “Memory in de Sitter space and Bondi-Metzner-Sachs-like supertranslations”. In: *Phys. Rev. D* 96.2 (2017), p. 023509. DOI: [10.1103/PhysRevD.96.023509](https://doi.org/10.1103/PhysRevD.96.023509). arXiv: [1702.06928 \[hep-th\]](https://arxiv.org/abs/1702.06928).
- [178] Daniel Harlow and Daniel Jafferis. “The Factorization Problem in Jackiw-Teitelboim Gravity”. In: *JHEP* 02 (2020), p. 177. DOI: [10.1007/JHEP02\(2020\)177](https://doi.org/10.1007/JHEP02(2020)177). arXiv: [1804.01081 \[hep-th\]](https://arxiv.org/abs/1804.01081).
- [179] S. W. Hawking. “Particle creation by black holes”. In: *Communications in Mathematical Physics* 43.3 (1975), pp. 199–220. DOI: [10.1007/BF02345020](https://doi.org/10.1007/BF02345020). URL: <https://doi.org/10.1007/BF02345020>.
- [180] S. W. Hawking. “The Information Paradox for Black Holes”. In: Sept. 2015. arXiv: [1509.01147 \[hep-th\]](https://arxiv.org/abs/1509.01147).
- [181] Stephen W. Hawking, Malcolm J. Perry, and Andrew Strominger. “Superrotation Charge and Supertranslation Hair on Black Holes”. In: *JHEP* 05 (2017), p. 161. DOI: [10.1007/JHEP05\(2017\)161](https://doi.org/10.1007/JHEP05(2017)161). arXiv: [1611.09175 \[hep-th\]](https://arxiv.org/abs/1611.09175).
- [182] Temple He, Daniel Kapec, Ana-Maria Raclariu, and Andrew Strominger. “Loop-Corrected Virasoro Symmetry of 4D Quantum Gravity”. In: *JHEP* 08 (2017), p. 050. DOI: [10.1007/JHEP08\(2017\)050](https://doi.org/10.1007/JHEP08(2017)050). arXiv: [1701.00496 \[hep-th\]](https://arxiv.org/abs/1701.00496).

- [183] Temple He, Vyacheslav Lysov, Prahar Mitra, and Andrew Strominger. “BMS supertranslations and Weinberg’s soft graviton theorem”. In: *JHEP* 05 (2015), p. 151. doi: [10.1007/JHEP05\(2015\)151](https://doi.org/10.1007/JHEP05(2015)151). arXiv: [1401.7026](https://arxiv.org/abs/1401.7026) [hep-th].
- [184] Temple He and Prahar Mitra. “Asymptotic Structure of Higher Dimensional Yang-Mills Theory”. In: (June 2023). arXiv: [2306.04571](https://arxiv.org/abs/2306.04571) [hep-th].
- [185] Temple He and Prahar Mitra. “Asymptotic symmetries and Weinberg’s soft photon theorem in Mink_{d+2} ”. In: *JHEP* 10 (2019), p. 213. doi: [10.1007/JHEP10\(2019\)213](https://doi.org/10.1007/JHEP10(2019)213). arXiv: [1903.02608](https://arxiv.org/abs/1903.02608) [hep-th].
- [186] Temple He and Prahar Mitra. “Asymptotic symmetries in $(d+2)$ -dimensional gauge theories”. In: *JHEP* 10 (2019), p. 277. doi: [10.1007/JHEP10\(2019\)277](https://doi.org/10.1007/JHEP10(2019)277). arXiv: [1903.03607](https://arxiv.org/abs/1903.03607) [hep-th].
- [187] Temple He and Prahar Mitra. “New Magnetic Symmetries in $(d+2)$ -Dimensional QED”. In: (2019). arXiv: [1907.02808](https://arxiv.org/abs/1907.02808) [hep-th].
- [188] Temple He, Prahar Mitra, Achilleas P. Porfyriadis, and Andrew Strominger. “New Symmetries of Massless QED”. In: *JHEP* 10 (2014), p. 112. doi: [10.1007/JHEP10\(2014\)112](https://doi.org/10.1007/JHEP10(2014)112). arXiv: [1407.3789](https://arxiv.org/abs/1407.3789) [hep-th].
- [189] Temple He, Prahar Mitra, and Andrew Strominger. “2D Kac-Moody Symmetry of 4D Yang-Mills Theory”. In: *JHEP* 10 (2016), p. 137. doi: [10.1007/JHEP10\(2016\)137](https://doi.org/10.1007/JHEP10(2016)137). arXiv: [1503.02663](https://arxiv.org/abs/1503.02663) [hep-th].
- [190] Temple He, Ana-Maria Raclariu, and Kathryn M. Zurek. “An Infrared On-Shell Action and its Implications for Soft Charge Fluctuations in Asymptotically Flat Spacetimes”. In: (Aug. 2024). arXiv: [2408.01485](https://arxiv.org/abs/2408.01485) [hep-th].
- [191] Temple He, Ana-Maria Raclariu, and Kathryn M. Zurek. “From Shockwaves to the Gravitational Memory Effect”. In: (May 2023). arXiv: [2305.14411](https://arxiv.org/abs/2305.14411) [hep-th].
- [192] R. w. Hellings and G. s. Downs. “UPPER LIMITS ON THE ISOTROPIC GRAVITATIONAL RADIATION BACKGROUND FROM PULSAR TIMING ANALYSIS”. In: *Astrophys. J. Lett.* 265 (1983), pp. L39–L42. doi: [10.1086/183954](https://doi.org/10.1086/183954).
- [193] S. Hild et al. “Sensitivity Studies for Third-Generation Gravitational Wave Observatories”. In: *Class. Quant. Grav.* 28 (2011), p. 094013. doi: [10.1088/0264-9381/28/9/094013](https://doi.org/10.1088/0264-9381/28/9/094013). arXiv: [1012.0908](https://arxiv.org/abs/1012.0908) [gr-qc].
- [194] Moritz Hübner, Colm Talbot, Paul D. Lasky, and Eric Thrane. “Measuring gravitational-wave memory in the first LIGO/Virgo gravitational-wave transient catalog”. In: *Phys. Rev. D* 101.2 (2020), p. 023011. doi: [10.1103/PhysRevD.101.023011](https://doi.org/10.1103/PhysRevD.101.023011). arXiv: [1911.12496](https://arxiv.org/abs/1911.12496) [astro-ph.HE].
- [195] Ling-Yan Hung, Robert C. Myers, Michael Smolkin, and Alexandre Yale. “Holographic Calculations of Renyi Entropy”. In: *JHEP* 12 (2011), p. 047. doi: [10.1007/JHEP12\(2011\)047](https://doi.org/10.1007/JHEP12(2011)047). arXiv: [1110.1084](https://arxiv.org/abs/1110.1084) [hep-th].

- [196] Henri Inchauspé, Silvia Gasparotto, Diego Blas, Lavinia Heisenberg, Jann Zosso, and Shubhanshu Tiwari. “Measuring gravitational wave memory with LISA”. In: *Phys. Rev. D* 111.4 (2025), p. 044044. DOI: [10.1103/PhysRevD.111.044044](https://doi.org/10.1103/PhysRevD.111.044044). arXiv: [2406.09228](https://arxiv.org/abs/2406.09228) [gr-qc].
- [197] Maximiliano Isi, Matthew Giesler, Will M. Farr, Mark A. Scheel, and Saul A. Teukolsky. “Testing the no-hair theorem with GW150914”. In: *Phys. Rev. Lett.* 123.11 (2019), p. 111102. DOI: [10.1103/PhysRevLett.123.111102](https://doi.org/10.1103/PhysRevLett.123.111102). arXiv: [1905.00869](https://arxiv.org/abs/1905.00869) [gr-qc].
- [198] Asuka Ito, Tomonori Ikeda, Kentaro Miuchi, and Jiro Soda. “Probing GHz gravitational waves with graviton–magnon resonance”. In: *Eur. Phys. J. C* 80.3 (2020), p. 179. DOI: [10.1140/epjc/s10052-020-7735-y](https://doi.org/10.1140/epjc/s10052-020-7735-y). arXiv: [1903.04843](https://arxiv.org/abs/1903.04843) [gr-qc].
- [199] Asuka Ito and Jiro Soda. “Exploring High Frequency Gravitational Waves with Magnons”. In: (Dec. 2022). arXiv: [2212.04094](https://arxiv.org/abs/2212.04094) [gr-qc].
- [200] Vivek Iyer and Robert M. Wald. “A Comparison of Noether charge and Euclidean methods for computing the entropy of stationary black holes”. In: *Phys. Rev. D* 52 (1995), pp. 4430–4439. DOI: [10.1103/PhysRevD.52.4430](https://doi.org/10.1103/PhysRevD.52.4430). arXiv: [gr-qc/9503052](https://arxiv.org/abs/gr-qc/9503052).
- [201] Vivek Iyer and Robert M. Wald. “Some properties of Noether charge and a proposal for dynamical black hole entropy”. In: *Phys. Rev. D* 50 (1994), pp. 846–864. DOI: [10.1103/PhysRevD.50.846](https://doi.org/10.1103/PhysRevD.50.846). arXiv: [gr-qc/9403028](https://arxiv.org/abs/gr-qc/9403028).
- [202] Ted Jacobson. “Entanglement Equilibrium and the Einstein Equation”. In: *Phys. Rev. Lett.* 116.20 (May 2016). arXiv:1505.04753, p. 201101. ISSN: 0031-9007, 1079-7114. DOI: [10.1103/PhysRevLett.116.201101](https://doi.org/10.1103/PhysRevLett.116.201101). arXiv: [1505.04753](https://arxiv.org/abs/1505.04753) [gr-qc].
- [203] Ted Jacobson and Manus Visser. “Gravitational Thermodynamics of Causal Diamonds in (A)dS”. In: *SciPost Phys.* 7.6 (2019), p. 079. DOI: [10.21468/SciPostPhys.7.6.079](https://doi.org/10.21468/SciPostPhys.7.6.079). arXiv: [1812.01596](https://arxiv.org/abs/1812.01596) [hep-th].
- [204] Fredrick A. Jenet and Joseph D. Romano. “Understanding the gravitational-wave Hellings and Downs curve for pulsar timing arrays in terms of sound and electromagnetic waves”. In: *Am. J. Phys.* 83 (2015), p. 635. DOI: [10.1119/1.4916358](https://doi.org/10.1119/1.4916358). arXiv: [1412.1142](https://arxiv.org/abs/1412.1142) [gr-qc].
- [205] Yonatan Kahn, Benjamin R. Safdi, and Jesse Thaler. “Broadband and Resonant Approaches to Axion Dark Matter Detection”. In: *Phys. Rev. Lett.* 117.14 (2016), p. 141801. DOI: [10.1103/PhysRevLett.117.141801](https://doi.org/10.1103/PhysRevLett.117.141801). arXiv: [1602.01086](https://arxiv.org/abs/1602.01086) [hep-ph].
- [206] Cynthia Keeler, Tucker Manton, and Nikhil Monga. “From Navier-Stokes to Maxwell via Einstein”. In: *JHEP* 08 (2020), p. 147. DOI: [10.1007/JHEP08\(2020\)147](https://doi.org/10.1007/JHEP08(2020)147). arXiv: [2005.04242](https://arxiv.org/abs/2005.04242) [hep-th].

- [207] T W B Kibble. “Topology of cosmic domains and strings”. In: *Journal of Physics A: Mathematical and General* 9.8 (Aug. 1976), p. 1387. DOI: [10.1088/0305-4470/9/8/029](https://doi.org/10.1088/0305-4470/9/8/029). URL: <https://dx.doi.org/10.1088/0305-4470/9/8/029>.
- [208] Taylor Knapp, Arianna Renzini, and Patrick Meyers. *Approximating Simulated Stochastic Gravitational Wave Background with Broken Splines and Power Laws via MCMC Fitting*. Technical Report LIGO-T2200252-v1. Accessed: 2025-04-13. LIGO Laboratory, 2022. URL: <https://dcc.ligo.org/LIGO-T2200252/public>.
- [209] Jun-ichirou Koga. “Asymptotic symmetries on Killing horizons”. In: *Phys. Rev. D* 64 (2001), p. 124012. DOI: [10.1103/PhysRevD.64.124012](https://doi.org/10.1103/PhysRevD.64.124012). arXiv: [gr-qc/0107096](https://arxiv.org/abs/gr-qc/0107096).
- [210] P. Kovtun, Dan T. Son, and Andrei O. Starinets. “Viscosity in strongly interacting quantum field theories from black hole physics”. In: *Phys. Rev. Lett.* 94 (2005), p. 111601. DOI: [10.1103/PhysRevLett.94.111601](https://doi.org/10.1103/PhysRevLett.94.111601). arXiv: [hep-th/0405231](https://arxiv.org/abs/hep-th/0405231).
- [211] Pavel Kovtun, Dam T. Son, and Andrei O. Starinets. “Holography and hydrodynamics: Diffusion on stretched horizons”. In: *JHEP* 10 (2003), p. 064. DOI: [10.1088/1126-6708/2003/10/064](https://doi.org/10.1088/1126-6708/2003/10/064). arXiv: [hep-th/0309213](https://arxiv.org/abs/hep-th/0309213).
- [212] Pavel K. Kovtun and Andrei O. Starinets. “Quasinormal modes and holography”. In: *Phys. Rev. D* 72 (2005), p. 086009. DOI: [10.1103/PhysRevD.72.086009](https://doi.org/10.1103/PhysRevD.72.086009). arXiv: [hep-th/0506184](https://arxiv.org/abs/hep-th/0506184).
- [213] R Kubo. “The fluctuation-dissipation theorem”. In: *Reports on Progress in Physics* 29.1 (Jan. 1966), pp. 255–284. DOI: [10.1088/0034-4885/29/1/306](https://doi.org/10.1088/0034-4885/29/1/306). URL: <https://doi.org/10.1088/0034-4885/29/1/306>.
- [214] Paul Langevin. “Sur la théorie du mouvement brownien”. In: *C. R. Acad. Sci. Paris* 146 (1908), pp. 530–533.
- [215] Paul D. Lasky, Eric Thrane, Yuri Levin, Jonathan Blackman, and Yanbei Chen. “Detecting gravitational-wave memory with LIGO: implications of GW150914”. In: *Phys. Rev. Lett.* 117.6 (2016), p. 061102. DOI: [10.1103/PhysRevLett.117.061102](https://doi.org/10.1103/PhysRevLett.117.061102). arXiv: [1605.01415](https://arxiv.org/abs/1605.01415) [[astro-ph.HE](https://arxiv.org/abs/1605.01415)].
- [216] J. Lee and Robert M. Wald. “Local symmetries and constraints”. In: *J. Math. Phys.* 31 (1990), pp. 725–743. DOI: [10.1063/1.528801](https://doi.org/10.1063/1.528801).
- [217] Vincent S. H. Lee, Kathryn M. Zurek, and Yanbei Chen. “Astronomical image blurring from transversely correlated quantum gravity fluctuations”. In: *Phys. Rev. D* 109.8 (2024), p. 084005. DOI: [10.1103/PhysRevD.109.084005](https://doi.org/10.1103/PhysRevD.109.084005). arXiv: [2312.06757](https://arxiv.org/abs/2312.06757) [[gr-qc](https://arxiv.org/abs/2312.06757)].

- [218] Don S. Lemons and Anthony Gythiel. “Paul Langevin’s 1908 paper "On the Theory of Brownian Motion" ["Sur la théorie du mouvement brownien," C. R. Acad. Sci. (Paris) 146, 530–533 (1908)]”. In: *American Journal of Physics* 65.11 (1997), pp. 1079–1081. ISSN: 0002-9505. DOI: [10.1119/1.18725](https://doi.org/10.1119/1.18725).
- [219] Dongjun Li, Vincent S. H. Lee, Yanbei Chen, and Kathryn M. Zurek. “Interferometer Response to Geontropic Fluctuations”. In: *Phys. Rev. D* 107.2 (Sept. 2022), p. 024002. DOI: [10.1103/PhysRevD.107.024002](https://doi.org/10.1103/PhysRevD.107.024002). arXiv: [2209.07543](https://arxiv.org/abs/2209.07543) [gr-qc].
- [220] Xiang Li et al. “Broadband sensitivity improvement via coherent quantum feedback with PT symmetry”. In: (Dec. 2020). arXiv: [2012.00836](https://arxiv.org/abs/2012.00836) [quant-ph].
- [221] Zheng-Cheng Liang, Zhi-Yuan Li, En-Kun Li, Jian-dong Zhang, and Yi-Ming Hu. “Sensitivity to anisotropic gravitational-wave background with space-borne detector networks”. In: *Phys. Rev. D* 110.4 (2024), p. 043031. DOI: [10.1103/PhysRevD.110.043031](https://doi.org/10.1103/PhysRevD.110.043031). arXiv: [2307.01541](https://arxiv.org/abs/2307.01541) [gr-qc].
- [222] *LIGO Document T2000062-v1*. 2020. URL: <https://dcc.ligo.org/cgi-bin/DocDB/ShowDocument?.submit=Identifier&docid=T2000062&version=1>.
- [223] Xiaolin Liu, Xiaokai He, and Zhoujian Cao. “Accurate calculation of gravitational wave memory”. In: *Phys. Rev. D* 103.4 (2021), p. 043005. DOI: [10.1103/PhysRevD.103.043005](https://doi.org/10.1103/PhysRevD.103.043005). arXiv: [2302.02642](https://arxiv.org/abs/2302.02642) [gr-qc].
- [224] Vyacheslav Lysov and Andrew Strominger. “From Petrov-Einstein to Navier-Stokes”. In: (Apr. 2011). arXiv: [1104.5502](https://arxiv.org/abs/1104.5502) [hep-th].
- [225] Michele Maggiore. “Gravitational wave experiments and early universe cosmology”. In: *Phys. Rept.* 331 (2000), pp. 283–367. DOI: [10.1016/S0370-1573\(99\)00102-7](https://doi.org/10.1016/S0370-1573(99)00102-7). arXiv: [gr-qc/9909001](https://arxiv.org/abs/gr-qc/9909001).
- [226] Michele Maggiore. *Gravitational Waves, Volume 1: Theory and Experiments*. Oxford University Press, 2007.
- [227] Juan Maldacena, Stephen H. Shenker, and Douglas Stanford. “A bound on chaos”. In: *JHEP* 08 (2016), p. 106. DOI: [10.1007/JHEP08\(2016\)106](https://doi.org/10.1007/JHEP08(2016)106). arXiv: [1503.01409](https://arxiv.org/abs/1503.01409) [hep-th].
- [228] Juan Martin Maldacena. “The Large N limit of superconformal field theories and supergravity”. In: *Adv. Theor. Math. Phys.* 2.4 (1998). arXiv:hep-th/9711200, pp. 231–252. ISSN: 00207748. DOI: [10.1023/A:1026654312961](https://doi.org/10.1023/A:1026654312961). arXiv: [hep-th/9711200](https://arxiv.org/abs/hep-th/9711200).
- [229] Vuk Mandic. *ICTS Summer Lectures on Stochastic Gravitational Wave Background*. July 2021.
- [230] A. Manu, Debodirna Ghosh, Alok Laddha, and P. V. Athira. “Soft radiation from scattering amplitudes revisited”. In: *JHEP* 05 (2021), p. 056. DOI: [10.1007/JHEP05\(2021\)056](https://doi.org/10.1007/JHEP05(2021)056). arXiv: [2007.02077](https://arxiv.org/abs/2007.02077) [hep-th].

- [231] Zachary Mark, Aaron Zimmerman, Song Ming Du, and Yanbei Chen. “A recipe for echoes from exotic compact objects”. In: *Phys. Rev. D* 96.8 (2017), p. 084002. DOI: [10.1103/PhysRevD.96.084002](https://doi.org/10.1103/PhysRevD.96.084002). arXiv: [1706.06155](https://arxiv.org/abs/1706.06155) [gr-qc].
- [232] Denis Martynov et al. “Exploring the sensitivity of gravitational wave detectors to neutron star physics”. In: *Phys. Rev. D* 99.10 (2019), p. 102004. DOI: [10.1103/PhysRevD.99.102004](https://doi.org/10.1103/PhysRevD.99.102004). arXiv: [1901.03885](https://arxiv.org/abs/1901.03885) [astro-ph.IM].
- [233] Denis V. Martynov et al. “Quantum correlation measurements in interferometric gravitational wave detectors”. In: *Phys. Rev. A* 95.4 (2017), p. 043831. DOI: [10.1103/PhysRevA.95.043831](https://doi.org/10.1103/PhysRevA.95.043831). arXiv: [1702.03329](https://arxiv.org/abs/1702.03329) [physics.optics].
- [234] L. McCuller et al. “LIGO’s quantum response to squeezed states”. In: *Phys. Rev. D* 104 (6 Sept. 2021), p. 062006. DOI: [10.1103/PhysRevD.104.062006](https://doi.org/10.1103/PhysRevD.104.062006). URL: <https://link.aps.org/doi/10.1103/PhysRevD.104.062006>.
- [235] Lee McCuller. “Single-Photon Signal Sideband Detection for High-Power Michelson Interferometers”. In: (Nov. 2022). arXiv: [2211.04016](https://arxiv.org/abs/2211.04016) [physics.ins-det].
- [236] Lee McCuller et al. “Probing Entanglement Entropy in Gravity with Photon Counting Michelson Interferometers of the GQuEST experiment”. In: *In Preparation* (2022).
- [237] Haixing Miao, Yiqiu Ma, Chunnong Zhao, and Yanbei Chen. “Enhancing the bandwidth of gravitational-wave detectors with unstable optomechanical filters”. In: *Phys. Rev. Lett.* 115.21 (2015), p. 211104. DOI: [10.1103/PhysRevLett.115.211104](https://doi.org/10.1103/PhysRevLett.115.211104). arXiv: [1506.00117](https://arxiv.org/abs/1506.00117) [quant-ph].
- [238] Hannah Middleton, Siyuan Chen, Walter Del Pozzo, Alberto Sesana, and Alberto Vecchio. “No tension between assembly models of super massive black hole binaries and pulsar observations”. In: *Nature Commun.* 9.1 (2018), p. 573. DOI: [10.1038/s41467-018-02916-7](https://doi.org/10.1038/s41467-018-02916-7). arXiv: [1707.00623](https://arxiv.org/abs/1707.00623) [astro-ph.GA].
- [239] Hannah Middleton, Walter Del Pozzo, Will M. Farr, Alberto Sesana, and Alberto Vecchio. “Astrophysical constraints on massive black hole binary evolution from Pulsar Timing Arrays”. In: *Mon. Not. Roy. Astron. Soc.* 455.1 (2016), pp. L72–L76. DOI: [10.1093/mnrasl/slv150](https://doi.org/10.1093/mnrasl/slv150). arXiv: [1507.00992](https://arxiv.org/abs/1507.00992) [astro-ph.CO].
- [240] Chiara M. F. Mingarelli, Stephen R. Taylor, B. S. Sathyaprakash, and Will M. Farr. “Understanding $\Omega_{\text{gw}}(f)$ in Gravitational Wave Experiments”. In: (Nov. 2019). arXiv: [1911.09745](https://arxiv.org/abs/1911.09745) [gr-qc].
- [241] Charles W. Misner, K. S. Thorne, and J. A. Wheeler. *Gravitation*. San Francisco: W. H. Freeman, 1973. ISBN: 978-0-7167-0344-0, 978-0-691-17779-3.

- [242] Keefe Mitman et al. “A review of gravitational memory and BMS frame fixing in numerical relativity”. In: *Class. Quant. Grav.* 41.22 (2024), p. 223001. DOI: [10.1088/1361-6382/ad83c2](https://doi.org/10.1088/1361-6382/ad83c2). arXiv: [2405.08868](https://arxiv.org/abs/2405.08868) [gr-qc].
- [243] Keefe Mitman et al. “Computation of displacement and spin gravitational memory in numerical relativity”. In: *Phys. Rev. D* 102.10 (2020), p. 104007. DOI: [10.1103/PhysRevD.102.104007](https://doi.org/10.1103/PhysRevD.102.104007). arXiv: [2007.11562](https://arxiv.org/abs/2007.11562) [gr-qc].
- [244] Prahar Mitra. “Asymptotic Symmetries in Four-Dimensional Gauge and Gravity Theories”. PhD thesis. Harvard U. (main), May 2017.
- [245] C J Moore, R H Cole, and C P L Berry. “Gravitational-wave sensitivity curves”. In: *Classical and Quantum Gravity* 32.1 (Dec. 2014), p. 015014. DOI: [10.1088/0264-9381/32/1/015014](https://doi.org/10.1088/0264-9381/32/1/015014). URL: <https://doi.org/10.1088/0264-9381/32/1/015014>.
- [246] Yuki Nakaguchi and Tatsuma Nishioka. “A holographic proof of Rényi entropic inequalities”. In: *JHEP* 12 (2016), p. 129. DOI: [10.1007/JHEP12\(2016\)129](https://doi.org/10.1007/JHEP12(2016)129). arXiv: [1606.08443](https://arxiv.org/abs/1606.08443) [hep-th].
- [247] NANOGrav Collaboration. *Evidence for a Gravitational-Wave Background*. <https://nanograv.org/15yr/Summary/Background>. 2023.
- [248] NASA Imagine the Universe! *Pulsar Gravitational Waves Win Nobel Prize*. Accessed: 2025-04-13. 1993. URL: https://imagine.gsfc.nasa.gov/educators/programs/cosmictimes/educators/guide/1993/gravitational_waves.html.
- [249] Kevin Nguyen. “Carrollian conformal correlators and massless scattering amplitudes”. In: *JHEP* 01 (2024), p. 076. DOI: [10.1007/JHEP01\(2024\)076](https://doi.org/10.1007/JHEP01(2024)076). arXiv: [2311.09869](https://arxiv.org/abs/2311.09869) [hep-th].
- [250] David A. Nichols. “Spin memory effect for compact binaries in the post-Newtonian approximation”. In: *Phys. Rev. D* 95.8 (2017), p. 084048. DOI: [10.1103/PhysRevD.95.084048](https://doi.org/10.1103/PhysRevD.95.084048). arXiv: [1702.03300](https://arxiv.org/abs/1702.03300) [gr-qc].
- [251] Dominik Nickel and Dam T. Son. “Deconstructing holographic liquids”. In: *New J. Phys.* 13 (2011), p. 075010. DOI: [10.1088/1367-2630/13/7/075010](https://doi.org/10.1088/1367-2630/13/7/075010). arXiv: [1009.3094](https://arxiv.org/abs/1009.3094) [hep-th].
- [252] Maulik Parikh and Frank Wilczek. “An Action for black hole membranes”. In: *Phys. Rev. D* 58 (1998), p. 064011. DOI: [10.1103/PhysRevD.58.064011](https://doi.org/10.1103/PhysRevD.58.064011). arXiv: [gr-qc/9712077](https://arxiv.org/abs/gr-qc/9712077).
- [253] Sabrina Pasterski, Monica Pate, and Ana-Maria Raclariu. “Celestial Holography”. In: *Snowmass 2021*. Nov. 2021. arXiv: [2111.11392](https://arxiv.org/abs/2111.11392) [hep-th].
- [254] Sabrina Pasterski and Andrea Puhm. “Shifting spin on the celestial sphere”. In: *Phys. Rev. D* 104.8 (2021), p. 086020. DOI: [10.1103/PhysRevD.104.086020](https://doi.org/10.1103/PhysRevD.104.086020). arXiv: [2012.15694](https://arxiv.org/abs/2012.15694) [hep-th].

- [255] Sabrina Pasterski, Andrea Puhm, and Emilio Trevisani. “Celestial diamonds: conformal multiplets in celestial CFT”. In: *JHEP* 11 (2021), p. 072. DOI: [10.1007/JHEP11\(2021\)072](https://doi.org/10.1007/JHEP11(2021)072). arXiv: [2105.03516](https://arxiv.org/abs/2105.03516) [hep-th].
- [256] Sabrina Pasterski and Shu-Heng Shao. “Conformal basis for flat space amplitudes”. In: *Phys. Rev. D* 96.6 (2017), p. 065022. DOI: [10.1103/PhysRevD.96.065022](https://doi.org/10.1103/PhysRevD.96.065022). arXiv: [1705.01027](https://arxiv.org/abs/1705.01027) [hep-th].
- [257] Sabrina Pasterski, Shu-Heng Shao, and Andrew Strominger. “Flat Space Amplitudes and Conformal Symmetry of the Celestial Sphere”. In: *Phys. Rev. D* 96.6 (2017), p. 065026. DOI: [10.1103/PhysRevD.96.065026](https://doi.org/10.1103/PhysRevD.96.065026). arXiv: [1701.00049](https://arxiv.org/abs/1701.00049) [hep-th].
- [258] Sabrina Pasterski, Shu-Heng Shao, and Andrew Strominger. “Gluon Amplitudes as 2d Conformal Correlators”. In: *Phys. Rev. D* 96.8 (2017), p. 085006. DOI: [10.1103/PhysRevD.96.085006](https://doi.org/10.1103/PhysRevD.96.085006). arXiv: [1706.03917](https://arxiv.org/abs/1706.03917) [hep-th].
- [259] Sabrina Pasterski, Andrew Strominger, and Alexander Zhiboedov. “New Gravitational Memories”. In: *JHEP* 12 (2016), p. 053. DOI: [10.1007/JHEP12\(2016\)053](https://doi.org/10.1007/JHEP12(2016)053). arXiv: [1502.06120](https://arxiv.org/abs/1502.06120) [hep-th].
- [260] Sabrina Pasterski and Herman Verlinde. “HPS meets AMPS: how soft hair dissolves the firewall”. In: *JHEP* 09 (2021), p. 099. DOI: [10.1007/JHEP09\(2021\)099](https://doi.org/10.1007/JHEP09(2021)099). arXiv: [2012.03850](https://arxiv.org/abs/2012.03850) [hep-th].
- [261] Eric Perlmutter. “A universal feature of CFT Rényi entropy”. In: *JHEP* 03 (2014), p. 117. DOI: [10.1007/JHEP03\(2014\)117](https://doi.org/10.1007/JHEP03(2014)117). arXiv: [1308.1083](https://arxiv.org/abs/1308.1083) [hep-th].
- [262] Eric Perlmutter. “Bounding the Space of Holographic CFTs with Chaos”. In: *JHEP* 10 (2016), p. 069. DOI: [10.1007/JHEP10\(2016\)069](https://doi.org/10.1007/JHEP10(2016)069). arXiv: [1602.08272](https://arxiv.org/abs/1602.08272) [hep-th].
- [263] E. S. Phinney. “A Practical theorem on gravitational wave backgrounds”. In: (July 2001). arXiv: [astro-ph/0108028](https://arxiv.org/abs/astro-ph/0108028).
- [264] Natalia Pinzani-Fokeeva and Marika Taylor. “Towards a general fluid/gravity correspondence”. In: *Phys. Rev. D* 91.4 (2015), p. 044001. DOI: [10.1103/PhysRevD.91.044001](https://doi.org/10.1103/PhysRevD.91.044001). arXiv: [1401.5975](https://arxiv.org/abs/1401.5975) [hep-th].
- [265] G. Policastro, Dan T. Son, and Andrei O. Starinets. “The Shear viscosity of strongly coupled N=4 supersymmetric Yang-Mills plasma”. In: *Phys. Rev. Lett.* 87 (2001), p. 081601. DOI: [10.1103/PhysRevLett.87.081601](https://doi.org/10.1103/PhysRevLett.87.081601). arXiv: [hep-th/0104066](https://arxiv.org/abs/hep-th/0104066).
- [266] Giuseppe Policastro, Dam T. Son, and Andrei O. Starinets. “From AdS / CFT correspondence to hydrodynamics”. In: *JHEP* 09 (2002), p. 043. DOI: [10.1088/1126-6708/2002/09/043](https://doi.org/10.1088/1126-6708/2002/09/043). arXiv: [hep-th/0205052](https://arxiv.org/abs/hep-th/0205052).

- [267] Giuseppe Policastro, Dam T. Son, and Andrei O. Starinets. “From AdS / CFT correspondence to hydrodynamics. 2. Sound waves”. In: *JHEP* 12 (2002), p. 054. DOI: [10.1088/1126-6708/2002/12/054](https://doi.org/10.1088/1126-6708/2002/12/054). arXiv: [hep-th/0210220](https://arxiv.org/abs/hep-th/0210220).
- [268] Denis Pollney and Christian Reisswig. “Gravitational memory in binary black hole mergers”. In: *Astrophys. J. Lett.* 732 (2011), p. L13. DOI: [10.1088/2041-8205/732/1/L13](https://doi.org/10.1088/2041-8205/732/1/L13). arXiv: [1004.4209 \[gr-qc\]](https://arxiv.org/abs/1004.4209).
- [269] Richard H. Price, Kip S Thorne, and Douglas A Macdonald. *Black holes : the membrane paradigm*. Yale University Press, 1986. ISBN: 0300037694.
- [270] Pranav Pulakkat. “On the charge algebra of causal diamonds in three dimensional gravity”. In: *JHEP* 07 (2024), p. 251. DOI: [10.1007/JHEP07\(2024\)251](https://doi.org/10.1007/JHEP07(2024)251). arXiv: [2404.03014 \[hep-th\]](https://arxiv.org/abs/2404.03014).
- [271] Mukund Rangamani. “Gravity and Hydrodynamics: Lectures on the fluid-gravity correspondence”. In: *Class. Quant. Grav.* 26 (2009). Ed. by A. M. Uranga, p. 224003. DOI: [10.1088/0264-9381/26/22/224003](https://doi.org/10.1088/0264-9381/26/22/224003). arXiv: [0905.4352 \[hep-th\]](https://arxiv.org/abs/0905.4352).
- [272] Daniel J. Reardon et al. “Search for an Isotropic Gravitational-wave Background with the Parkes Pulsar Timing Array”. In: *Astrophys. J. Lett.* 951.1 (2023), p. L6. DOI: [10.3847/2041-8213/acdd02](https://doi.org/10.3847/2041-8213/acdd02). arXiv: [2306.16215 \[astro-ph.HE\]](https://arxiv.org/abs/2306.16215).
- [273] Nick van Remortel, Kamiel Janssens, and Kevin Turbang. “Stochastic gravitational wave background: Methods and implications”. In: *Prog. Part. Nucl. Phys.* 128 (2023), p. 104003. DOI: [10.1016/j.pnpnp.2022.104003](https://doi.org/10.1016/j.pnpnp.2022.104003). arXiv: [2210.00761 \[gr-qc\]](https://arxiv.org/abs/2210.00761).
- [274] Daniel A. Roberts and Brian Swingle. “Lieb-Robinson Bound and the Butterfly Effect in Quantum Field Theories”. In: *Phys. Rev. Lett.* 117.9 (2016), p. 091602. DOI: [10.1103/PhysRevLett.117.091602](https://doi.org/10.1103/PhysRevLett.117.091602). arXiv: [1603.09298 \[hep-th\]](https://arxiv.org/abs/1603.09298).
- [275] Joseph D. Romano and Bruce Allen. “Answers to frequently asked questions about the pulsar timing array Hellings and Downs curve”. In: *Class. Quant. Grav.* 41.17 (2024), p. 175008. DOI: [10.1088/1361-6382/ad4c4c](https://doi.org/10.1088/1361-6382/ad4c4c). arXiv: [2308.05847 \[gr-qc\]](https://arxiv.org/abs/2308.05847).
- [276] Joseph D. Romano and Neil J. Cornish. “Detection methods for stochastic gravitational-wave backgrounds: a unified treatment”. In: *Living Rev. Rel.* 20.1 (2017), p. 2. DOI: [10.1007/s41114-017-0004-1](https://doi.org/10.1007/s41114-017-0004-1). arXiv: [1608.06889 \[gr-qc\]](https://arxiv.org/abs/1608.06889).
- [277] Carlo Rovelli and Francesca Vidotto. *Covariant Loop Quantum Gravity: An Elementary Introduction to Quantum Gravity and Spinfoam Theory*. Cambridge Monographs on Mathematical Physics. Cambridge University Press, Nov. 2014. ISBN: 978-1-107-06962-6, 978-1-316-14729-0.

- [278] Shinsei Ryu and Tadashi Takayanagi. “Aspects of Holographic Entanglement Entropy”. In: *JHEP* 08 (2006), p. 045. doi: [10.1088/1126-6708/2006/08/045](https://doi.org/10.1088/1126-6708/2006/08/045). arXiv: [hep-th/0605073](https://arxiv.org/abs/hep-th/0605073).
- [279] R. Sachs. “Asymptotic symmetries in gravitational theory”. In: *Phys. Rev.* 128 (1962), pp. 2851–2864. doi: [10.1103/PhysRev.128.2851](https://doi.org/10.1103/PhysRev.128.2851).
- [280] R. K. Sachs. “Gravitational waves in general relativity. 8. Waves in asymptotically flat space-times”. In: *Proc. Roy. Soc. Lond. A* 270 (1962), pp. 103–126. doi: [10.1098/rspa.1962.0206](https://doi.org/10.1098/rspa.1962.0206).
- [281] Yasuhiro Sekino and Leonard Susskind. “Fast Scramblers”. In: *JHEP* 10 (2008), p. 065. doi: [10.1088/1126-6708/2008/10/065](https://doi.org/10.1088/1126-6708/2008/10/065). arXiv: [0808.2096](https://arxiv.org/abs/0808.2096) [[hep-th](https://arxiv.org/abs/hep-th)].
- [282] Konstadinos Sfetsos. “On gravitational shock waves in curved space-times”. In: *Nucl. Phys. B* 436 (1995), pp. 721–745. doi: [10.1016/0550-3213\(94\)00573-W](https://doi.org/10.1016/0550-3213(94)00573-W). arXiv: [hep-th/9408169](https://arxiv.org/abs/hep-th/9408169).
- [283] Stephen H. Shenker and Douglas Stanford. “Black holes and the butterfly effect”. In: *JHEP* 03 (2014), p. 067. doi: [10.1007/JHEP03\(2014\)067](https://doi.org/10.1007/JHEP03(2014)067). arXiv: [1306.0622](https://arxiv.org/abs/1306.0622) [[hep-th](https://arxiv.org/abs/hep-th)].
- [284] Stephen H. Shenker and Douglas Stanford. “Multiple Shocks”. In: *JHEP* 12 (2014), p. 046. doi: [10.1007/JHEP12\(2014\)046](https://doi.org/10.1007/JHEP12(2014)046). arXiv: [1312.3296](https://arxiv.org/abs/1312.3296) [[hep-th](https://arxiv.org/abs/hep-th)].
- [285] Stephen H. Shenker and Douglas Stanford. “Stringy effects in scrambling”. In: *JHEP* 05 (2015), p. 132. doi: [10.1007/JHEP05\(2015\)132](https://doi.org/10.1007/JHEP05(2015)132). arXiv: [1412.6087](https://arxiv.org/abs/1412.6087) [[hep-th](https://arxiv.org/abs/hep-th)].
- [286] Masaru Shibata and Keisuke Taniguchi. “Merger of binary neutron stars to a black hole: disk mass, short gamma-ray bursts, and quasinormal mode ringing”. In: *Phys. Rev. D* 73 (2006), p. 064027. doi: [10.1103/PhysRevD.73.064027](https://doi.org/10.1103/PhysRevD.73.064027). arXiv: [astro-ph/0603145](https://arxiv.org/abs/astro-ph/0603145).
- [287] Sebastian Silva. “Black hole entropy and thermodynamics from symmetries”. In: *Class. Quant. Grav.* 19 (2002), pp. 3947–3962. doi: [10.1088/0264-9381/19/15/306](https://doi.org/10.1088/0264-9381/19/15/306). arXiv: [hep-th/0204179](https://arxiv.org/abs/hep-th/0204179).
- [288] Sergey N. Solodukhin. “Conformal description of horizon’s states”. In: *Phys. Lett. B* 454.3-4 (May 1999), pp. 213–222. doi: [10.1016/S0370-2693\(99\)00398-6](https://doi.org/10.1016/S0370-2693(99)00398-6). arXiv: [hep-th/9812056](https://arxiv.org/abs/hep-th/9812056). URL: <https://doi.org/10.1016%2Fs0370-2693%2899%2900398-6>.
- [289] Dam T. Son and Andrei O. Starinets. “Viscosity, Black Holes, and Quantum Field Theory”. In: *Ann. Rev. Nucl. Part. Sci.* 57 (2007), pp. 95–118. doi: [10.1146/annurev.nucl.57.090506.123120](https://doi.org/10.1146/annurev.nucl.57.090506.123120). arXiv: [0704.0240](https://arxiv.org/abs/0704.0240) [[hep-th](https://arxiv.org/abs/hep-th)].

- [290] Huichao Song, Steffen A. Bass, Ulrich Heinz, Tetsufumi Hirano, and Chun Shen. “200 A GeV Au+Au collisions serve a nearly perfect quark-gluon liquid”. In: *Phys. Rev. Lett.* 106 (2011). [Erratum: *Phys.Rev.Lett.* 109, 139904 (2012)], p. 192301. DOI: [10.1103/PhysRevLett.106.192301](https://doi.org/10.1103/PhysRevLett.106.192301). arXiv: [1011.2783](https://arxiv.org/abs/1011.2783) [nucl-th].
- [291] Varun Srivastava et al. “Science-driven Tunable Design of Cosmic Explorer Detectors”. In: *Astrophys. J.* 931.1 (2022), p. 22. DOI: [10.3847/1538-4357/ac5f04](https://doi.org/10.3847/1538-4357/ac5f04). arXiv: [2201.10668](https://arxiv.org/abs/2201.10668) [gr-qc].
- [292] Nathan Steinle et al. “Implications of pulsar timing array observations for LISA detections of massive black hole binaries”. In: *Mon. Not. Roy. Astron. Soc.* 525.2 (2023), pp. 2851–2863. DOI: [10.1093/mnras/stad2408](https://doi.org/10.1093/mnras/stad2408). arXiv: [2305.05955](https://arxiv.org/abs/2305.05955) [astro-ph.HE].
- [293] Hans Stephani, ed. *Exact Solutions of Einstein’s Field Equations*. 2nd ed. Cambridge Monographs on Mathematical Physics. Cambridge, UK ; New York: Cambridge University Press, 2003. ISBN: 978-0-521-46136-8.
- [294] Andrew Strominger. “Asymptotic Symmetries of Yang-Mills Theory”. In: *JHEP* 07 (2014), p. 151. DOI: [10.1007/JHEP07\(2014\)151](https://doi.org/10.1007/JHEP07(2014)151). arXiv: [1308.0589](https://arxiv.org/abs/1308.0589) [hep-th].
- [295] Andrew Strominger. “Lectures on the Infrared Structure of Gravity and Gauge Theory”. In: (2017). arXiv: [1703.05448](https://arxiv.org/abs/1703.05448) [hep-th].
- [296] Andrew Strominger. “Magnetic Corrections to the Soft Photon Theorem”. In: *Phys. Rev. Lett.* 116.3 (2016), p. 031602. DOI: [10.1103/PhysRevLett.116.031602](https://doi.org/10.1103/PhysRevLett.116.031602). arXiv: [1509.00543](https://arxiv.org/abs/1509.00543) [hep-th].
- [297] Andrew Strominger. “On BMS Invariance of Gravitational Scattering”. In: *JHEP* 07 (2014), p. 152. DOI: [10.1007/JHEP07\(2014\)152](https://doi.org/10.1007/JHEP07(2014)152). arXiv: [1312.2229](https://arxiv.org/abs/1312.2229) [hep-th].
- [298] Andrew Strominger and Alexander Zhiboedov. “Gravitational Memory, BMS Supertranslations and Soft Theorems”. In: *JHEP* 01 (2016), p. 086. DOI: [10.1007/JHEP01\(2016\)086](https://doi.org/10.1007/JHEP01(2016)086). arXiv: [1411.5745](https://arxiv.org/abs/1411.5745) [hep-th].
- [299] Andrew Strominger and Alexander Zhiboedov. “Superrotations and Black Hole Pair Creation”. In: *Class. Quant. Grav.* 34.6 (2017), p. 064002. DOI: [10.1088/1361-6382/aa5b5f](https://doi.org/10.1088/1361-6382/aa5b5f). arXiv: [1610.00639](https://arxiv.org/abs/1610.00639) [hep-th].
- [300] Shuo Sun, Changfu Shi, Jian-dong Zhang, and Jianwei Mei. “Detecting the gravitational wave memory effect with TianQin”. In: *Phys. Rev. D* 107.4 (2023), p. 044023. DOI: [10.1103/PhysRevD.107.044023](https://doi.org/10.1103/PhysRevD.107.044023). arXiv: [2207.13009](https://arxiv.org/abs/2207.13009) [gr-qc].
- [301] Leonard Susskind. “Addendum to Fast Scramblers”. In: (Jan. 2011). arXiv: [1101.6048](https://arxiv.org/abs/1101.6048) [hep-th].

- [302] Leonard Susskind, Larus Thorlacius, and John Uglum. “The Stretched horizon and black hole complementarity”. In: *Phys. Rev. D* 48 (1993), pp. 3743–3761. DOI: [10.1103/PhysRevD.48.3743](https://doi.org/10.1103/PhysRevD.48.3743). arXiv: [hep-th/9306069](https://arxiv.org/abs/hep-th/9306069).
- [303] Stephen R. Taylor. *Nanohertz Gravitational Wave Astronomy*. 1st. CRC Press, 2022. ISBN: 9780367768621.
- [304] ET Science Team. *Einstein gravitational wave Telescope conceptual design study*. ET-0106C-10. June 2011. DOI: [10.5281/zenodo.3911261](https://doi.org/10.5281/zenodo.3911261). URL: <https://doi.org/10.5281/zenodo.3911261>.
- [305] The LIGO Scientific Collaboration, The Virgo Collaboration, and The KAGRA Collaboration. “First joint observation by the underground gravitational-wave detector, KAGRA, with GEO600”. In: (2022). DOI: [10.48550/ARXIV.2203.01270](https://arxiv.org/abs/2203.01270). URL: <https://arxiv.org/abs/2203.01270>.
- [306] K. S. Thorne, R. Price, and D. Macdonald, eds. *Black Holes: The Membrane Paradigm*. Yale University Press, 1986.
- [307] Kip S. Thorne. “Gravitational-wave bursts with memory: The Christodoulou effect”. In: *Phys. Rev. D* 45.2 (2 Jan. 1992), pp. 520–524. DOI: [10.1103/PhysRevD.45.520](https://doi.org/10.1103/PhysRevD.45.520).
- [308] Eric Thrane. “Measuring the non-Gaussian stochastic gravitational-wave background: A method for realistic interferometer data”. In: *Phys. Rev. D* 87 (4 Feb. 2013), p. 043009. DOI: [10.1103/PhysRevD.87.043009](https://link.aps.org/doi/10.1103/PhysRevD.87.043009). URL: <https://link.aps.org/doi/10.1103/PhysRevD.87.043009>.
- [309] Eric Thrane et al. “Probing the anisotropies of a stochastic gravitational-wave background using a network of ground-based laser interferometers”. In: *Phys. Rev. D* 80 (2009), p. 122002. DOI: [10.1103/PhysRevD.80.122002](https://arxiv.org/abs/0910.0858). arXiv: [0910.0858](https://arxiv.org/abs/0910.0858) [[astro-ph.IM](https://arxiv.org/abs/0910.0858)].
- [310] M. Tse et al. “Quantum-Enhanced Advanced LIGO Detectors in the Era of Gravitational-Wave Astronomy”. In: *Phys. Rev. Lett.* 123.23 (2019), p. 231107. DOI: [10.1103/PhysRevLett.123.231107](https://doi.org/10.1103/PhysRevLett.123.231107).
- [311] Makoto Tsuneto, Asuka Ito, Toshifumi Noumi, and Jiro Soda. “A strategy for detecting non-gaussianity of stochastic gravitational waves”. In: *15th Marcel Grossmann Meeting on Recent Developments in Theoretical and Experimental General Relativity, Astrophysics, and Relativistic Field Theories*. 2022. DOI: [10.1142/9789811258251_0227](https://doi.org/10.1142/9789811258251_0227).
- [312] Erik Verlinde and Kathryn M. Zurek. “Modular fluctuations from shockwave geometries”. In: *Phys. Rev. D* 106.10 (Nov. 2022), p. 106011. DOI: [10.1103/PhysRevD.106.106011](https://doi.org/10.1103/PhysRevD.106.106011). arXiv: [2208.01059](https://arxiv.org/abs/2208.01059) [[hep-th](https://arxiv.org/abs/2208.01059)]. URL: <https://doi.org/10.1103/PhysRevD.106.106011>.
- [313] Erik Verlinde and Kathryn M. Zurek. “Spacetime Fluctuations in AdS/CFT”. In: *JHEP* 04.4 (Nov. 2020), p. 209. ISSN: 1029-8479. DOI: [10.1007/JHEP04\(2020\)209](https://arxiv.org/abs/1911.02018). arXiv: [1911.02018](https://arxiv.org/abs/1911.02018) [[hep-th](https://arxiv.org/abs/1911.02018)].

- [314] Erik P. Verlinde and Kathryn M. Zurek. “Observational signatures of quantum gravity in interferometers”. In: *Phys. Lett. B* 822 (Nov. 2021). arXiv:1902.08207, p. 136663. ISSN: 03702693. DOI: [10.1016/j.physletb.2021.136663](https://doi.org/10.1016/j.physletb.2021.136663). arXiv: [1902.08207](https://arxiv.org/abs/1902.08207) [gr-qc].
- [315] Sander M. Vermeulen et al. “An Experiment for Observing Quantum Gravity Phenomena using Twin Table-Top 3D Interferometers”. In: *Class. Quant. Grav.* 38.8 (2021), p. 085008. DOI: [10.1088/1361-6382/abe757](https://doi.org/10.1088/1361-6382/abe757). arXiv: [2008.04957](https://arxiv.org/abs/2008.04957) [gr-qc].
- [316] Robert M. Wald and Andreas Zoupas. “A General definition of ‘conserved quantities’ in general relativity and other theories of gravity”. In: *Phys. Rev. D* 61 (2000), p. 084027. DOI: [10.1103/PhysRevD.61.084027](https://doi.org/10.1103/PhysRevD.61.084027). arXiv: [gr-qc/9911095](https://arxiv.org/abs/gr-qc/9911095).
- [317] Chuming Wang et al. “Boosting the sensitivity of high-frequency gravitational wave detectors using PT -symmetry”. In: *Phys. Rev. D* 106.8 (2022), p. 082002. DOI: [10.1103/PhysRevD.106.082002](https://doi.org/10.1103/PhysRevD.106.082002). arXiv: [2206.13224](https://arxiv.org/abs/2206.13224) [gr-qc].
- [318] J. B. Wang et al. “Searching for gravitational wave memory bursts with the Parkes Pulsar Timing Array”. In: *Mon. Not. Roy. Astron. Soc.* 446 (2015), pp. 1657–1671. DOI: [10.1093/mnras/stu2137](https://doi.org/10.1093/mnras/stu2137). arXiv: [1410.3323](https://arxiv.org/abs/1410.3323) [astro-ph.GA].
- [319] J. Weber. “Detection and Generation of Gravitational Waves”. In: *Phys. Rev.* 117 (1960), pp. 306–313. DOI: [10.1103/PhysRev.117.306](https://doi.org/10.1103/PhysRev.117.306).
- [320] Kate Ziyang Yang, Vuk Mandic, Claudia Scarlata, and Sharan Banagiri. “Searching for Cross-Correlation Between Stochastic Gravitational Wave Background and Galaxy Number Counts”. In: *Mon. Not. Roy. Astron. Soc.* 500.2 (2020), pp. 1666–1672. DOI: [10.1093/mnras/staa3159](https://doi.org/10.1093/mnras/staa3159). arXiv: [2007.10456](https://arxiv.org/abs/2007.10456) [astro-ph.CO].
- [321] Hang Yu, Denis Martynov, Rana X. Adhikari, and Yanbei Chen. “Exposing gravitational waves below the quantum sensing limit”. In: *Phys. Rev. D* 106.6 (2022), p. 063017. DOI: [10.1103/PhysRevD.106.063017](https://doi.org/10.1103/PhysRevD.106.063017). arXiv: [2205.14197](https://arxiv.org/abs/2205.14197) [gr-qc].
- [322] Ya. B. Zel’dovich and A. G. Polnarev. “Radiation of gravitational waves by a cluster of superdense stars”. In: *Sov. Astron. Lett.* 18 (Aug. 1974), p. 17.
- [323] P. -M Zhang, C. Duval, G. W. Gibbons, and P. A. Horvathy. “The Memory Effect for Plane Gravitational Waves”. In: *Phys. Lett. B* 772 (2017), pp. 743–746. DOI: [10.1016/j.physletb.2017.07.050](https://doi.org/10.1016/j.physletb.2017.07.050). arXiv: [1704.05997](https://arxiv.org/abs/1704.05997) [gr-qc].
- [324] Yiwen Zhang and Kathryn M. Zurek. “Stochastic description of near-horizon fluctuations in Rindler-AdS”. In: *Phys. Rev. D* 108.6 (Apr. 2023), p. 066002. DOI: [10.1103/PhysRevD.108.066002](https://doi.org/10.1103/PhysRevD.108.066002). arXiv: [2304.12349](https://arxiv.org/abs/2304.12349) [hep-th].

- [325] Zhi-Chao Zhao and Zhoujian Cao. “Stochastic gravitational wave background due to gravitational wave memory”. In: *Sci. China Phys. Mech. Astron.* 65.11 (2022), p. 119511. DOI: [10.1007/s11433-022-1965-y](https://doi.org/10.1007/s11433-022-1965-y). arXiv: [2111.13883](https://arxiv.org/abs/2111.13883) [gr-qc].
- [326] L. Zhong et al. “Results from phase 1 of the HAYSTAC microwave cavity axion experiment”. In: *Phys. Rev. D* 97.9 (2018), p. 092001. DOI: [10.1103/PhysRevD.97.092001](https://doi.org/10.1103/PhysRevD.97.092001). arXiv: [1803.03690](https://arxiv.org/abs/1803.03690) [hep-ex].
- [327] Kun Zhou, Jun Cheng, and Liangliang Ren. “Detecting anisotropies of the stochastic gravitational wave background with TianQin”. In: (June 2023). arXiv: [2306.14439](https://arxiv.org/abs/2306.14439) [gr-qc].
- [328] Kathryn M. Zurek. “On vacuum fluctuations in quantum gravity and interferometer arm fluctuations”. In: *Phys. Lett. B* 826 (Mar. 2022). arXiv:2012.05870, p. 136910. ISSN: 03702693. DOI: [10.1016/j.physletb.2022.136910](https://doi.org/10.1016/j.physletb.2022.136910). arXiv: [2012.05870](https://arxiv.org/abs/2012.05870) [hep-th].
- [329] Kathryn M. Zurek. “Snowmass 2021 White Paper: Observational Signatures of Quantum Gravity”. In: (May 2022). arXiv: [2205.01799](https://arxiv.org/abs/2205.01799) [gr-qc].
- [330] Lorenz Zwick, David O’Neill, Kai Hendriks, Philip Kirkeberg, and Miquel Miravet-Tenés. “Gravitational wave memory imprints on the CMB from populations of massive black hole mergers”. In: *Astron. Astrophys.* 694 (2025), A95. DOI: [10.1051/0004-6361/202450664](https://doi.org/10.1051/0004-6361/202450664). arXiv: [2404.06927](https://arxiv.org/abs/2404.06927) [astro-ph.CO].
- [331] B. Zwiebach. *A first course in string theory*. Cambridge University Press, July 2006. ISBN: 978-0-521-83143-7, 978-0-511-20757-0.